



Technical University of Madrid (UPM)

School of Naval Architecture and Ocean Engineering (ETSIN)

**EXPERIMENTAL AND STATISTICAL INVESTIGATION OF  
CANONICAL PROBLEMS IN SLOSHING**

AUTHOR

**Elkin Mauricio Botia Vera**

Mechanical Engineer, University of Pamplona, Colombia

DIRECTOR

**Antonio Souto Iglesias**

Professor. DMFPA, ETSIN, UPM

CO-DIRECTOR

**Gabriele Bulian**

Naval Architect, Dott. Ing., Ph.D.

This dissertation is submitted for the degree of

*Doctor of Philosophy*

Ciencias y Tecnologías Navales y Oceánicas

July 2015

# Contents

|  |           |
|--|-----------|
| <b>Abstract</b>  | <b>6</b>  |
| <b>Resumen</b>   | <b>8</b>  |
| <b>Acknowledgements</b>  | <b>10</b> |
| <b>1 Introduction</b>  | <b>11</b> |
| 1.1 General . . . . .  | 11        |
| 1.2 Characteristics of LNG market . . . . .                              | 12        |
| 1.3 LNG carriers . . . . .   | 13        |
| 1.4 Sloshing in LNGC tanks . . . . .                                     | 18        |
| <b>2 Objectives</b>  | <b>24</b> |
| <b>3 Methodology</b>   | <b>26</b> |
| <b>4 Experimental Setup and Data Processing</b>                          | <b>28</b> |
| 4.1 Introduction . . . . .   | 28        |
| 4.2 UPM Sloshing Testing Rig . . . . .                                   | 30        |
| 4.3 Sensors . . . . .  | 35        |
| 4.4 Signal Conditioning, Data Acquisition and Control . . . . .          | 39        |
| <b>5 Forced Regular Motion Sloshing Impacts</b>                          | <b>43</b> |
| 5.1 Introduction . . . . .   | 43        |
| 5.2 Experimental setup . . . . .   | 46        |
| 5.3 Physical Phenomenon . . . . .  | 46        |
| 5.4 Statistical Analysis . . . . .                                       | 54        |
| 5.5 Summary . . . . .  | 72        |
| <b>6 Forced Irregular Motion Sloshing Impacts</b>                        | <b>76</b> |
| 6.1 Introduction . . . . .   | 76        |
| 6.2 Pressure Peak Selection . . . . .                                    | 78        |
| 6.3 Fitting of tail distribution and extreme values statistics . . . . . | 81        |

|          |   |            |
|----------|---|------------|
| 6.4      | Fourier Transformations of the Irregular Driving Motion Signals . . . . . | 85         |
| 6.5      | Results . . . . .   | 89         |
| 6.6      | Summary . . . . .   | 146        |
| <b>7</b> | <b>Coupled Sloshing and Angular Motion</b>                                | <b>151</b> |
| 7.1      | General . . . . .   | 151        |
| 7.2      | Experimental Setup . . . . .  | 153        |
| 7.3      | Results . . . . .   | 158        |
| 7.4      | Summary . . . . .   | 162        |
| <b>8</b> | <b>Fluid Structure Interaction (FSI)</b>                                  | <b>164</b> |
| 8.1      | Experimental Setup . . . . .  | 165        |
| 8.2      | Results . . . . .   | 168        |
| 8.3      | Summary . . . . .   | 172        |
| <b>9</b> | <b>Conclusions</b>  | <b>173</b> |
| 9.1      | Conclusions . . . . .   | 173        |
| 9.2      | Future work . . . . .   | 176        |
|          | <b>Thesis publications</b>  | <b>178</b> |
|          | <b>Bibliography</b>   | <b>190</b> |

# Nomenclature

$1 - CDF$  Exceedance Distribution Function

$2D$  Two Dimensional

$3D$  Three Dimensional

$^{\circ}C$  Celsius Degrees

$A$  Amperes

$A/D$  Analog/Digital

$ABS$  American Bureau of Shipping

$ADC$  Analog Digital Converter

$BIV$  Bubble Image Velocimetry

$CDF$  Cumulative Distribution Function

$CEHINAV$  Technical University of Madrid Model Basin Research Group

$CFD$  Computer Fluid Dynamics

$CoV$  Coefficient of Variation

$DAS$  Data Acquisition System

$deg$  Angular Degrees

$DNV$  Det Norske Veritas

$DOF$  Degrees of Freedom

$ELPs$  Elementary Loading Processes

$EV$  Extreme Value

$FEM$  Finit Element Method

*FLNG* Floating Liquified Natural Gas  
*FSI* Fluid Structure Interaction  
*g* Gravity  
*GPD* Generalized Pareto Distribution  
*GTT* Gaz Transport and Technigaz  
*GUI* Graphic User Interface  
*Hz* Hertz  
*I/O* Input/Output  
*ICP* Integrated Circuit Piezoelectric  
*IEPE* Integrated Electronics Piezo-Electric  
*IHI – SPB* Prismatic IMO type B LNG tanks  
*INVAR* Nickel–iron Alloy  
*ISOPE* International Society of Offshore and Polar Engineers  
*Kg* kilogram  
*kHz* Kilo-Hertz  
*kS* kilo-samples  
*KS2* Kolmogorov-Smirnov Test  
*kW* kilowatts  
*LED* Light-Emitting Diode  
*LNG* Liquified Natural Gas  
*LNGC* Liquified Natural Gas Carrier  
*LRS* Lloyd’s Register of Shipping  
*m<sup>3</sup>* Cubic Meters  
*mA* milliamperes  
*mb* millibars

*mm* Millimeters

*MOM* Method of the Moments

*MOSS* Kvaerner-Moss System Spherical Tanks

*ms* milliseconds

*mV* millivolts

*Nm* Newtons-meter

*PIV* Particle Image Velocimetry

*POT* Peaks Over Threshold

*PSD* Power Spectral Density

*psi* Pounds-Force per Square Inch

*RAO* Response Amplitude Operator

*RP* Return Period

*RTDs* Resistance Temperature Detectors

*SDOF* Single Degree of Freedom

*SPH* Smoothed-Particle Hydrodynamics

*TLD* Tuned Liquid Damper

*UPM* Technical University of Madrid

*USB* Universal Serial Bus

*V* Volts

# Abstract

In hydrodynamics, we refer to *sloshing* as the motion of liquids in containers subjected to external forces with large free-surface deformations. The liquid motion dynamics can generate loads which may affect the structural integrity of the container and the stability of the vehicle that carries such container. The prediction of these dynamic loads is a major challenge for engineers around the world working on the design of both the container and the vehicle.

The sloshing phenomenon has been extensively investigated mathematically, numerically and experimentally. The latter has been the most fruitful so far, due to the complexity of the problem, for which the numerical and mathematical models are still incapable of accurately predicting the sloshing loads. The sloshing flows are usually characterised by the presence of multiphase interaction and turbulence. Reducing as much as possible the complexity of the sloshing problem without losing its essence is the main challenge of this phd thesis, where experimental work on selected canonical cases are presented and documented in order to better understand the phenomenon and to serve, in some cases, as an useful information for numerical validations.

Liquid sloshing plays a key roll in the liquified natural gas (LNG) maritime transportation. The LNG market growth is more than three times the rated growth of the oil and traditional gas markets. Engineers working in research laboratories and companies are continuously looking for efficient and safe ways for containing, transferring and transporting the liquified gas. LNG carrying vessels (LNGC) have evolved from a few 75000  $m^3$  vessels thirty years ago to a huge fleet of ships with a capacity of 140000  $m^3$  nowadays and increasing number of 175000  $m^3$  and 250000  $m^3$  units.

The concept of FLNG (Floating Liquified Natural Gas) has appeared recently. A FLNG unit is a high value-added vessel which can solve the problems of production, treatment, liquefaction and storage of the LNG because the vessel is equipped with a extraction and liquefaction facility. The LNG is transferred from the FLNG to the LNGC in open sea. The combination of partial fillings and wave induced motions may generate sloshing flows inside both the LNGC and the FLNG tanks.

This work has dealt with sloshing problems from a experimental and statistical point of view. A series of tasks have been carried out:

1. A sloshing rig has been set up. It allows for testing tanks with one degree of freedom angular motion. The rig has been instrumented to measure motions, pressure and conduct video and image recording.
2. Regular motion impacts inside a rectangular section LNGC tank model have been studied, with forced motion tests, in order to characterise the phenomenon from a statistical point of view by assessing the repeatability and practical ergodicity of the problem.
3. The regular motion analysis has been extended to an irregular motion framework in order to reproduce more realistic scenarios.
4. The coupled motion of a single degree of freedom angular motion system excited by an external moment and affected by the fluid moment and the mechanical energy dissipation induced by sloshing inside the tank has been investigated.
5. The last task of the thesis has been to conduct an experimental investigation focused on the strong interaction between a sloshing flow in a rectangular section of a LNGC tank subjected to regular excitation and an elastic body clamped to the tank. It is thus a fluid structure interaction problem.



# Resumen

En hidrodinámica, el fenómeno de *Sloshing* se puede definir como el movimiento de la superficie libre de un fluido dentro de un contenedor sometido a fuerzas y perturbaciones externas. El fluido en cuestión experimenta violentos movimientos con importantes deformaciones de su superficie libre. La dinámica del fluido puede llegar a generar cargas hidrodinámicas considerables las cuales pueden afectar la integridad estructural y/o comprometer la estabilidad del vehículo que transporta dicho contenedor.

El fenómeno de *Sloshing* ha sido extensivamente investigado matemática, numérica y experimentalmente, siendo el enfoque experimental el mas usado debido a la complejidad del problema, para el cual los modelos matemáticos y de simulación son aun incapaces de predecir con suficiente rapidez y precisión las cargas debidas a dicho fenómeno. El flujo generado por el *Sloshing* usualmente se caracteriza por la presencia de un fluido multifase (gas-liquido) y turbulencia. Reducir al máximo posible la complejidad del fenómeno de *Sloshing* sin perder la esencia del problema es el principal reto de esta tesis doctoral, donde un trabajo experimental enfocado en casos canónicos de *Sloshing* es presentado y documentado con el objetivo de aumentar la comprensión de dicho fenómeno y por tanto intentar proveer información valiosa para validaciones de códigos numéricos.

El fenómeno de *Sloshing* juega un papel importante en la industria del transporte marítimo de gas licuado (LNG). El mercado de LNG en los últimos años ha reportado un crecimiento hasta tres veces mayor al de los mercados de petróleo y gas convencionales. Ingenieros en laboratorios de investigación e ingenieros adscritos a la industria del LNG trabajan continuamente buscando soluciones económicas y seguras para contener, transferir y transportar grandes volúmenes de LNG. Los buques transportadores de LNG (LNGC) han pasado de ser unos pocos buques con capacidad de  $75000\text{ m}^3$  hace unos treinta años, a una amplia flota con una capacidad de  $140000\text{ m}^3$  actualmente. En creciente numero, hoy día se construyen buques con capacidades que oscilan entre  $175000\text{ m}^3$  y  $250000\text{ m}^3$ .

Recientemente un nuevo concepto de buque LNG ha salido al mercado y se le conoce como FLNG. Un FLNG es un buque de gran valor añadido que solventa los problemas de extracción, licuefacción y almacenamiento del LNG, ya que cuenta con equipos de extracción y licuefacción a bordo, eliminando por tanto las tareas de transvase de las esta-

ciones de licuefacción en tierra hacia los buques LNGC. EL LNG por tanto puede ser transferido directamente desde el FLNG hacia los buques LNGC en mar abierto. Niveles de llenado intermedios en combinación con oleaje durante las operaciones de trasvase inducen movimientos en los buques que generan por tanto el fenómeno de *Sloshing* dentro de los tanques de los FLNG y los LNGC.

El trabajo de esta tesis doctoral lidia con algunos de los problemas del *Sloshing* desde un punto de vista experimental y estadístico, para ello una serie de tareas, descritas a continuación, se han llevado a cabo :

1. Un dispositivo experimental de *Sloshing* ha sido configurado. Dicho dispositivo ha permitido ensayar secciones rectangulares de tanques LNGC a escala con movimientos angulares de un grado de libertad. El dispositivo experimental ha sido instrumentado para realizar mediciones de movimiento, presiones, vibraciones y temperatura, así como la grabación de imágenes y videos.
2. Los impactos de olas generadas dentro de una sección rectangular de un LNGC sujeto a movimientos regulares forzados han sido estudiados mediante la caracterización del fenómeno desde un punto de vista estadístico enfocado en la repetitividad y la ergodicidad del problema.
3. El estudio de los impactos provocados por movimientos regulares ha sido extendido a un escenario mas realístico mediante el uso de movimientos irregulares forzados.
4. El acoplamiento del *Sloshing* generado por el fluido en movimiento dentro del tanque LNGC y la disipación de la energía mecánica de un sistema no forzado de un grado de libertad (movimiento angular) sujeto a una excitación externa ha sido investigado.
5. En la ultima sección de esta tesis doctoral , la interacción entre el *Sloshing* generado dentro en una sección rectangular de un tanque LNGC sujeto a una excitación regular y un cuerpo elástico solidario al tanque ha sido estudiado. Dicho estudio corresponde a un problema de interacción fluido-estructura.

# Acknowledgements

Foremost, my most sincerely thanks goes to my family for the support they provided me through my entire life and in particular, I must acknowledge my mother, whose love and her constant support contribute considerably in my personal and professional success.

I would like to express my gratitude to my supervisor, Dr. Antonio Souto Iglesias, whose expertise, understanding, and patience, added considerably to my graduate experience. His guidance helped me in all the time of research and writing of this thesis. I could not have imagined having a better mentor for my Ph.D study.

I would like to acknowledge and extend my heartfelt gratitude to Dr. Luis Perez Rojas, director of the Towing Tank Basin of the Polytechnic University of Madrid and all of its staff members for their invaluable knowledge and experience forwarded to me. A very special thanks goes out to Dr. Gabriele Bulian. I would like to thank him for the professional guidance and support. Whose contributions made possible the publishing of the most important publications related to this thesis.

My heartfelt thanks goes to all my friends, their support, patience and motivation, specially in moments of doubt and non-clearness are invaluable. I express my most sincerely thanks and gratitude to the doctoral program of the Polytechnic University of Madrid, this research would not have been possible without the support, both academic and financial provided by the institution during the Phd period.

# Chapter 1

## Introduction

### 1.1 General

The sloshing phenomenon can be defined as the violent movement of liquids inside partially filled containers as a result of the violent fluid motion, severe hydrodynamic loads, traduced in structural damages in the container walls and loss of stability of the vehicle transporting the containers may be induced. The prediction of these loads defined by the hydrodynamic pressure distribution, forces, moments and natural frequencies of the free-liquid surface and its application in liquid production, storage and carrying process is the main challenge for mechanical, aerospace, civil, nuclear and naval engineers as well as for physicists and mathematicians.

In the last few decades researchers have investigated sloshing of liquid numerically as well as experimentally. Abundant literature can be found related to liquid sloshing; the most prominent and indispensable review was compiled by Ibrahim (2005) who treats the fundamentals of liquid sloshing from the basic theory to advanced analytical and experimental results. Another prominent work is the manual by Faltinsen and Timokha (2009), where the sloshing phenomenon is discussed through several theoretical and experimental results by treating topics of special interest in the marine area, such as antiroll tanks, linear sloshing, viscous wave loads, damping, and slamming.

Sloshing research has extended to different application areas such seismology where the effects of liquid sloshing have been studied on water tanks and large dams subjected to earthquake excitation (Novo et al., 2013). In the aerospace industry, the sloshing generated by the propellant play a key roll in the vehicle stability (Abramson, 1966), same concept is applied to on-land liquid carrying process where the vehicle stability plays a key roll in dangerous liquid transportation. But not always sloshing is considered as a negative effect, in the building industry case, liquid tanks on roofs are employed as passive dampers to mitigate the movement of the structure due to wind loading or ground

motions (Kareem et al., 1999) and antiroll tanks in vessels to dampen roll motion (see e.g. Souto-Iglesias et al. (2006)). Sloshing phenomenon is also an important issue in the oil and gas industry specifically in the carrying process of LNG where the ships have to be designed against not only the static pressure but also the dynamic pressure generated by sloshing when the ship moves across the ocean where the severe environmental conditions together with the sloshing phenomenon may also affect the motion and stability of the ship.

Sloshing is applicable to different engineering areas and its depends on the type of external loads, amplitude and frequency of the vehicle-container motion, liquid-fill depth, liquid properties and container shape where the free liquid surface may experience different types of motion. This thesis is an experimental study of the sloshing mainly focused on the maritime transporting of LNG.

## 1.2 Characteristics of LNG market

The natural gas is gaseous fossil which can be extracted from both oil-gas fields and isolated gas fields. It is composed, approximately by 95% methane ( $\text{CH}_4$ ) and others hydrocarbons in less quantity such ethane ( $\text{C}_2\text{H}_6$ ), propane ( $\text{C}_3\text{H}_8$ ), butane ( $\text{C}_4\text{H}_{10}$ ) and nitrogen ( $\text{N}_2$ ). The gas is colorless, odorless, non-toxic, non-carcinogenic and lighter then air (approx. 50% density of air).

According to the *BP Statistical Review of World Energy 2014* (BP, 2014), the worldwide proved natural gas reserves in 1993 were estimated in 118.4 trillion cubic meters, 155.7 trillion cubic meters in 2003 and 185.7 trillion cubic meters in 2013. The worldwide natural consumption in billion cubic meters in 2003 was of the order of 2596.6 and 3347.6 in 2013. Natural gas producers in descending order are Europe-Eurasia (30.6%), North America (26.9%), Asia-Pacific (14.5%), Middle East (16.8%), South and Central America (5.2%) and Africa (6%). Gas producers do not always overlap with gas consumers, large consumers by regions, in descending order are the following: Europe-Eurasia (31.7%), North America (27.8%), Asia-Pacific (19%), Middle East (12.8%), South and Central America (5%) and Africa (3.7%). Consumption of natural gas worldwide is projected to increase by an average of 2.2 percent annually, this increasing seems to be covered by the estimated 185.7 trillion reserves for many years. New oil-gas fields and isolated gas fields are continuously being discovered, thus, some of the already consumed reserves are being recovered.

Since the location and production of natural gas does not always match, a need of transporting the gas arises. Currently approximately 75% of volume is transported by pipelines and the rest 25% by cargo containments systems. Cargo containment systems are actually the most reliable way of long distance overseas transportation of large volumes of gas in a reduced cost-effective space. Cargo containment systems commonly carry the gas in the liquid form, called LNG (Liquified Natural Gas). LNG is obtained by the process of

cooling the natural gas down to a temperature of  $-163^{\circ}\text{C}$  approximately at atmospheric pressure. The liquid obtained has density of  $0.42\text{ t/m}^3$ . LNG maritime transporting has increased dramatically together with the increasing in volume transportation, safety and cargo containment systems technology evolution. LNG carriers evolution, tank systems for LNG transporting and the *Sloshing* phenomenon associated to the transporting of the LNG, will be described in the following sections.

### 1.3 LNG carriers

Liquid sloshing play a key roll in the liquified natural gas (LNG) maritime transportation. The LNG market growing is at more than three times the rated growing of the oil and traditional gas markets. This growth of the natural gas market has led to a growth in the size of LNG tankers, which are increasing in capacity and decreasing in transportation cost. However larger LNGC containers may suggest larger sloshing loads. The first LNG carrier was the Methane Pioneer 1.1, taken into service in 1959. It was a merchant vessel converted to a cargo ship capable of carrying  $640\text{ m}^3$ . Due to the success of the first LNGC, following carriers such as the Methane Princess shown in figure 1.2 and its twin Methane Progress with a capacity of  $34500\text{ m}^3$  were taken into service in 1964 . Today the majority of the new ships under construction are in the size between  $210000\text{ m}^3$  and  $266000\text{ m}^3$  and are equipped with a re-liquefaction plant, most significant are the Q-Flex and Q-Max LNGC, latter one shown in figure 1.3.



Figure 1.1: Methane Pioneer, the first LNG carrier



Figure 1.2: Methane Princess, a  $34500\text{ m}^3$  LNG carrier



Figure 1.3: Q-Max, modern fleet of a  $266000\text{ m}^3$  LNGC



### 1.3.1 Tank systems for gas transporting

Since the first LNG marine transporting system (Methane Pioneer) taken into service in 1959, LNG Cargo Containment System has been developed into different types of LNG transport in accordance with the development of materials and manufacturing technologies, the evolution of the cargo systems has follow mainly two tank design lineup to know: The membrane-type tanks and self-supporting tanks also called independent type tanks. Figure 1.4 shows the typical types of LNG cargo containment system separated into the two aforementioned design lineup groups. Self-supporting tanks are that they are independent

| SELF-SUPPORTING TANKS  |  | MEMBRANE-TYPE TANKS   |  |
|--|--|---|--|
| IHI-SPB (a)  | MOSS (b)   | GTT NO 96 (c)   | GTT Mark-III(d)  |
|  |  |  |  |
| Al alloy 5083<br>Max. 30mm   | Al alloy 5083<br>50mm  | Invar 0.7mm   | SUS 304L 1.2mm   |
| PUF 270mm  | PUF 250mm  | Plywood+Perlite<br>530mm  | R-PUF 270mm  |

Figure 1.4: Types of LNG cargo containment system

from the hull and do not directly transmit the fluid loading to the hull plating, but only integrated forces through the supports. Whereas membrane-type tanks are supported by the hull steel structure. Although the reputation of the membrane-type tanks was slightly affected by the sloshing issues, the membrane-type tank has played a major role in LNG marine transportation, because of the economical advantages in manufacturing, storage efficiency and operational reliability (Kuo et al., 2009).



## Self-supporting tanks

The fleet of LNG carriers with self-supporting tanks is dominated by the Moss spherical tank design (Figure 1.4 (b)). Spherical tanks show a favorable fluid behavior that minimises sloshing loading by allowing ship acceleration energy to be transformed to a rotation of the bulk LNG. The first LNG carrier with spherical tanks, the so-called Kvaerner-Moss System (MOSS), was the "Norman Lady" ( $87600\text{ m}^3$ ) launched in Stavanger, Norway in 1973. Although the first carriers had storage tanks that were made of 9% nickel-steel, that technology was quickly replaced by aluminium tanks. Aluminium storage tanks proved to be more resistant to mechanical stress, rupture, and it was easier to correctly form them into a sphere. MOSS tank system can be fabricated entirely, thus allowing the shipyard to construct the hull and the tanks in parallel and then install the entire tanks in the hull. As the LNG is kept at  $-163^\circ\text{C}$ , the steel structure needs to be covered with an insulation system composed by several different layers, some of which are: glass wool, aluminium "foil" and various expansion foams. Until year 2000, 54% of all LNG carriers were spherical, primarily because Japanese shipyards had a license for the construction of only this type of ships, and since at the same time the Japanese are the largest LNG importers. Today, membrane type ships have "surpassed" the spherical ships in number. One of the future advantages of the spherical tanks will be for the terminals which will be located in the polar region (Russia).

The IHI-SPB (Prismatic IMO type B LNG tanks) shown in Figure 1.4(a), was developed by the Ishikawajima-Harima Heavy Industries since 1960 till 1985. Only two  $87,500\text{ m}^3$  vessels currently have this IHI-SPB containment system, the *Polar Eagle* and the *Arctic Sun* taking into service in 1993. IHI-SPB tanks are made by using aluminum alloy 5083 with a maximum thickness of 30 mm. No sloshing problems ever happened on IHI-SPB LNG tanks, this feature is inherent to its arrangement of internal structures, especially bulkhead, which leads to the advantage that it can avoid resonance between internal liquid motion and ship motion. This is an important advantage over Membrane LNG carrier tanks which may break due to sloshing impact, therefore destroying the ship's hull. This is also of prime relevance for FPSO LNG (or FLNG) future designs.

## Membrane-type tanks (GTT Technology)

Presently, the membrane system dominates among new constructions. A reason for this fact is the inherent inefficiency of hull space usage in ships with the MOSS system, resulting in high tonnage canal fees and a large hull height of such ships, resulting in constraints regarding passing under bridges in terminals. GTT technology represents two main types of membrane-type ships and recently, after the union between Gaz Transport and Technigaz in 1994, a third type of membrane-type carriers emerged.

The two basic concepts of GTT technology are the Mark III and No. 96 system shown in figure 1.4 (c)(d). The membrane-type ships were developed during the 1960s, and both concepts use a thin flexible metal "membrane" which is in contact with the cargo. The system has the characteristics of a sandwich where the cargo presses on the membrane; the insulation material presses on the membrane and in the end, everything leans on the ship's inner hull. This sandwich type assembly disposition can be shown in figure 1.5, where two membranes and two insulation material can be appreciated together with the ship's inner hull and the final assembly disposition. Both No. 96 Mark III tanks includes a pump tower thus allowing the LNG loading and discharging by the using of pumps, pipes and level gauges which are supported by 3 or 4 vertical pipes and a number of bracing members. The pump tower is typically located near the center of the aft transverse bulkhead.

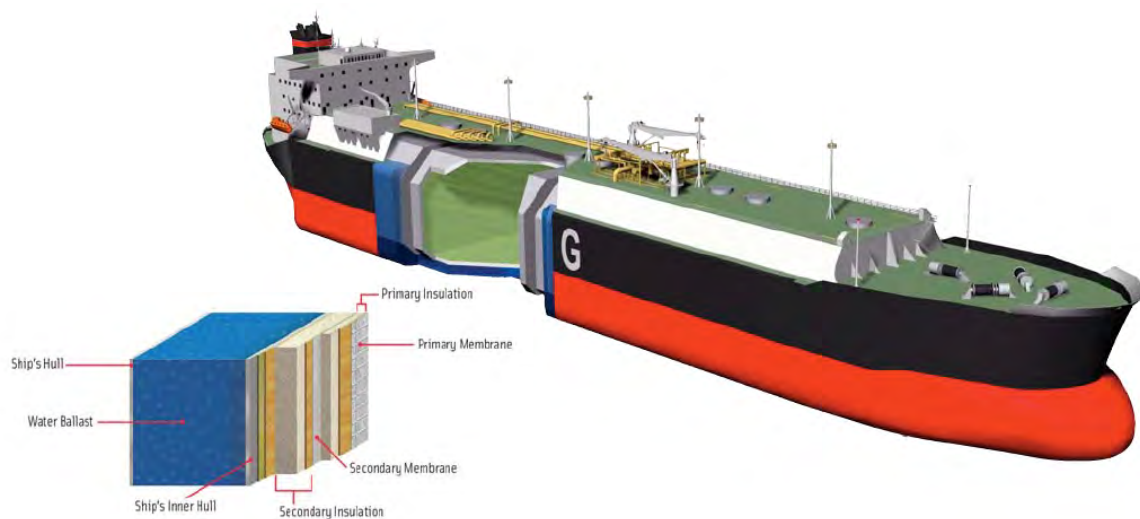


Figure 1.5: Membrane LNG cargo containment system

- No. 96 System – (Gaz Transport System)

The primary and secondary membranes are equal in this system and they are made of INVAR, and each membrane is only 0,7 millimetres thick. INVAR is a material containing 36% nickel and the rest is steel, and as such has a minimal, that is, negligible dilatation coefficient. This system uses plywood boxes filled with perlite as insulation. Perlite is a material based on treated volcanic rocks and has good insulation characteristics which do not change over time. The system is made of a primary membrane which leans on the first insulation layer, a secondary membrane which leans on the second insulation layer and finally, the second insulation layer leans on the ship's inner hull. The total thickness of the system amounts to 0, 5 meters. Figure 1.5 shows the schematic assembly of this membrane-insulation system.

- Mark III System – (Technigaz System)

The primary membrane in this system is made of low-temperature stainless steel and has a thickness of 1,2 millimetres. Since steel has a significant dilatation coefficient, these membranes are well-defined and the joints enable them to move in two directions under light loads. As insulation material for these ships, the polyurethane foam is reinforced with fibreglass. The secondary barrier is much cheaper and simpler, and is made of triplex. Triplex is a type of a plastic mass which is vapour permeable but which on the other hand can contain liquid. The total thickness of the system depends on the type of project for which the ship is intended. In both membrane systems, boil-off of 0, 15% is guaranteed although in reality its quantity is much smaller. Until 2000, there were only a few membrane ships but due to their significant flexibility and changes in the LNG spot market, in the past few years they have "surpassed" spherical ships in number. This type of ship is mostly produced in South Korea, but China has "produced" three membrane LNG carriers in the past three years.

Membrane LNG tankers are of interest in this thesis due to their susceptibility to violent fluid impacts generated by the sloshing phenomena.

## 1.4 Sloshing in LNGC tanks

The sloshing physics in LNGC tanks is indeed complex due to the numerous physical phenomena involved. The main characteristic of the sloshing in LNGC tanks is the high nonlinearity and randomness of the fluid flow. Depending of the fluid acceleration, container shape, filling level and fluid phase, different kind of flows take place in the container. High velocity overturning and breaking waves with or without gas entrapment, gas cushion, run-up of fluid and slamming are common. The mixture between the liquid and the boiled gas induce compressibility, flow separation and turbulence.

In every flow case and depending of its intensity, hydrostatic and dynamic pressures are generated in the tank walls. Every flow impact towards the walls may generate the called *pressure peaks* which are dynamic loads characterized by high intensity pressure values in a short duration; similar to a pulsating load, these pressure peaks can induce damages in the integrity of the container. Characterizing the pressure peaks both spatially and temporally and estimating the influence of the pressure peaks in the structure during the life service of the container is the main aim of the sloshing research in LNGC tanks.

Sloshing dynamics is highly dependent on the filling level, which is a variable inherent to the LNG trade specially during transfer processes. Filling levels between 10%-30% of the tank height  $H$  show a typical fluid dynamic phenomenon called *hydraulic jump* or

*bore* (DNV, 2006). Dynamically, is a non breaking wave which travels at high speed and cause large impacts in the both longitudinal and transversal bulkheads of the LNGC tanks. Figure 1.6 shows a hydraulic jump in a longitudinal section of a LNGC. Gas is not entrapped during its occurrence and therefore the process can be modelled as incompressible.

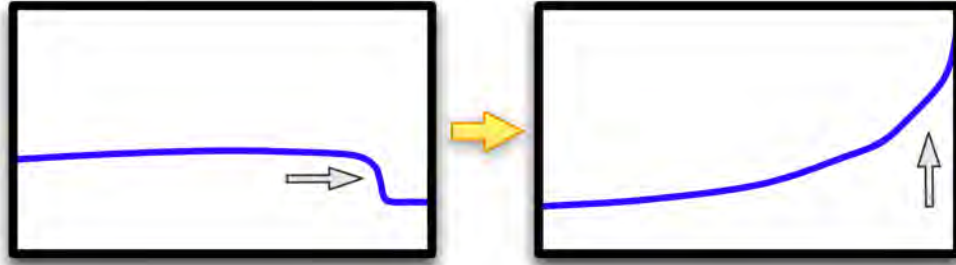


Figure 1.6: Hydraulic Jump or Bore

In some cases the violent free surface motion produces *breaking waves*. The dynamics of this phenomenon is similar to the *hydraulic jump* with the exception that some gas is entrapped previously to wall impact. Therefore the process can be considered as compressible. An oscillation can be noticed in the pressure peak generated, due to the presence of a pulsating gas bubble (with the effect of gas compressibility). The frequency of this oscillation is proportional to the dimensions of the bubble entrapped, and to the characteristics of the gas (Lugni et al., 2010). Figure 1.7 shows the dynamic scheme of the *breaking waves* phenomena.

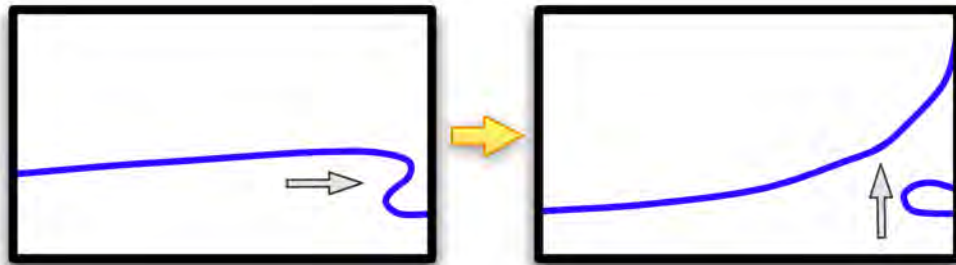


Figure 1.7: Breaking Wave

In high filling levels between 40%-70% the traveling and breaking waves disappear and roof impacts may take place. Gas pockets can be generated during this process (Loysel et al., 2012). Figure 1.8 shows the dynamic scheme of the *run-up* phenomena in the longitudinal and transversal bulkheads. An oscillation can be noticed in the signal of the pressure, due to the pulsating gas bubble (with the effect of gas compressibility).

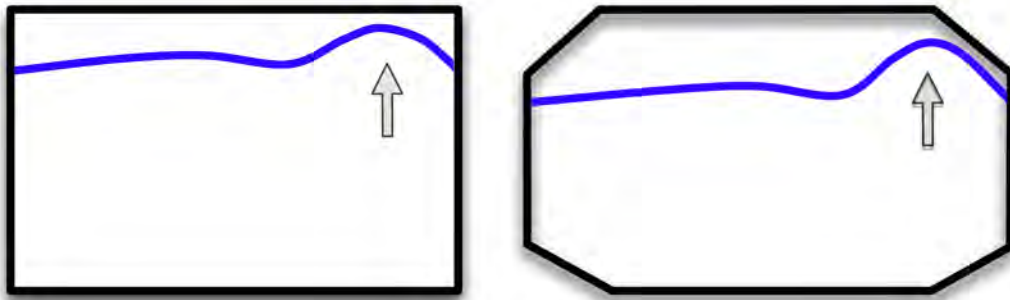


Figure 1.8: Roof Impacts

Filling levels have been rigorously protocolled in the operation of these vessels to keep the sloshing induced damages associated with partial fillings under control, with the by-product of inducing significant losses of economical efficiency and/or operational flexibility. Nonetheless a new vessel concept, consisting of natural gas floating liquefaction units (FLNG) is nowadays under consideration (Pastoor et al., 2009; Diebold, 2010). Partial fillings should be feasible for these vessels and for the LNG carriers to which the liquefied gas is offloaded. The increase in cargo capacity and the partial fillings are associated with potentially larger dynamic loads due to the possible presence of severe sloshing phenomena. To soundly incorporate such loads in the design cycle, the prediction/modelling of sloshing related loads is hence extremely important, from an engineering point of view, for the safe transport of the cargo, especially considering the fact that harsh environmental conditions can be encountered during the ship operation.

At the same time, sloshing impact loads represent a complex issue due to the physical phenomenon being highly nonlinear. For many years, the problem of sloshing loads on cargo hold structures has been addressed both experimentally and through computational fluid dynamics tools. Notwithstanding the advances in computational fluid dynamics tools, the complexity of the problem still requires, in most cases, the application of the direct experimental approach. The experimental sloshing assessment procedures for LNG vessels and floating production and storage units are based on risk assessment techniques (DNV, 2006; LRS, 2009; Gervaise et al., 2009; Kuo et al., 2009; Diebold, 2010).

In such procedures, the statistical characterization of the sloshing loads relies, in most of the cases on the data obtained from model scale experimental campaigns. Significant material and human resources need to be allocated in order to carry out these campaigns. Nonetheless, obtaining comparable results from different facilities is still an open problem (Kim et al., 2012; Loysel et al., 2012, 2013a). Due to the extra costs that derive from these campaigns, a mid-term goal of designers is to characterize sloshing loads using CFD technologies.

Controlled full scale experiments are extremely complex and only the ground-breaking SLOSH project (Kaminski and Bogaert, 2009) has been able to shed some light into full scale characteristics of sloshing impacts as well as identify elementary loading models (Lafeber et al., 2012) associated with those impacts. During the SLOSH project, four categories of wave impacts were identified depending on the advancement of the breaking process when hitting the wall, the different identified lateral wave impacts can be seen in figure 1.9.

Unfortunately, however, applying those procedures is not viable for routine industry

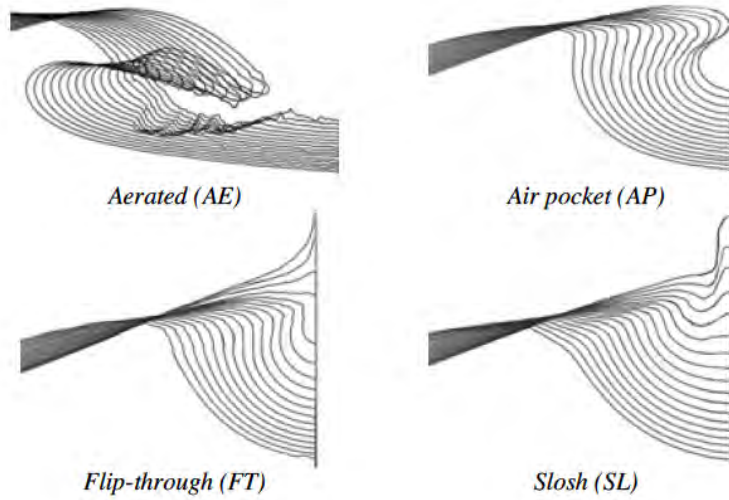


Figure 1.9: Different Kind of Lateral Wave Impacts

sloshing assessments. Hence, the most reliable and controllable source of knowledge regarding sloshing impact pressure loads comes from scale model experiments under regular or irregular excitation with different numbers of degrees of freedom (DOF) for the tank containing the fluid. Notwithstanding the obvious higher feasibility of model scale experiments, their setup execution and subsequent analysis is complicated due to many factors (scale, two-dimensionality, repeatability, behavior of pressure sensors, ullage pressure, hydroelastic behavior of the employed structures, etc.), making a proper and meaningful experimentation still a challenging research topic.

Sloshing experiments using regular excitations may be of limited use due to the high non-linearity of the sloshing phenomena. Notwithstanding this, transfer functions for narrow banded sea spectra have been elaborated by authors such as Gran (1981), and a regular excitation analysis is used in the pre-screening phases of LNG sloshing assessment procedures by important stake-holders such as Hyundai, which is the leading LNG carriers shipbuilder (Park et al., 2011). Harmonic motions were also used by Kim et al. (2010), who performed both 2D regular motion and 3D irregular motion experiments. They sta-

tistically analyzed different properties of impacts (impact pressure, rising time, duration, etc.) through scatter plots and distribution fitting. However, the type of experimental data presented therein did not allow a direct comparison between the two-dimensional and the three-dimensional case, due to the differences in tanks and forcing.

Chen et al. (2013) recently published experimental data obtained with regular angular motion sloshing tests, focusing on run-up events, and used this data to validate their own SPH method simulations. More interestingly, regular motion impacts can be used to systematically explore the low probability levels of certain types of impacts, such as those arising from the influential SLOSHEL JIP project elementary loading processes (ELPs) taxonomy (Lafeber et al., 2012).

Furthermore, Song et al. (2013) recently investigated the kinematics and dynamics of sloshing impact events using regular motions, looking at the correlation between impact pressures and velocities, with the latter measured by means of the bubble image velocimetry (BIV) technique. Focussing on a single specific excitation case, they were able to find consistent pressure-velocity correlations and substantially different correlation factors depending on whether lateral or roof impacts were considered.

In regards to sloshing physics in general, significant contributions are due to Lugni et al. (2006, 2010), who described the extraordinary accelerations associated to wave impact events. Their work is nonetheless not specifically devised so as to be useful as a reference for CFD validation attempts. If the focus is put on to the statistical characterization of sloshing pressures, major contributions are due to Graczyk and Moan (2008); Graczyk et al. (2007) who provided a statistical fitting for long series of sloshing impact pressure recordings aimed at building simplified models of sloshing events load histories for structural finite element analysis.

Repeatability in sloshing tests has not received much attention in the literature. Bogaert et al. (2010) paid attention to wave heights during single impacts experiments within the SLOSHEL project, finding variation coefficients of the order of 1%. Kimmoun et al. (2010), in the framework of the same project, looked at pressure records but with a limited set of repetitions, not large enough to obtain general conclusions.

With the aim of addressing the influence that experimental uncertainties may have on extreme pressure peaks statistics, sensitivity of impact pressures statistics to minor variations in the experimental setup and parameters (filling levels, motion amplitudes, etc..) is recently receiving more attention. As examples of such efforts, and within the framework of a benchmark led by GTT (Loysel et al., 2012, 2013a), Mehl and colleagues looked at the influence of motion characteristics (Mehl et al., 2013a) and filling levels (Mehl et al., 2014) on such statistics. Within the conditions considered in the benchmark, the single impact

ones were selected for the motion sensitivity analysis. The influence of motion amplitude, period, and basic motion formula were analyzed. The shape of the free surface during the events and the impact pressure average values were shown to significantly depend on such minor variations.

Regarding the filling level sensitivity, Mehl et al. (2014) found, once again for single impact conditions, that filling level variations of the order of 1mm at model scale did not produce any significant effects on impact pressure statistics. A similar analysis was carried out by Neugebauer et al. (2014) who, in turn, found a significant influence for filling level differences of around  $\pm 1$  mm (on fillings of the order of 800mm). However, their quantitative analysis of the sensitivity of the results to the filling level may have been too limited in order to consider their outcomes clear and conclusive.

Interesting sensitivity analyses have also been conducted by Choi et al. (Choi et al., 2010, 2012) and by Pistani and Thiagarajan (Pistani and Thiagarajan, 2012). They looked at the influence of minor variations in the mounting (flushness) of the sensors. According to Choi et al. (Choi et al., 2010, 2012), mounting differences as small as 1mm could induce a large influence on the pressure registers; Pistani and Thiagarajan did not, on the other hand, find such a strong dependence.

Regarding the two-dimensionality of the flow in planar motion sloshing impacts, Schreier and Mehl (2012) provided some insight into the matter. They used translational motions with two tanks of different widths within the aforementioned GTT ISOPE 2012 benchmark (Loysel et al., 2012) finding larger pressures with the thinner tank. This aspect is relevant since the CFD codes used for these problems are, for the moment, usually run considering 2D flows, with their outcomes validated through a comparison with real experiments in which the actual two-dimensionality of the flow is not discussed in depth. Along the same line, but comparing, using regular motions, a 3D model of a membrane tank and a section of such tank, Kim et al. (2013) looked at the influence of such full 3D and 2D configurations on the top 10% impact pressure average values. They found the 3D values to be larger than the 2D ones in the majority of considered cases.



# Chapter 2

## Objectives

The nature of sloshing phenomenon is investigated in the present thesis using experimental techniques. The simplest configurations able to keep the most relevant features of the phenomenon are sought. The specific objectives are set aiming at addressing the open questions referred in chapter one. They are:

1. Determine the statistical properties of the pressure field during impact events due to forced harmonic angular motions in a rectangular tank. To do so, the answers to the following questions are sought:
  - (a) Is the statistical distribution of the maximum impact pressure different from peak to peak?
  - (b) In case of differences, is there convergence to a steady-state for the distribution as the impact number increases? And if so, which is the steady state result?
  - (c) Is there any correlation or dependence between peak pressures registered at different peaks?
  - (d) Can we obtain information on the distribution of the impact pressure using a single very long experiment? In other words, can we consider the process “practically ergodic” as it is often implicitly done in practical applications?
  - (e) How are measurements affected by the sensor type?
2. Investigate the statistical properties of impact pressure in force irregular motions. The following questions can be addressed:
  - (a) Is the statistical distribution of the maximum impact pressure measured during irregular roll motion similar in different realizations of the same experiment?
  - (b) How is the impact pressure distribution affected by variations in driving motion?
  - (c) Depending of the choice of the fit of statistical distribution, how does this selection affect the extreme pressure values estimation?

3. Investigate the capabilities of sloshing flows, in a rectangular tank able to rotate freely, to interact and dissipate an external power. A coupled sloshing configuration will be setup with the external perturbation provided through a harmonic moving mass thus creating a moment on the system. The following questions may be addressed:
  - (a) Which is the system response with the empty tank?
  - (b) How does the response change with the tank partially filled with fluids of different viscosity?
  - (c) How does the response when the moving mass excites the system with different frequencies and amplitudes?
  - (d) Is the fluid an enhancer or damper of the system motion?
4. Investigate the interaction between sloshing flows in a rectangular tank subjected to harmonic roll motion and a deformable body attached to the tank inside the flow. Address the question of the influence of the body length and clamping position on the body motion and the fluid structure interaction.

# Chapter 3

## Methodology

To achieve the objectives enumerated in previous chapter the following tasks will be undertaken:

1. New capabilities will be implemented in the existing sloshing rig. Those capabilities are composed by the replacement of the rig actuator by incorporating a linear actuator capable of perform regular and irregular roll motions, together with the possibility of incorporate starting and ending ramps in the imposed motions. A new set of pressure sensors will be incorporated together with a new data acquisition system. The qualitative point of view of the sloshing phenomenon will be covered by the using a high speed camera and high resolution photographs. Special attention will be paid to the experimental sensitivity parameters and the repetitiveness of the experiments.
2. A new set of scaled rectangular sections of LNG sloshing will be built. Two different types of sensors housing will be prepared in the locations nearby to the place where the sloshing phenomenon take place.
3. Software and hardware tools will be implemented in order to create a non assisted sloshing rig capable of performing several experiments in a reduced execution time. Chapter 4 of the thesis will cover these three items.
4. Regular motion test matrix will be defined and experiments conducted and analysed. This analysis has ben included in chapter 5.
5. Irregular motion test matrix will be defined and experiments conducted and analysed in chapter 6. A new software tool will be developed in order to facilitate the pressure peaks data post-processing during the irregular experiments realisations.
6. In the coupled problem a mechanical model for the empty tank case will be defined and validated with decay tests.

7. For the same case, a test matrix covering different motion amplitudes of the moving mass motion frequency and liquids with different viscosity will be defined and experiments conducted. The coupled problem will be the subject of chapter 7 of the thesis.
8. For the FSI problem, a dedicated tank with clamp mechanism and probes will be built. A test matrix with different probs series and clamping positions will be defined and experiments conducted and documented in chapter 8 of this thesis.
9. Conclusions and future work threads will be enumerated to close the thesis.

# Chapter 4

## Experimental Setup and Data Processing

### 4.1 Introduction

The research on sloshing from the experimental point of view has been mainly led by classification societies like DNV, ABS or LRS. Obtaining a detailed description of these experiments is often difficult due to the confidentiality of these studies. Berg (1987) and Olsen (1976) both for DNV and Bass et al. (1985) studied the impact pressures in sloshing flows, as well as the very interesting and intricate issue of the scaling of sloshing experimental values to full scale. In another seminal work, Gran (1981) used a regular excitation tests as the basis for predicting the impact pressure distribution under irregular excitation. These studies suffered from limitations due to the limited recording and sampling capabilities of the data acquisition systems, that were state of the art at that time. They were not capable of capturing high frequency modes in the pressure signals nor long series of data which were necessary to perform a rigorous probabilistic analysis.

The situation has evolved in the last 40 years from those seminal studies by incorporating recent data acquisition and motion technologies. Nowadays the sloshing rigs are more complex and accurate and the number of sensors and degrees of freedom have increased. Depending on the degrees of freedom (DOF), the sloshing rigs can be classified as rod-crank(1 DOF), cradle(2,3 DOF) and hexapods (6 DOF). Several sloshing rigs can be found in literature, i.e with one degree of freedom in linear displacements (Panigrahy et al., 2009; Eswaran et al., 2009) or angular motion rigs(Akyildiz and Ünal, 2005) and six degrees of freedom platforms that allow the reproduction of complex ship motions(Pistani et al., 2010).

The more complex sloshing rigs nowadays are collected and compared in the *First & Second Sloshing benchmarks* (Loysel et al., 2012, 2013b). This study was coordinated by GTT who

aims at comparing measurements, especially impact pressures, from sloshing model tests, performed by different laboratories, involving the same nominal input conditions. The participants of this study have been the Ecole Centrale de Marseille (ECM), Ecole Centrale de Nantes paired with Bureau Veritas (ECN-BV), Gaztransport et Technigaz (GTT1,2,3), Marintek, Pusan National University (PNU), Universität Duisburg-Essen (UDE), Technical University of Madrid (UPM) and Universität Rostock (UR). Figure 4.1 shows the sloshing rigs of the aforementioned laboratories. Detailed descriptions and capabilities of

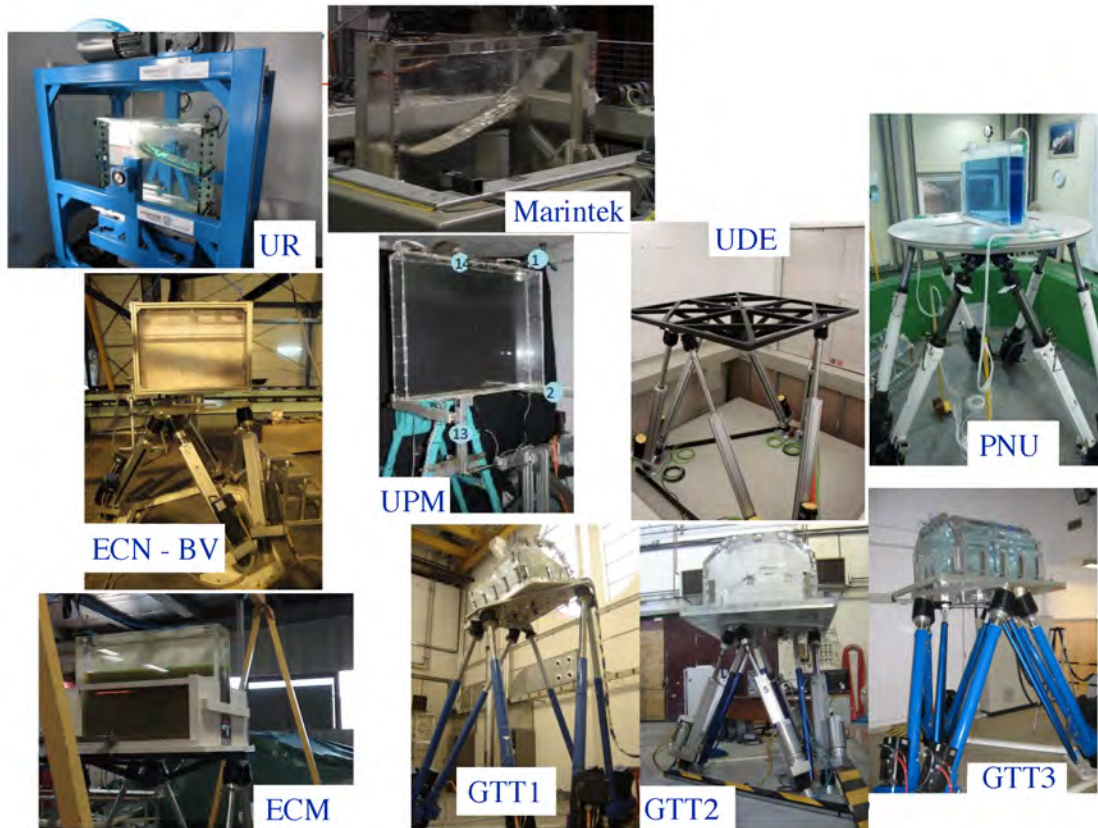


Figure 4.1: Sloshing Testing Rigs

some sloshing rigs can be found in: Bureau Veritas (Baudin E., 2013), Gaztransport et Technigaz (Gervaise et al., 2009), Marintek (Graczyk et al., 2012) and Pusan National University (Kim et al., 2009).

## 4.2 UPM Sloshing Testing Rig

The experimental testing rig presented in this chapter <sup>1</sup> corresponds to the sloshing laboratory of the CEHINAV group at Technical University of Madrid (UPM). It was installed in 2003 and continuously upgraded ever since. The original testing rig is shown in figure 4.2. The rig was used by *Louis Delorme* during his PhD (Delorme, 2009). The driving system is a rod-crank mechanism at the back of the rig that transforms the rotational motion of an electrical engine (element 10 in figure 4.2) into a harmonic rolling motion of the moving part of the rig (elements 1, 2, 13 in figure 4.2) at the front. This moving part is designed to embrace a partially filled tank (figure 5.2). The back and front parts of the rig are connected by a steel shaft (element placed from points 3 to 4 in figure 4.2). The crank can be attached to the rod (element 11 in figure 4.2) at different positions, making it possible to change the amplitude of the roll motion from 2 to 15 degrees with increments of 1 deg. Although differently dimensioned, the underlying concept of the testing rig is similar to the one used by Akyildiz and Ünal (2005).

The harmonic rolling motion of the crank is transmitted to the moving part of the rig through a torque transducer with a maximum rated torque of 200 Nm (element 3 in figure 4.2). The maximum roll frequency is 2 Hz. This depends mainly on the admissible torque of the torque transducer. Higher frequencies mean transmitting a larger torque to the moving part and this could saturate the torque meter device. A 5000 pulses rotary optical encoder Heidenhain ERN120 with a precision of 0.072 deg (element 4 in figure 4.2) registers the roll angle at the roll shaft.

The upper and lower arms (elements 1 and 2 in figure 4.2 respectively) of the moving part of the rig can be displaced along a vertical linear guide (element 13 in figure 4.2). This allows easy modification of the vertical position of the tank from one test to another. The bottom arm has two side telescopic supplements which are designed to easily hold tanks of different breadths. At the lower end of the linear guide a linear digital wire encoder (number 7 in figure 4.2) has been connected. In conjunction with the shaft encoder they register the harmonic rolling motion. The use of a linear encoder HONTKO HLS-S-05 increases the angle measurement up to a 0.0012 deg of resolution.

The angular speed control is carried out with a frequency inverter (number 12 in figure 4.2) with which it is possible to modify the angular velocity of the electrical engine (number 10 in figure 4.2), and therefore the frequency of the shaft oscillation. The harmonic movement induced in the shaft produces the fluid motion inside the tank. The waves produced inside the tank hit the tank walls generating high pressures on them, which

---

<sup>1</sup> The main materials of this chapter is linked with the following paper:  
Souto-Iglesias, A., Botia-Vera, E., Martín, A., and Pérez-Arribas, F. 2011, A set of canonical problems in sloshing. Part 0: Experimental setup and data processing. *Ocean Engineering*, 38 (2011).

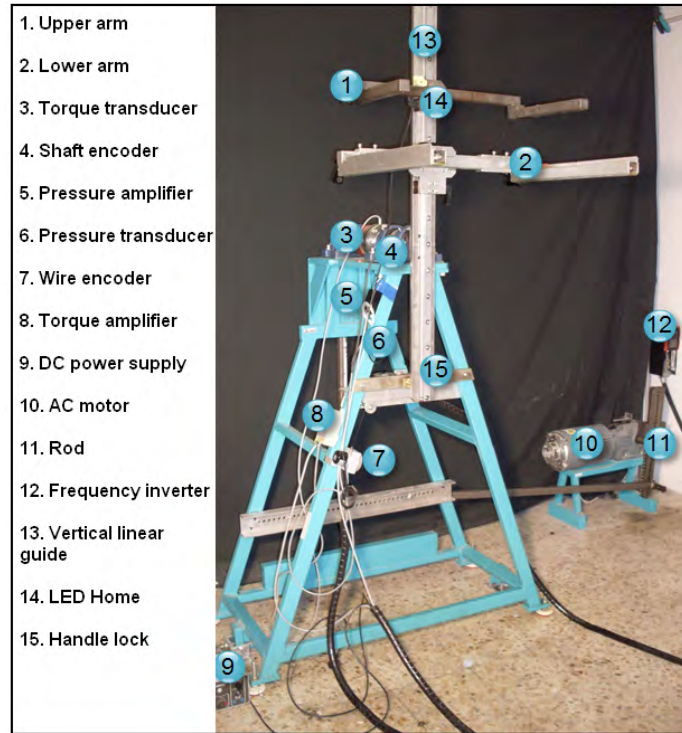


Figure 4.2: 2003 Testing Rig

are measured by pressure transducers, to be later described. A reference zero position is defined by a locking handle (number 14 in figure 4.2). It is relevant in the repetitiveness of the tests. An optical LED (number 14 in figure 4.2) shows the start of the movement using the first pulse of the aforementioned shaft rotatory encoder. This LED is used to synchronize the video recording with the movement signal. The motion starts commonly counter-clockwise, which corresponds to positive angles but the possibility exists of applying an anti-clockwise rotation.

In 2011-2013 due to new experimental requirements, mainly the participation in the GTT benchmark (Loysel et al. (2012)), new improvements in the testing rig were introduced. Figure 4.3 shows a global view of the sloshing rig facility and its improvements. The main improvement consisted in the driving system replacement. Initially it was composed by the rod-crank mechanism aforementioned where the lack of repetitiveness in the initial position, global rigidity, torque limitations and the necessity of perform large series of regular-irregular experiments motivated the solution of incorporating a 1.3 kW linear actuator (FESTO DNCE 63-300-BS-10-PQ), as can be seen in the element 1 of the figure 4.3, attached to the lower part of the vertical linear guide (element 2, figure 4.3), exactly where the wire encoder is attached. The new configuration of the linear actuator solve all the problems detected in the preliminary version of the sloshing testing rig by adding also



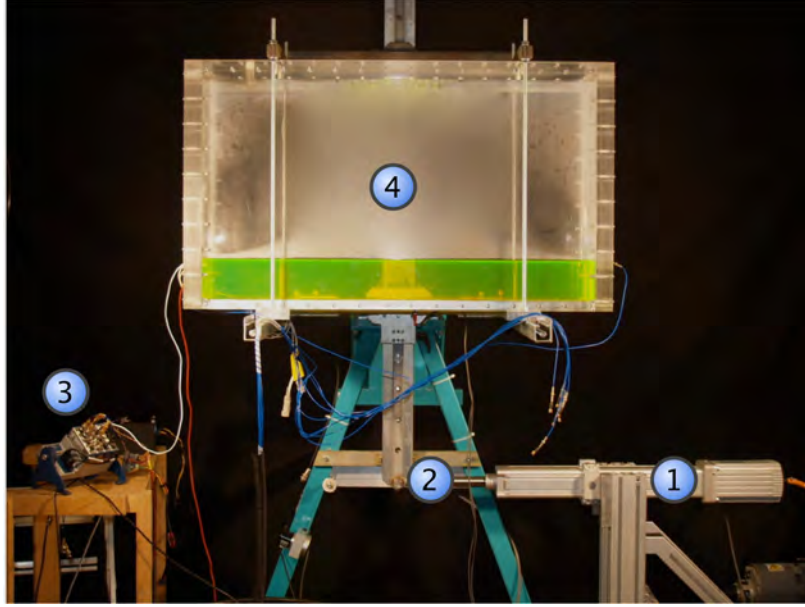


Figure 4.3: 2011-2015 Testing Rig

the possibility of incorporate an acceleration ramp in the initial stage of the driving motion history to be later described. The amplitude of the motion is similar to the previous rod-crank mechanism ( $\pm 15$  deg) and the maximum oscillation frequency is 2.5 Hz. Maximum force generated by the linear actuator is 300 Kg.

The linear actuator speed control is carried out with a servo driver (FESTO CMMP-AS-C5-3A), which controls the movement of the electric motor. The motion control includes the generation of regular, irregular and ramped motions by an incorporated feature of this electric actuators called *Joystick Mode* which basically compare and match an analog driving signal with the encoder feedback signal, thus allowing the linear motor to follow complex interpolated motions. The linear actuator is controlled by a series of digital signals together with a driving analog signal. Such signals are generated by the data acquisition and control system Compact DAQ of National Instruments (element 3, figure 4.3).

The linear actuator is capable of performing regular and irregular motions. In regular ones the motion is sinusoidal with a given period. In the irregular ones, the motion is a combination of sinusoidal motions obtained from a combination of wave spectra and RAO, figure 4.4 shows a portion of an irregular driving motion provided by GTT during the second sloshing benchmark realization (Loysel et al., 2013b). In both cases a polynomial ramp  $R(t)$  is imposed as a multiplicative factor to the nominal driving motion  $\phi_{steady}(t)$  in order to smooth the start and stop of the sloshing rig. The motion description is as

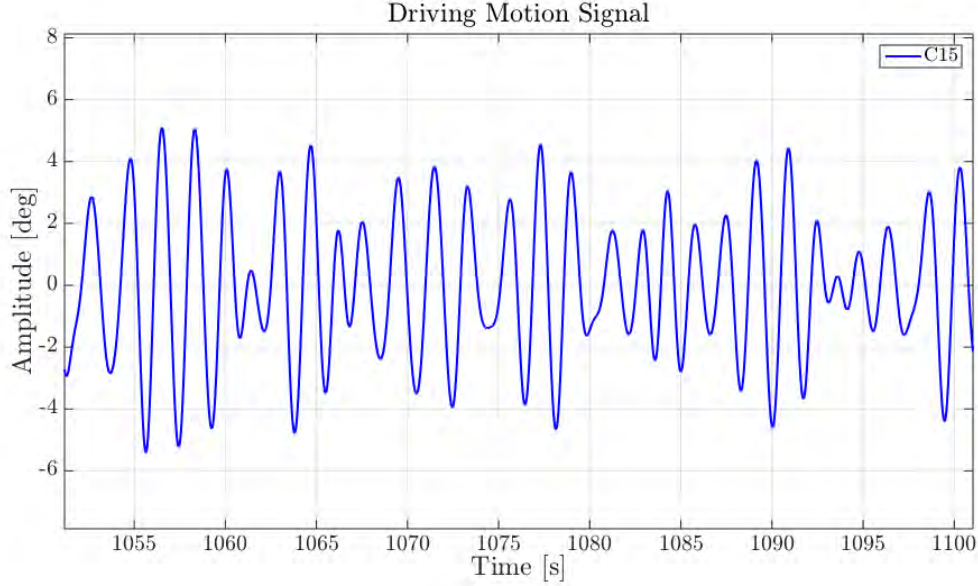


Figure 4.4: Portion of an irregular angular roll motion driving signal

follows:

$$\begin{aligned}\phi(t) &= R(t) \cdot \phi_{steady}(t) \\ \phi_{steady}(t) &= A \cdot \sin\left(\frac{2\pi}{T} \cdot t\right)\end{aligned}$$

The amplitude of the steady motion  $\phi_{steady}(t)$  can be set between 1-15 deg. The starting ramp  $R(t)$  has the following expression, which guarantees continuity up to the third derivative in  $t = 0s$  and at the end of the initial ramping time  $t = T_R$ :

$$\begin{cases} R(\xi) = 0 & \text{for } \xi < -0.5 \\ R(\xi) = \frac{1}{2} + \frac{35}{16} \cdot \xi - \frac{35}{4} \cdot \xi^3 + 21 \cdot \xi^5 - 20 \cdot \xi^7 & \text{for } -0.5 \leq \xi \leq 0.5 \\ R(\xi) = 1 & \text{for } 0.5 < \xi \\ \xi = \frac{t}{T_R} - \frac{1}{2} \end{cases}$$

The ramping time was set to  $T_R = 1.75 \cdot T$  since such a length for the initial transient guaranteed a good balance between maximum starting acceleration and overall length of the ramp. The same ramp, albeit reversed in time, was applied at the end of the time history. An example of the measured tank motion with amplitude  $A = 4 \text{ deg}$  is shown in figure 4.5, together with the indication of the end of initial ramp ( $t = T_R$ ) and the plotting of the nominal steady motion. An analysis of the measured motion of tank indicates the very high repeatability of the system as can be seen in figure 4.6 where 120 measured signals were superimposed. The analysis of the measured oscillation period for the considered case indicates that the maximum error with respect to the nominal imposed period is negligibly small (less than 0.001%).

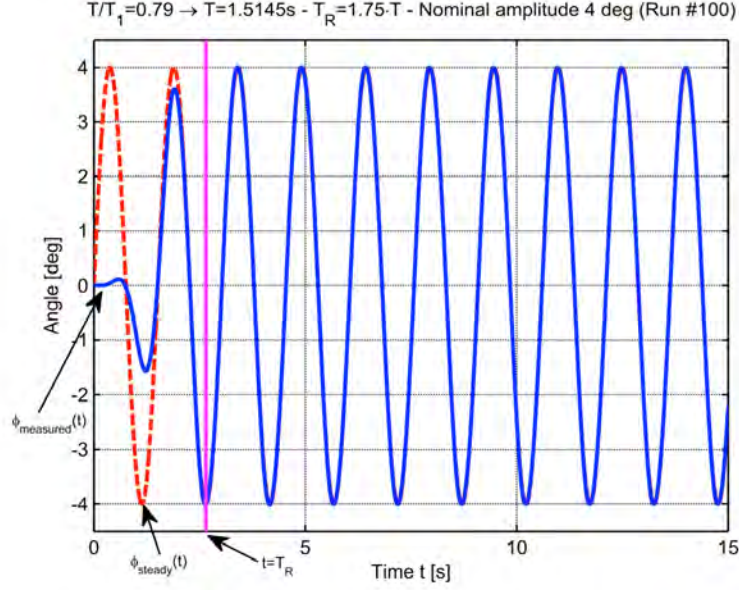


Figure 4.5: Example of a sample time history for an imposed angular regular motion

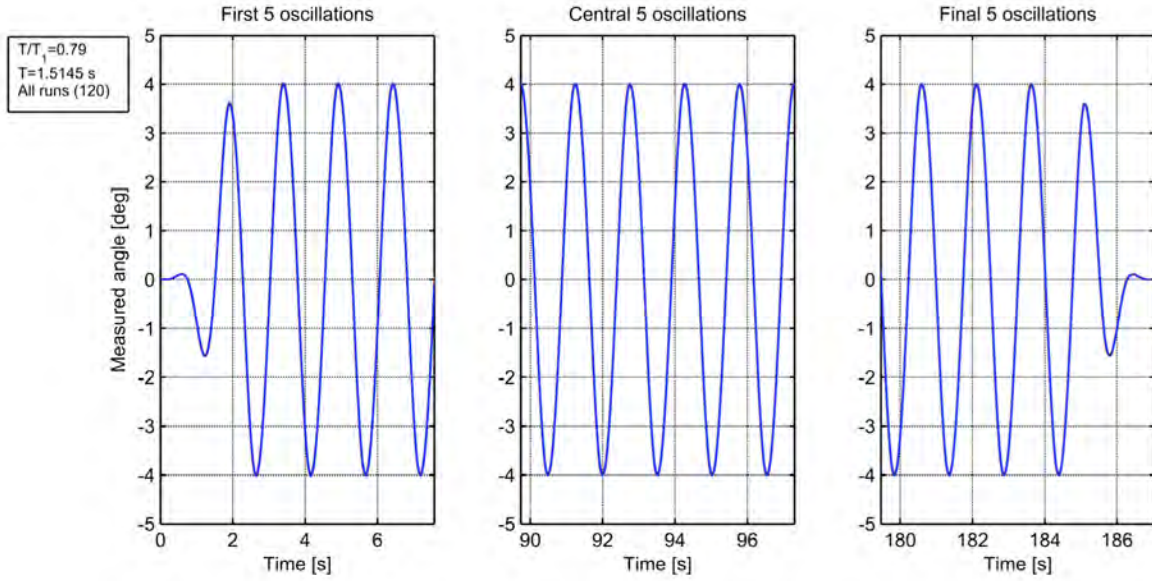


Figure 4.6: Example of angular motion repeatability, 120 signals superimposed

### 4.2.1 Tanks

The wall thickness, size, sensor locations, reinforcements and extra components of each rectangular LNG section tank used during this Phd thesis, were setup accordingly to the needs of each experiment, thus a dedicated experimental setup section regarding the tank

setup can be found in each chapter. In general, the tanks were manufactured with plexiglass (poly methyl methacrylate) by using a 5 axis milling machine and assembled with stainless steel screws and silicone. In order to make the tank completely watertight, some glue was applied to the critical junctions.

## 4.3 Sensors

In order to construct a sloshing experimental laboratory there are indispensable elements such as tank models, testing rig, pressure sensors, data acquisition systems, temperature sensors and high speed cameras. Sensors play a key role, specifically the pressure ones who are the most important instruments among the experimental equipment because accuracy and reliability of the pressure measurement are critical to define the loads that may affect the structural response of the container subject to sloshing loads. It is possible to find in the market various types of pressure-sensing technologies, such as piezo-resistive, capacitive, electromagnetic, piezoelectric, optical, and potentiometric, being the piezo-resistive and piezo-electric type the most used by sloshing laboratories around the world (e.g. Choi et al. (2010); Pistani et al. (2010)).

### 4.3.1 Pressure Sensors Overview

Sloshing facilities use mainly pressure sensors made by KISTLER, KULITE, and PCB companies. Large facilities such as GTT (Gaztransport & Technigaz) perform the most complete sloshing experiments nowadays with a large amount of piezo-electric sensors (around 600 PCB model 112A21) together with a National Instruments DAS. Marintek however prefers to use KULITE XCL-8M-100 (Graczyk and Moan, 2008) and HBM DAS. A similar setup can be found in the facilities of the University of Western Australia (Pistani et al., 2010; Pistani and Thiagarajan, 2012). Seoul National University (Kim et al., 2009) and Pusan National University (Choi et al., 2010), both with similar facilities, use the ICP piezo-electric KISTLER 211B5. In UPM facilities the KULITE XTEL-190M and PCB112A21 sensors were used during the experimental campaigns to be latter discussed in this document. As can be seen, there is not a clear tendency to use a specific sensor brand its choice depends of many factors.

The results can show discrepancies depending on what the experiment focuses on, i.e. in order to catch the peaks, PCB sensors are more suitable and allow to allocate more sensors in a reduced size (see figure 4.7), whilst Kulite sensors are convenient when the hydrostatic part of the impact is also taken into account. Regarding the sloshing application, the piezo-resistive sensor is good at measuring slow varying pressure, while the piezoelectric sensor is good at capturing dynamic load with very short time duration. In

the piezo-electric sensors, the cabling is less troublesome (only a 2-wires coaxial cable is necessary), the sensor excitation and signal share the same cable but this feature increases the cost of the circuitry due to the complexity of the piezo-electric signals, in comparison to the cheaper piezo-resistive circuitry, composed by a simple amplifier and a voltage readout to acquire the signal. The measurement principles of these sensors is discussed below.

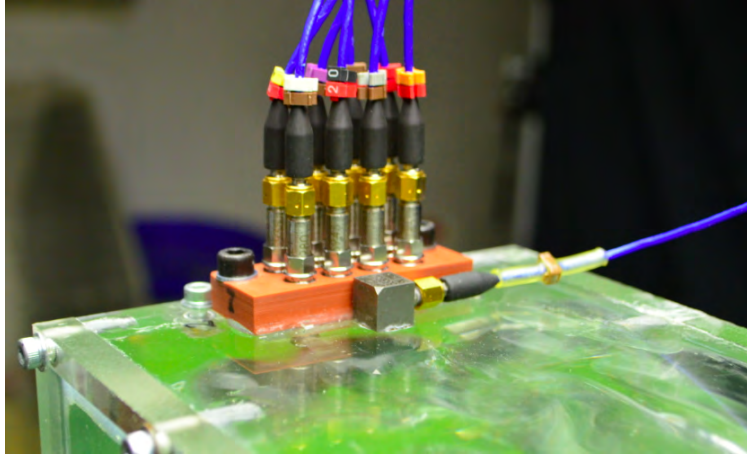


Figure 4.7: PCB Matrix Configuration

The piezo-resistive sensor uses the piezo-resistive effect, i.e. the change of resistivity of a semiconductor (quartz crystal) due to applied mechanical load. This type of sensor is stable to temperature differences between the sensor and material. It is good at measuring slowly varying pressure. Piezo-electric sensors use the piezoelectric effect, through which piezoelectric materials produce electric potential when a mechanical load is applied, however, if this load is constant, the crystal returns no signal. Therefore these sensors are useful only for dynamic measurements of pressure. This type of sensor is regarded as a mature technology with an outstanding inherent reliability. The piezoelectric material has high modulus of elasticity and thus has almost zero deflection and an extremely high natural frequency. Moreover, it has excellent linearity over a wide amplitude range. However, it is known that an additional signal change can be generated when the sensor touches material with a different temperature, this sensor behaviour is called *Thermal Drift* and is discussed extensively in Choi et al. (2010).

In sloshing experiments, it has not been determined which type of pressure sensor is most adequate to be used to measure the sloshing impact pressure. It is regarded that the piezo-electric sensor is better than the piezo-resistive sensor in order to capture the short duration impact pressure peaks which happens within 1-10 milliseconds. However, the piezo-resistive sensor shows better performance for capturing relatively slow varying pressure, i.e. the hydrostatic fall after the impact pressure peaks, which happens within 100-1000 milliseconds. It is regarded that both short impact and slow varying pressure are important to evaluate the strength of a cargo tank.

Piezoelectric sensors can be separated into two groups. The first one is charge mode type sensors, which need an amplifier to measure pressure signals. The second is IEPE (Integrated Electronics PiezoElectric) or ICP (Integrated Circuit Piezoelectric) type sensors such as the PCB 112A21 and Kistler 211B5 aforementioned. These sensors have the amplifier included in the sensor. The charged mode type sensor is good for high temperature and the sensitivity of the sensor can be changed. However, it needs a huge amount of space when a large number of measuring points are required.

### 4.3.2 UPM Pressure Sensors

Two kinds of pressure transducers have been used in the experimental campaigns: Kulite piezo-resistive pressure sensors model Xtel-190(M) with a 5 psi measuring range and with a 4.2mm diameter sensing area, and PCB Piezotronics 112A21 piezo-electric with a 100 psi measuring range and a 5.54mm diameter sensing area. The sensors were placed both in the lateral and roof plate of the tanks. The pressure reported in all cases is relative to the atmospheric pressure.

### 4.3.3 Temperature Sensor

A temperature sensor Electrotherm K4-E-2LS-200 is located nearby the Kulite pressure sensors, in order to record temperature variations during the sloshing tests. Indeed, there are natural variations of temperature in the room and the temperature is registered in order to discard it as a possible exogenous factor of variation in the recorded impact pressure.

### 4.3.4 Acceleration Sensor

Vibrations in a lateral and roof plate have been measured with one piezo-electric accelerometer; model PCB 333B32 shown in figure 4.7. The sensor range is 50g with its resonant frequency over 40 kHz. Acquisition is done similarly to the pressure ones, using a coaxial cable. The sensor is adhered to the tank walls in the proximity of the sensors where the impact pressure took place. A hammer test has been conducted on the filled tank, by exciting vibrations with a hammer stroke on the lateral panel. Results from such test are presented in figure 4.8 and figure 4.9. A low frequency mode is identified around 7 Hz and high frequency modes appear around 0.8-1.9 kHz. The former corresponds to the whole moving part of the rig.

As a comparison, modeling the lateral plate, where the impact takes place and where the pressure sensor is positioned, as a 40mm thick simply supported Plexiglas plate, the first dry natural mode turns out to be 1015 Hz (eq. 3.18 in Rossing T.D. (2004)). On the other hand, when modeling the lateral panel as a fully clamped plate gives a first dry natural mode of 2127 Hz (eq 3.10 in Rossing T.D. (2004)). The observed peaks in the power



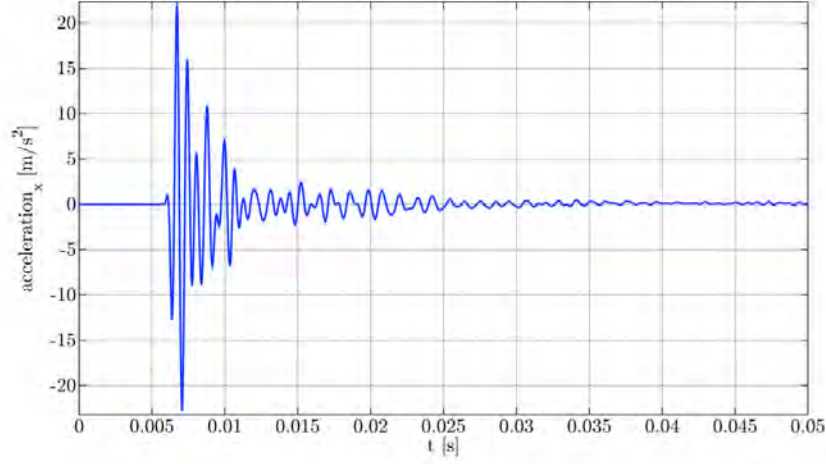


Figure 4.8: Hammer test vibration time history

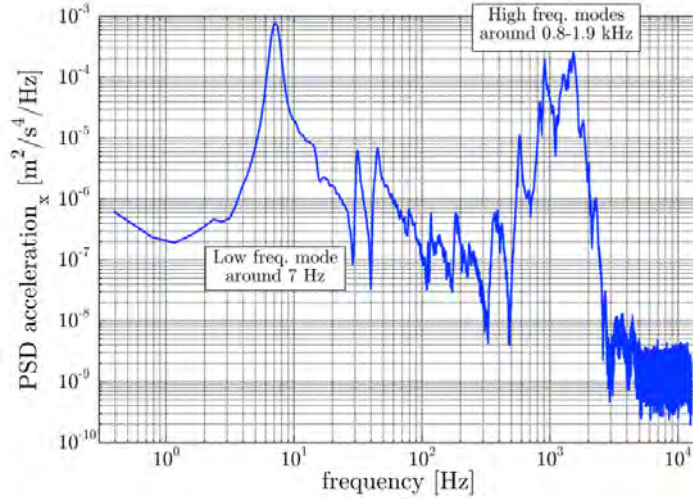


Figure 4.9: PSD of accelerations normal to the lateral plate of the tank during the hammer test

spectral density in figure 4.9 are therefore likely associated with a natural vibration mode of the lateral plate. The most relevant information extracted from 4.9 is that the vibration analysis does not show any evident mode around 200-300 Hz, i.e. the range where some peak pressure oscillations have been observed.

### 4.3.5 Cameras

The qualitative point of view of our phenomena is captured with photographic and video recording by two camera devices. One of them has the capability to capture high speed videos (CASIO EX-F1) and the other one has the capability to take photographs with high shutter speed (CANON 450D). In order to synchronize the movement signal with the high speed video camera, the control software turns on a LED light when the first digital pulse coming from the position encoder is registered. This obviously indicates that the movement has started.

## 4.4 Signal Conditioning, Data Acquisition and Control

### 4.4.1 Signal Conditioning

Converting one type of electronic signal into another type is known as signal conditioning. Its primary use is to convert a signal that may be difficult to read by conventional instrumentation into a more easily read format. The analog signals can be mainly voltage, current and capacitance. In the case of the piezo-resistive and piezo-electric sensors the output signal is a voltage (mV) which needs to be converted prior to data digitalizing and recording. The signal conditioning needs a number of steps listed below:

- **Excitation:** Many sensors require some form of excitation for them to operate. Piezo-resistive sensors need a constant voltage excitation to operate. Piezo-resistive sensors are composed by strain gauges which need a *Wheastone Bridge* in order to measure small changes in the resistance. The output of the bridge is a readable voltage. The nominal input voltage of the bridge ranges between 2-10 volts, coming from a single stabilized voltage source, whereas the Piezo-electric sensors IEPE (Integral Electronics Piezoelectric) type are powered by a constant current source, typically 2 mA to 20 mA. This is supplied by either a signal conditioner or certain specialized data acquisition systems. The output signal from the accelerometer is a voltage signal that is superimposed onto the same line on which constant current is supplied.
- **Amplification:** When a signal is amplified, the overall magnitude of the signal is increased. Converting a 0-18/20 mV output signal of a KULITE SENSOR to a 0 - 10V signal is an example of amplification. This amplification ensures that the span of the A/D converter matches the sensor output and guarantees a correct digitalization of the analog signal.
- **Electrical Isolation:** Electrical isolation breaks the galvanic path between the input and output signal. That is, there is no physical wiring between the input and output. The input is normally transferred to the output by converting it to an optical or



magnetic signal to be reconstructed on the output. By breaking the galvanic path between input and output, unwanted signals on the input line are prevented from passing through to the output. Isolation is required when a measurement must be made on a surface with a voltage potential far above ground. Isolation is also used to prevent ground loops.

- **Linearization:** Converting a non-linear input signal to a linear output signal is known as linearization, nevertheless the output of the piezo-resistive and piezo-electric sensors is proportional to the applied load and no linearization it is necessary.

The aforementioned steps are carried out by the hardware provided by National Instruments composed by a modular 4 slots USB chassis *CDAQ 9174* with a 4 channels IEPE card NI 9234, 4 channels Bridge card NI 9237, 4 channels digital I/O card NI 9402 and 8 channels analog card NI 9201, an USB card NI 6008 is used to generate the commanding analog signal of the linear actuator. Figure 4.10 shows a schematic view of the signal conditioning, data acquisition and control system.

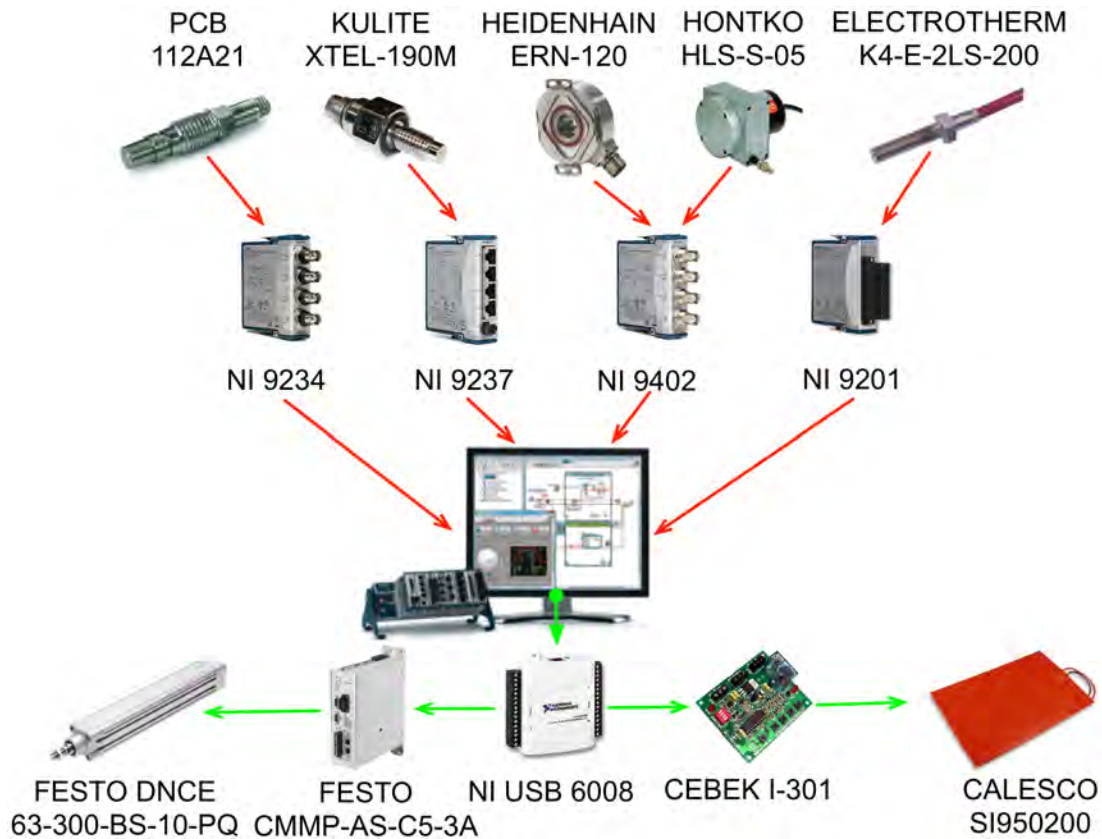


Figure 4.10: Data Acquisition and Control System

#### 4.4.2 Data Acquisition

The data acquisition system (NI CDAQ 9174) acquires the signals generated in the sensors and the NI USB 6008 generates the necessary signals for the linear actuator controller. The NI 9237 card is used to measure the pressure coming from the KULITE pressure sensors. This module incorporates the excitation, conditioning and analog digital (ADC) conversion of strain base sensors such the KULITE ones. The ADC is 24-bit of resolution, the analog input voltage is maximum  $\pm 25$  mV/V and it can sample 4 simultaneously analog inputs at a 50 kS/s maximum sampling rate, which is enough considering that Repalle et al. (2010) recommends perform sloshing experiments with at least 20 KHz sampling rate. The signal conditioning is possible due to the programmable half- and full-bridge completion; sensor excitation is internal with a maximum of 10V.

NI 9234 is a 4 channels IEPE sensors (Integral Electronic Piezoelectric) acquisition card, it is suitable for piezo-electric sensors such the PCB 112A21 which is packaged with a built-in charge amplifier or voltage amplifier ICP(Integrated Circuit Piezoelectric), ICP is a trademark of PCB Piezotronics, Inc. and refers specifically to the IEPE devices that they manufacturer. Nevertheless the chosen ICP pressure and acceleration sensors, PCB 112A21 and PCB 333B32 respectively, are fully compatible with the NI 9234 acquisition card. NI 9234 can sample 4 simultaneously IEPE channels at 51.2 kS/s per-channel maximum sampling rate, during the experiments a sampling rate of 25.6 kHz was chosen as the closest to 20 kHz frequency found in literature (this non-standard value is mandated by the NI 9234 internal clock). Similar to the NI 9237 card the ADC is also 24-bit of resolution, the maximum analog input is  $\pm 5$  V input and the excitation is software-selectable IEPE signal conditioning (0 or 2 mA).

NI 9402 is a 4 channels digital I/O, this card is able to read and generate digital signals, including high frequency pulses trains such the ones generated by quadrature encoders. Two incremental encoders are attached to this card, the HEIDENHAIN ERN120 and HONTKO HLS-S-05, rotary and linear respectively, they employ two outputs called A & B, which are called quadrature outputs, as they are 90 degrees out of phase, this outputs are registered by the 4 channels of the NI 9402 I/O card and following decoded into angular or linear position. Signal conditioning is not necessary for this sensors.

NI 9201 is a 12 bits analog input card which integrate 8 multiplexed channels multiplexed and is used to read the voltage coming from the ELECTROTHERM K4-E-2LS-200, this temperature sensor is a RTDs (Resistance Temperature Detectors) specifically a PT100 which means that at 0 °C the output resistance is 100 ohms, every °C the resistance increases 1 ohm. The signal conditioning is implemented by a simple voltage divider calculated in order to match the maximum admissible voltage ( $\pm 10$ V) of the NI 9201 card. Temperature doesn't varies dramatically as happen with a critical variable like the pressure, so the sampling rate for this sensor is settle as 100 Hz.

All the aforementioned cards are inserted in the CDAQ 9174 chassis and connected via USB to a desktop computer where the software *LABVIEW* perform the tasks of data acquisition, data storage and control. *LABVIEW* offers a graphic programming environment specially dedicated to the data collection. Data acquisition cards and *LABVIEW* belongs to the same company (National Instruments). Figure 4.11 shows the Labview GUI programmed for the experiments.

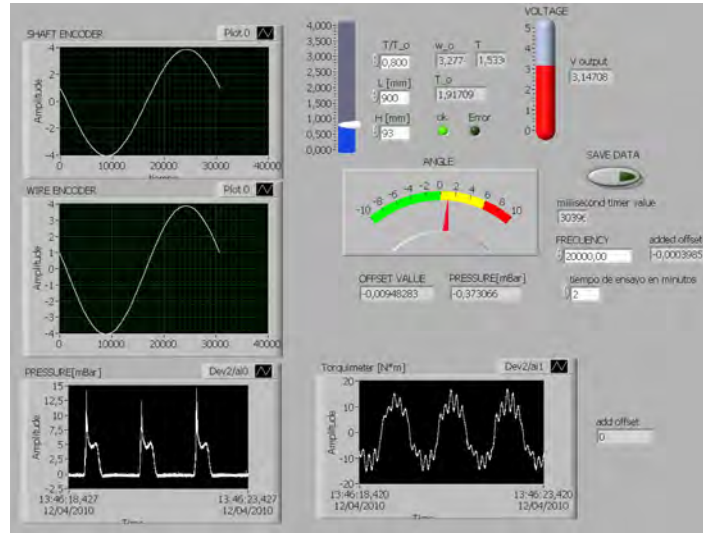


Figure 4.11: Labview Graphic Programming

### 4.4.3 Control

The NI USB 6008 is a low cost analog/digital I/O card connected to the computer via USB, this card commands the analog/digital signals necessary during the control routines. One of the two analog output channels is dedicated to the analog driving motion signal generation, this signal is transferred to the motor controller FESTO CMMP-AS-C5-3A and converted into a linear displacement of the actuator FESTO 63-300-BS-10-PQ. The controller is able to reproduce a linear motion proportional to this analog signal, this is known as *Joystick Mode* and permit generates regular and irregular sinusoidal motions.

One of the digital output signals commands the temperature control card CEBEK I-30 which along with the temperature sensor and a flexible foil heater CALESCO SI950200 500 Watts, compounds the temperature control loop used specifically for the experiments where the fluid is oil, the aim of the control loop is to maintain the viscosity of the fluid as constant as possible to avoid exogenous effects such the thermal drift.

# Chapter 5

## Forced Regular Motion Sloshing Impacts

### 5.1 Introduction

Compared to irregular excitation tests, regular periodic excitation tests can be considered less relevant if the interest is in directly determining typical pressure loads for design purposes. However, from the point of view of the physics of the phenomenon, experimental tests under regular periodic excitation can as well provide very valuable insights, also because they are depurated from the inherent variability induced by the irregular excitation. Moreover, regular excitation tests have proven to be more suitable for the validation of CFD tools aimed at predicting sloshing impact pressure (Delorme et al., 2009; Khayyer and Gotoh, 2009; Brizzolara et al., 2011; Cheng et al., 2009). In this context, it is also worth mentioning the work of Bredmose et al. (2003) as an useful example of experimental and mathematical modeling of steep tank waves. Bredmose et al. (2003) experimentally generated and numerically simulated steep waves in a rectangular tank forced by deterministic (although not strictly periodic in all cases) horizontal and vertical motions, with this latter type of motion leading to the inception of Faraday waves. Bredmose et al. (2003) mainly concentrated their attention on the behaviour of the free surface and of the jets created by the waves within the tank or at the tank walls. However, they also partially discussed the impact pressure at the side wall under horizontal forcing, by comparing experiments and numerical simulation, and reported some difficulties in obtaining satisfactory experimental pressure signals. In general, experience indicates that even under highly repeatable conditions, impact pressures tend to show an inherent variability, which, in turn, seems to indicate a significant dependence on initial/boundary conditions. The studies by Faltinsen and Timokha (2000); Faltinsen et al. (2006); Forbes (2010); Bouscasse et al. (2013) indicate the possibility of inception of complex free surface behaviors and/or long transients under periodic excitation, and this, together with the highly-nonlinear local behaviour of the free surface close to the impact point and instant (wave breaking, free surface frag-

mentation, possible air entrapment, etc. ) can contribute to the observed variability of the measured impact pressure. In this respect, the results given by Bouscasse et al. (2013) are particularly interesting, since they report the free surface elevation in horizontally forced sloshing motions in a rectangular tank, as obtained from both SPH numerical simulations and also physical experiments. In conditions characterized by violent flow behaviors with wave breaking, jets and significant free surface fragmentation, such results indicate that the free surface elevation exhibits a low level of cycle-to-cycle repeatability both in physical experiments and in numerical simulations. Since comparable results are obtained from both experiments and numerical simulations, this seems to indicate that the limited cycle-to-cycle repeatability observed in such conditions is an inherent characteristic of underlying fluid dynamics. Such a characteristic is likely driven by the strongly nonlinear, and thus potentially sensitive to variations in initial conditions, behaviour of the fluid when the flow becomes violent and complex. The work of Souto-Iglesias et al. (2012) indicates that the level of variability of the recorded pressure is significantly influenced by several parameters such as type of fluid, three dimensional effects, presence of drops on the tank walls, etc. . Interestingly, the possible disturbing effect of droplets falling from the tank top was also highlighted by Bredmose et al. (2003). This situation suggests the need, in general, for the application of a statistical approach for the analysis of impact pressure data even for, in principle, deterministic sloshing experiments.

In the past, several studies have focused on different characteristics of pressure field during sloshing impact events: (Delorme et al., 2009) and Peregrine (2003) focused on the pressure impulse (time integral of the pressure at a specific point), claiming it as quite a repeatable quantity; Yung et al. (2010), Fillon et al. (2011) and Gran (1981) mainly focused on the pressure peaks values, while Graczyk and Moan (2008), Kim et al. (2010) and Graczyk et al. (2007) analyzed rise time and impact duration in order to create simplified load models to incorporate sloshing events in structural FEM analysis. Amongst the aforementioned characteristics, the peak pressure value, which is most relevant in liquid containers design and the most challenging to model, is the most variable quantity due to its extremely local nature in time and space (Lugni et al., 2006). This quantity will therefore be the focus of the analysis carried out herein.

With the aforementioned in mind, the work reported in this chapter <sup>1</sup> focuses on the

---

<sup>1</sup> The main materials of this chapter is linked with the following papers:

Bulian, G., Botia-Vera, E., and Souto-Iglesias, A. (2014). Experimental sloshing pressure impacts in ensemble domain: transient and stationary statistical characteristics. *Physics of Fluids*, 26, 3.

Bulian, G., Botia-Vera, E., Castellana, F., Souto-Iglesias, A., and Mas-Soler, J. (2012). Repeatability and practical ergodicity of 2D sloshing experiments. In 22nd International Offshore and Polar Engineering Conference (ISOPE).

Souto-Iglesias, A., Botia-Vera, E., and Bulian, G. (2012). Repeatability and Two-Dimensionality of model scale sloshing impacts. In International Offshore and Polar Engineering Conference (ISOPE).

statistical characterization of the pressure peaks measured experimentally on the lateral wall of a rectangular tank subject to harmonic rotational excitation. The main scope of the chapter is to look at the physics of the impact pressure from a statistical point of view. To do so, a systematic methodology of analysis, which is general in nature, is presented, although herein, for sake of brevity, is applied in detail to a particular case. The core of the analysis method, and hence the focus of this chapter, is on the ensemble domain statistical characterization of the impact pressure, whereas, the analysis of pressure impacts is typically (usually for practical design reasons) carried out in time domain, with the implicit assumption of ergodicity. The ensemble domain analysis, i.e. the statistical analysis in the domain of the realizations, is a powerful tool to outline transient behaviors and to identify the achievement of a steady state (from the statistical point of view). Moreover, when a stochastic process is to be characterized, such characterization must initially be done in the ensemble domain, whereas the time domain characterization of the process is to be considered as a consequence of the ensemble domain characteristics (Bulian et al., 2006; Ochi, 1990). Moreover, carrying out a proper ensemble domain analysis should always be a pre-requisite for working under the assumption of ergodicity in time domain. Indeed, before using the assumption of ergodicity, it is necessary to check that such assumption could presumably be applied to the problem at hand. It is the opinion that the methodology presented and applied in this chapter can highlight characteristics which could be overlooked, or could be impossible to spot out, if using only a "classical" time domain approach.

The chapter is organized as follows. Firstly, a fundamental physics of the problem is given. Then the chapter continues with a thorough statistical analysis of the maximum impact pressure at different impacts in case of a specific excitation period. The analysis addresses: the possible dependence of the maximum pressure distribution on the impact event, the checking and justification of the often implicitly used assumption of "practical ergodicity" and the checking for (un)correlation and (in)dependence of maximum pressures at different impacts with the associated consequences.

## 5.2 Experimental setup

The experimental campaign was carried out at the facilities of the Polytechnic University of Madrid using the sloshing rig detailed in 4.2. The parallelepipedal tank used in this chapter, it was originally dimensioned to be a 1/60 scaled model of a longitudinal section of a 138000  $m^3$  LNGC. The length of the tank is  $L = 900mm$ , the height is  $H = 508mm$  and the breadth  $B = 186mm$  as can be appreciate in figure 5.2. Tank walls, except the base, was built with 40mm thick Plexiglas in order to avoid the hydroelastic effects due to insufficient stiffness in the plates during the fluid impact. The base of this new tank was built with a 20mm thick aluminum plate, allowing for a fluid temperature control loop by sticking a silicon heater to the bottom side of the aluminum plate.

The filling level for this experiments is 18% ( $H=93mm$ ), corresponding to a first linear natural sloshing period  $T_1 = 1.9171s$ . Low filling level below 30% is considered as a lateral wave impact problem. The rotation is defined assuming a centre of rotation at the origin of the coordinate system as can be seen in figure 5.2. The fluid used in this chapter was fresh water, the measured temperature ranged from 18.8°C to 19.8°C in all the experiments. The fluid could be considered Newtonian with the density  $997 kg m^{-3}$ , the kinematic viscosity  $8.9 \cdot 10^{-7} m^2 s^{-1}$  and surface tension  $0.072 N m^{-1}$ .

Lateral walls of the tank was prepared to allocate a cluster of 4 sensors in each face as can be seen in figure 5.1, sensors are piezo-resistive (Kulite) and piezo-electric (PCB). Although a four sensor array is available on each lateral panel of the tank, the pressure records reported herein correspond to the sensors placed at the still water level (93 mm) in each of these lateral panels.

## 5.3 Physical Phenomenon

The physical phenomenon under analysis is the impact of the wave front against the wall of the oscillating tank as a consequence of the sloshing of the internal fluid. For the considered liquid depth and motion amplitude, impact events may or may not occur depending on the oscillation period. When impact events take place, their type is also dependent on these same parameters. Before focusing the statistical analysis reported in the following sections on a particular case, a preliminary screening of the phenomenon has been carried out for a set of values of the  $T/T_1$  ratio,  $T$  being the tank motion period and  $T_1$  the first linear sloshing resonance frequency. This screening was carried out in the range  $T/T_1 = 0.77 - 0.81$  with  $0.01 \cdot T/T_1$  steps. In all cases, the amplitude of the rotational motion was set to 4 deg. Each experiment is carried out for a total of 120 steady cycles excluding starting and closing ramps as described in the section 4.2, leading to a total of 123.5 oscillations periods

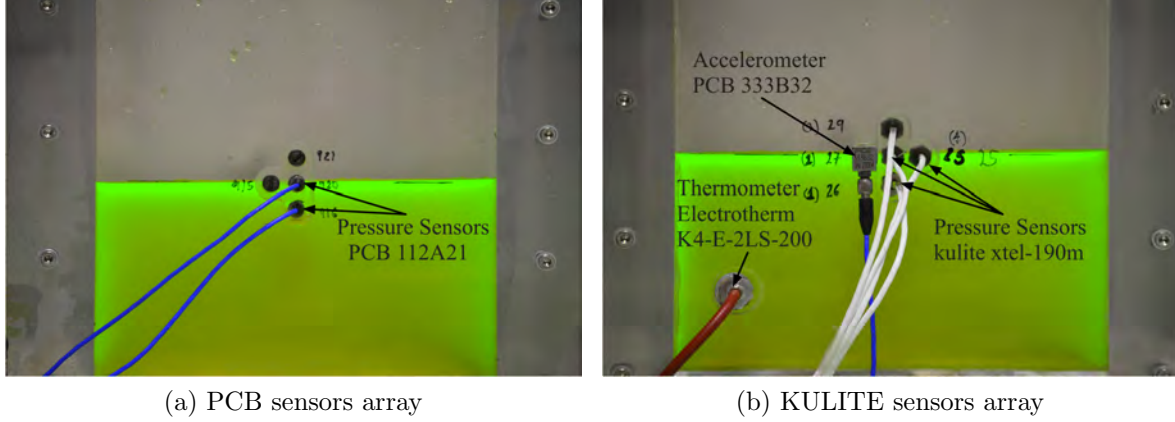


Figure 5.1: Configuration of Kulite pressure sensors, accelerometer and thermometer (left) and PCB (right) on the lateral panels of the tank

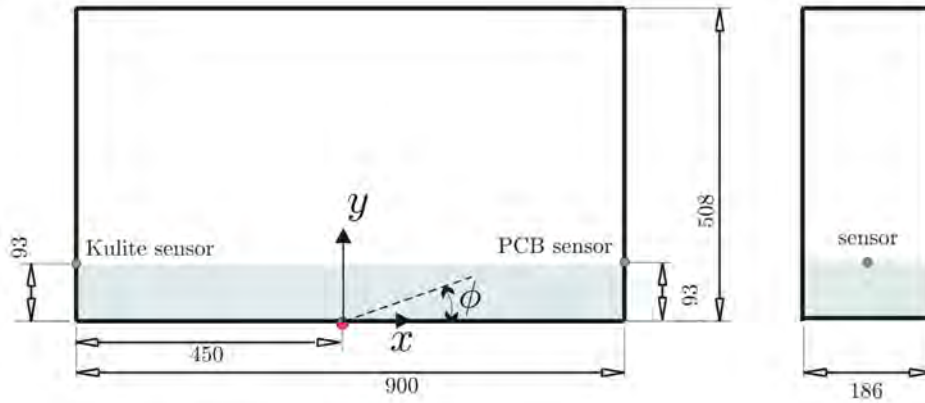


Figure 5.2: Rectangular Sloshing Tank

for each time series. A total of 120 experiments have been carried out for each period. After a certain number of cycles a periodic steady state is reached in all cases the details of this will later be discussed.

Referring to the stationary part of the experiments, no impact events are present below  $T/T_1 = 0.78$ . On the other side, impacts found above  $T/T_1 = 0.81$  are of similar type, but with a decreasing intensity as  $T/T_1$  is increased. The sloshing and impact behaviour in the stationary regime for the range  $T/T_1 = 0.77 - 0.81$ , is undoubtedly more interesting and diversified. A description of the impact behaviour in such range will be given in the following, making also reference to the work by Lugni et al. (2006). Indeed, in the work by Lugni et al. (2006) three modes of wave approaching the wall in flip-through events have been described, namely:



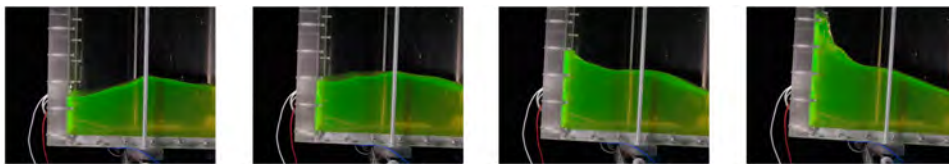


Figure 5.3:  $T/T_1 = 0.77$  snapshots series

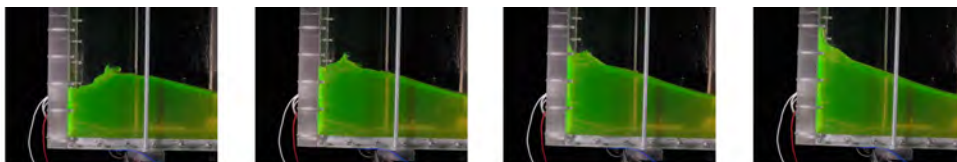


Figure 5.4:  $T/T_1 = 0.78$  snapshots series

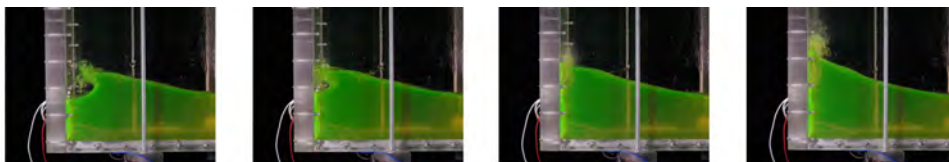


Figure 5.5:  $T/T_1 = 0.79$  snapshots series

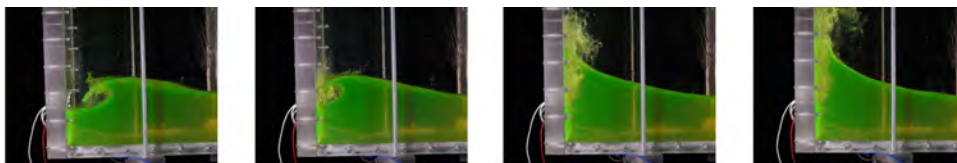


Figure 5.6:  $T/T_1 = 0.80$  snapshots series

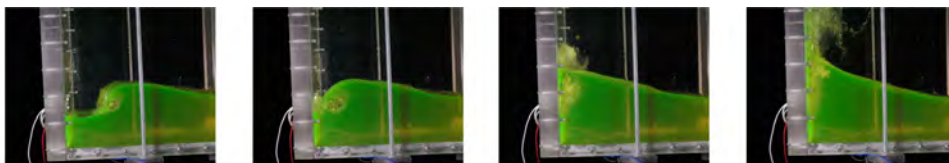


Figure 5.7:  $T/T_1 = 0.81$  snapshots series

- Mode (a): Impact of an incipient breaking wave.
- Mode (b): Impact of a broken wave with no phase mixing.
- Mode (c): Impact of a broken wave with air/water mixing.

Due to the difference in the experimental setup and experimental parameters, it is not possible to have a perfect sharp matching between the experimental observations described in this work and the categorizations given above. Nevertheless, the categorization given by Lugni et al. (2006) for flip-through impact cases is able to provide a qualitative reference for a categorization of the impacts seen in the present experimental campaign. The categorization in "mode (a)", "mode (b)" and "mode (c)" has therefore been taken herein as a sort of qualitative scale of the air entrapment behaviour during the impact.

Accordingly, the sloshing behaviour in the range can be described as follows:

- Figure 5.3: while some impacts occur in the initial transient, no proper impacts take place at steady-state and just a mild run-up can be appreciated. This case is therefore discarded for the analysis.
- Figure 5.4: a weak flip through (Lugni et al., 2006) type impact event takes place. The stationary impact is similar to a "mode (a)" impact (Lugni et al., 2006). In this case there is no air entrapment and there is no strong free surface fragmentation.
- Figure 5.5: an overturning wave entrapping an air pocket while impacting on the wall takes place and the stationary impact is similar to a "mode (b)" impact (Lugni et al., 2006). Indeed, in this case an air pocket is entrapped and the phase mixing is very limited. The fragmentation of the free surface occurs as a result of the impact with the wall of the incoming wave crest which is starting overturning slightly before impacting. As will later be discussed, this case is characterised by a short transient part during the first impacts and significant enough variability to consider it statistically relevant. This case has been chosen as the reference case study for the statistical analysis later presented in this chapter.
- Figure 5.6: an overturning wave entrapping a large air pocket and impacting on the wall takes place. The stationary impact is similar to a "mode (c)" impact (Lugni et al., 2006), although it has still some reminiscence of a "mode (b)" impact (Lugni et al., 2006). Indeed, an overturning wave impacts the wall while entrapping a large air zone. Compared to the case  $T/T_1 = 0.79$  the overturning of the wave crest starts earlier. However, although the zone of entrapped air looks like a large air pocket (as would be for a "mode (b)" impact  $T/T_1 = 0.78$ ), an internal mixing of phases is clearly visible (as would be for a "mode (c)" impact  $T/T_1 = 0.78$ ). This is the most energetic case;

- Figure 5.7: in this case, an air bubble is firstly entrapped by a wave which plunges before impacting the wall. The wave with air entrapped then partially collapses and impacts the wall and an evident phase mixing also occurs. The stationary impact is more similar to a "mode (c)" impact (Lugni et al., 2006).

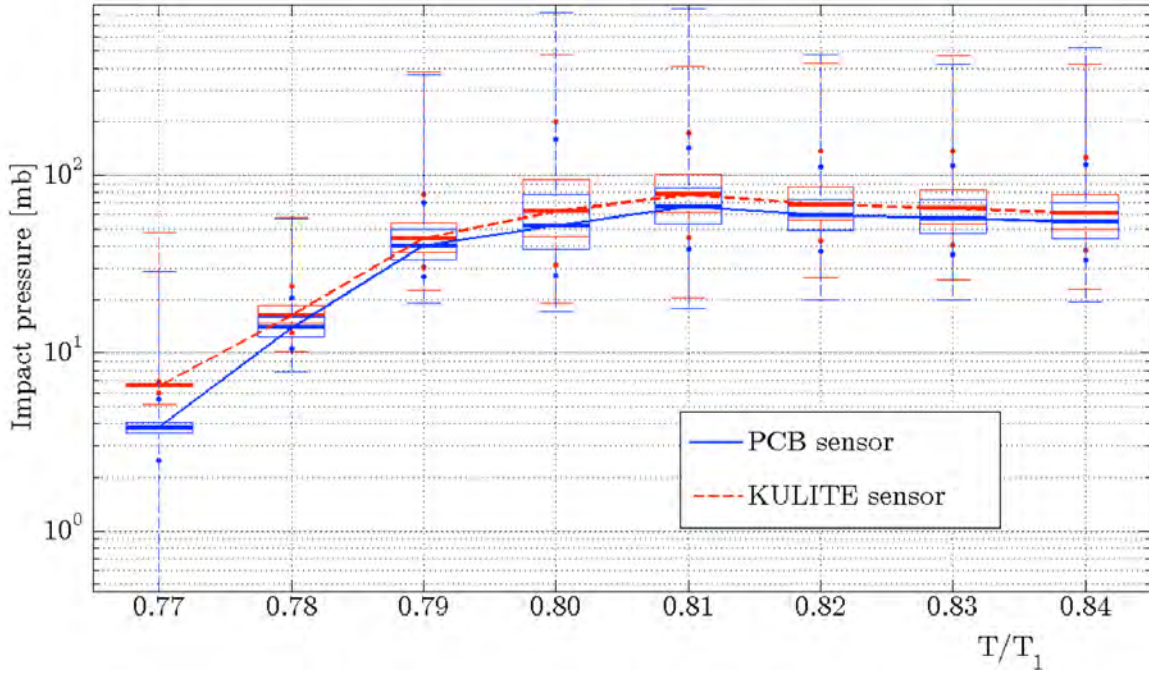


Figure 5.8:  $T/T_1 = 0.77 - 0.83$  peak pressure box plots for preliminary screening

In each oscillation cycle, the maximum of the pressure, referred as a *peak*, is registered. If the peaks corresponding to the initial part of the records are removed, a collection of the order of 10000 peaks is obtained for each excitation period and sensor. For the considered cases and both sensors, a graph with box plots of these peaks is presented in 5.8. Box plots report the following quantities estimated from the sample of data for each period:

- The lower and upper limit of each box indicate the 25% and 75% percentile levels, i.e. the lower and upper quartile respectively;
- The central mark indicates the 50% percentile level, i.e. the median;
- The whiskers indicate the observed minimum and the observed maximum;
- The lower and upper additional markers represent the estimated 5% and 95% percentile levels respectively.

Looking at the results in figure 5.8 it can be noticed that there is a systematic shift of roughly 10 mb in the median pressure between the PCB and the Kulite sensor that we attribute to the fact that PCB sensor does not record the hydrostatic component of the pressure field. In regards to the maximum values, they are consistent when comparing the two sensors, apart from the cases  $T/T_1 = 0.80$  and  $T/T_1 = 0.81$ , where Kulite sensors saturate. It is necessary to remind that though the motion is symmetric, to the rig precision, the Kulite sensor is positioned on one side while the PCB sensor is symmetrically placed on the opposite side of the tank.

It can be appreciated that a maximum in the median is reached within this range of forcing periods and occurs at a frequency which is not the first sloshing one and is about  $T/T_1 = 0.81$ . This shift in the maximum impact pressure from the resonance frequency is a well known phenomenon in shallow depth sloshing (Delorme et al., 2009). This shift towards shorter periods seems to also be in line with the nonlinear free surface behaviour, which shows maxima in the elevation for forcing periods which are shorter than the first natural sloshing period, as shown by Faltinsen and Timokha (2000) and Bouscasse et al. (2013). More precisely, although the forcing motion in Bouscasse et al. (2013) is horizontal whilst the tank is rotationally forced herein, we can refer to the results from "Series 4" and also figure 23 in Bouscasse et al. (2013) as a qualitative comparison example. Such cases are indeed characterized by a filling depth-tank length ratio of 0.125, which is similar to that used in the present experiments (0.103). The mentioned results from Bouscasse et al. (2013) show a peak of the near-wall free surface elevation response at about  $T/T_1 = 0.87$ , while herein the peak of the impact pressure response is observed at  $T/T_1 = 0.81$  (see figure 5.8).

At the end of the preliminary screening, the case  $T/T_1 = 0.79$ , corresponding to  $T = 1.5145s$ , has been selected because it shows dynamics as interesting as higher pressure ones, without having the maximum values of the pressure saturating the Kulite sensor (5 psi-350 mb). Interesting peculiar characteristics have also been identified for case  $T/T_1 = 0.78$ , which, according to the foregoing description, is on the borderline between impact and non-impact conditions. However, for sake of compactness, this latter case is not dealt with in the present chapter, and it is left for a future work. The foregoing discussion focused on the stationary part of the time series. However, from visual observation of the impact dynamics, it is possible to highlight some differences between the first impact and the subsequent ones. To this end, figure 5.3 reports some example snapshots comparing the free surface between impact #1 and impact #5 for the selected case  $T/T_1 = 0.79$ . Looking at figure 5.3 it can be noticed, particularly from the lateral view pictures, that the geometry of the free surface visibly changes between the first impact and the later one used for comparison. On the first impact, the free surface is quite regular and symmetric with respect to the centre plane of the tank, as visible in figure 5.3B). On the other hand, from the second impact onwards, the geometry of the free surface at the moment of impact becomes more

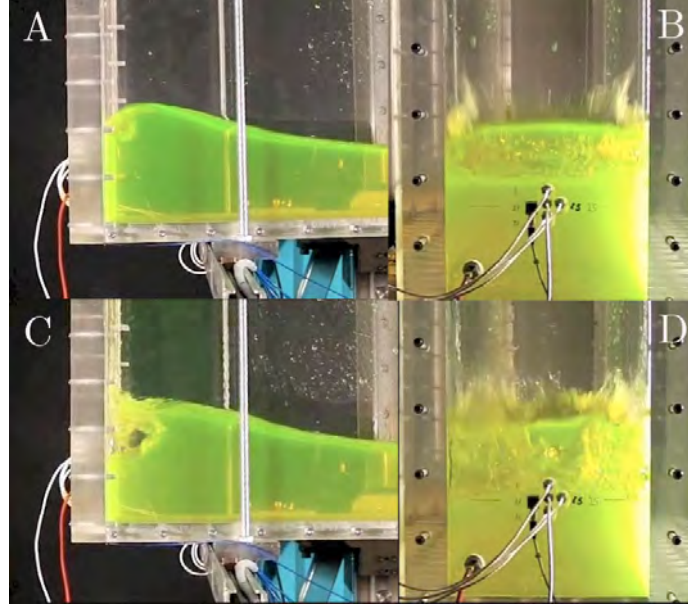


Figure 5.9: Examples of impacts  $T/T_1 = 0.79$ . A) Frontal view of impact #1, B) Lateral view just before the occurrence of impact #1, C) Frontal view of impact #5, D) Lateral view just before impact #5.

fragmented, asymmetric and irregular, as shown for impact #5 in figure 5.3D). Coming to the frontal view, a clean quasi laminar direct impact of a plunging breaking wave takes place on the first impact figure 5.3A). Subsequent impacts present a fragmented irregular wave front before impacting, as noticeable in figure 5.3C). The reported images clearly show that the three-dimensional effects of the flow are not negligible, similarly to what was underlined in the experimental campaign by Souto-Iglesias et al. (2012). It is possible that the behaviour observed in figure 5.3 could be linked, in whole or in part, with the statistical characteristics of the impact pressure to be discussed later.

Considering now to recorded pressure time histories, an example from a single experiment is shown in figure 5.10. The left plot is meant to show the variability of the maximum pressure peaks from impact to impact (i.e. from cycle to cycle). The right plot shows the initial part of the record with time history of the tank rotational angle superimposed. Due to the ramp used at the start, no impact occurs in the first two cycles whilst after that, one impact occurs for each cycle. The pressure time signal of each impact has the classical "church roof" shape (Lugni et al., 2006; Peregrine, 2003). Although the shape is similar from impact to impact, each event is characterized by its own maximum pressure peak and by its own evolution of the pressure time history during the impact event.

A closer view of the recorded pressure time signals reveals additional details. Figure 5.11 shows example records of impacts for runs #1 to #4. At first, a high impact pressure



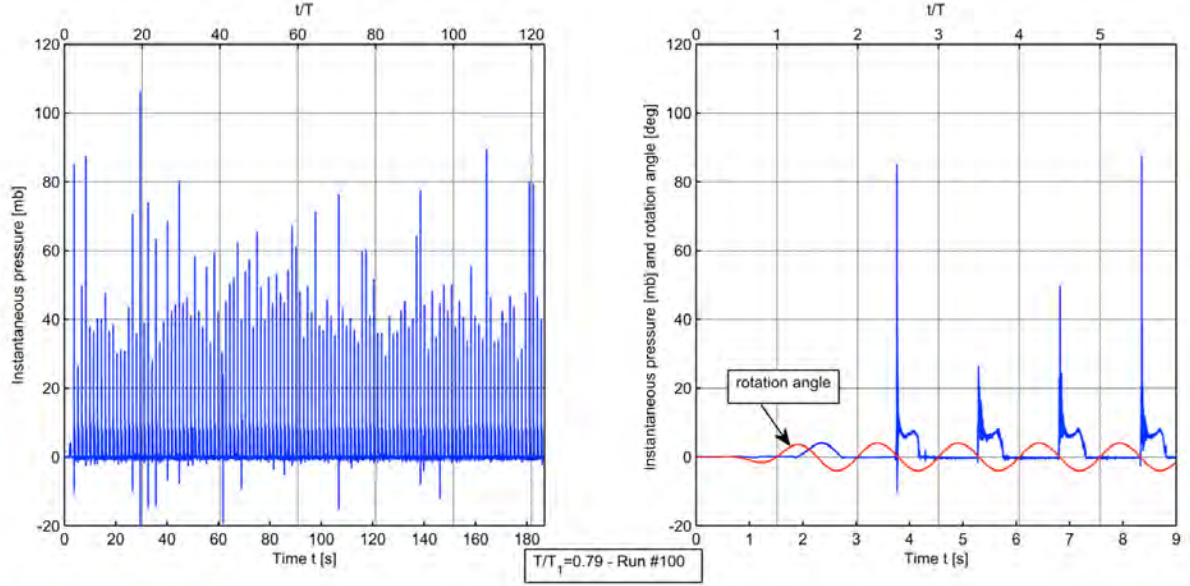


Figure 5.10: Example of pressure time history.  $T/T_1 = 0.79$  Run #100.

is evident at the beginning of the impact event, with secondary oscillations visible after this first peak. Compared to later impacts, the first impact is characterized by the most coherent oscillations, as is visible in figure 5.11. Such oscillations in the pressure signal tend to occur at a frequency of around 230-240 Hz. Considering the vibrations analysis reported previously in chapter 4.3, which did not show clear strong natural vibration modes of the structure in this frequency range, there is some evidence that the observed pressure oscillations cannot be attributed to exogenous hydroelastic effects. As can be appreciated in figure A)-B) an air cavity is entrapped by the incoming wave and, in general, the flow shows a good run-to-run repeatability, particularly when compared with later impacts. The observed pressure behaviour is similar to that observed by Lugni et al. (2010), where an air cavity was also entrapped by the incoming wave. Lugni et al. (2010) tried to correlate the size of the bubble with the frequency of oscillation of the pressure register. Since this study is mostly interested in the peak value, this type of analysis is left for future work. The referred oscillations decay in about 30-50 ms to a zone where the pressure is essentially hydrostatic. Eventually, the pressure falls back to the pressure associated with the dry-sensor condition.

Compared to the first impact, later impacts are characterized by a pressure time history with a much less repeatable behaviour, both from the qualitative and from the quantitative point of view. This could be linked with the observed reduced repeatability of the flow, as pointed out previously. As an example, figure 5.12 shows the pressure registered at the 50th impact for runs #1-#4. It can be noticed that some post-impact oscillations are visible, but the variability, from run to run, is higher. The qualitative difference with the

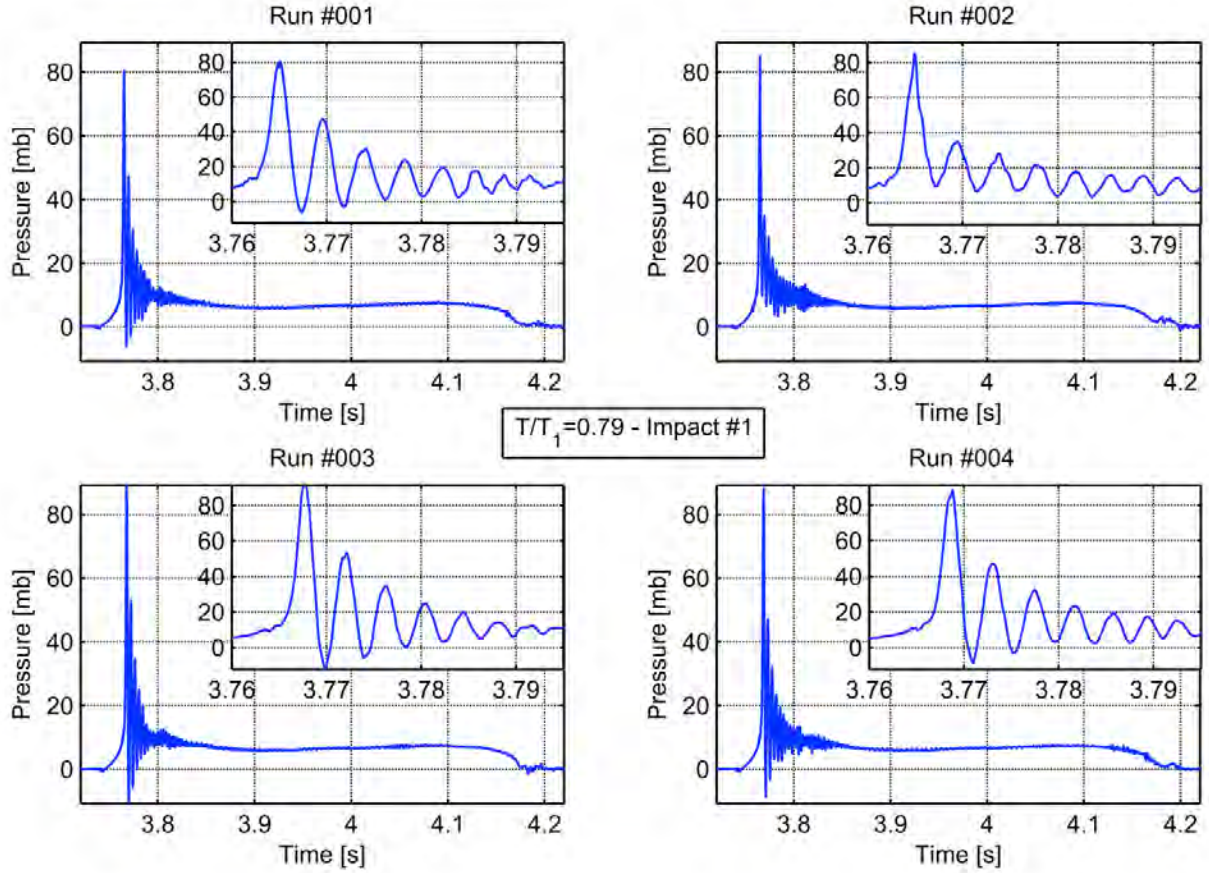


Figure 5.11: Example of pressure time histories.  $T/T_1 = 0.79$  ; Impact #1 ; Runs #1-#4.

behaviour of the first impact is clearly noticeable. Typically, the most coherent oscillations in later impacts tend to occur at frequencies in the range 200-270 Hz and, to a lesser extent, up to about 400 Hz. The vibrations analysis reported previously in 4.3, would again indicate that such pressure oscillations cannot be attributed to exogenous hydro-elastic effects. However, pressure signals are, in general, characterized by the presence of a much more wide-band noise and in some cases oscillations can be observed, with variable amplitudes, in a wide range of frequencies.

## 5.4 Statistical Analysis

### 5.4.1 General Considerations

The maximum impact pressure during sloshing experiments, even under a constant amplitude harmonic excitation, shows a high impact-to-impact (Gran, 1981; Kim et al., 2009; Abramson et al., 1974) and run-to-run (Lugni et al., 2010; Abrahamsen and Faltinsen,

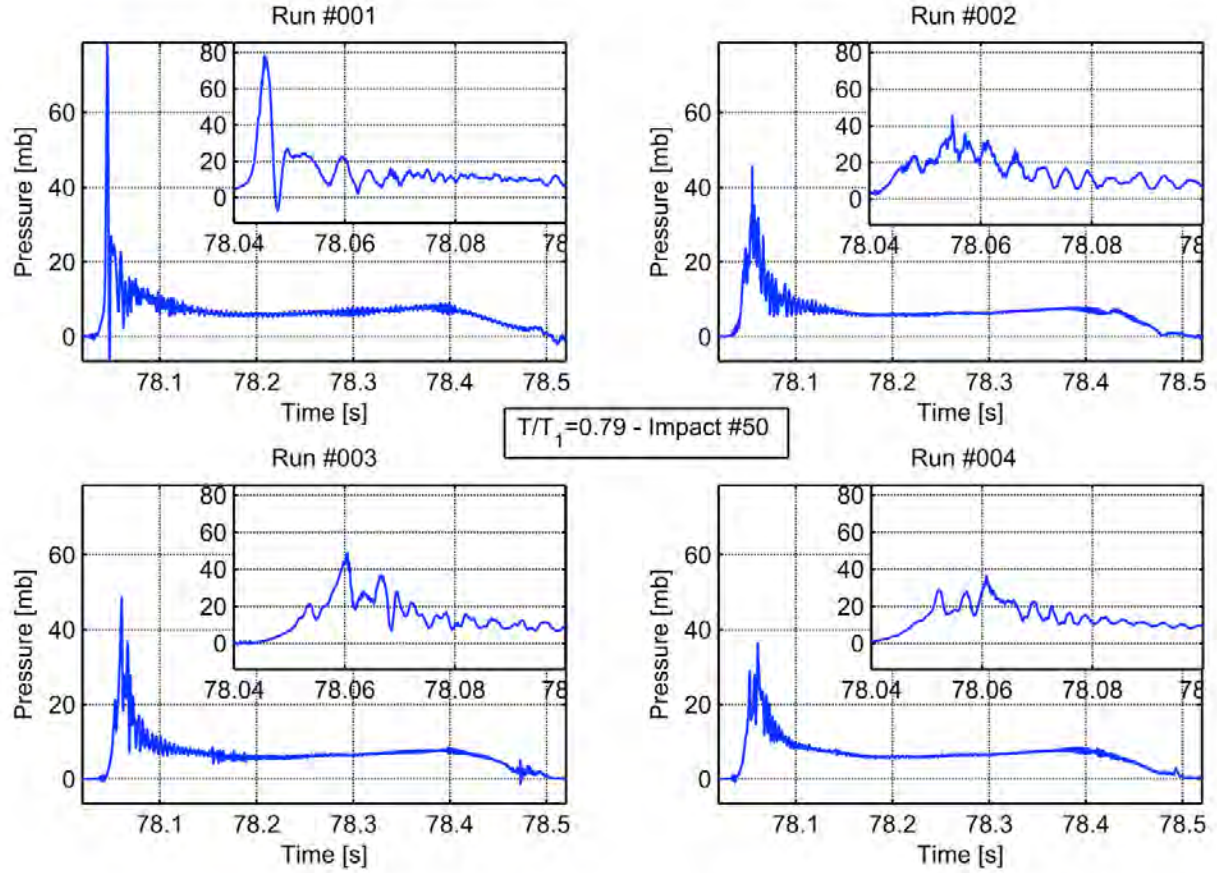


Figure 5.12: Example of pressure time histories.  $T/T_1 = 0.79$  ; Impact #50 ; Runs #1-#4.

2011) variability, indicating an inherent low level of experimental repeatability for the phenomenon under analysis. Such high variability from peak to peak, and especially from experiment to experiment, indicates that, possibly/partially due to some variables not under control and possibly/partially due to the highly nonlinear, hence possibly chaotic, dynamics of the problem, it is not possible to analyze the experimental results through a deterministic approach.

The causes of variability can be categorized as having an “internal”/”endogenous” nature, i.e. aspects which are inherent in the phenomenon under analysis, or an “external”/”exogenous” nature, i.e. those “disturbances” that, although being an integral part of the experiments, should be removed in a “perfect”/”ideal” experiment setup aimed at studying the phenomenon of interest. For instance, in the present case, the nonlinear, possibly chaotic, fluid behavior, as well as the possible entrapment of air in the fluid, could be potential endogenous sources of variability for the impact pressure. On the other hand, the possible effects of drops falling down from the ceiling of the tank, as well as the possible



effects of structural vibrations, could be potential exogenous sources of variability. The categorization of a source of variability as endogenous or exogenous is, however, subjective and depends on the focus of the experimentation. It is indeed possible that an exogenous source of variability, like structural vibrations, could become endogenous if the hydroelastic behavior is explicitly considered to be part of the phenomenon under study.

Irrespective of what is considered as an endogenous or exogenous source of variability, the basically non-deterministic behavior of the maximum impact pressure requires the application of a probabilistic framework of analysis. With reference to the maximum impact pressure at each impact event, the series of subsequent maximum impact pressures will be considered as a stochastic process occurring at discrete "time instants", where, in this framework, a "time instant" actually corresponds to the discrete time when the maximum pressure is measured inside a time window during which an impact event occurs. Within this framework the statistical analysis will address the following items:

- Is the distribution of the maximum impact pressure different from peak to peak?.
- In case of differences, is there convergence to a steady-state for the distribution as the impact number increases? And if so, which is the steady state result?.
- Is there any correlation or dependence between peak pressures registered at different peaks?.
- Can we obtain information on the distribution of the impact pressure using a single very long experiment? In other words, can we consider the process "practically ergodic" as it is often implicitly done in practical applications?.

The analysis herein will be carried out for a particular example experimental case corresponding to  $T/T_1 = 0.79$ . For this chosen case, a set of 119 repeated experiments (one experiment was removed due to possible saturation of the Kulite pressure sensor in one single impact) and, for each experiment, a total of 119 impact events (starting and closing ramp periods have been neglected), are considered. The harmonic excitation guarantees that one impact occurs for each cycle, with the exception of the two initial forcing periods. This situation is different from the case of irregular excitation, where it is usually necessary to use the peak-over-threshold (POT) approach to identify impacts (Graczyk and Moan, 2008; Kim et al., 2012). Therefore, in the case under analysis, for each event the pressure time history is available, from which a maximum pressure, which will be called the maximum impact pressure for that event, can be obtained. Each maximum pressure sample can be indicated as  $P_{ij}$  where the index  $i$  indicates the run number, and the index  $j$  indicates the impact number.

In order to provide a probabilistic characterization of the impact pressure, the statistical analysis of the data is to be carried out in the ensemble domain, i.e. by considering the

impact index  $j$  as fixed. On the other hand, performing an analysis in time domain means fixing the run index  $i$ . The characterization of a stochastic process is always performed in the ensemble domain, i.e. in the domain of the realizations. Only when a process is ergodic, a time domain analysis can be used as an equivalent alternative to the ensemble domain analysis to obtain the characteristics of the process (instantaneous distribution, joint distributions, covariance matrices, higher order moments, etc.). Moreover, in order for a process to be ergodic, it is necessary (but not sufficient) for it to be a stationary process (Ochi, 1990; Parkus, 1969). In the analysis of the process with respect to the problem of "ergodicity", use will be made of concepts previously applied in case of continuous time stochastic processes such as roll motion under parametric excitation

#### **5.4.2 Ensemble domain analysis of maximum impact pressure: identification of transient and stationary regions**

The first part of the statistical analysis fully concentrates on the ensemble domain analysis of the data. To have an initial statistical overview of location and dispersion of data, the ensemble mean and the ensemble standard deviation of the maximum impact pressure for each impact have been calculated. The results of these estimations are shown in figure 5.13. For each impact (the horizontal axis in figure 5.13 reports the impact number), the upper plot of figure 5.13 shows the estimated ensemble mean impact pressure, while the lower plot shows the estimated ensemble standard deviation. Both estimations are reported with their respective 95% confidence intervals, which are based on the availability of 119 repeated runs for each impact. Confidence intervals for the mean have been computed using the standard t-Student approach. In case of the standard deviation, two confidence intervals have been calculated using distinct approaches. The first one (red bars in the lower plot of figure 5.13) is the standard chi-squared approach, which assumes that underlying data are normally distributed. The second one (green bars in the lower plot of figure 5.13) is the "Adjusted Degrees of Freedom" method described by Hummel et al. (2005). This latter method does not rely on the normality assumption and is based on a matching of the distribution of the variance estimator by means of a scaled chi-squared distribution where the scale parameter and the "adjusted" number of degrees of freedom are determined by means of the variance and the kurtosis as estimated from the sample data. Looking at the results, a series of observations can be made:

- The first impact has a mean pressure which is significantly larger than the ensemble mean pressure estimated for other subsequent impacts. Moreover, the ensemble standard deviation for the first impact is the smallest among all impacts. This indicates that the first impact for the considered case ( $T/T_1 = 0.79$ ) is less dispersed compared to all the subsequent impacts. This is particularly true when considering the relative dispersion. This characteristics makes the first impact much more suitable for CFD

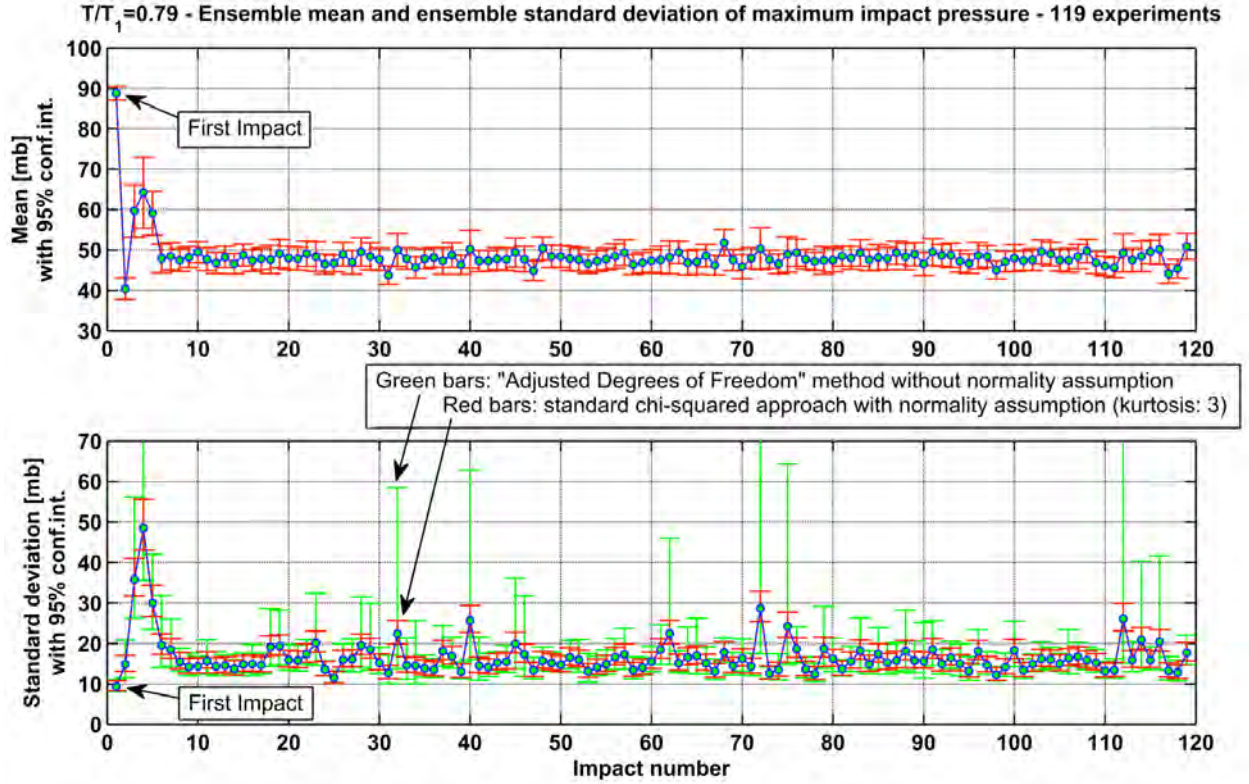


Figure 5.13: Estimator of ensemble mean (upper plot) and ensemble standard deviation (lower plot) for each impact. Connecting lines between different discrete events are reported only for graphical purposes.

validation than subsequent ones.

- The second impact is the impact associated with the smallest ensemble mean pressure, still keeping, however, a relatively small standard deviation, while the fourth impact is associated with the maximum dispersion.
- The behavior of the mean value and of the standard deviation as functions of the event number is quite interesting, because it shows what can be considered an initial transient (from a probabilistic point of view), followed by a quite evident steady state. It is indeed possible to see that the first impact has a high mean and low standard deviation (high repeatability). When moving to the second impact, the mean reduces, attaining a minimum, while the standard deviation increases. For subsequent impacts a hump is visible in both the mean and the standard deviation. The standard deviation and the mean keep increasing until the fourth impact, where they both reach a maximum. Subsequent impacts show a reduction in the mean impact pressure and in the standard deviation, with a stabilization from around impact #8.

This indicates that, after approximately 8-10 impacts, the ensemble mean and the ensemble standard deviation of the impact pressure can be considered, for practical purposes, as independent of the impact number, i.e. the system seems to achieve a steady state, in a probabilistic sense, with respect to mean and standard deviation. Although the achieving of a steady state for the mean and the standard deviation is, in general, only a necessary though not sufficient conditions for guaranteeing that a stochastic stationary state has really been achieved, a stable mean and standard deviation often provide quite good first indications of stationarity.

As anticipated, the ensemble mean and standard deviation represent only two moments (the first and the second) of the (ensemble) distribution of the peak pressure at each impact. Although their behavior provides a good initial regarding the stationarity of the peak pressure distribution at each event, it is necessary to go deeper into the analysis of the characteristics of such distribution. To this end, similarly to figure 5.8, a representation was prepared of the ensemble peak pressure distribution for each impact in terms of box-plots (25%, 50%, 75% percentiles), whiskers (maximum, minimum), plus 5% and 95% estimated percentile values. The results are reported in figure 5.14 for the whole set of impacts, while figure 5.15 shows only the initial impacts to have a clearer understanding of the initial transient part. Looking at figure 5.14 and figure 5.15 it is possible to provide the following comments regarding impact events:

- A behavior of the reported percentile levels can be seen, which reflects what was already observed for the mean and the standard deviation in figure 5.13. There is an initial transient stage, in terms of ensemble distribution of peak pressure. This transient behavior is more evident for the first impact case. After that, in the long run, the distribution of the peak pressure at each event tends to achieve a steady state in a probabilistic sense.
- The distribution of the maximum impact pressure is clearly non-symmetric. There is a clear skew of the distribution towards the high-pressure side, with a long high-pressure tail compared to the low pressure tail;
- Among the impact cases, the first impact shows the distribution with the smallest dispersion in absolute and in relative terms (see figure 5.15). Quantitatively speaking, the ensemble distribution of the first impact event is characterized by a median of about 88.3 mb, a lower quartile (25% percentile level) of about 83.4 mb and an upper quartile (75% percentile level) of about 95.4 mb, which lead to an interquartile range of about 12.0 mb (0.14 when normalized with respect to the median). If, for comparison, the same quantities are determined for a later impact, e.g. impact #50, the results are: median 44.2 mb, lower quartile 36.5 mb, upper quartile 59.2 mb, interquartile range 22.7 mb (0.51 when normalized with respect to the median). These results indicate a much smaller sensitiveness of the behavior of the first impact to initial conditions and/or variables not under control.

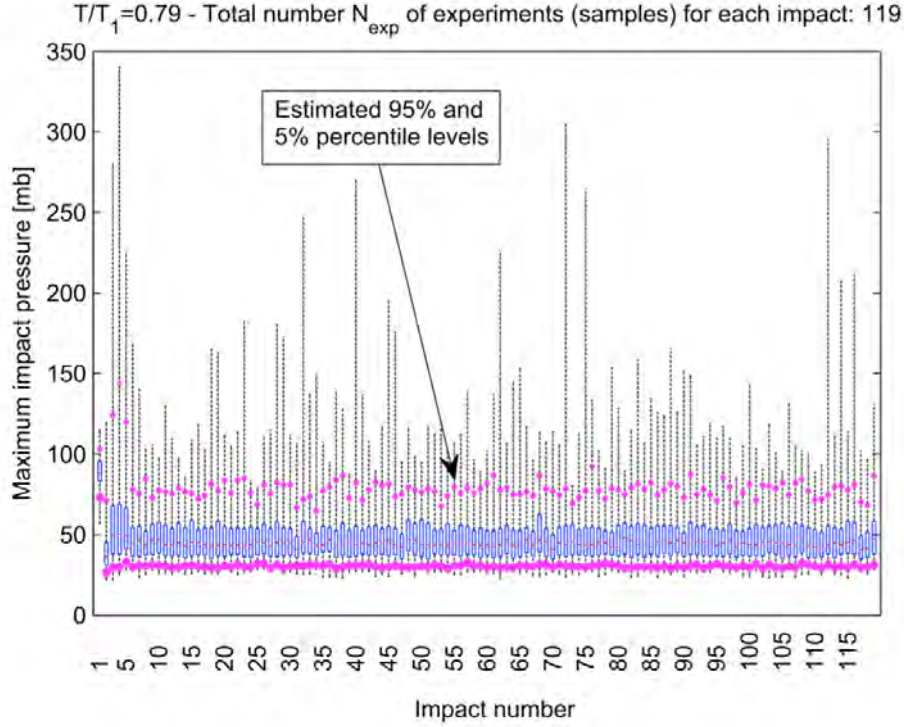


Figure 5.14: Box-plots, with whiskers reporting maximum and minimum, plus 5% and 95% percentile values. All impacts.

Discussing the behavior of percentile levels in figure 5.14 and figure 5.15, it was noticed that the ensemble distribution of the maximum impact pressure for the first impact is significantly different from the distribution of later impacts. This difference can be clearly seen in the example comparison reported in figure 5.16, where the cumulative distribution (CDF) of the maximum impact pressure for the first impact is compared with the distribution of the same quantity, but for a later impact (in the reported case the arbitrarily chosen 50th impact). From the comparison in 5.16, the much smaller data dispersion for the first impact, as well as the difference in the median value, are both evident. The reduced dispersion for the first impact could possibly be a consequence of the higher flow repeatability as identified when discussing the physical phenomenon (see previous comments to figures 5.3, 5.11 and 5.12). Although from the analysis of the data, the achieving of a stationary state for the ensemble distribution was quite evident, it is not very clear how long the "transient" (in terms of number of impacts) is to be considered. This aspect can be analyzed by checking when two ensemble distributions are significantly different from a statistical point of view, by using the two-sample Kolmogorov-Smirnov test (KS2 for sake of brevity). The KS2 test is a non-parametric hypothesis test which checks the null hypothesis that two samples of data actually come from the same underlying distribution without assuming an a-priori underlying distribution of the data (Press et al., 2007).

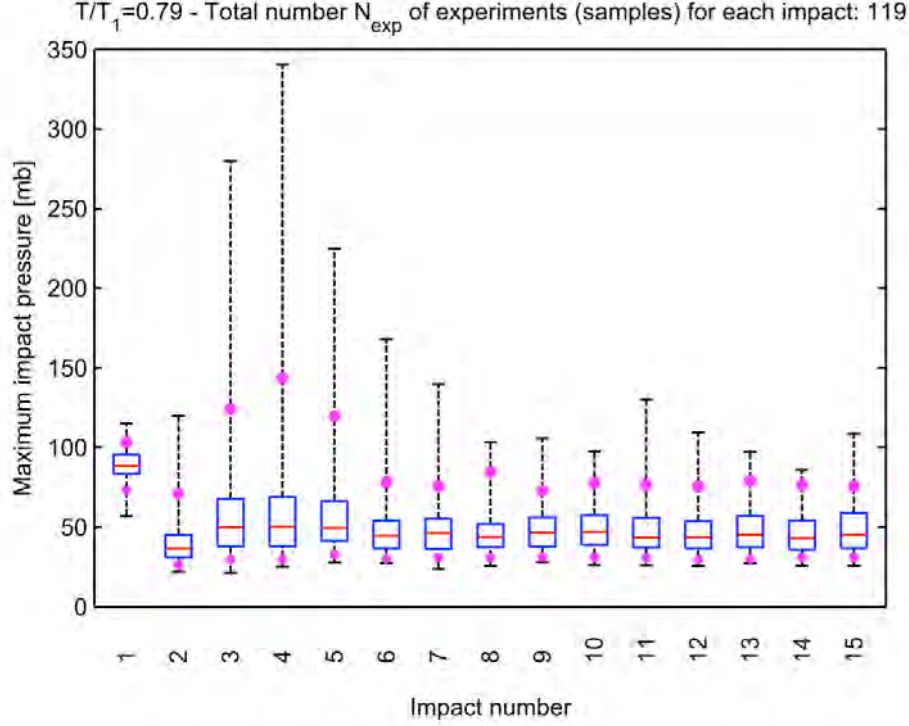


Figure 5.15: Box-plots, with whiskers reporting maximum and minimum, plus 5% and 95% percentile values. Initial 15 impacts.

In the context of this study, the KS2 test has been applied in the ensemble domain by systematically comparing the ensemble distribution of impact pressure for each impact versus the ensemble distribution of all the other impacts. The scope of the comparison is to identify those impacts with significantly different (from a statistical point of view) ensemble distributions. For each comparison, the KS2 test either rejects or does not reject the null-hypothesis of equal distribution at the considered significance level  $\alpha$ , which, herein, has been taken equal to the typical value of 0.050. A square binary matrix  $\underline{\underline{H}}_{KS2}$  can therefore be arranged, containing either 0 or 1 depending on whether the null-hypothesis has been rejected or not for each performed comparison.

Results from the ensemble domain analysis based on the KS2 test are shown in figure 5.17, where the binary matrix  $\underline{\underline{H}}_{KS2}$  is graphically shown and where only impact cases have been considered. Dark points are associated with rejections of the null hypothesis of equal underlying distribution for the two samples under testing, while light points are associated with non-rejection of the null hypothesis at the specified significance level. Observing the results reported in figure 5.17 some comments can be provided:

- When comparing the distribution of each of the first five impacts with the distribution



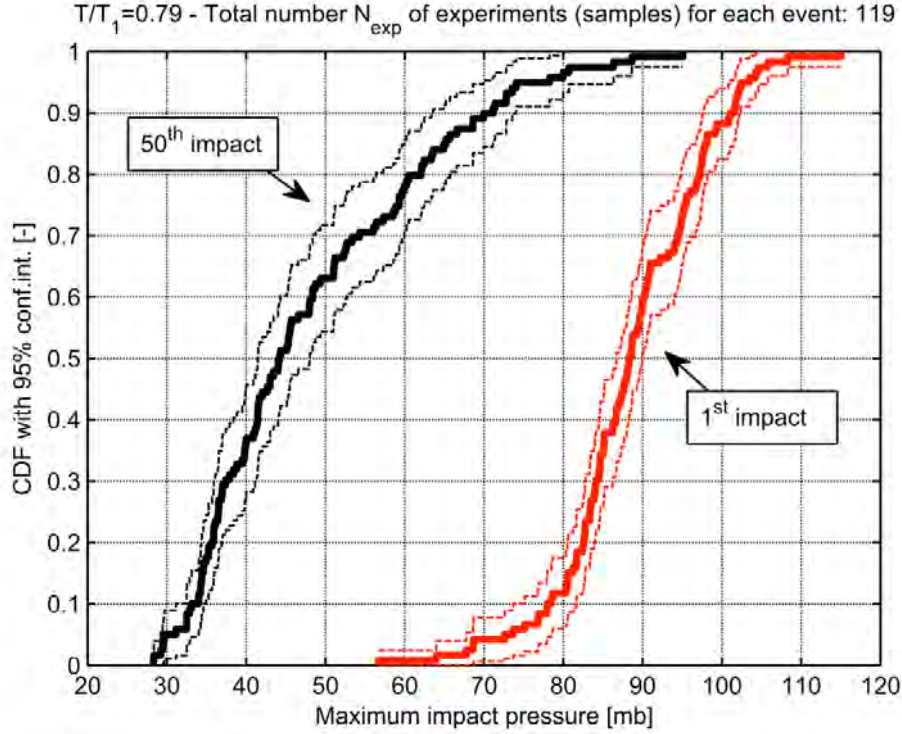


Figure 5.16: Ensemble distribution (with 95% conf. int.) of maximum impact pressure. Comparison between 1st and 50th impact.

of all other events, the KS2 test tends to reject the hypothesis of equal distribution. At the same time, there is a tendency for the distributions of impacts #3-#5, to be quite similar to each other.

- The above observations can therefore be considered as an indication that the distribution of the first five impacts tend to be different from the distribution of all other subsequent events.
- The above observations also indicate the transient nature of the distribution of maximum impact pressure for the initial impacts.
- Additional non-systematic rejections are visible, which are likely to be considered as a natural statistical outcome of the hypothesis test at the considered significance level. Later impacts #31, #70 and #117 are exceptions, since for these impacts there is a clearly higher fraction of rejections.
- The limited number of non-systematic rejections after the fifth impact indicates the achievement of a stationary regime after the initial transient.

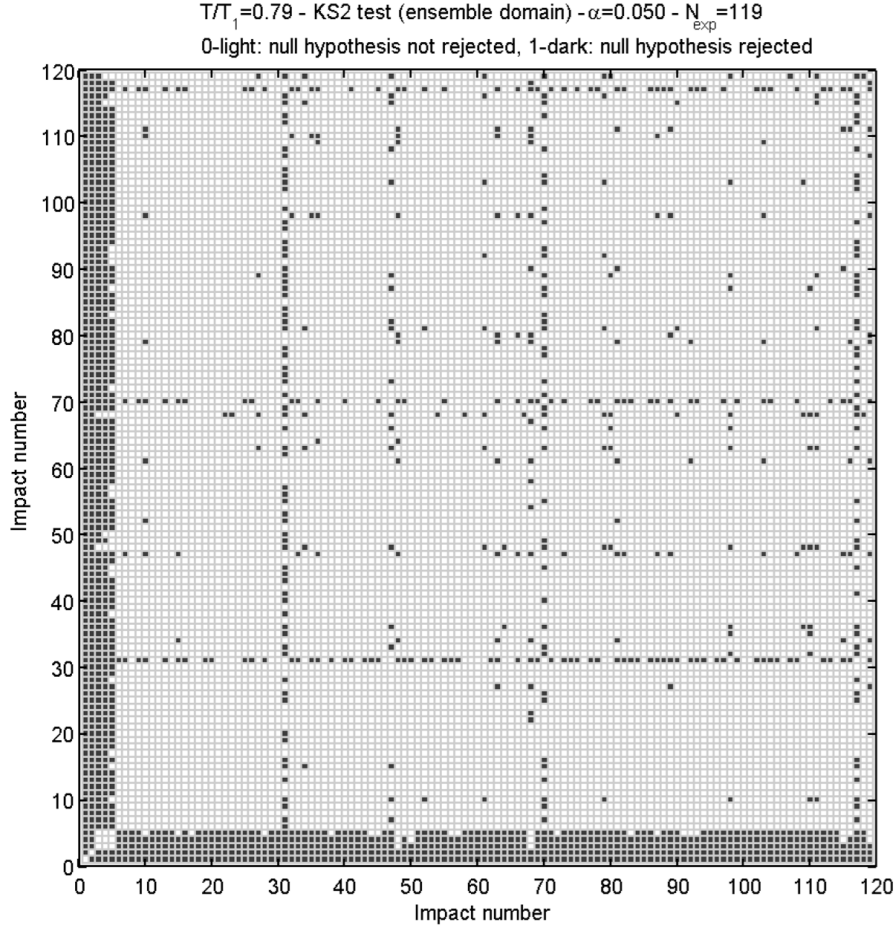


Figure 5.17: Systematic application of two-sample Kolmogorov-Smirnov test in ensemble domain.

### 5.4.3 From ensemble domain to time-domain: justifying the usual working assumption of (practical) ergodicity

As pointed out in the previous section, in order to characterize a stochastic process, it is necessary to work, firstly, in the ensemble domain. However by definition of "ergodicity", if the process is ergodic, it is possible to obtain a full characterization of the process from a single, infinitely long, realization. In reality, for practical purposes, what is usually sufficient is that a "sufficiently long" realization could allow us to determine "sufficiently accurate" statistical estimations. A necessary condition for having an ergodic process is that the process is stationary. However, stationarity is not sufficient to guarantee, at least in principle, the ergodicity of a process (Parkus, 1969). Indeed, it may in principle happen that a process is stationary, but not ergodic (e.g. the limiting Dirac-delta spectrum



example discussed by Bulian et al. (2006)). Fortunately real world stochastic processes in classical mechanics are typically quite well behaved. Therefore it is typically expectable to have to deal with processes for which sufficiently long time histories can provide sufficiently accurate estimates, i.e. what, for practical/technical purposes, can be considered, according to the nomenclature of Belenky et al. (2001), "practically ergodic" processes (Bulian et al., 2006).

In sloshing literature, the ergodicity property is typically implicitly assumed and usually not discussed (e.g. Gran (1981); Graczyk and Moan (2008); Fillon et al. (2011) to mention a few). The whole statistical analysis is often carried out on the basis of long time series of data directly in time domain instead of working in ensemble domain. Although ergodicity itself is quite expectable, it is the aim of this study to show how to check in more detail whether, and to what convergence rate, a single long run of impact pressures due to sloshing can provide a distribution converging to the observed steady state distribution obtained from ensemble domain analysis, and which are the limitations / requirements to perform the "switching" from ensemble-domain to time-domain analysis.

To address the issue of ergodicity check from a sound and systematic point of view, an approach has been applied herein which relies on an ensemble domain analysis. The approach is intended to check whether, and to quantify at which rate, the running estimators (mean and standard deviation in this case) converge when increasing the experiment length.

Herein, "running estimators" (Bulian et al., 2006) are intended as statistical estimators based on time domain analysis, which, for a generic run, take into account a certain number of initial impacts (after having removed the initial transient stage). For instance, the running estimator  $\hat{\mu}_i(j)$  is the estimator of the mean impact pressure as obtained for the  $i - th$  run considering only the first  $j$  impacts (after transient). Similarly,  $\hat{v}_i(j)$  is the corresponding running estimator of the variance. This concept also applies to the empirical estimation of higher order moments and whole *CDF* of a random variable originating from time domain data. The "running estimators" for  $\hat{\mu}_i(j)$  and  $\hat{v}_i(j)$  can be determined from the experimental data as follows:

$$\begin{cases} \hat{\mu}_i(j) = \frac{1}{j} \sum_{h=1}^j P_{ih} \\ \hat{v}_i(j) = \hat{s}_i^2(j) = \frac{1}{j-1} \sum_{h=1}^j (P_{ih} - \hat{\mu}_i(j))^2 \end{cases}$$

where  $P_{ih}$  is the maximum impact pressure at  $h - th$  impact (after transient) for the  $i - th$  run, and  $\hat{s}_i(j)$  is the running estimator of the standard deviation. Note that  $\hat{\mu}_i(j)$ ,  $\hat{v}_i(j)$  and  $\hat{s}_i(j)$  are stochastic processes defined at discrete "time instants"  $j = 1, 2, 3, \dots$  representing, in the case of the present study, indices associated with impact events. In general, if the process is ergodic, then all the estimators tend to converge (in a probabilistic sense)

as the instant  $j \rightarrow \infty$ . This means that, in practice, the longer the experiments, the "better" the estimator we expect to obtain.

To measure the rate of convergence of the estimators as the run-length increases, the "Coefficient of Variation" (CoV) of the running estimator of the mean and of the standard deviation have been estimated from the available set of experiments. The results of this analysis are shown in figure 5.18. The upper plots show the running mean  $\hat{\mu}_i(j)$  and standard deviation  $\hat{s}_i(j)$  for all 119 realizations. The bottom plots show the behavior of the coefficient of variation for the two estimators obtained from the data in the upper plots. Note that the impact numbering starts from impact #10 because the initial part has been neglected considering it as a transient region. Looking at the results in figure 5.18 it is

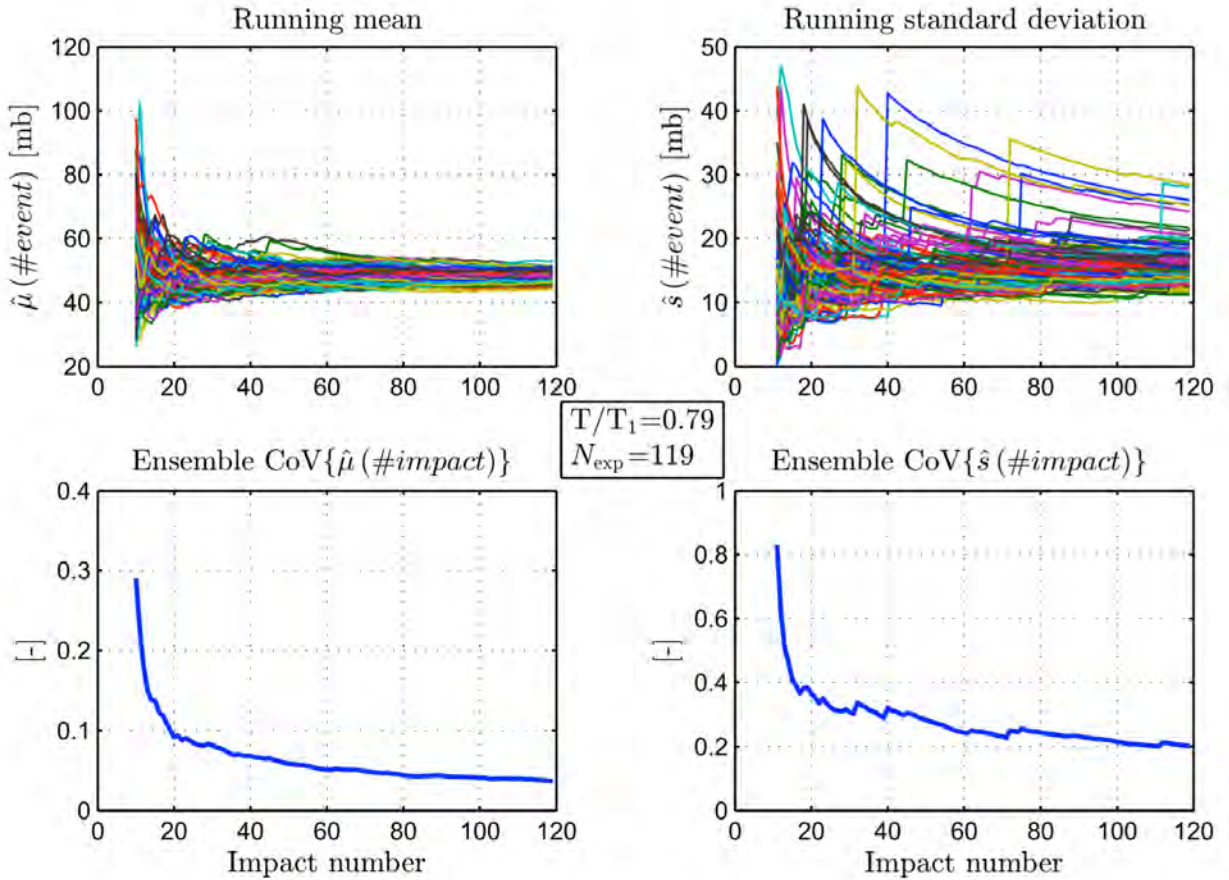


Figure 5.18: Convergence analysis of running mean and standard deviation.

possible to notice that, as expected, there is a convergence of the estimators as the run length increases, and this convergence is indicated by the reduction of the coefficient of variation of both the estimators as the run length increases. The observed behavior of both running estimators is an indication of a possible ergodic behavior, at least regarding

the two considered statistical moments. Given the run length, the coefficient of variation for the estimator of the mean is significantly smaller than that of the standard deviation. This means that, for the tested conditions and for a given acceptable uncertainty in the considered estimator, it is sufficient to carry out shorter tests (in terms of number of impact events) if we are only interested in the mean of the impact pressure. However, if we are interested in higher moments, as, e.g., the variance, it is then necessary to carry out longer tests to achieve the same level of confidence in the estimation.

According to the indications given by figure 5.18 it could be possible to consider the assumption of ergodicity as a valid assumption. However, results in figure 5.18 only address two statistical moments (mean and standard deviation) and therefore only give a partial indication. In order to have an indication associated with the whole distribution of impact pressure it is necessary to perform a systematic comparison between time domain and ensemble domain estimations. This can be accomplished by means of the KS2 test, in a way similar to that used to produce figure 5.17. We can indeed consider a binary  $N_{\text{exp}} \times N_{\text{Pan}}$  matrix, where  $N_{\text{exp}}$  is the number of available experiments and  $N_{\text{Pan}}$  is total number of impact events used in the analysis. The generic element of this matrix is the result of a KS2 test between one sample from ensemble domain analysis and one sample from time domain analysis (depurated from its initial transient).

Results from this mixed ensemble domain vs. time domain analysis are shown in figure 5.19, where all the experiments have been considered, but where the initial nine impacts have been discarded in order to remove, with a safety factor, the initial transient region, which, identified as having a length of about 5 impacts in the previous section. As a result, impacts in figure 5.19 start from impact #10. From the results in figure 5.19 it can be seen that the number of rejections of the null hypothesis of equal distribution is quite limited. There are some more systematic rejections when comparing ensemble distributions only for impacts #31, #70 and #117, which are the same impacts already singled out when discussing the results of figure 5.17. In general, the outcome in figure 5.19 confirms the generally good agreement between distributions obtained from time domain and ensemble domain analysis, i.e. the ergodicity of the process with respect to the estimation of the stationary distribution. An example of comparison between ensemble domain and time domain estimations is shown in figure 5.20. In this figure, the empirical *CDF* of the impact pressure taken from a single experiment and the empirical *CDF* obtained from ensemble analysis of one impact event have been compared. A KS2 test has also been carried out with details reported in the figure. It can be seen that the distribution estimated from an example ensemble domain analysis (single event) and that estimated from an example time domain analysis (single experiment) match well, as would be expected from an ergodic process when considering a sufficient number of available samples. Finally, the analysis carried out in this section supports the generally used assumption of (practical) ergodicity of the process. However, it is important to underline that the stationarity analysis carried out in

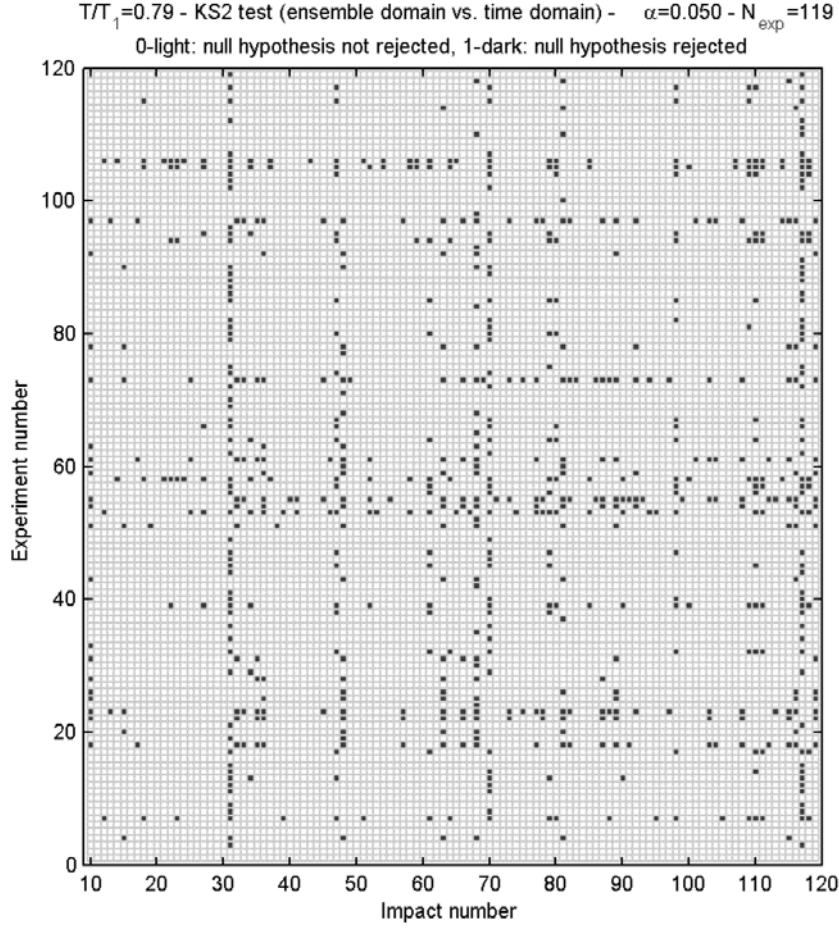


Figure 5.19: Systematic application of two-sample Kolmogorov-Smirnov test between ensemble domain and time domain samples.

the previous section has identified a visible initial transient stage (about 5 impacts for this particular case). As a consequence, the ergodicity assumption can only be used after neglecting a sufficient number of initial peaks which are representative of the initial transient. The reported method of analysis is very general in nature and can therefore be applied to any set of experimental data spanning the ensemble-domain and the time-domain in order to identify, from a statistical point of view, the length of the transient for the particular case under analysis.

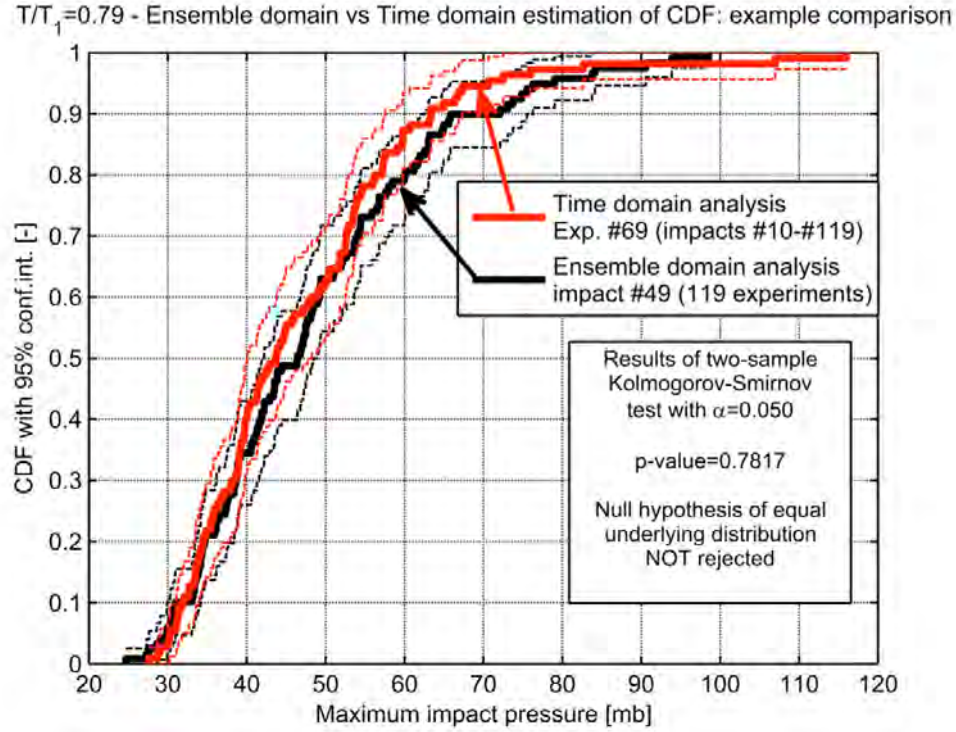


Figure 5.20: Example of comparison of cumulative distribution of impact pressure from time domain and ensemble domain analysis.

#### 5.4.4 Checking for linear correlation between different events

With the information available up to this point, it is possible to have some confidence that assuming the ergodicity of the process could be a reasonable assumption. There is however another interesting point which is worth some additional consideration: the independence (or not) of the maximum impact pressure between subsequent peaks. Indeed, assuming the process to be ergodic, the presence of a statistical dependence between different impacts can have consequences on the rate of convergence of statistical estimators as the run length increases. This is a known fact for continuous time processes (see, e.g. Bulian et al. (2006) and references therein) and similar considerations apply to discrete time processes, as in this case. An analysis regarding the problem of statistical dependence between different impacts was carried out by Souto-Iglesias et al. (2012). Herein the check for independence was carried out in two steps. First, the degree of linear correlation between the samples coming from different impacts was checked. Afterwards, a Pearson's chi-squared independence test was also carried out. The scope of the application of the aforementioned tests is to either identify any systematic correlation/dependence, or, alternatively, to not reject the assumption of independence of the maximum impact pressure between different impact events (an assumption often implicitly in the statistical analysis of sloshing impact data).

The first check is based on the determination of the linear correlation coefficient  $\rho$  between ensemble domain samples associated with different impacts. The scope of this analysis is to check whether there is any evident/significant/systematic linear correlation between different impacts, or, alternatively, whether the outcomes from different impact events can be considered as uncorrelated. To do so, the linear correlation coefficient between each couple of impacts was estimated and used to eventually create a symmetric matrix  $\hat{\rho}$ , where the element  $\left(\hat{\rho}\right)_{hk}$  of the matrix is the estimated correlation coefficient between ensemble domain data for the  $h - ht$  impact and for the  $k - ht$  impact.

Results from the application of the reported procedure are shown in figure 5.21. The color scale of the aforementioned figure was limited to the range  $[-0.4, 0.4]$  in order to enhance the view, considering the estimated maximum (0.385) and minimum (-0.287) off-diagonal correlation coefficients. From the results in figure 5.21 it is not possible to identify any clear visible structure and the correlation coefficient always tends to be quite small. This outcome was confirmed by checking the pattern of combinations where the estimated correlation coefficient is, from a statistical point of view, significantly different from zero, at 0.050 significance level. From the obtained results it could be quite safely concluded that, for this particular testing condition, maximum impact pressures measured at different impact events can be considered, with good practical approximation, as uncorrelated random variables. Independent random variables are always uncorrelated, while the opposite is not always true. Although a lack of linear correlation is often a good indicator of independence, it is in general not possible to decide on the independence by only looking at the analysis of the degree of linear correlations. However, in this case, the assumption of independence is supported by the application of a Pearson's chi-squared independence test (Bernstein and Bernstein, 1999).

#### **5.4.5 Consequences of the assumption of independent identically distributed (i.i.d.) maximum impact pressures at different impact events and of (practical) ergodicity**

As a result of the analysis based out in the previous section, it can be said that, for the particular test condition under analysis, the modelling of maximum impact pressure from different events as independent random variables is supported by the experimental data. Moreover, considering the results and associated discussion of the systematic application of the two-sample Kolmogorov-Smirnov test in figure 5.17, it can also be said that the distribution of the maximum impact pressure at different impact events is independent of the event provided the initial, say 5-10, impacts are neglected, since they have been identified as having transient statistical properties. Globally, it can be said that, for the particular case under analysis, the maximum impact pressures at different impact events can be modelled, after transient, as independent identically distributed (i.i.d.) random variables.



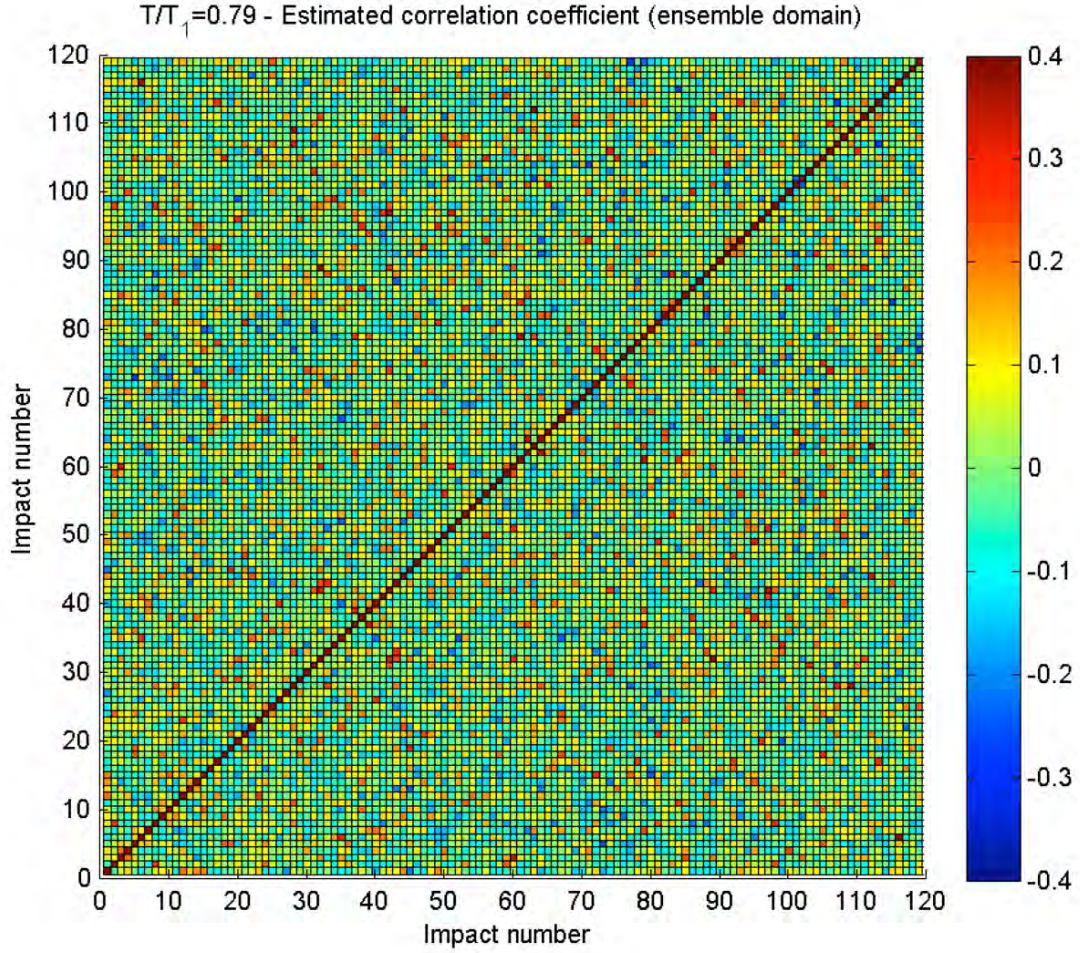


Figure 5.21: Estimated linear correlation coefficient between different events.

This has the direct consequence that the process can be assumed to be ergodic, which is additionally supported by the analyses in figure 5.18 and 5.19. These statistical properties of the process under analysis, which are often a-priori assumed and then used, but that have been here thoroughly checked to actually be usable for the analyzed case, allow providing uncertainty bounds for statistical estimators when working in time domain with the intention of estimating statistical characteristics pertaining, in principle, to the ensemble domain. Indeed, according to the observed behavior, pressure measurements coming from different impact events during a single long harmonic forcing test can be considered as independent samples (i.i.d. property) from the ensemble distributions of pressure impact ( (practical) ergodicity property).

Under the above assumptions, it is possible to look again at the outcomes in figure 5.18 regarding, for instance, the coefficient of variation of the running mean( $COV \{\hat{\mu}(j)\}$ ). In-

deed, under the assumption of i.i.d. random variables (actually, in this case, it is sufficient that the variables have the same mean and variance and that they are uncorrelated), the variance  $Var \{\hat{\mu}(j)\}$  of the estimator of the mean would be given by:

$$Var \{\hat{\mu}(j)\} = \frac{\sigma^2}{j} \Rightarrow \sqrt{Var \{\hat{\mu}(j)\}} = \frac{\sigma}{\sqrt{j}} \quad (5.1)$$

where  $\sigma^2$  is the true variance of the process and  $j$  is the total number of samples used in the calculation of  $\hat{\mu}(j)$ . Note that, in case of linear correlation being present between peaks, it is possible to rewrite expression 5.1 taking into account the degree of linear dependence between different peaks, i.e. by using information given by the autocorrelation function of the process (similarly to what can be done for continuous processes (Bulian et al., 2006)).

In order to check whether expression 5.1 properly describes the behavior of data reported in figure 5.18, an "ergodic" estimation of the standard deviation of the population has been determined by considering all the experiments and all the impacts from impact #10 (to remove transient effects) up to impact #119 for the available 119 experiments. This eventually leads to a total of 13090 samples and an estimated standard deviation  $\hat{\sigma} = 16.4mb$  (95% confidence interval: [16.2, 16.6 mb] using standard chi-squared approach, [15.7, 17.1 mb] using the "Adjusted Degrees of Freedom" method (Hummel et al., 2005)). The direct estimation of  $\sqrt{Var \{\hat{\mu}(j)\}}$  from the data was then compared with the modelling 5.1, which has been applied using the estimator  $\hat{\sigma}$  in place of the actual true standard deviation  $\sigma$ .

The obtained result is shown in figure 5.22. The good agreement visible in figure 5.22 seems to indicate that the assumption of i.i.d. random variables could be considered, for practical purposes, as a good working assumption when assessing the statistical confidence of estimators obtained from time domain analyses for this particular case. However, it is to be noticed that such simplified modelling tends to slightly underestimate the uncertainty in the estimator of the mean compared to what can be directly obtained from the available data.

By considering the fact that the assumption of (practical) ergodicity and the assumption of i.i.d. pressure peaks are supported by the data for this particular case, it is finally possible to provide the estimated cumulative distribution of the maximum impact pressure for the experimental condition under analysis, by making use of impacts #10-#119 for all the 119 experiments (13090 samples) and assuming the samples, with good approximation, as independent random samples from the same underlying distribution. The final result is shown in figure 5.23. It is also worth noting that the characteristics identified so far for the impact pressure process for this particular case, would be such to justify, at least approximately, the application of asymptotic extreme values distributions in case an analysis of extreme values statistics for the impact pressure would be of interest (Ochi, 1990).



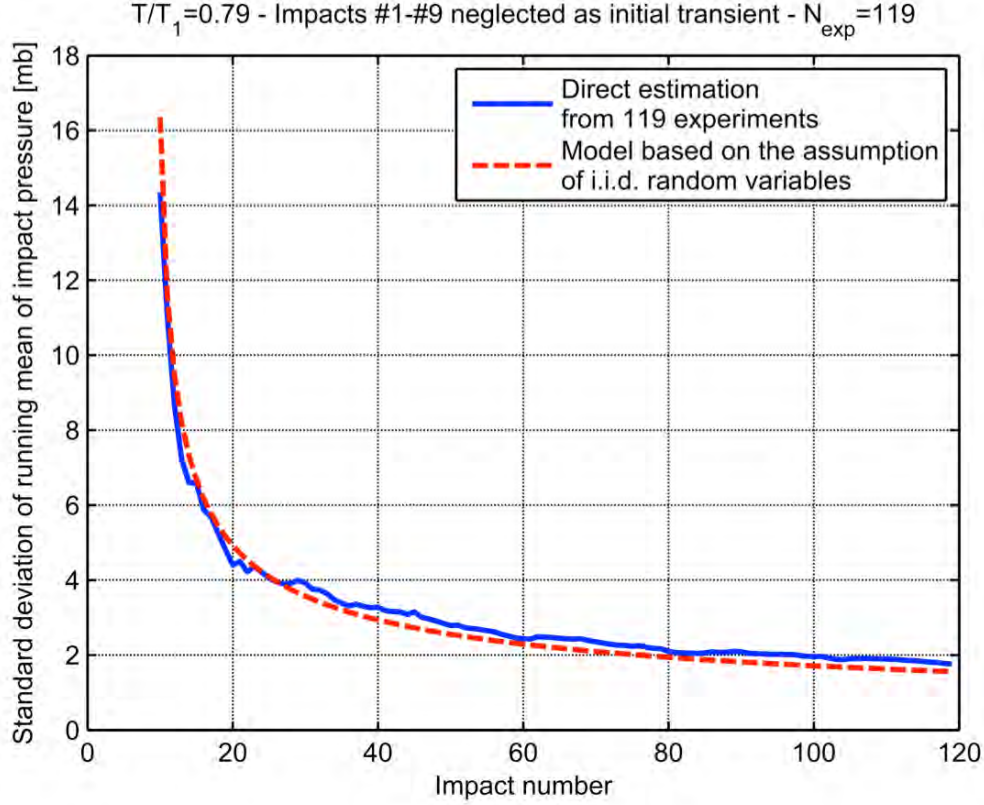


Figure 5.22: Directly estimated standard deviation of running mean compared with modelling based on the assumption of independent identically distributed random variables for the impact pressures at different impacts.

## 5.5 Summary

The analysis of impact pressure in sloshing experiments inevitably requires making use of statistical tools. Indeed, even under highly repeatable excitations, experimental outcomes show an inherent level of variability which cannot be addressed, in an efficient way, through a deterministic scheme of analysis. Moreover, concepts pertaining to the theory of stochastic process need to be used, being the impact pressure the result of the dynamics of the fluid inside the tank and of the fluid structure interaction.

Following these considerations, a statistical analysis of impact pressure registers in repeated model scale sloshing experiments under harmonic rotational forcing has been considered. The case investigated in this study has been the lateral fluid impact in a rectangular tank, using water as the fluid for these experiments. A series of more than 100 experiments each comprising more than 100 impact events has been conducted, seeking the highest feasible repeatability. Different excitation periods have been considered in a preliminary screening,

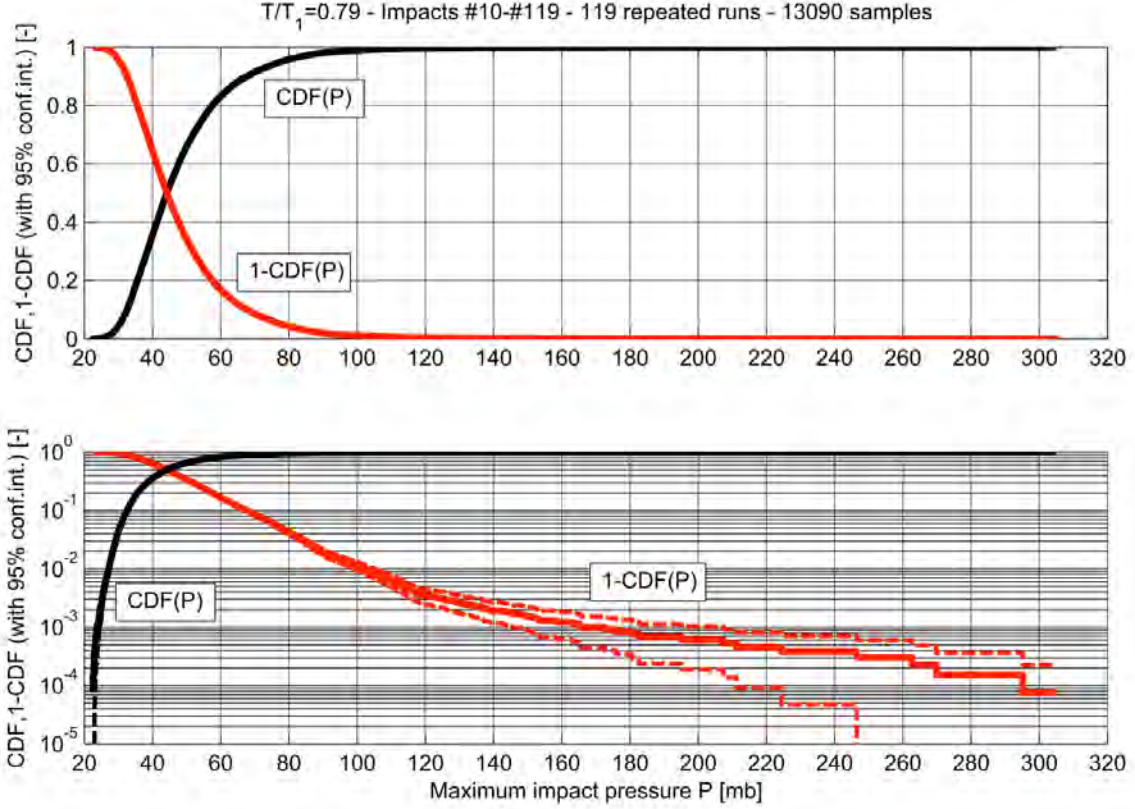


Figure 5.23: Estimated distribution of maximum impact pressure.

describing the main features of the impact dynamics. Since, even under a nominally deterministic periodic excitation, the pressure at each impact event is characterised by a high cycle-to-cycle and run-to-run variability, a statistical approach is thus used, treating the impact pressure as a stochastic process. The analysis was carried out to a large extent in the ensemble domain, as it should be in order to characterise a general stochastic process. For one selected excitation period, the analysis of the data was carried out considering the maximum pressure for each impact event and for each run. The analysis was aimed at identifying the main characteristics of the phenomenon, as well as the presence and extent of transient effects before the achievement of a stationary regime. This identification did not focus on finding an accurate distribution of the pressure peaks values, although this is a natural result of the whole analysis process. Instead, the analysis focused on the study of more global characteristics, such as the presence or not and, if present, the length/duration of a transient stage, the presence or not of correlation/dependence between different impacts, the variation or not of the distribution from peak to peak, the suitability or not of the (practical) ergodicity assumption, etc. Indeed, the understanding of such global characteristics may help in developing better simplified, though still effective, modelling of the phenomenon and may also help in carrying out a more sound analysis of experimental data.

For the condition under analysis, a transient stage, having a length of about 5-10 impacts, was identified by looking at the behaviour of ensemble mean and standard deviation of the impact pressure and through a systematic application of the two-sample Kolmogorov-Smirnov statistical hypothesis test on the ensemble distribution of the maximum impact pressure. The observed transient phase in the distribution of impact pressure is likely to be associated, at least partially, with the transient free surface behaviour of the global sloshing. The analysis of the data indicated the achievement of a subsequent stationary stage and also justifies the often implicitly used assumption of (practical) ergodicity, under which statistical characteristics of the maximum impact pressure can be obtained from a single, "sufficiently long", experimental run, instead of working in the ensemble domain. Attention should be paid, however, to remove the initial transient data, providing a clean stationary sample for the analysis. It has been shown that, in the tested case, both single (long) experiment and single impact ensemble samples can be considered equivalent from the statistical point of view (after the removal of the initial transient data). Moreover, it was shown that maximum impact pressures at different impacts can be considered with good approximation as independent identically distributed random variables for the particular analysed case. Regarding the overall level of data dispersion (repeatability), the first impact was shown, in this particular case, to be the most repeatable with distinctive characteristics compared to other impacts.

Although a particular sample application was considered, the general scope of this chapter was indeed to show how the systematic application of a statistical analysis technique, based on ensemble domain analysis, can help in addressing the main features of the problem in a consistent framework. The method of analysis presented in this chapter through the considered example case, is general in nature and is considered to be highly portable. In particular, it is considered to be able to allow a more thorough understanding of non-deterministic events, such as those considered herein, by looking at them from a sound statistical perspective. Typically, sloshing impact experiments are analysed directly in time domain, implicitly using the underlying assumption of ergodicity. However, a proper use of the ensemble domain analysis, as shown in this chapter, allows for the analysing, and possibly disclosing, of more features associated with the phenomenon than those which are typically addressed at steady state under the ergodicity assumption. In particular, transient characteristics as well as statistical correlation/dependence between impacts can be spotted out and quantified through ensemble domain analysis. A proper quantification of the length of the initial transient is necessary to avoid the contamination of data from non-steady samples. Furthermore, the analysis of correlation/dependence can, on one side, indirectly reflect the behaviour of the physics of the impact when looking at it from the perspective of stochastic processes, improving our overall understanding of the phenomenon. On the other side, the analysis of correlation/dependence can allow for the development of better models for the rate of convergence of statistical estimators as the

run length increases, going beyond, if proved necessary, the assumption of uncorrelation between different peaks. This can help in designing more efficient experimental techniques after having decided the required level of accuracy required for the estimators.

In addition to the above, the thorough description of the whole experimental setup makes the presented data suitable for comparison purposes and for validation of theoretical/numerical approaches.

# Chapter 6

## Forced Irregular Motion Sloshing Impacts

### 6.1 Introduction

Due to the stochastic nature of the wave excitation, if experiments can to be used for the determination of design loads, they should be performed, in preference, on scaled tanks excited by irregular motions, representing the actual motions experienced by the tank on-board the ship. As a matter of fact, sloshing assessments procedures recommended by the classification societies are based on this idea (DNV, 2006; ABS, 2006; Diebold, 2010). Usually, the tank is attached to a sloshing rig which should be able to reproduce both regular and irregular motions as specified by time series from a ship motion analysis in one or multiple DOF.

In the last decade, the number of experimental facilities that are able to carry out irregular sloshing experiments has increased and the size of such facilities has grown. The largest are located in: Ecole Centrale Nantes (Baudin E., 2013), Gaztransport et Technigaz (Gervaise et al., 2009), Marintek (Graczyk et al., 2012) and Seoul National University (Kim et al., 2009).

In recent years, more systematic methodologies or concepts for the experimental assessment of sloshing loads have been introduced, all of them following a statistical analysis of the pressure peaks obtained under irregular motion excitation of model scale tanks and looking as well at the very interesting and intricate issue of the scaling of sloshing experimental values to full scale. (Graczyk and Moan, 2008; Graczyk et al., 2006; Kuo et al., 2009; Berg, 1987; Olsen, 1976; Bass et al., 1985; Karimi et al., 2013).

In this chapter, the SDOF sloshing rig used during this study and described in chapter 4, is used to reproduce irregular motions. The content of this chapter focus on the

sloshing pressure peaks generated under SDOF irregular angular motion in a rectangular tank and its subsequent analysis from an statistical point of view, based on the extreme value distributions. It investigates aspects that has not been given much attention in the literature such as the sensitivity of the extreme value distribution to different realizations of the same motion spectrum.

The content of this chapter is structured as follows:

1. The sloshing pressure peak selection considerations are first described.
2. The obtained pressure peak clusters are then used as the input for the statistical distribution fitting by using Weibull and Pareto statistical distributions. Those distributions are used in order to estimate the extreme pressure values used in the cargo containment system structural design.
3. The selected irregular sloshing case (called C15), derived from the second sloshing benchmark (Loysel et al., 2012, 2013b), is discussed.
4. The repeatability of the statistical distributions of the pressure peaks across a set of experiments with the same irregular motion is also discussed.
5. The statistical fitting and therefore the estimation of the extreme values, depend on many experimental and theoretical aspects. The study of the sensitivity, to the variation of certain aspects is relevant for establishing the reliability of the extreme values estimation. The aspects under study have been the following:
  - (a) Influence on the generation of sloshing loads due to the driving motion signals when they differ in time domain but share the same power spectral density. This means that a set of random driving motion realizations for a given spectra are created.
  - (b) Influence on the pressure data collection and statistical fitting by simulating a malfunctioning of the sloshing rig in terms of reproducibility of the driving motion by inducing a random uniformly distributed BIAS (i.e.  $1\% \text{BIAS} = U([-0.01, 0.01])$ ) in the original driving motion signal.

## 6.2 Pressure Peak Selection

An impact pressure peak is defined as a pulsating load, short in duration and large in intensity. It is remarkable that, in some the cases, the impact pressure is around 25 times the hydrostatic pressure at the bottom of the tank. Commonly, impact pressure events are characterized by the well-known *church roof shape* (Peregrine, 2003). The pressure event is defined as the portion of the pressure register which contains the impact pressure peak (see figure 6.1).

As can be seen in figure 6.1, where a sample time history interval for a single sensor

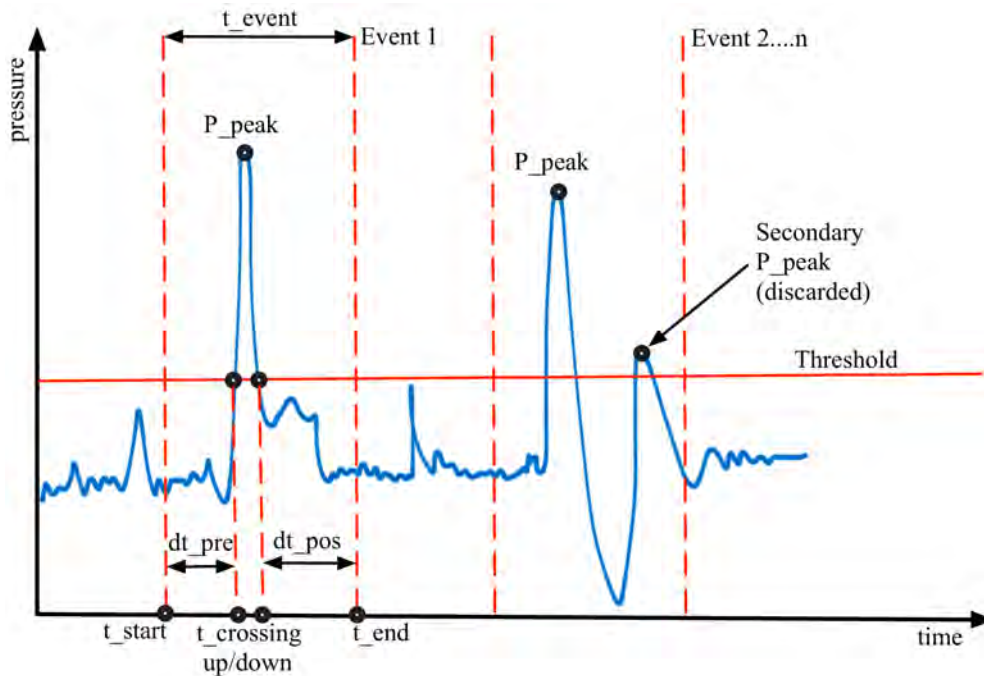


Figure 6.1: Pressure Peak and Event definition

is presented, the most important quantity in order to detect an impact event is the pressure threshold ("Threshold" in figure 6.1). Above such pressure level, it is considered that an impact event has taken place. The intersection between the pressure trace and the threshold occurs at time  $t_{crossing}(up/down)$ . The event is considered to start at a certain time  $t_{start} = t_{crossing}(up) - dt_{pre}$  before the pressure *Threshold* is exceeded. It is considered to end at  $t_{end} = t_{crossing}(down) + dt_{pos}$  a certain time after the pressure measured by the sensor has remained under the pressure *threshold*. Therefore, the event duration  $t_{event} = t_{end} - t_{start}$  depends on the impact.

In order to simplify the algorithms, in the sloshing benchmark Loysel et al. (2013b), it was proposed to use a fixed duration of the events  $t_{event} = 0.05s$ , a  $threshold = 4000Pa$  and a  $dt_{pre} = 0.015s$ .

The total duration of the event  $t_{event}$  is also known, in the literature, as *timewindow*. A correct selection of the  $t_{event}$  or *timewindow* guarantees a correct elimination of secondary peaks, originated by pressure signal oscillations, such oscillations can be due to, e.g. the presence of gas bubbles (Lugni et al., 2010).

From the derived events, the peak impact pressure, called  $P_{peak}$ , is extracted for the given event and only the  $P_{peak}$  over a fixed pressure value *threshold*, is extracted (see figure 6.1). This method is called *Peak Over Threshold (POT)* (Pickands, 1975) and is widely used in the statistical analysis of extremes. The *POT* method basically discards low non representative pressure peaks which may affect the accuracy of the statistical fittings.

A dedicated program done in *Matlab* scans the recorded pressure registers for each sensor

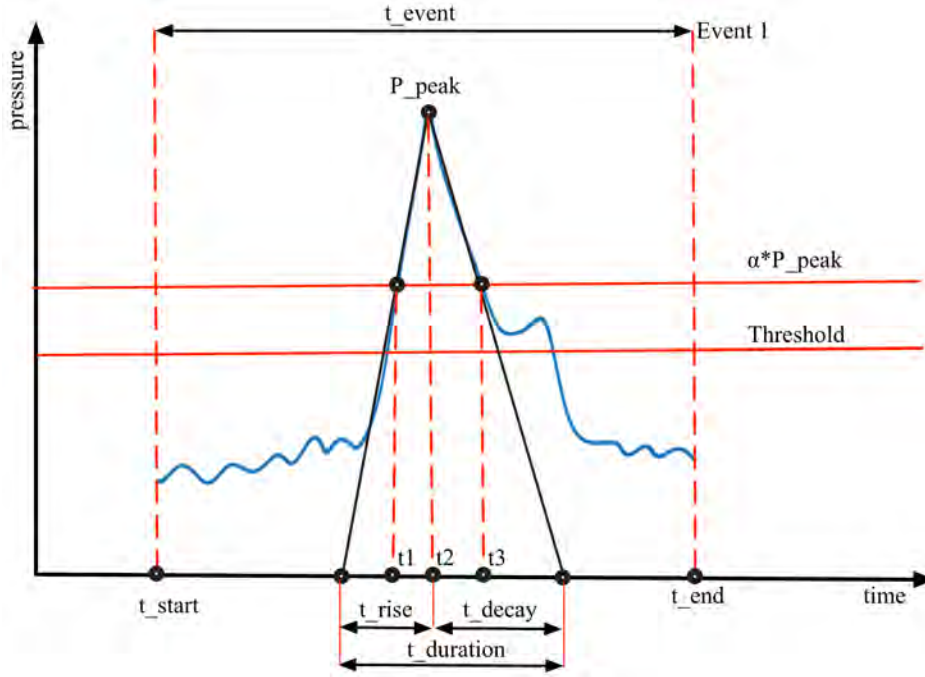


Figure 6.2: Triangular Model

and for each case, extracts the pressure events, get the  $P_{peak}$  clusters, and adds extra information extracted from the triangular model definition shown in figure 6.2. Such values will be used during the statistical post-processing.



According to figure 6.2,  $t_{rise}$  is the time taken from a reference pressure until  $P_{peak}$  occurs whilst  $t_{decay}$  is the time taken from the occurrence time of  $P_{peak}$  until the pressure reach the zero reference.  $\alpha * P_{peak}$  is an intermediate pressure value which can be the same for the rise and decay zones. ABS (ABS, 2006), SNU (Kim et al., 2010) and GTT (Eric Gervaise, Thibaut Loysel, 2013) propose using the values of  $\alpha_{rise} = \alpha_{decay} = 0.5$ . MARINTEK (Kim et al., 2010) propose uses  $\alpha_{rise} = 0.2$  and  $\alpha_{decay} = 0.5$ . The time  $t1$  is the corresponding time at the intermedium pressure value  $\alpha_{rise} * P_{peak}$ ,  $t2$  is the time of  $P_{peak}$  and  $t3$  is the time value at the  $\alpha_{decay} * P_{peak}$ .

Using the previous definitions the relations 6.1-6.6 can be written as follows:

$$t_{rise} = \frac{t2 - t1}{1 - \alpha_{rise}} \quad (6.1)$$

$$t_{decay} = \frac{t3 - t2}{1 - \alpha_{decay}} \quad (6.2)$$

$$t_{duration} = t_{rise} + t_{decay} \quad (6.3)$$

$$Skewness = 2 * \frac{t_{rise}}{t_{duration}} \quad (6.4)$$

$$A_1 = \frac{1}{2} P_{peak} * t_{rise} \quad (6.5)$$

$$A_2 = \frac{1}{2} P_{peak} * t_{duration} \quad (6.6)$$

The *Skewness* is a parameter that varies from 0 to 2 and depends on the peak shape.  $A_1$  is the rise zone area and  $A_2$  is the decay zone area.

The values used for the  $P_{peak}$  cluster collection in this work, also in agreement with the 2nd sloshing benchmark (Eric Gervaise, Thibaut Loysel, 2013) requirements have been set to  $\alpha_{rise} = \alpha_{decay} = 0.5$ .

## 6.3 Fitting of tail distribution and extreme values statistics

### 6.3.1 General

This section attempts to explain briefly the statistical methods commonly used in the sloshing pressure peaks statistical analysis and extremes pressure calculations.

The statistical fitting distributions applied herein are the *Weibull 3 parameters*, widely accepted by the industry, and the *Generalized Pareto Distribution* denoted by GPD by following the methods explained in Graczyk et al. (2006). Both distributions uses the *Peak Over Threshold* method (POT) (Pickands, 1975). In order to discard the low pressure peaks, the POT analysis method uses only data exceeding a given threshold in the statistical analysis. The reduced set of peaks is assumed to allow a better statistical fitting at the tail of the pressure peak distributions.

The information about the correct selection of the threshold value is an open problem and is typically left to the experience of the sloshing laboratories. Graczyk et al. (2006) studied the sensitivity to the threshold level  $u$  corresponding to the quantiles 70%-98% ( $q=0.70-0.98$ ) on the estimated extreme pressure calculations in order to find the proper threshold level  $u$ . Although the POT method (Pickands, 1975) implies the use of a high threshold level, Graczyk et al. (2006) report that the quantile  $q=0.87$  seems to be the limiting value of the threshold level; above this value the estimated parameters exhibit significant variation due to the small sample size. The quantile  $q=0.87$  is then adopted as the threshold level for this study.

### 6.3.2 The Weibull three parameters distribution

According to Cousineau (2009), the Weibull 3 parameters distribution with non-zero shift has three parameters:  $\gamma$  is the shape parameter responsible of the skewness of the distribution,  $\beta$  is the scale parameter and finally  $\delta$  the shift parameter, sometimes referred to as the location parameter, specifies the lower bound of the probability distribution function. There is an extensive literature about the Weibull 3 parameters estimation. Due to its simplicity and previous references the selected parameters estimation method has been the *Method of Moments* (MOM), applied by Kim et al. (2010).

## Weibull Cumulative Distribution Function (CDF) and Exceedance Function (1-CDF)

The Weibull 3 parameters *Cumulative Distribution Function (CDF)* (Kim et al., 2010), also know as *Non-Exceedance Function*, is given by:

$$CDF = F(x) = 1 - e^{[-(\frac{x-\delta}{\beta})^\gamma]}, \text{ where } \delta \leq x < \infty \quad (6.7)$$

The Weibull 3 parameters *Exceedance Function* is given by equation 6.8

$$1 - CDF = e^{[-(\frac{x-\delta}{\beta})^\gamma]}, \text{ where } \delta \leq x < \infty \quad (6.8)$$

## Parameters estimation using method of moments MOM

Equations 6.9-6.11 (Kim et al., 2010), can be used to determine the distribution parameters  $\beta$ ,  $\sigma$  and  $\gamma$  from the observed data. The procedure is as follows:

$$\beta \Gamma \left( 1 + \frac{1}{\gamma} \right) + \delta \approx \hat{\mu} = \frac{1}{n} \sum_{i=1}^n x_i \quad (6.9)$$

$$\beta^2 \left[ \Gamma \left( 1 + \frac{2}{\gamma} \right) - \Gamma^2 \left( 1 + \frac{1}{\gamma} \right) \right] \approx \hat{\sigma}^2 = \frac{1}{n-1} \sum_{i=1}^n (x_i - \hat{\mu})^2 \quad (6.10)$$

$$\frac{\Gamma \left( 1 + \frac{3}{\gamma} \right) - 3 \Gamma \left( 1 + \frac{1}{\gamma} \right) \Gamma \left( 1 + \frac{2}{\gamma} \right) + 2 \Gamma^3 \left( 1 + \frac{1}{\gamma} \right)}{\left[ \Gamma \left( 1 + \frac{2}{\gamma} \right) - \Gamma^2 \left( 1 + \frac{1}{\gamma} \right) \right]^{3/2}} \approx \hat{\gamma}_1 = \frac{1}{n} \sum_{i=1}^n \left( \frac{x_i - \hat{\mu}}{\hat{\sigma}} \right)^3 \quad (6.11)$$

In the previous equations  $\gamma$  is defined as the *Skewness* and describes the asymmetry from the normal distribution in a set of statistical data.  $\Gamma$  is the *Gamma* distribution function and is defined as:

$$\Gamma(n) = \int_0^{\infty} e^{-x} x^{n-1} dx \quad (6.12)$$

Using an bisection method it is possible to find the equation roots in the equation (6.11), calculating the value of the shape parameter  $\gamma$  for a given precision (e.g,  $1 \cdot 10^{-8}$ ). With the  $\gamma$  parameter and equation (6.10) it is possible to determine the scale parameter  $\beta$  by direct solution. The shift parameter  $\delta$  also know as location is calculated by direct solution using equation (6.9) and using the previously calculated parameters  $\gamma$  and  $\beta$ .

### Extreme values estimation

The equation (6.7) gives the cumulative probability value  $p$  or  $F(x)$  for a given  $x$  value (impact pressure). Considering the inverse case, for a given cumulative probability  $p$  it is possible calculate the  $x$  value. The concept of return period can be used to define a value for  $p$ , eventually leading for  $x(p)$ , which is referred shortly as "Extreme Value" (Hemer, 2006).

For a number of occurrences or pressure peaks  $n$ , in a specific experimental time duration  $T$  in hours, the mean frequency  $\varsigma$  between peaks is:

$$\varsigma = \frac{n}{T} \quad (6.13)$$

The mean period between peaks is:

$$\frac{T}{m} \quad (6.14)$$

The CDF of the probable extreme value expected to occur in  $m\varsigma$  observations or probability level allocated to one exceedance in  $m$  hours is :

$$q = 1 - \frac{1}{m\varsigma} \quad (6.15)$$

Applying two times logarithms to the equation (6.7) and solving for  $x$ , the extreme value  $x$  can be estimated using the equation (6.16) by replacing the previously defined values of  $q, c, \lambda$  and  $\delta$ .

$$\begin{aligned} \ln(-\ln(1-q)) &= c \ln(x - \delta) - c \ln \lambda \\ a &= \ln(-\ln(1-q)) \\ b &= c \ln \lambda \end{aligned}$$

$$x = e^{\left(\frac{a+b}{c}\right)} + \delta \quad (6.16)$$

### 6.3.3 The Generalized Pareto Distribution GPD and POT method

The Peaks over threshold (POT) method considers all values greater than a sufficiently high threshold value,  $u$ . The distribution of those values asymptotically follows the Generalized Pareto Distribution (GPD) (Pickands, 1975).

#### Generalized Pareto Cumulative Distribution Function (CDF) and Exceedance Function (1-CDF)

The distribution of the peaks over the threshold is described by the cumulative distribution function:

$$CDF = F(x) = F_X(x)[1 - F(u)] + F(u), x \geq u \quad (6.17)$$

Where  $F(u)$  is the quantile (probability value) previously defined using the threshold value  $u$ , therefore  $1 - F(u)$  is the probability for the random variable  $X$  to exceed  $u$ .  $F_X(x)$  is the distribution of the peaks over the threshold. According to (Pickands, 1975),  $F_X(x)$  asymptotically follows the Generalized Pareto Distribution (GPD) and then can be expressed by the cumulative distribution functions (Graczyk et al., 2006):

$$F_X(x) = 1 - (1 + c(x - u)/\lambda)^{-1/c}, c \neq 0 \quad (6.18)$$

$$F_X(x) = 1 - e^{-(x-u)/\lambda}, c = 0 \quad (6.19)$$

The Exceedance Function (1-CDF) of the peaks over the threshold is calculated using the equation (6.20)

$$1 - CDF = 1 - F(x) = [1 - F_X(x)][1 - F(u)] \quad (6.20)$$

### Parameters Estimation, Method of the Moments (MOM)

Due to its simplicity the MOM (Hosking and Wallis, 1987) is used in order to estimate the parameters of GPD in equations (6.18) and (6.19). This method uses the mean  $\mu$  and variance  $\sigma^2$  of the peaks over threshold sample. The mean  $\mu$  and variance  $\sigma^2$  are then respectively:

$$\mu = \frac{\lambda}{1 - c}, c < 1 \quad (6.21)$$

$$\sigma^2 = \frac{\lambda^2}{(1 - 2c)(1 - c)^2}, c < \frac{1}{2} \quad (6.22)$$

The moment estimators  $\hat{c}$  and  $\hat{\lambda}$  of  $c$  and  $\lambda$  are then given by:

$$\hat{c} = \frac{1}{2} \left( 1 - \frac{\hat{\mu}^2}{\hat{\sigma}^2} \right) \quad (6.23)$$

$$\hat{\lambda} = \frac{1}{2} \hat{\mu} \left( 1 + \frac{\hat{\mu}^2}{\hat{\sigma}^2} \right) \quad (6.24)$$

Where  $\hat{\mu}$  and  $\hat{\sigma}^2$  are the sample mean and sample variance of the excesses given by:

$$\hat{\mu} = \frac{1}{N_u} \sum_{i=1}^{N_u} (x_i - u) \quad (6.25)$$

$$\hat{\sigma}^2 = \frac{1}{N_u - 1} \sum_{i=1}^{N_u} (x_i - u - \hat{\mu})^2 \quad (6.26)$$

Where  $N_u$  is the number of peaks exceeding the threshold  $u$ .

## Extreme values estimation

The procedure for extreme values estimation using the GPD distribution fitting is similar to the used in the section 6.3.2, with the exception that the number of occurrences  $N_u$  is the number of peaks over the threshold  $u$ , due this, the mean frequency between clusters  $\varsigma$  is redefined by equation (6.27).

$$\varsigma = \frac{N_u}{T} \quad (6.27)$$

The CDF of the probable extreme value expected to occur in  $m\varsigma$  observations or probability level allocated to one exceedance in  $m$  hours is :

$$q = 1 - \frac{1}{m\varsigma} \quad (6.28)$$

The extreme value  $x$  is estimated, according to the value of  $(c)$ , using the equations 6.29-6.30 which are the inverse of the equations 6.18-6.19 respectively and by replacing the values of  $q$ ,  $c$ ,  $u$  and  $\lambda$  previously obtained.

$$x = u + \frac{\lambda}{c} [(1 - q)^{-c} - 1], c \neq 0 \quad (6.29)$$

$$x = u - \lambda \ln(1 - q), c = 0 \quad (6.30)$$

## 6.4 Fourier Transformations of the Irregular Driving Motion Signals

### 6.4.1 General

The irregular driving motion signals, used in sloshing experiments, are derived from the combination of a wave spectrum (selected according to the operational target place of the vessel) and the motions RAO's of the vessel. Wave spectra are statistically modelled based on ocean buoy measurements or standard models whilst the RAO's are obtained by using numerical calculation methods and/or experimental approaches.

A sensitivity study regarding the influence of the driving motion signals in the sloshing peak pressure data collection is provided herein. This influence is based on two modifications of the original driving motion signal (named C15 and provided by GTT). The first modification called *Case 1*, applies a random lag to each component of the original signal. This lag aims at reproducing the nature of the random generation of the irregular driving motion signals which share the same FFT but lead to different realizations in the time domain. The second modification, called *Case 2*, introduces a random uniformly distributed

BIAS (i.e.  $1\% \text{BIAS} = U([-0.01, 0.01])$ ) in the original driving motion signal in order to mimic either differences in the motion RAO computation, or wrong reproducibility due to malfunctioning or wrong calibration of the sloshing rig control and actuators. Both modifications are based on *Fourier* transformations of the original driving motion signals and are explained in the following.

### 6.4.2 Case 1: LAG

For a given discrete signal  $x[n]$  such as the driving motion signal  $C15$

$$\{x[n]\}_{n=0}^{N-1}$$

The DFT (Discrete Fourier Transformation)  $X[k]$  for  $k = 0, \dots, N-1$  with  $\omega_N = e^{\frac{2\pi j}{N}}$  is :

$$X[k] = \sum_{n=0}^{N-1} x[n] \omega_N^{-nk} \quad (6.31)$$

And the IDFT (Inverse Discrete Fourier Transformation)  $x[n]$  is:

$$x[n] = \frac{1}{N} \sum_{k=0}^{N-1} X[k] \omega_N^{nk} \quad (6.32)$$

Different time domain signals coming from the same spectrum can be generated by applying a lag to the DFT( $X[k]$ ) (6.31) of the original signal  $x[n]$  ( $C15$  in this case) as follows:

$$X[k]_{LAG} = X[k] \cdot e^{jLAG[k]} \quad (6.33)$$

where  $LAG[k]$  is defined as a uniformly distributed random variable:

$$LAG[k] = U([0, 2\pi]), k = 0, \dots, N-1 \quad (6.34)$$

The generated signal with lag ( $x[n]_{LAG}$ ) is computed as:

$$x[n]_{LAG} = \frac{1}{N} \sum_{k=0}^{N-1} X[k]_{LAG} \omega_N^{nk} \quad (6.35)$$

A total of five new signals were generated for this study. Figure 6.3 shows a portion of the original  $C15$  and the  $C15_{LAG1}$  and  $C15_{LAG2}$  driving motions, where the differences in the time domain signals are clearly noticeable. Figure 6.4 shows the Fourier harmonics of the  $C15$ ,  $C15_{LAG1}$  and  $C15_{LAG2}$  driving motions signals, where not differences can be appreciate in their corresponding spectrum as expected (see figure 6.4d).

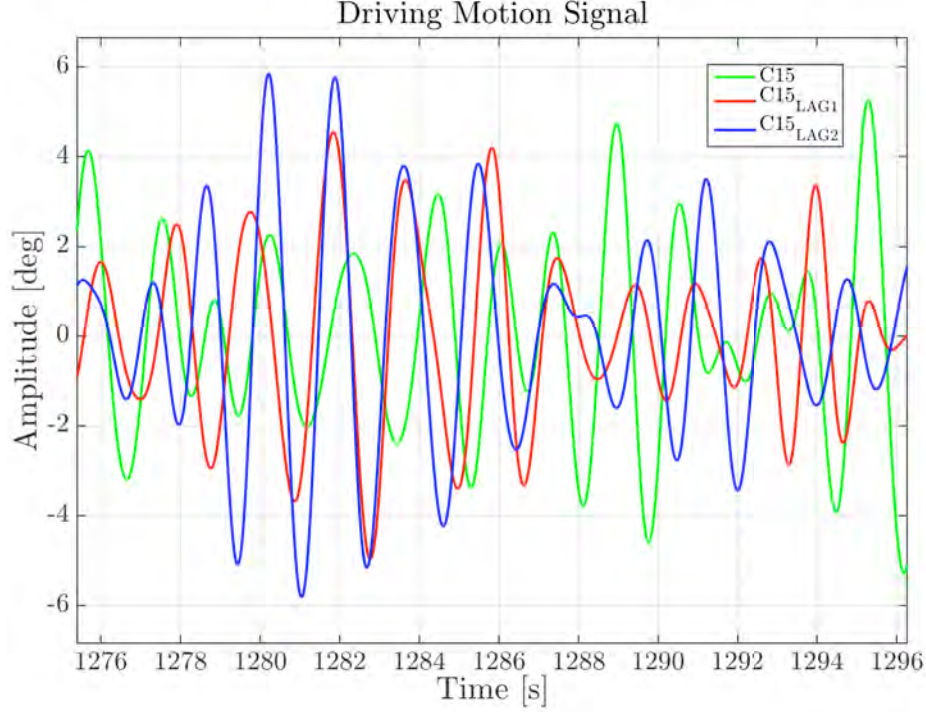


Figure 6.3:  $C15$ ,  $C15_{LAG1}$  and  $C15_{LAG2}$  driving motions signals

### 6.4.3 Case 2: BIAS

In order to apply a random  $BIAS$  of  $\pm 1\%$  to the original signal ( $C15$ ), the biased DFT  $X[k]_{BIAS}$  (6.36) is computed as:

$$X[k]_{BIAS} = X[k] \cdot (1 + BIAS[k]) \quad (6.36)$$

Where  $BIAS[k]$  (6.37) is a random variable  $X$ , uniformly distributed on  $[-0.01, 0.01]$ . Therefore each harmonic  $X[k]$  is perturbed by a random value between  $[-0.01, 0.01]$  ( $BIAS[k]$ ). The 1%  $BIAS$  vector is defined as:

$$BIAS[k](1\%) = U([-0.01, 0.01]), k = 0, \dots, N - 1 \quad (6.37)$$

The reconstructed biased signal  $x[n]_{BIAS}$  (6.38) is written as:

$$x[n]_{BIAS} = \frac{1}{N} \sum_{k=0}^{N-1} X[k]_{BIAS} \omega_N^{nk} \quad (6.38)$$

$x[n]$  and  $x[n]_{BIAS}$  correspond to the original irregular driving motion  $C15$  and the biased driving motion signal  $C15_{BIAS(1\%)}$ , respectively. The driving motion signals of the cases  $C15_{BIAS(2\%)}$ ,  $C15_{BIAS(5\%)}$  and  $C15_{BIAS(10\%)}$  are then reconstructed, following the same formulation of 6.38, but replacing the unitary  $BIAS[k]$  vector by:

$$BIAS[k](2\%) = U([-0.02, 0.02]), k = 0, \dots, N - 1 \quad (6.39)$$



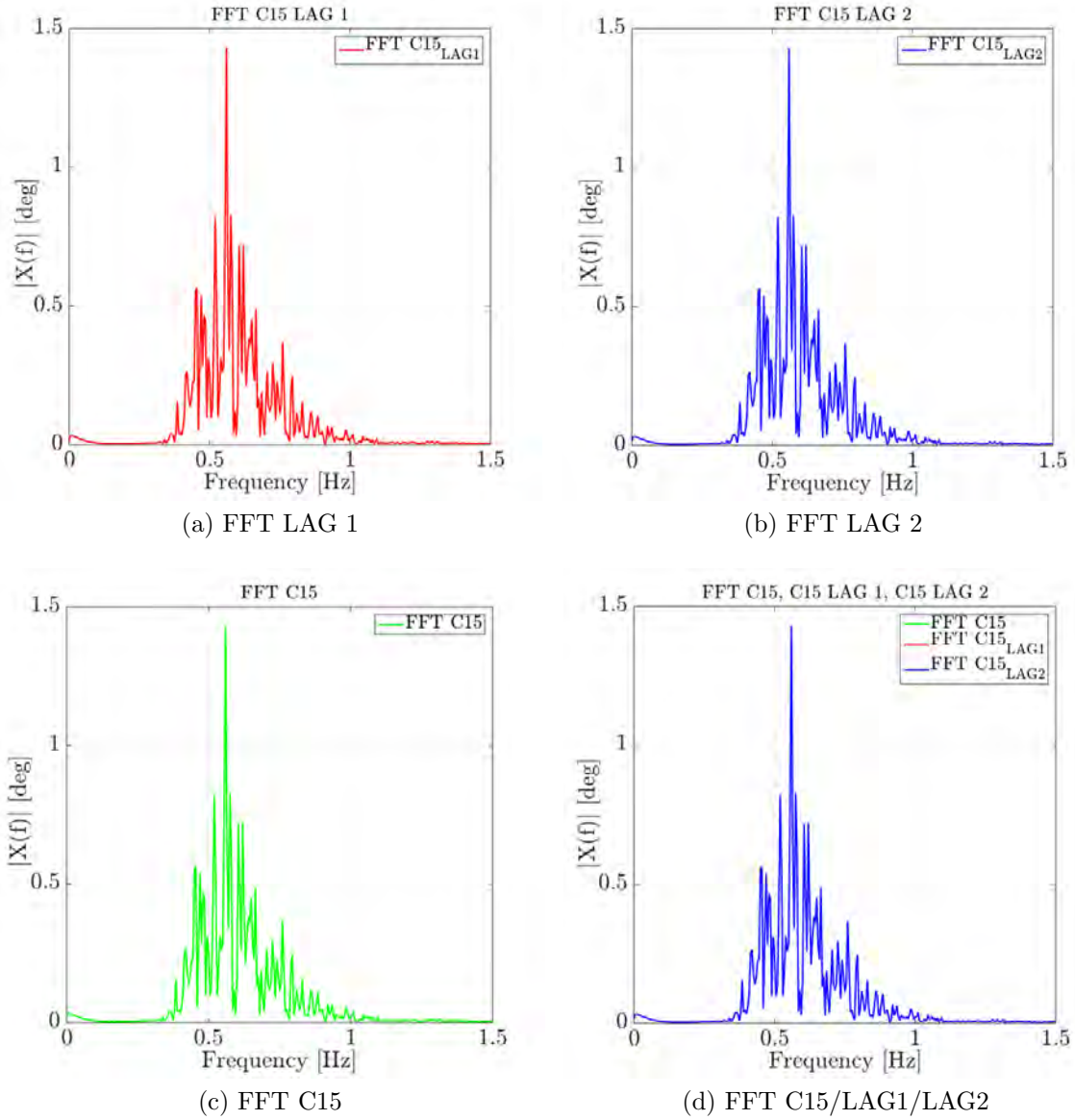


Figure 6.4: FFT of the signals  $C15$ ,  $C15_{LAG1}$  and  $C15_{LAG2}$

$$BIAS[k](5\%) = U([-0.05, 0.05]), k = 0, \dots, N - 1 \quad (6.40)$$

$$BIAS[k](10\%) = U([-0.10, 0.10]), k = 0, \dots, N - 1 \quad (6.41)$$

The new biased signals  $C15_{BIAS(1\%)}$ ,  $C15_{BIAS(2\%)}$ ,  $C15_{BIAS(5\%)}$  and  $C15_{BIAS(10\%)}$  are then used as the driving motion signals of the *Case2*. Figure 6.5 shows a portion of the original  $C15$ ,  $C15_{BIAS(5\%)}$  and  $C15_{BIAS(10\%)}$  driving motions where the random perturbation in the amplitude is clearly noticeable. This variation in the amplitude aims at mimicking a malfunctioning of the sloshing rig due to inaccuracies in the the driving motion reproduction

or wrong calibration of the actuators. It can be also seen as a difference due to numerical errors or modelling parameters in the computation of the motion RAO's.

Figure 6.6 shows the FFT of the  $C15$ ,  $C15_{BIAS(5\%)}$  and  $C15_{BIAS(10\%)}$  driving motions signals. Slightly variations in their corresponding spectrum are immediately noticed, in terms of the amplitude of the signals in each frequency component as can be seen in figure which shows a superimposed FFT of the signals  $C15$ ,  $C15_{BIAS(5\%)}$  and  $C15_{BIAS(10\%)}$

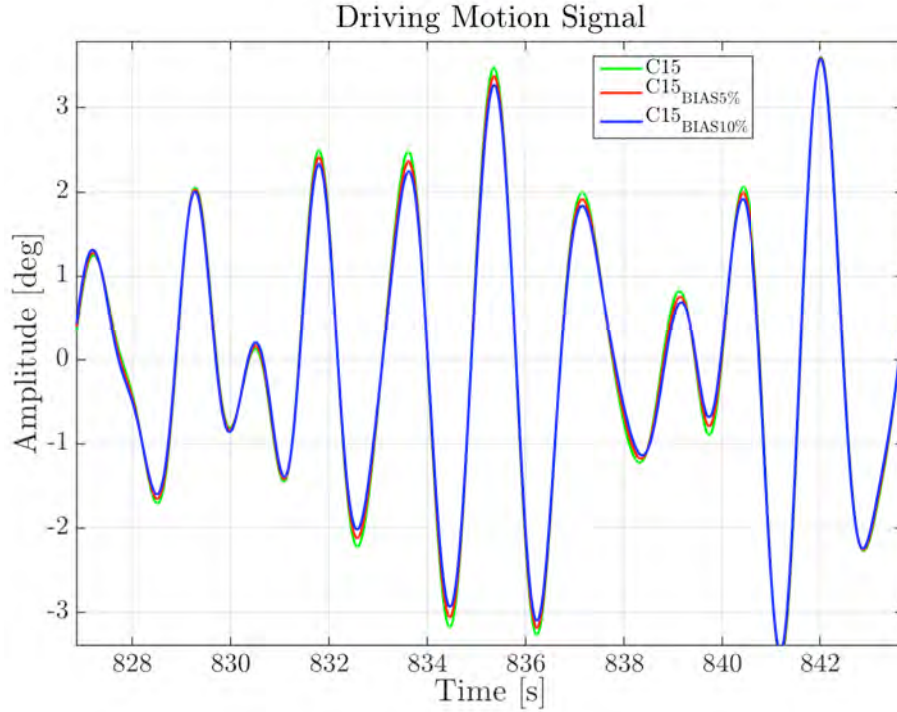


Figure 6.5:  $C15$ ,  $C15_{BIAS(5\%)}$  and  $C15_{BIAS(10\%)}$  driving motions signals

## 6.5 Results

### 6.5.1 General

The results presented in this section correspond to a sensitivity analysis in the sloshing pressure generated in high filling levels, continuing the work proposed by *GTT* and documented in Loysel et al. (2012, 2013b), where several facilities, sensors and cases were compared. The work of Loysel et al. (2013b) analyses external factors which may affect the reproducibility of the sloshing phenomenon in order to obtain similar results from different sloshing facilities under the same initial conditions. The first sloshing committee proposed to pay attention to some parameters such as filling level, tank alignment and

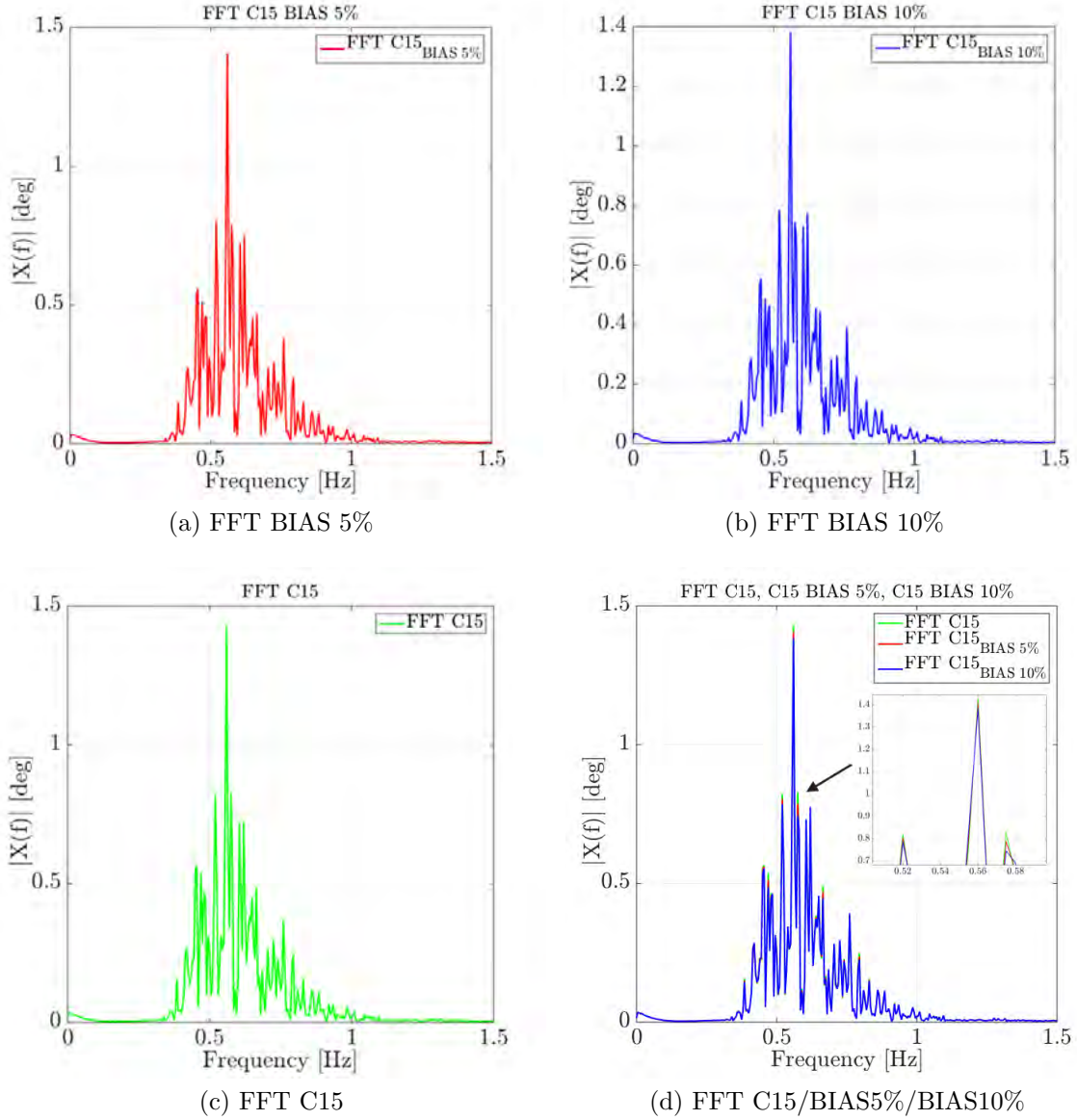


Figure 6.6: FFT of the signals  $C15$ ,  $C15_{BIAS(5\%)}$  and  $C15_{BIAS(10\%)}$

driving motion during the second sloshing benchmark realization (Eric Gervaise, Thibaut Loysel, 2013). Although the data provided by the different facilities improved consistently in comparison with the 1st sloshing benchmark (Loysel et al., 2012), there is a noticeable discrepancy related to the pressure data collection.

This chapter aims at characterizing the influence in the pressure data collection by applying slightly modifications on the original driving motion. The chosen driving motion

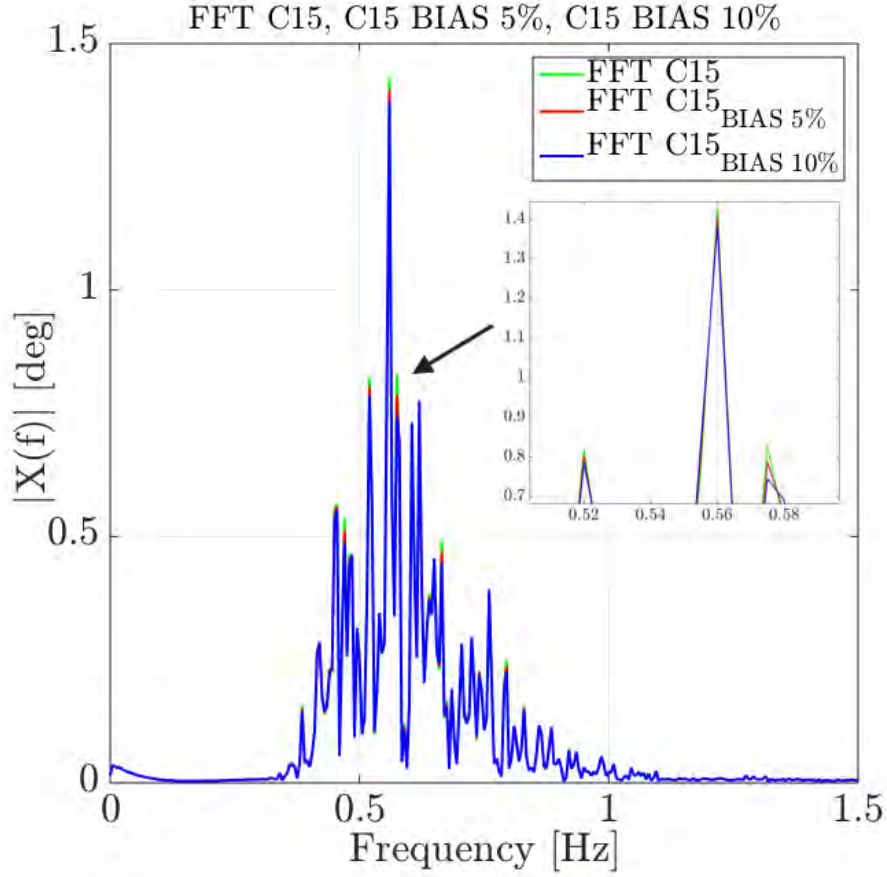


Figure 6.7: Superimposed FFT of the signals  $C15$ ,  $C15_{BIAS(5\%)}$  and  $C15_{BIAS(10\%)}$

( $C15$ ) is derived from the 2nd sloshing benchmark (Loysel et al., 2013b). Similar work was previously documented in (Mehl et al., 2013b), where the influence of small changes in the exciting motion (translational single-wave impact cases) on the sloshing behaviour was carried out. The  $C15$  case is an irregular rotation case in 1DOF (Y axis) which can be carried out in the sloshing rig previously detailed in section 4.2.

The content of this chapter addresses sensitivity to some parameters in the sloshing pressure data collection by considering three cases as follows:

1. *Case 0*: This case corresponds to the original  $C15$  case without any perturbation in the original driving motion.  $GTT$  proposed at least 6 repetitions of this case during the 2nd sloshing benchmark in order to collect a large enough impact pressure samples for a reliable statistical post-processing. Herein this case was repeated 100 times in order to ensure the repetitiveness of the phenomenon and guarantee convergence of statistical estimators. This case is used as the reference one during the statistical comparison. Every run is 1 hour duration, composed by 10 minutes of resting time between experiments and 50 minutes of duration.

2. *Case 1*: This case studies the influence in the pressure data collection of the randomness introduced through different driving motion realizations for a given spectrum (spectrum obtained by Fourier analysis of the original *C15* motion time history). It means that the driving motion signals differ in the time history but share the same power spectral density (PSD). A total of 5 new *C15* driving motion signals were generated. Every sub case is repeated 10 times.
3. *Case 2*: This case introduces a motional malfunctioning of the sloshing rig in terms of reproducibility of the driving motion (*C15*) by inducing a random BIAS (1,2,5,10%) in the original driving motion signal and study the influence of it in the pressure data collection. Every sub-case is repeated 10 times.

## 6.5.2 Experimental setup

The experimental campaign was carried out at the facilities of the Polytechnic University of Madrid using the sloshing rig detailed in section 4.2. The tank is a rectangular longitudinal section of a 1:40 scale LNG tank whose geometry was provided by *GTT* for the benchmark (Loysel et al., 2012) and whose dimensions are shown in figure 6.8. The filling level for the *C15* case is 85%. The fluid used during the experiments is water at standard conditions. Special attention was paid to the temperature monitoring of the fluid inside the tank and the temperature in the room.

The irregular motion *C15* provided by *GTT* was reported to have been obtained from sea keeping calculations by Froude scaling at scale 1:40. The rotation is defined assuming a centre of rotation at the origin of the coordinate system as can be seen in figure 6.8. The irregular motion is approximately 50 minutes, is composed by 2966 seconds including 60 seconds for initial ramp and 60 seconds for ending ramp. The irregular *C15* motion including the ramps was provided by *GTT*. The sensors configuration matches the reduced configuration proposed by *GTT* during the second sloshing benchmark. A total of 16 PCB 112A21 sensors, previously described in section 4.3, are located at the top corners of the tank and distributed in two sensor arrays. Those arrays are located near the upper corners of the tank and their dimensions can be seen in figure 6.9. Figure 6.10 shows the real sensors setup and cabling. The pressure given by the sensors was registered at 50 kHz and post-processed in real time by a *National instruments PXI* hardware shown in figure 6.11 in conjunction with a dedicated *Labview* application. Both hardware and software was borrowed from *GTT* in 2013.

## 6.5.3 Case 0: *GTT* benchmark case *C15*

### Exceedance Distribution Function ( $1 - CDF$ )

The *Exceedance Distribution Function* ( $1-CDF$ ) provides the probability that a specified value of the random variable is exceeded. It is commonly used to define statistical char-

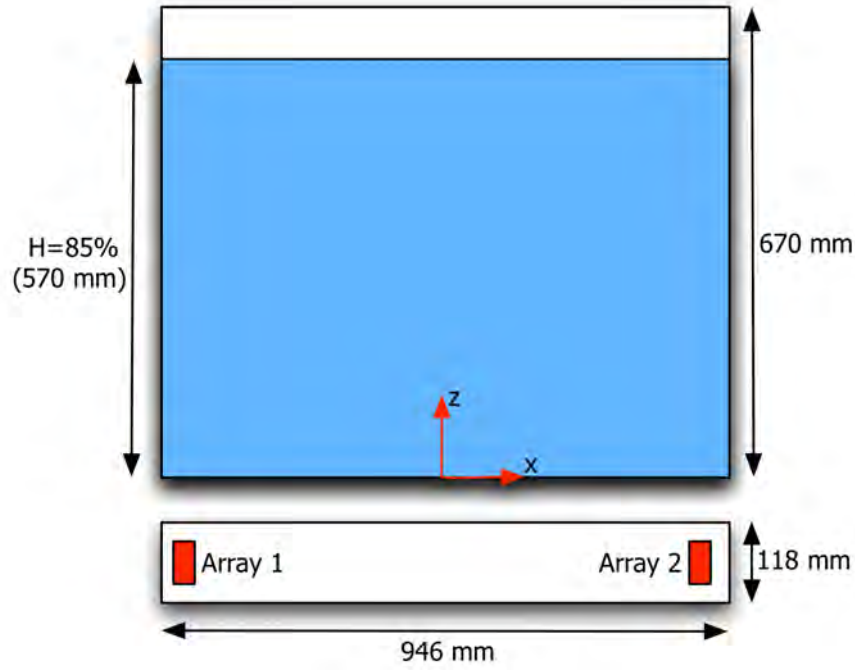


Figure 6.8: Tank Geometry

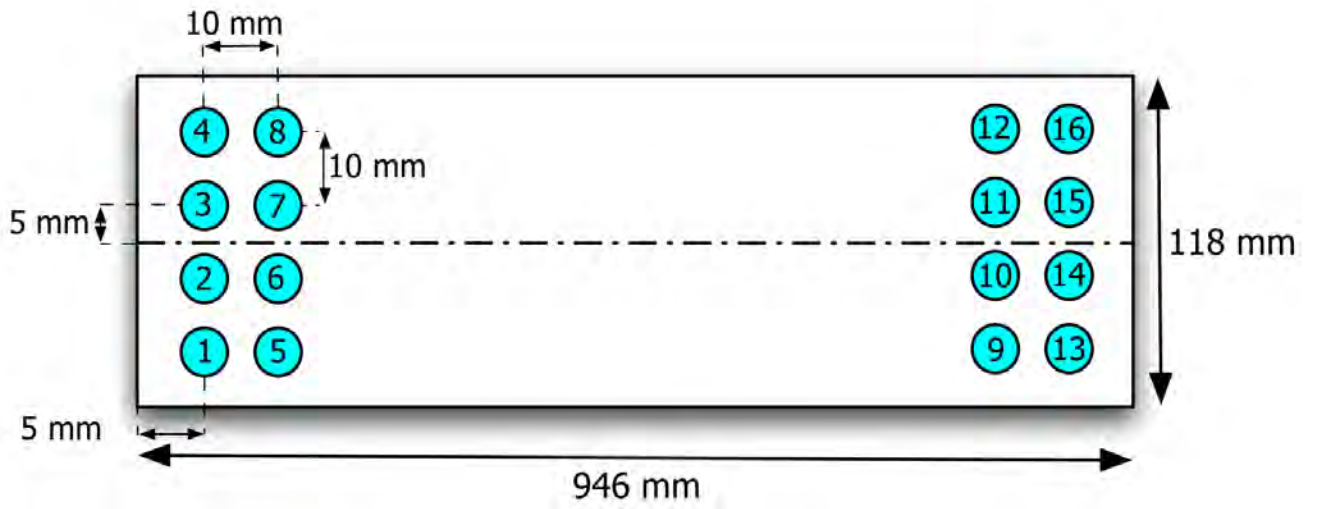


Figure 6.9: Sensors array configuration

acteristics and assess sloshing severity. It is obtained from the *Cumulative Distribution Function* (*CDF*) by definition as  $1 - CDF$  where *CDF* corresponds to the function which describes that the probability of the random variable  $X$  takes on a value less than or equal to  $x$  ( $CDF = F(x) = P\{X \leq x\}$ ). The *CDF* and therefore the  $1 - CDF$ , are built by



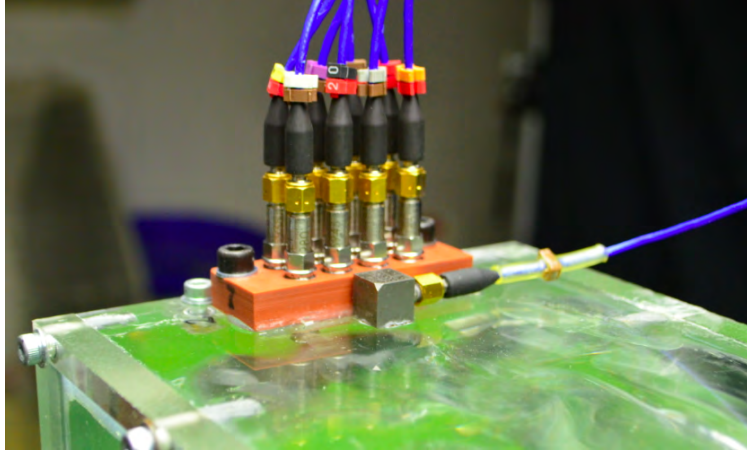


Figure 6.10: Sensors setup and cabling

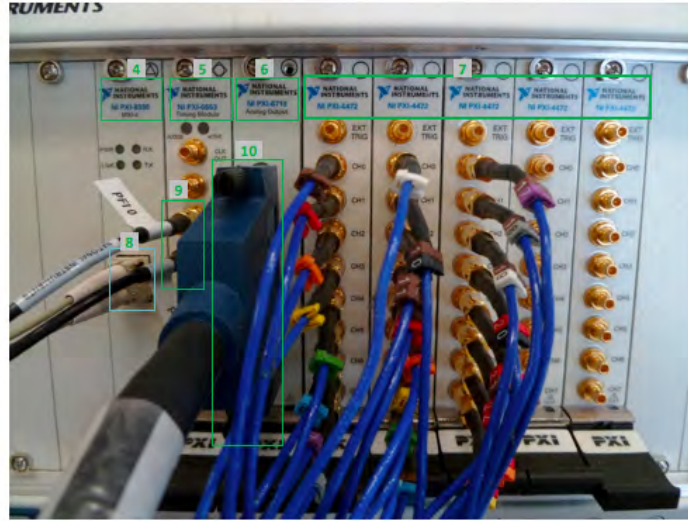


Figure 6.11: NI-PXI data acquisition system

using the impact pressure samples collected during the experiments.  $1 - CDF$  plots are a useful tool for comparing not only experiments, but also sensors and facilities in terms of the collected impact pressure samples.

Figure 6.12 shows the  $1 - CDF$  of all the available sensors and runs of the Case 0. This case comprises 100 repetitions or runs of the C15 case. C15 corresponds to a irregular experiment of 50 min of duration (ramps included) provided by GTT during the second sloshing benchmark (Loysel et al., 2013b) . Every repetition comprises a variable number of peaks, between 300-350 for each sensor. Only the peaks over the threshold are registered. The 100 repetitions allow, to collect a large amount of peaks, called impact pressure samples,

which is then used in the statistical analysis. The impact pressure samples is defined as the global set of peaks over threshold for each sensor in all the repetitions. Since the number of collected peaks is variable across experiments, also the impact pressure samples differs according to the sensor: the smallest cluster comprises 30851 peaks (sensor S7) located in array 1, while the largest 34175 peaks (sensor S10) located in array 2. Selected sensors S6, S10 and S11 comprises 32503, 34175 and 31918 peaks respectively.

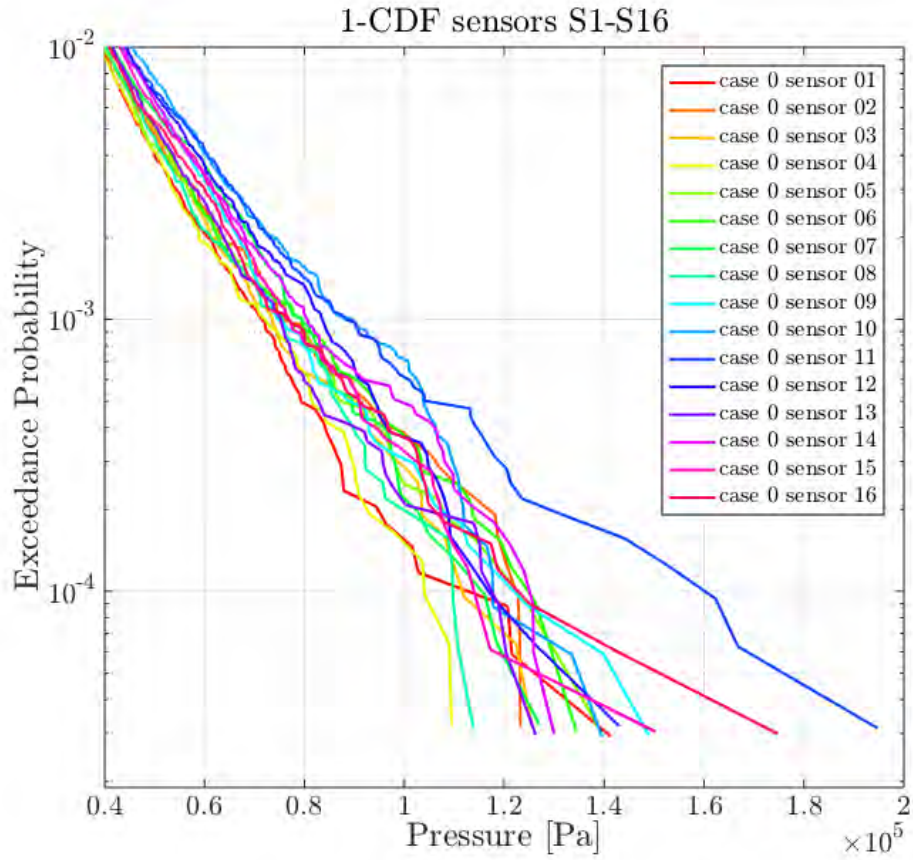


Figure 6.12:  $1 - CDF$  Case 0 sensors 1-16

### Spatial Pressure Distribution

The largest pressures per sensor will be used to collect the P10 set (average of the 10 largest impact pressure peaks) and to analyze, therefore the spatial distribution of the pressure according to the array and sensor location. Figure 6.13 shows the spatial distribution of the P10 average pressure according to the sensor and array location. Following the



figure 6.13(a), it is noticeable that the sensor S6 (sensor 2, row 2) shows the maximum pressure registered for array 1 during the 100 C15 repetitions. Figure 6.13(b) shows the P10 average pressure in array 2. Comparing with array 1, array 2 shows the maximum pressure registered during the 100 repetitions and it corresponds to S11. The second largest (S16) is even higher than S6 in array 1, therefore array 2 is registering the maximum global pressures. Intriguingly sensor S4, the symmetric one to S16, records the lowest P10 in all the experiments. This denotes the high variability not only in the P10 magnitude but also in the sensor location. Sensors S6 (Maximum P10 in array 1) and S11 (Maximum P10 in array 2) are both located away the tank corners and almost symmetric each other. In general, the P10 average in array 2 for every sensor is higher than the P10 in array 1. The extreme pressure estimation study will be focused, as the pressure sensors arrays can exhibit different statistical behaviors, in those sensors with maximum P10 per array. Those sensors are S6 (array 1) and S11 (array 2). Sensors S6 and S11 are then compared with the following cases (*Case 1*, *Case 2*) and the deviation in the results will be explained.

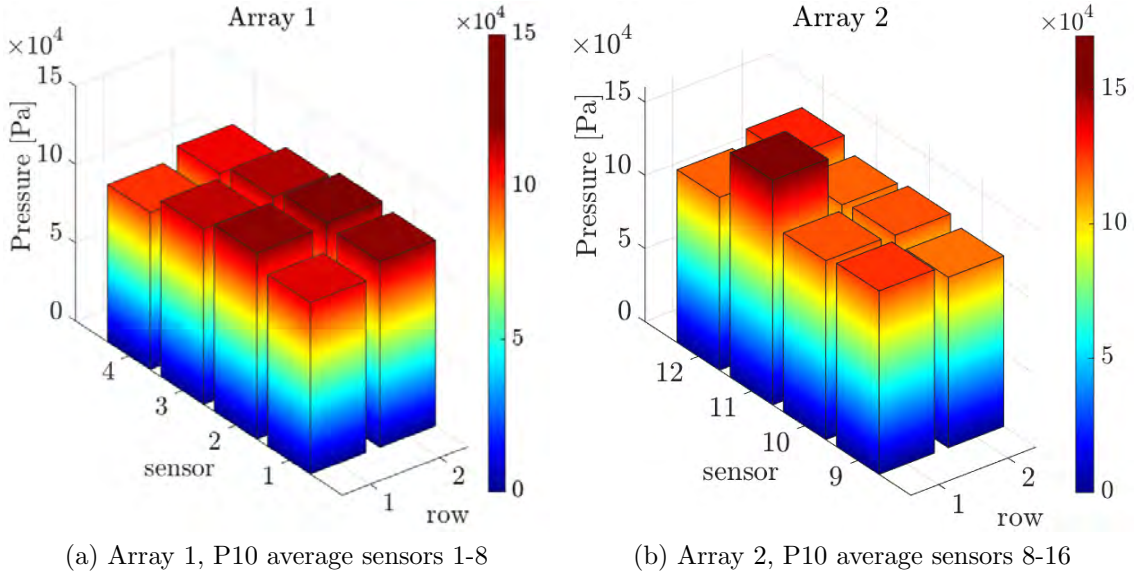


Figure 6.13: Array 1,2 P10 average sensors 1-16

### Extreme Values Estimation

The aim of this section is to check the ability of the statistical models *Weibull* and *GPD* to estimate, from the pressure peak clusters of 100 repetitions collected in *Case 0*, the pressures associated to a greater return periods (RP) (i.e 200, 500, 1000 hours). The estimated pressure is then called *Extreme Value* (EV). The return periods below 100 runs of the *Case 0* will be used as “reference” values when comparing with less repetitions cases such the *Case 1* and *Case 2* (10 runs). Each run is 50 min duration, therefore 100 runs

corresponds to a experimental time duration of  $T = 83.33[hours]$ . For sensor S6, the number of occurrences or pressure peaks is  $n=32503[peaks]$  and the mean frequency between peaks calculated using the equation 6.13 is  $\varsigma = 390.03[peaks/hour]$ . The quantiles  $q$  are then calculated using the equation 6.15. Table 6.1 shows the estimated extreme values for the given return periods for sensor S6. Figure 6.14 shows the  $1 - CDF$  plot for sensor

| RP [hours] | q [%]   | EV Weibull [Pa] | EV GPD [Pa] |
|------------|---------|-----------------|-------------|
| 1          | 99.7436 | 59750           | 60033       |
| 10         | 99.9744 | 94773           | 97911       |
| 20         | 99.9872 | 106463          | 110931      |
| 50         | 99.9949 | 122674          | 129431      |
| 100        | 99.9974 | 135488          | 144470      |
| 200        | 99.9987 | 148760          | 160473      |
| 500        | 99.9995 | 166987          | 183213      |
| 1000       | 99.9997 | 181274          | 201699      |

Table 6.1: Extreme Values Sensor S6 Case 0, with  $T = 83.33[hours]$ ,  $n=32503[peaks]$  and  $\varsigma = 390.03[peaks/hour]$

S6 in conjunction with the 95% confidence intervals, the statistical fitting of the pressure data following the Weibull Three Parameters and GPD exceedance distributions and the probability levels corresponding to the return periods of the table 6.1.

Following the figure 6.14, it can be observed that the selected distributions can be well used in order to fit accurately the pressure data for the sensor S6 at the tail of the distribution. Nevertheless, looking at 6.1, it can be noticed that the GPD distribution tends to provide larger extreme values compared to the Weibull distribution. In any case only minor differences in the extreme values are observed even of high return period values such 1000 hours. This denotes that the two distributions models provide a similar fit for the long duration data (100 runs) and therefore guarantees a comparable estimation of the extreme pressure beyond 100 runs.

For sensor S11 the number of occurrences or pressure peaks is  $n=31918[peaks]$  and the mean frequency between peaks calculated using the equation 6.13 is  $\varsigma = 383.01[peaks/hour]$ . The quantiles  $q$  are then calculated using the equation 6.15. Table 6.2 shows the estimated extreme values for sensor S11. Similar to sensor S6, GPD tends to overestimate the extreme pressure values but also minor differences even in high return periods are noticeable. Figure 6.15 shows the  $1 - CDF$  for sensor S11 with the 95% lower and upper confidence bounds where it can also be observed that the fitted distributions (Weibull, GPD) follow the  $1 - CDF$  plot.

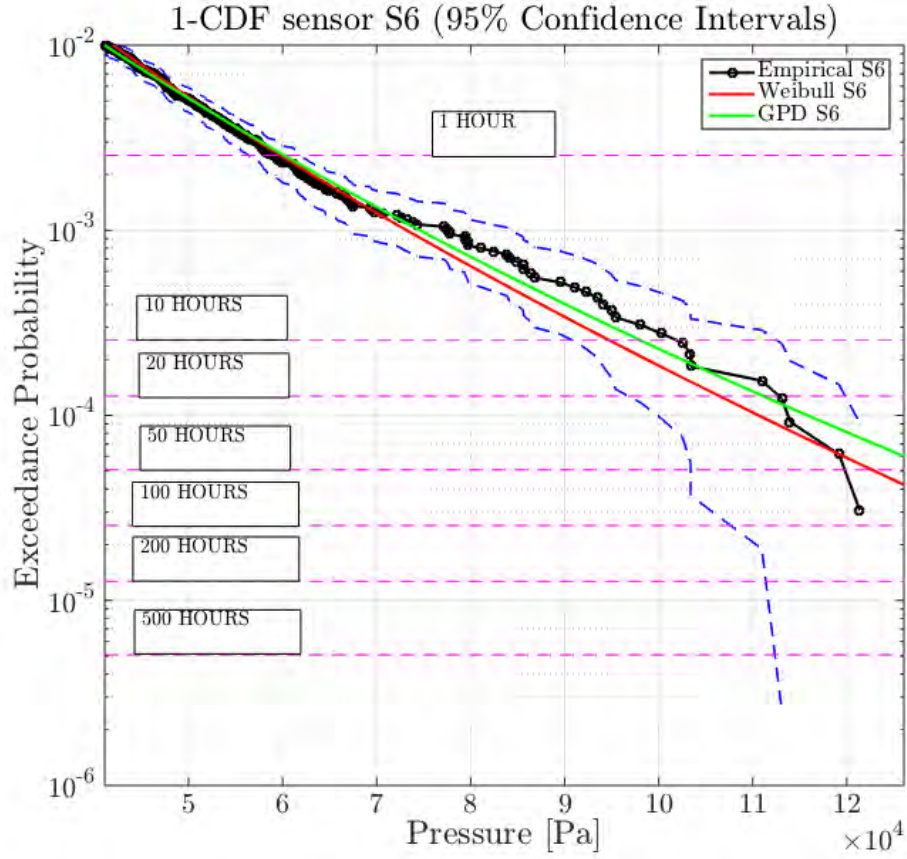


Figure 6.14: Weibull and GPD Fitting for S6,  $1 - CDF$  plotted with 95% confidence intervals

| RP [hours] | q [%]   | EV Weibull [Pa] | EV GPD [Pa] |
|------------|---------|-----------------|-------------|
| 1          | 99.7389 | 66567           | 67579       |
| 10         | 99.9739 | 111635          | 114160      |
| 20         | 99.9869 | 127170          | 129994      |
| 50         | 99.9948 | 149039          | 152355      |
| 100        | 99.9974 | 166567          | 170422      |
| 200        | 99.9987 | 184925          | 189547      |
| 500        | 99.9995 | 210438          | 216556      |
| 1000       | 99.9997 | 230664          | 238379      |

Table 6.2: Extreme Values Sensor S11 Case 0, with  $T = 83.33[hours]$ ,  $n=31918[peaks]$  and  $\varsigma = 383.01[peaks/hour]$

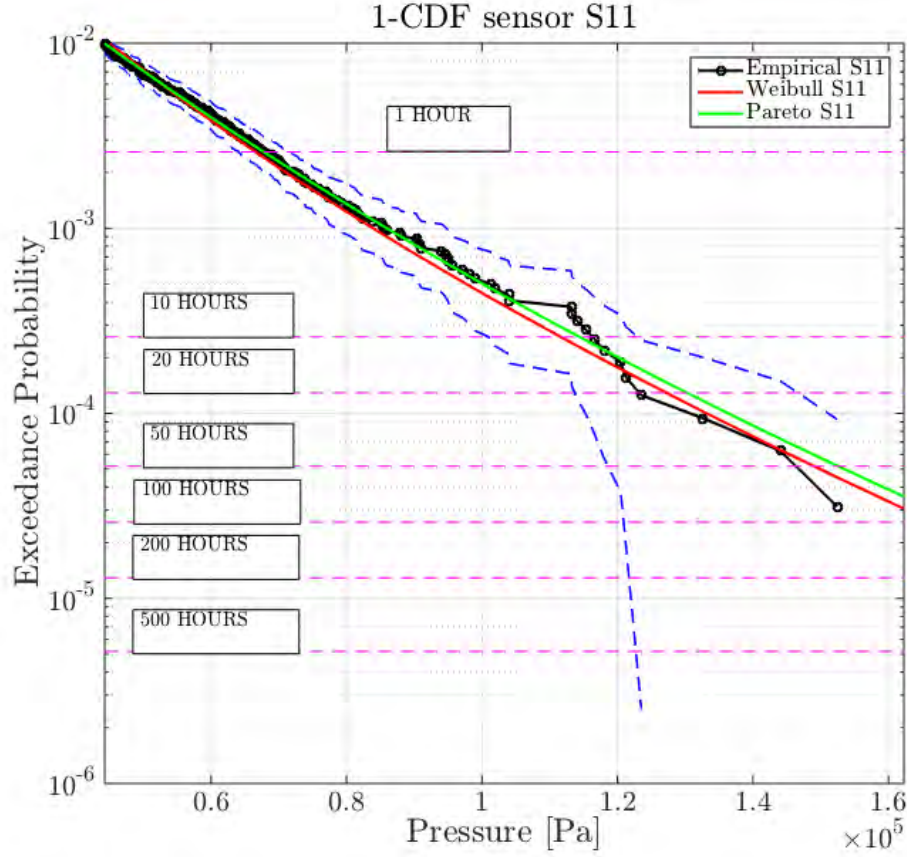


Figure 6.15: Weibull and GPD Fitting for S11,  $1 - CDF$  plotted with 95% confidence intervals

Due to interesting results found, later, in the other cases, for the sensor S10, although this sensor does not exhibit a particular behaviour as can be noticed in the figure 6.13b, it was decided to include this sensor in the following comparisons. For sensor S10 the number of occurrences or pressure peaks is  $n=34175[peaks]$  and the mean frequency between peaks calculated using the equation 6.13 is  $\varsigma = 410.10[peaks/hour]$ . The quantiles  $q$  are then calculated using the equation 6.15. The extreme values EV for this sensor are summarized in table 6.3 and will serve as the comparing reference values for the consecutive cases.

#### 6.5.4 *Case 1: Influence of the Random driving motion realizations in the Spatial Pressure Distribution and Extreme Values Estimation*

The influence on the pressure data collection and therefore on the extreme pressures calculations, due to the 5 new random driving motion realizations is reported in this section.

| RP [hours] | q [%]   | EV Weibull [Pa] | EV GPD [Pa] |
|------------|---------|-----------------|-------------|
| 1          | 99.7562 | 66434           | 69511       |
| 10         | 99.9756 | 108224          | 106922      |
| 20         | 99.9878 | 122393          | 117691      |
| 50         | 99.9951 | 142186          | 131591      |
| 100        | 99.9976 | 157939          | 141858      |
| 200        | 99.9988 | 174345          | 151915      |
| 500        | 99.9995 | 197008          | 164895      |
| 1000       | 99.9998 | 214872          | 174482      |

Table 6.3: Extreme Values Sensor S10 Case 0, with  $T = 83.33[hours]$ ,  $n=34175[peaks]$  and  $\varsigma = 410.10[peaks/hour]$

Every sub case, five in total (called R1-R5) are repeated 10 times using the same driving motions generated according to section 6.4.1. Estimated extreme values will be compared with the *Case 0* (100 runs), previously described.

This section will be structured as follows: A spatial pressure distribution will provide an indication of the P10 pressures accordingly to the array, sensors, and sub cases. Following, exceedance plots of selected sensors together with  $KS2$  tests and impact pressure samples box plots, will provide an estimation of the dispersion in the impact pressure samples distributions. Finally the empirical distributions will be fitted by following the two extreme value models Weibull and Generalized Pareto (GPD) and the extreme pressure values will be estimated for every sensor and sub case and the influence in the extreme pressures calculation due to the different driving motion realizations will be reported.

### Spatial Pressure Distribution

The spatial distribution of the pressure maximum in each sensor according to each sub case (i.e *Case 1* R1) can be appreciated in figures 6.16 and 6.17 which shows the derived average of the maximum 10 pressures P10 plots of the array 1 and array 2 respectively, obtained during the *Case 1* execution.

The average of the maximum 10 pressures (P10) of the array 1 denotes that the maximum pressure is not registered at the selected sensor (S6) during the execution of the *Case 1*, as can be seen in figure 6.16. Bear in mind that S6 was the sensor with maximum average P10 in *Case 0* 100 runs. However, in *Case 1*, average of the maximum 10 pressures P10 seems to change its location in every sub case, sometimes at the vicinity of the sensor S6 as can be seen in 6.16a, 6.16b and 6.16d for the sub cases R1, R2 and R5. Location of the maximum average P10 in sub cases R3 and R5 are out of the vicinity of sensor S6 as can be seen in figures 6.16c and 6.16e. The change of location of the maximum average P10

suggests, apart from the inherent randomness of the phenomenon, that *Case 1* introduces variability in terms of the maximum pressure location, which can take place at any of the sensors of array 1. This can be observed in figure 6.16f, where the P10 distribution in array 1 obtained during the *Case 0*, seems to be homogeneous in all the array 1 covered area. Bear in mind that *Case 1* is 10 runs and its results are being compared with *Case 0* (100 runs).

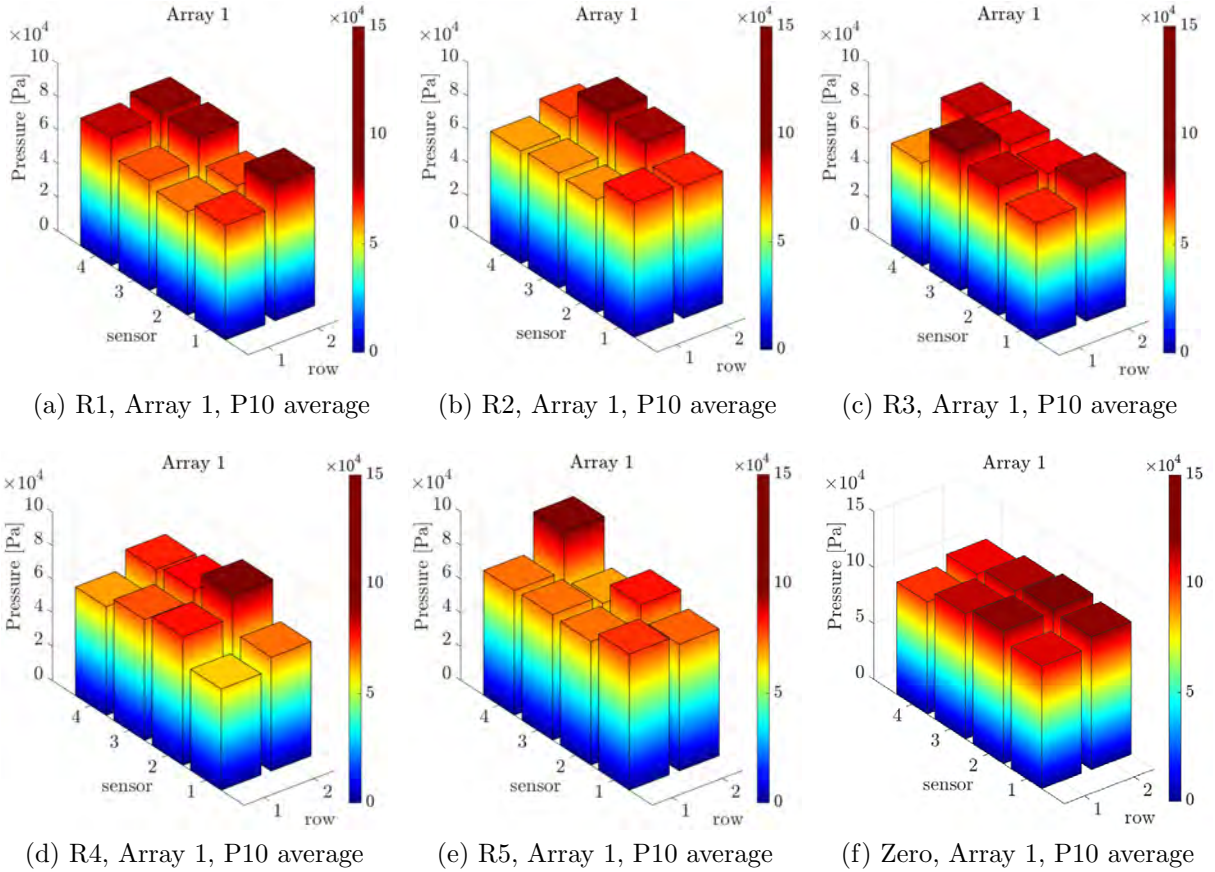


Figure 6.16: *Case 1* vs Case 0, Array 1, P10 [Pa] average sensors 1-8



In comparison with array 1, the pressure spatial distribution in array 2 seems to be more consistent, in terms of the location of the registered maximum, which in most of the cases coincides with sensor S10, as can be seen in figures 6.17a, 6.17c and 6.17e. Therefore, sensor S10 will be introduced and compared in this section due to the reported behaviour. Sub cases R2 and R4 report their maximum P10 located at sensors S11 and S12 respectively as can be appreciated in figures 6.17b and 6.17d. Sensors S10, S11 and S12 are all located in the row 1 of the array 2, this means that even introducing a new driving motion in the experiments the pressure maximum is recorded at the vicinity of the row 1.

Figure 6.17f shows the P10 of array 2 *Case 0*, where the maximum is registered in

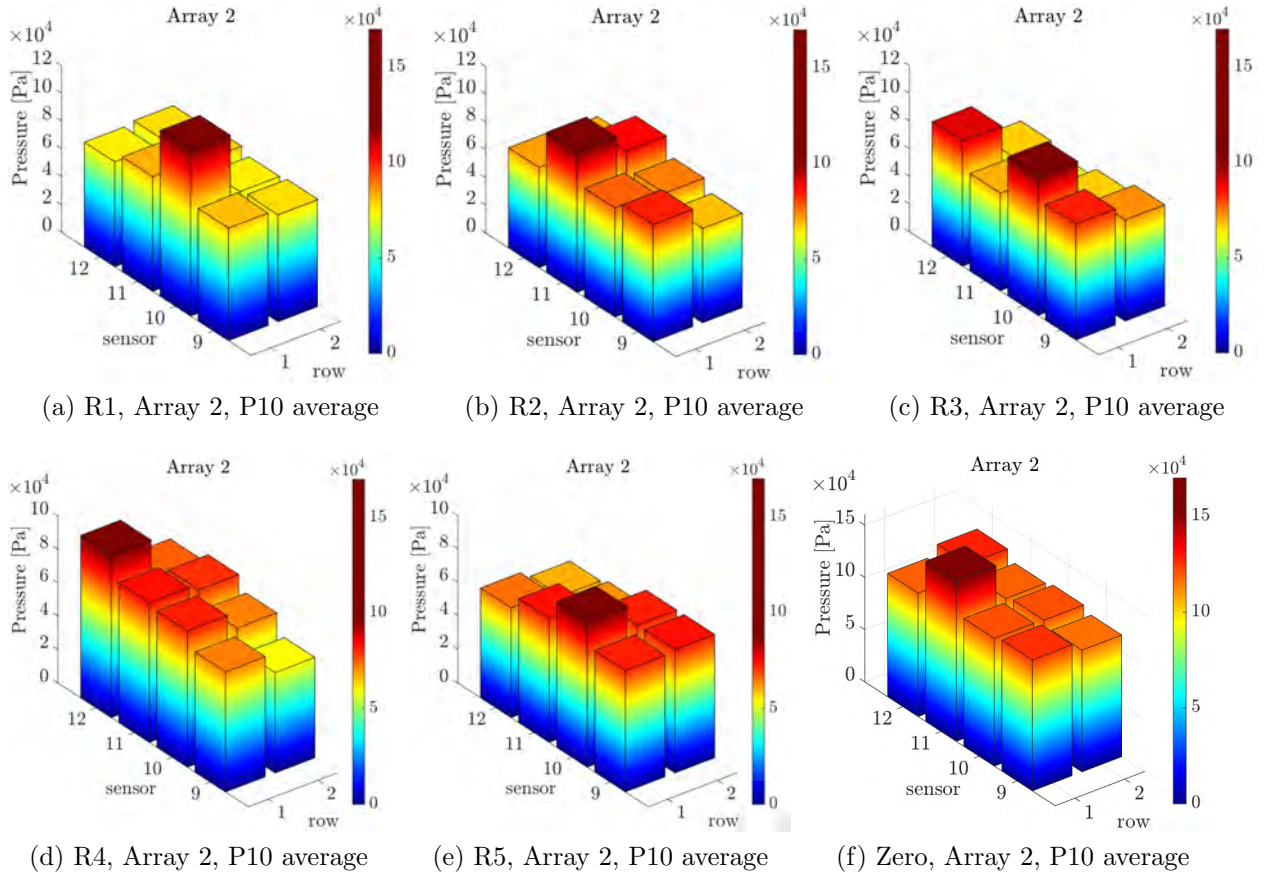


Figure 6.17: *Case 1* vs *Case 0*, Array 2, P10 [Pa] average sensors 8-16

sensor S11 which is the maximum global P10 ( $\sim 15 \cdot 10^4$  Pa) and is clearly visible from others sensors. Maximum P10 for *Case 1* is reported by sensor S10 in the sub case R1 ( $\sim 12 \cdot 10^4$  Pa). The aforementioned suggests that the different driving motion realizations change of location of the maximum average P10 at the vicinity of the row 1 array 2. In general, the pressures reported in array 1 are smaller than in array 2.



### Exceedance Function (1-CDF) comparisons: *Case 0* vs *Case 1*

In order to compare the dispersion between the *Case 1* sub cases, a probability level of  $10^{-3}$  was selected. This probability level was adopted from the first sloshing benchmark Loysel et al. (2012)). The level of probability to compare the *Case 1* results depends on the number of studied peaks.  $10^{-3}$  or 1000 peaks seems to be enough to allow fair comparisons because many of the participants during the first sloshing benchmark Loysel et al. (2012) reported a converge to close results at this probability level.

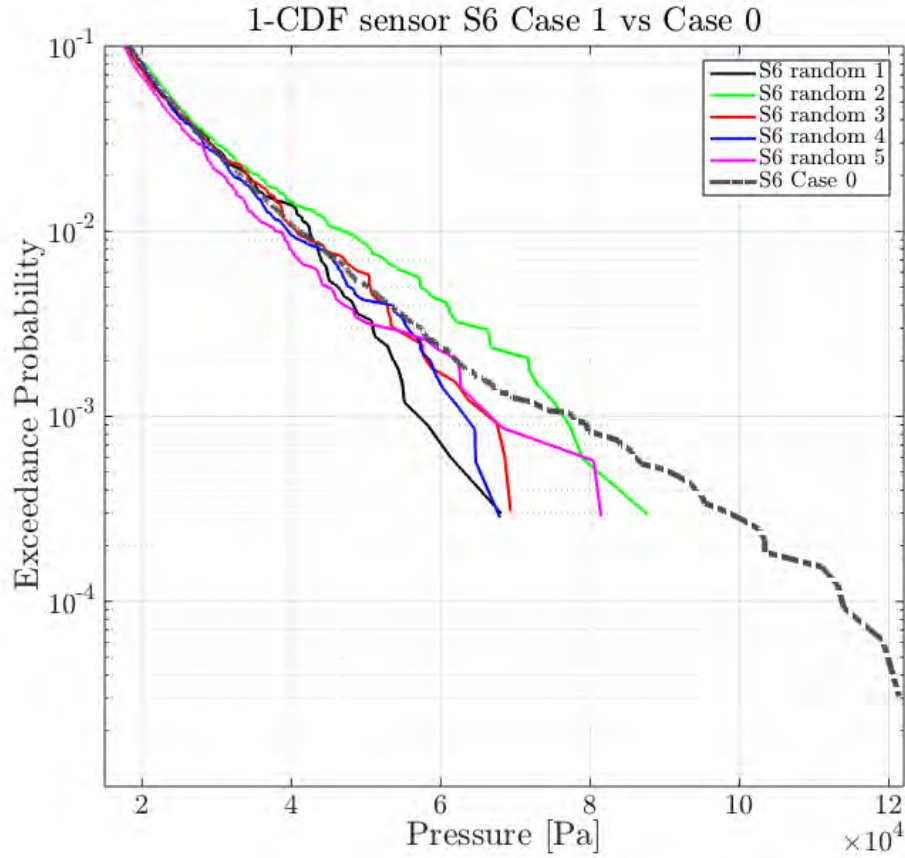


Figure 6.18: 1 – CDF S6 *Case 1*

The results for the lower pressure, higher pressure and maximum difference at the probability level  $10^{-3}$ , including also the *Case 0* are extracted from figures 6.18-6.20, and have been summarized in table 6.4. The last row of table 6.4 also compares S11 with the new random sub cases (R1-R5), by excluding the *Case 0* of the figure 6.20, in order to check

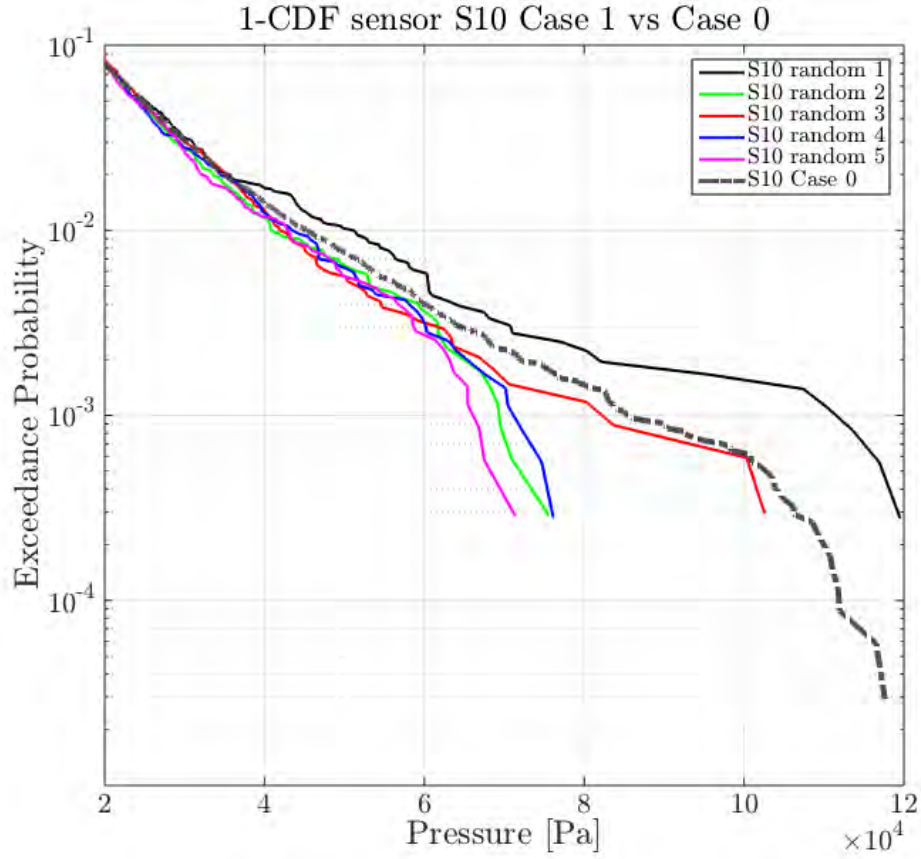


Figure 6.19: 1 – *CDF* S10 *Case 1*

the dispersion between the consecutive random realizations of the *Case 1*.

| Sensor | Min pressure [Pa]      | Max pressure [Pa]          | Max difference [Pa] |
|--------|------------------------|----------------------------|---------------------|
| S6     | $5.7 \cdot 10^4$ (R1)  | $7.64 \cdot 10^4$ (R2)     | $1.94 \cdot 10^4$   |
| S10    | $6.61 \cdot 10^4$ (R5) | $11.15 \cdot 10^4$ (R1)    | $4.54 \cdot 10^4$   |
| S11    | $6.24 \cdot 10^4$ (R3) | $8.56 \cdot 10^4$ (case 0) | $2.32 \cdot 10^4$   |
| S11    | $6.24 \cdot 10^4$ (R3) | $7.175 \cdot 10^4$ (R2)    | $0.935 \cdot 10^4$  |

Table 6.4: *Case 1* pressure dispersion at a probability level of  $10^{-3}$

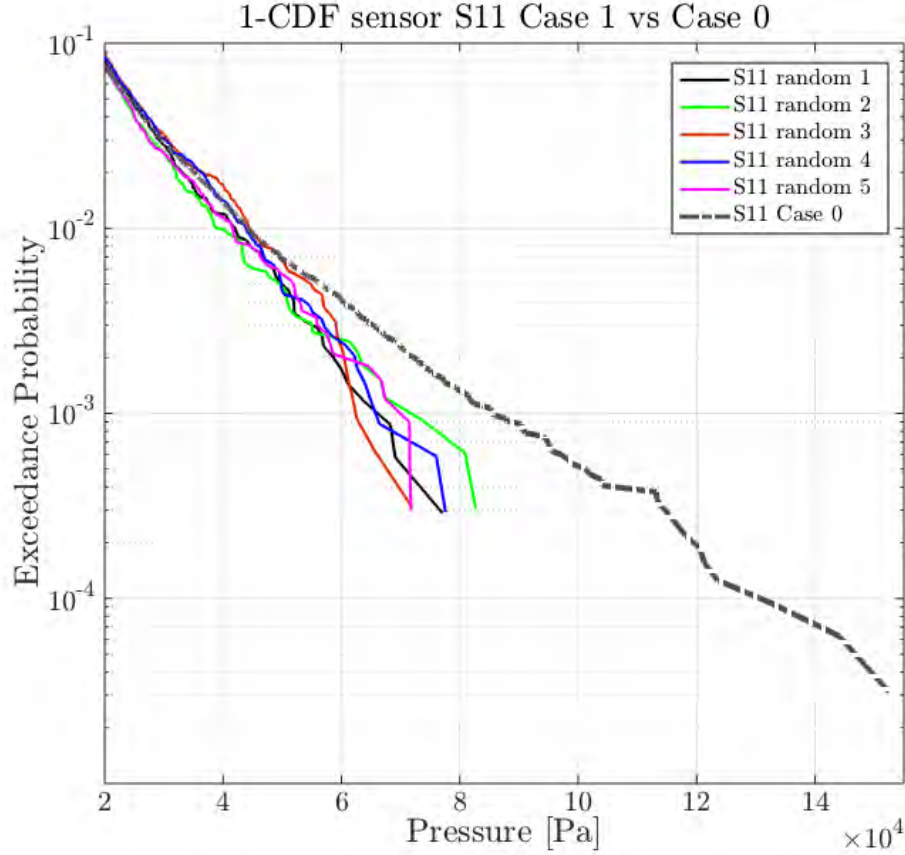


Figure 6.20: 1 – *CDF* S11 *Case 1*

The *KS2* test performed for every sub *Case 1* (R1-R5) against *Case 0* for sensor s6, is reported in table 6.5. Some rejections of the hypothesis of equal underlying distributions at 5% significance level ( $\alpha = 0.05$ ) are noticed (R1 vs. R2, R1 vs. R5 and R5 vs. Case 0). *KS2* test only provides criteria. Cases which have not been rejected can be considered to be likely close to the underlying pressure probability distribution. On the contrary, fitting model which have been rejected are very likely a poor approximation of the underlying pressure probability distribution. Nevertheless, looking at the  $p - value$  of some of the *KS2* tests, although the null hypothesis of equal underlying distributions is accepted ( $p - value > \alpha$ ), the evidence of  $p - value$  close to  $\alpha$  indicates that is highly probably to fail into accept the null hypothesis of equal underlying distributions (i.e. R2 vs. Case 0  $p - value = 0.089$ ).

| CASE                           | R2     | R3     | R4     | R5     | CASE 0 |
|--------------------------------|--------|--------|--------|--------|--------|
| R1                             | 1      | 0      | 0      | 1      | 0      |
|                                | 0.0429 | 0.4061 | 0.135  | 0.0133 | 0.176  |
|                                | 0.0336 | 0.0218 | 0.0279 | 0.0382 | 0.02   |
| R2                             | 0      | 0      | 0      | 0      | 0      |
|                                | 1      | 0.681  | 0.6491 | 0.7023 | 0.089  |
|                                | 0      | 0.0175 | 0.0177 | 0.017  | 0.0224 |
| R3                             |        | 0      | 0      | 0      | 0      |
|                                |        | 1      | 0.4682 | 0.3071 | 0.7491 |
|                                |        | 0      | 0.0205 | 0.0235 | 0.0124 |
| R4                             |        |        | 0      | 0      | 0      |
|                                |        |        | 1      | 0.3446 | 0.1711 |
|                                |        |        | 0      | 0.0223 | 0.0196 |
| R5                             |        |        |        | 0      | 1      |
|                                |        |        |        | 1      | 0.0176 |
|                                |        |        |        | 0      | 0.0274 |
| CASE 0                         |        |        |        |        | 0      |
|                                |        |        |        |        | 1      |
|                                |        |        |        |        | 0      |
| h (h=0 accepted, h=1 rejected) |        |        |        |        |        |
| p-value ( $\alpha = 0.05$ )    |        |        |        |        |        |
| test statistic                 |        |        |        |        |        |

Table 6.5: *KS2* Matrix Sensor S6 *Case 1* vs *Case 0*

The *KS2* test for sensor S10, reported in table 6.6, does not exhibit too many rejections as happened in the *KS2* test for sensor S6, only one rejection is visible and corresponds to *R4* vs. *Case 0*. A noticeable amount of rejections can be observed in the *KS2* test for sensor S11, most of the rejections corresponds with the *KS2* of the random cases vs *Case 0* as can be appreciate in table 6.7. According to the figure 6.20 and taking into account the results of the *KS2*, the random cases (R1-R5) for sensor S11 seems does not follow the same underlying pressure distribution of *Case 0*.

| CASE  | R2               | R3               | R4               | R5               | CASE 0           |
|---|------------------|------------------|------------------|------------------|------------------|
|   | 0                | 0                | 0                | 0                | 0                |
| R1  | 0.7116<br>0.0166 | 0.3812<br>0.0217 | 0.0749<br>0.0302 | 0.9722<br>0.0115 | 0.6375<br>0.0130 |
|   | 0                | 0                | 0                | 0                | 0                |
| R2  | 1<br>0           | 0.6076<br>0.0183 | 0.5275<br>0.0193 | 0.9885<br>0.0107 | 0.3167<br>0.0171 |
|   |                  | 0                | 0                | 0                | 0                |
| R3  |                  | 1<br>0           | 0.7260<br>0.0165 | 0.7920<br>0.0156 | 0.0986<br>0.0220 |
|   |                  |                  | 0                | 0                | 1                |
| R4  |                  |                  | 1<br>0           | 0.1324<br>0.0276 | 0.0026<br>0.0320 |
|   |                  |                  |                  | 0                | 0                |
| R5  |                  |                  |                  | 1<br>0           | 0.3890<br>0.0160 |
|   |                  |                  |                  |                  | 0                |
| CASE 0  |                  |                  |                  |                  | 1<br>0           |
| h (h=0 accepted, h=1 rejected)<br>p-value ( $\alpha = 0.05$ )<br>test statistic |                  |                  |                  |                  |                  |

Table 6.6: *KS2* Matrix Sensor S10 *Case 1* vs *Case 0*

Box plots of sensors S6, S10 and S11 (*Case 1*) are shown in figures 6.21, 6.22 and 6.23 respectively. The box plots report the following quantities estimated from the collected impact pressure samples of each sub case compared with *Case 0*:

- The lower and upper limit of each box indicate the 25% and 75% percentile levels, i.e. the lower and upper quartile respectively;
- The central mark indicates the 50% percentile level, i.e. the median;
- The whiskers indicate the observed minimum and the observed maximum;
- The lower and upper additional markers represent the estimated 5% and 95% percentile levels respectively.

Looking at the results of figures 6.21, 6.22 and 6.23 it can be noticed that the median pressure (%50 percentile level) of the collected impact pressure samples, according to each sub case, does not exhibit a noticeable variation, due mainly to the reason that the larger

| CASE                           | R2     | R3     | R4     | R5     | CASE 0 |
|--------------------------------|--------|--------|--------|--------|--------|
| R1                             | 0      | 0      | 1      | 0      | 0      |
|                                | 0.1357 | 0.1275 | 0.0279 | 0.6134 | 0.2031 |
|                                | 0.0282 | 0.0287 | 0.0351 | 0.0183 | 0.0191 |
| R2                             | 0      | 0      | 0      | 0      | 1      |
|                                | 1      | 0.7946 | 0.5082 | 0.3390 | 0.0347 |
|                                | 0      | 0.0160 | 0.0200 | 0.0230 | 0.0260 |
| R3                             |        | 0      | 0      | 0      | 1      |
|                                |        | 1      | 0.9369 | 0.6307 | 0.0214 |
|                                |        | 0      | 0.0131 | 0.0184 | 0.0278 |
| R4                             |        |        | 0      | 0      | 1      |
|                                |        |        | 1      | 0.2587 | 0.0040 |
|                                |        |        | 0      | 0.0245 | 0.0316 |
| R5                             |        |        |        | 0      | 0      |
|                                |        |        |        | 1      | 0.5464 |
|                                |        |        |        | 0      | 0.0145 |
| CASE 0                         |        |        |        |        | 0      |
|                                |        |        |        |        | 1      |
|                                |        |        |        |        | 0      |
| h (h=0 accepted, h=1 rejected) |        |        |        |        |        |
| p-value ( $\alpha = 0.05$ )    |        |        |        |        |        |
| test statistic                 |        |        |        |        |        |

Table 6.7: *KS2* Matrix Sensor S11 *Case 1* vs *Case 0*

pressure values corresponds only to the 5% of the total impact pressure sample as can be appreciated in the box plots. For sensors S6, S10 and S11 the maximum variation in the median pressure value are  $\tilde{300}$  Pa,  $\tilde{400}$  Pa and  $\tilde{400}$  Pa respectively. Similar observations can be done for the 5% 25% and 75% and 95% percentile levels where not appreciable variations were noticed.

In regards to the maximum values, the larger variability is noticed for S11, the one reporting previously the higher number of *KS2* rejections. Larger pressure values are in fact, the responsible of the variations in the tail shape of the distributions and therefore plays a key roll in the Weibull and GPD fittings and extreme values estimation. Kim et al. (2010) reports that the inclusion/exclusion of only one larger impact pressure sample can provide dramatic difference in the probability distribution and in the magnitude of the estimated extreme pressure.

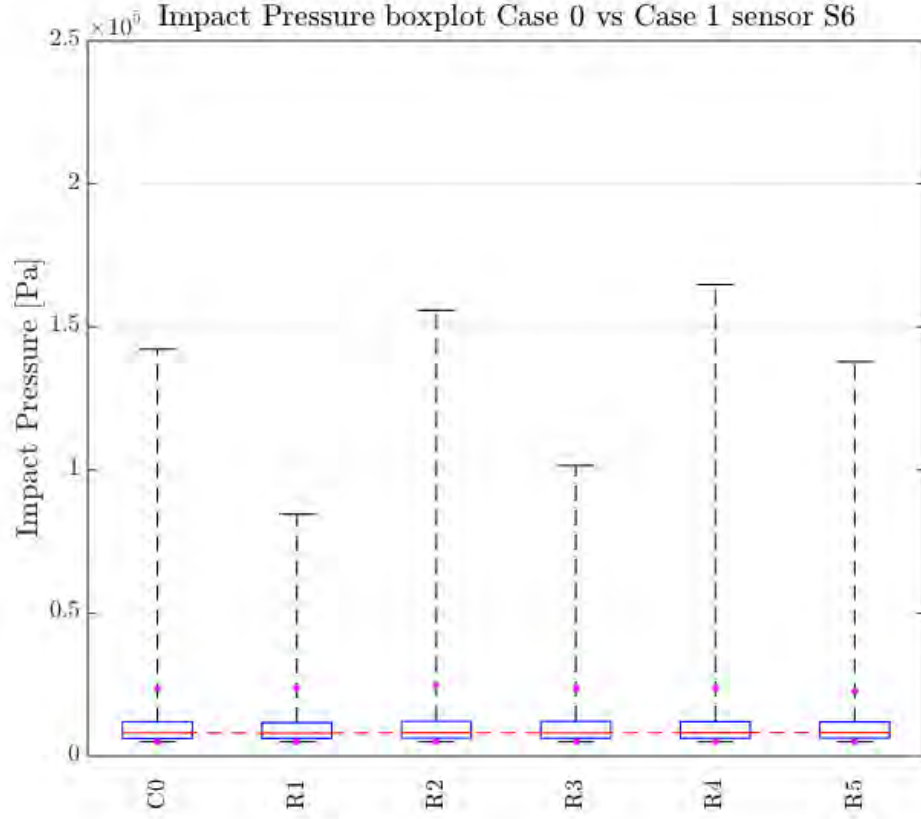


Figure 6.21: Box plot sensor S6 *Case 1* vs. *Case 0*, 5%, 25%, 75%, 95% percentile levels, minimum and maximum pressure

### Extreme Values Estimation

The number of occurrences or pressure peaks  $n$ , the mean frequency between peaks  $\varsigma$  and the experimental time  $T$  of the *Case 1* sub cases (R1-R5) for sensors S6, S10 and S11 are summarized in table 6.8. This values will be used for the estimation of the extreme values. The results of the table 6.8, suggests that the different driving motion realizations of *Case 1* does not have a strong influence in the number of collected pressure peaks  $n$  and in the mean frequency between peaks  $\varsigma$ .

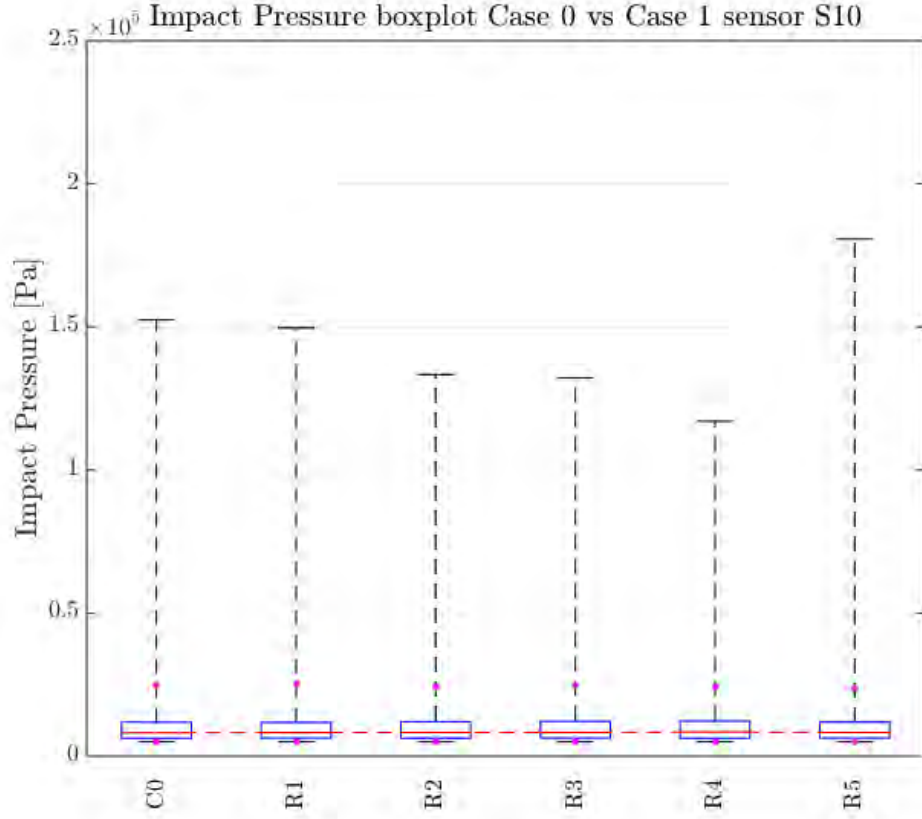


Figure 6.22: Box plot sensor S10 *Case 1* vs. *Case 0*, 5%, 25%, 75%, 95% percentile levels, minimum and maximum pressure

The extreme values for *Case 1* in the selected sensors (S6, S10 and S11) are obtained by using the two statistic of extremes fitting distributions under study (Weibull and GPD) for the selected return periods. Results are then compared with the reference extreme values obtained in *Case 0*.

Figure 6.24 shows the *Weibull* fitting and figure 6.25 shows the *GPD* fitting for sensor S6 according to the *Case 1* random realizations R1-R5 together with the *Case 0*.



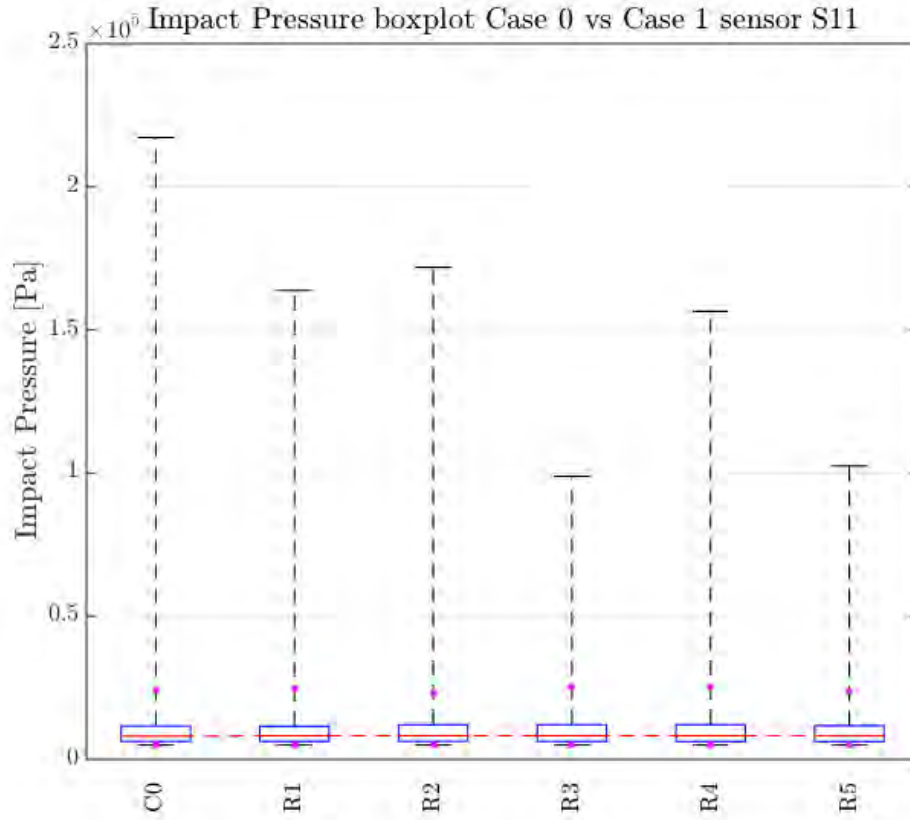


Figure 6.23: Box plot sensor S11 *Case 1* vs. *Case 0*, 5%, 25%, 75%, 95% percentile levels, minimum and maximum pressure

As can be appreciated in figure 6.24, at the comparing return period (100 hours) a high dispersion can be noticed in most of the cases except in R3 (red plot) whose fitting is similar to *Case 0* (yellow plot). This means, that at least one of the random cases (R3) under the assumption of equal spectrum follows almost the same *Weibull* distribution of the *Case 0*. The minimum percentage of difference (*Weibull* fitting) with respect to *Case 0* at  $RP=100$  hours is estimated in 1.72% (*Case 1-R3*). The maximum percentage of difference found in the *Weibull* fitting of figure 6.24 at  $RP=100$  hours is 55.32% and corresponds to *Case 1-R4*. The percentage of difference is calculated as the absolute relative error referred to the corresponding EV obtained for the selected sensors (S6, S10 and S11) in the *Case 0* (see tables 6.1, 6.3 and 6.2).

| Case                     | R1     | R2     | R3     | R4     | R5     | Case 0 |
|--------------------------|--------|--------|--------|--------|--------|--------|
| <b>Sensor S6</b>         |        |        |        |        |        |        |
| n [peaks]                | 3345   | 3404   | 3270   | 3521   | 3475   | 32503  |
| T [hours]                | 8.33   | 8.33   | 8.33   | 8.33   | 8.33   | 83.33  |
| $\varsigma$ [peaks/hour] | 401.4  | 408.48 | 392.4  | 422.5  | 417    | 390.03 |
| <b>Sensor S10</b>        |        |        |        |        |        |        |
| n [peaks]                | 3601   | 3463   | 3395   | 3566   | 3506   | 34175  |
| T [hours]                | 8.33   | 8.33   | 8.33   | 8.33   | 8.33   | 83.33  |
| $\varsigma$ [peaks/hour] | 432.12 | 415.56 | 407.4  | 427.92 | 420.72 | 410.1  |
| <b>Sensor S11</b>        |        |        |        |        |        |        |
| $n$ [peaks]              | 3455   | 3282   | 3216   | 3420   | 3342   | 31918  |
| $T$ [hours]              | 8.33   | 8.33   | 8.33   | 8.33   | 8.33   | 83.33  |
| $\varsigma$ [peaks/hour] | 414.6  | 393.84 | 385.92 | 410.4  | 401.04 | 383.01 |

Table 6.8: *Case 1* pressure peaks  $n$ , mean frequency between peaks  $\varsigma$  and experimental time  $T$

Observing figure 6.25, it can be appreciate that the *GPD* fitting of the *Case 1-R3* is also similar with respect to *Case 0*: *Case 1-R3* also reaches the minimum percentage of difference at  $RP=100$  hours which is estimated in 3.85%. Maximum difference in this case corresponds to *Case 1-R2* and it is estimated in 80.47% of difference with respect to *Case 0* (*GPD* fitting).

The largest dispersion is clearly noticeable in the *GPD* fittings. Nevertheless, in both fittings (Weibull and *GPD*), at the comparing return period (100 hours), it can be noticed that the *Case 1*, even under the assumption of equal spectra induces a high variability in the shape of the distributions and therefore on the extreme values estimation, with differences in the estimation reaching up to a 80.47% (*GPD* fitting, *Case 1-R2*) of difference with respect to *Case 1*.

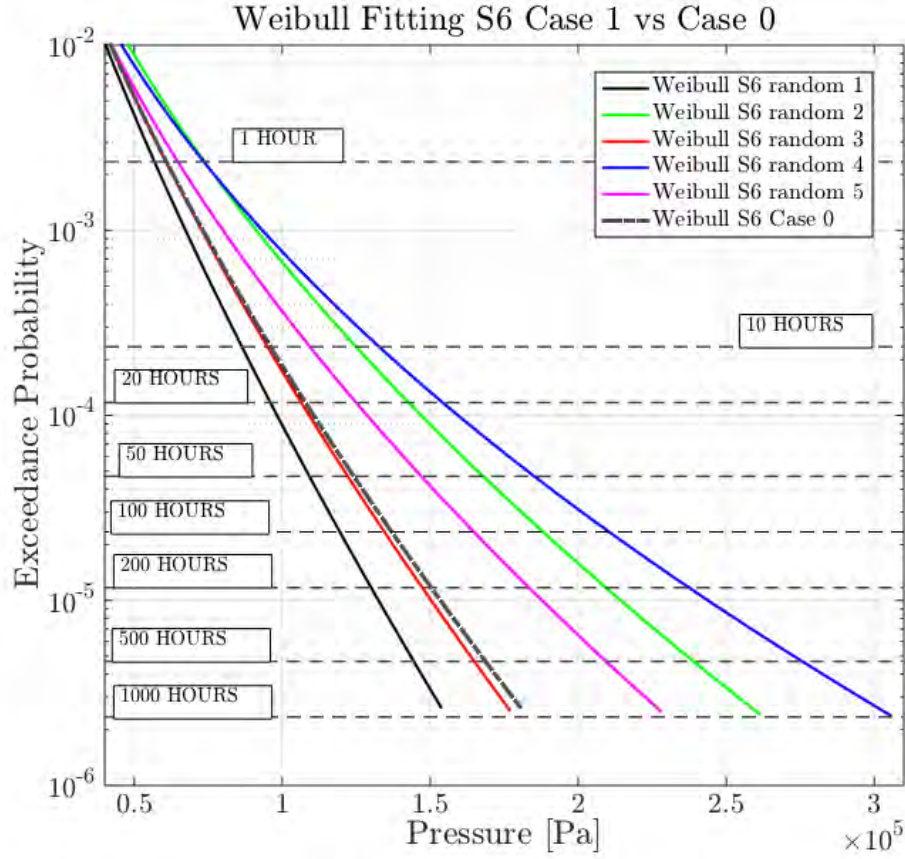


Figure 6.24: Weibull Fitting *Case 1* sensor S6

The EV for sensor S6 *Case 1* (R1-R5) according to the selected return periods are summarized in table 6.9 whilst the percentages of difference in the EV estimation according to *Case 0* are summarized in table 6.10.

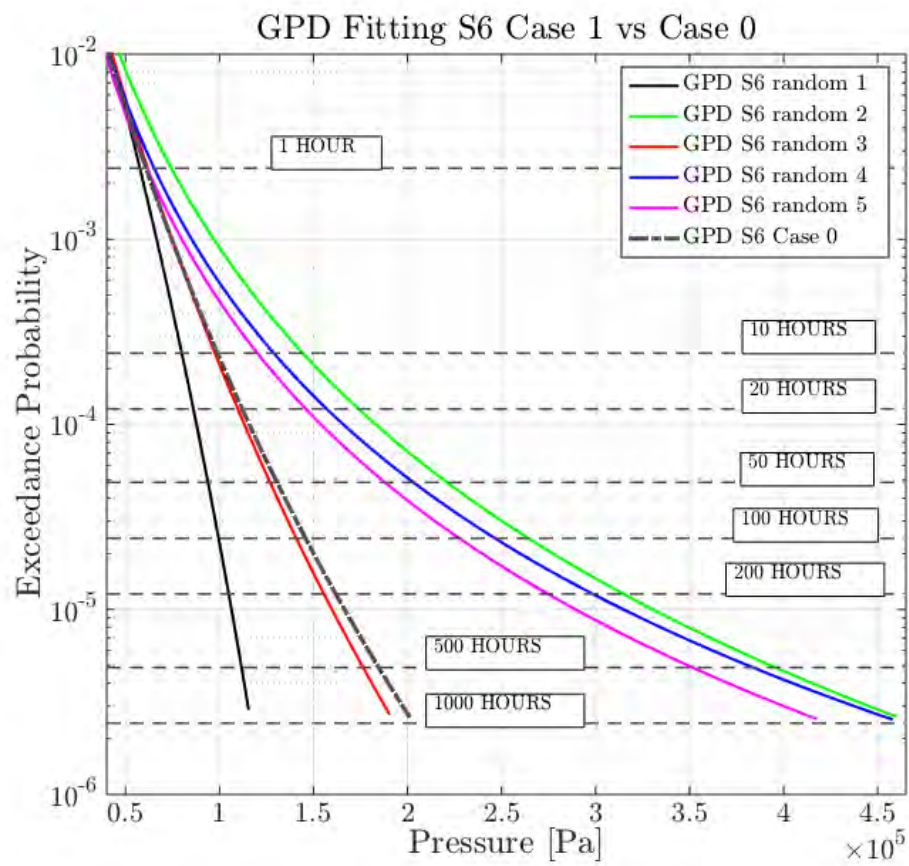


Figure 6.25: GPD Fitting *Case 1* sensor S6

| Case       | R1     |        | R2     |        | R3     |        | R4     |        | R5     |        |
|------------|--------|--------|--------|--------|--------|--------|--------|--------|--------|--------|
|            | W [Pa] | P [Pa] | W [Pa] | P [Pa] | W [Pa] | P [Pa] | W [Pa] | P [Pa] | W [Pa] | P [Pa] |
| RP [hours] |        |        |        |        |        |        |        |        |        |        |
| 1          | 56220  | 56922  | 73067  | 73172  | 59709  | 60444  | 73498  | 64837  | 64483  | 60884  |
| 10         | 85671  | 79310  | 124114 | 142316 | 93839  | 95944  | 132754 | 128194 | 109098 | 119149 |
| 20         | 95261  | 85495  | 141856 | 171531 | 105162 | 108026 | 154206 | 156227 | 124644 | 144761 |
| 50         | 108405 | 93308  | 166931 | 218178 | 120817 | 125098 | 185120 | 202202 | 146644 | 186606 |
| 100        | 118685 | 98954  | 187102 | 260729 | 133160 | 138902 | 210436 | 245258 | 164362 | 225647 |
| 200        | 129242 | 104382 | 208290 | 310761 | 145917 | 153521 | 237412 | 297054 | 182991 | 272462 |
| 500        | 143607 | 111237 | 237834 | 390645 | 163395 | 174180 | 275615 | 382002 | 208994 | 348946 |
| 1000       | 154771 | 116190 | 261325 | 463516 | 177067 | 190884 | 306436 | 461557 | 229688 | 420308 |

Table 6.9: Extreme Values (EV) *Case 1* (random cases R1-R5) for Sensor S6

| Case       | % Difference R1 |        | % Difference R2 |        | % Difference R3 |        | % Difference R4 |        | % Difference R5 |        |
|------------|-----------------|--------|-----------------|--------|-----------------|--------|-----------------|--------|-----------------|--------|
|            | W [Pa]          | P [Pa] | W [Pa]          | P [Pa] | W [Pa]          | P [Pa] | W [Pa]          | P [Pa] | W [Pa]          | P [Pa] |
| RP [hours] |                 |        |                 |        |                 |        |                 |        |                 |        |
| 1          | 5.91            | 5.18   | 22.29           | 21.89  | 0.07            | 0.69   | 23.01           | 8.00   | 7.92            | 1.42   |
| 10         | 9.60            | 19.00  | 30.96           | 45.35  | 0.99            | 2.01   | 40.08           | 30.93  | 15.12           | 21.69  |
| 20         | 10.52           | 22.93  | 33.24           | 54.63  | 1.22            | 2.62   | 44.84           | 40.83  | 17.08           | 30.50  |
| 50         | 11.63           | 27.91  | 36.08           | 68.57  | 1.51            | 3.35   | 50.90           | 56.22  | 19.54           | 44.17  |
| 100        | 12.40           | 31.51  | 38.10           | 80.47  | 1.72            | 3.85   | 55.32           | 69.76  | 21.31           | 56.19  |
| 200        | 13.12           | 34.95  | 40.02           | 93.65  | 1.91            | 4.33   | 59.59           | 85.11  | 23.01           | 69.79  |
| 500        | 14.00           | 39.29  | 42.43           | 113.22 | 2.15            | 4.93   | 65.05           | 108.50 | 25.16           | 90.46  |
| 1000       | 14.62           | 42.39  | 44.16           | 129.81 | 2.32            | 5.36   | 69.05           | 128.83 | 26.71           | 108.38 |

Table 6.10: Percentage of difference in the Extreme Values (EV) for *Case 1* vs *Case 0*, Sensor S6

Figures 6.26 and 6.27 are the fittings of *Weibull* and *GPD* respectively of the sensor S10 for the *Case 1 R1-R5*. In both figures the corresponding fitting of the *Case 0*, which serves as reference during both qualitative and quantitative comparisons, is also included. By following the *Weibull* fitting for sensor S10 in figure 6.26, it can be seen that *Case 1 R2* and *Case 1 R4* follow almost the same distribution of the reference *Case 0*. It is also noticeable that the shape of the fitting distributions of *Case 1 R3* and *Case 1 R5* are similar but a noticeable difference when comparing with the *Case 0* is observed. *Case 1 R1* shows the largest tail and hence the estimated extreme values. *Case 1 R1* shows the maximum difference in comparison with *Case 0*.

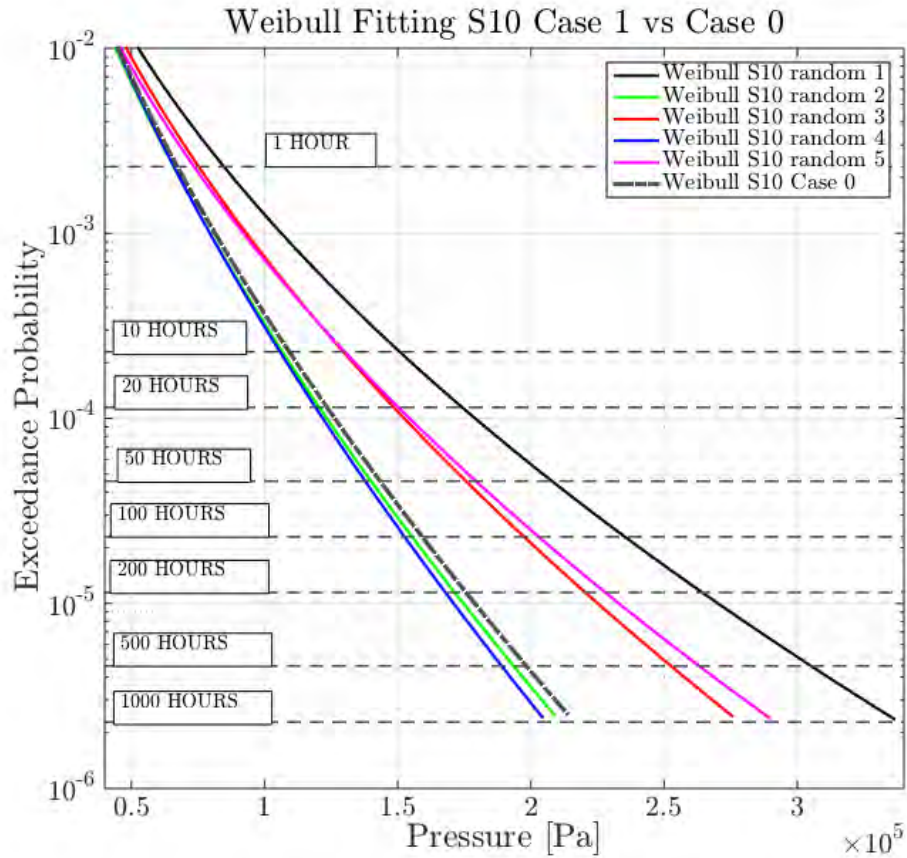


Figure 6.26: Weibull Fitting *Case 1* sensor S10

The minimum percentage of difference (*Weibull*) with respect to *Case 0* at RP=100 hours for sensor S10 is estimated in 2.19% (*Case 1-R2*). This difference remains almost constant when the RP increases as can be seen in the table 6.12 where at RP=1000 hours the maximum deviation in compare with *Case 0* is 2.25%. From table 6.12 it also can be concluded that the *Case 1-R4* also presents small differences with respect to the *Case 0*, up to 4.39% at RP=1000 hours. The differences with respect to *Case 0* of *Case 1-R3* and *Case 1-R5* at RP=100 hours are 23.79% and 27.87% respectively. The maximum difference found in the Weibull fitting of figure 6.26 at RP=100 hours is 48.96% and corresponds to *Case 1-R4* (see table 6.12).

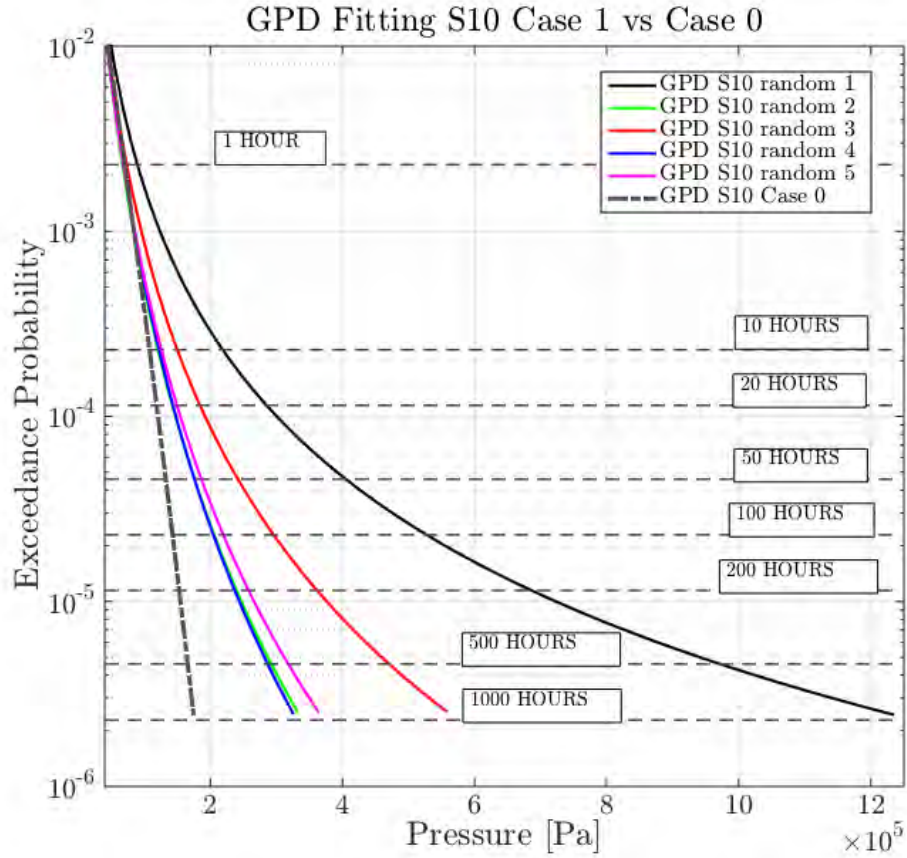


Figure 6.27: GPD Fitting *Case 1* sensor S10

Figure 6.27 shows the *GPD* fitting of the sensor S10 according to *Case 0*. Large differences with respect to the *Weibull* fitting at RP=100 hours are immediately noticed. None of the *GPD* fittings follow the same underlying distribution of the *Case 0*. The good results of the aforementioned *Weibull* fitting can not be reproduced by the *GPD* fitting in this case. This suggests that the *GPD* fitting is not able to fit the empirical data at the tail of the distributions with the selected threshold and fitting parameters, at least in the 10 runs experiments where the amount of collected pressure peaks ( $n$ ) is reduced considerably in comparison to *Case 0*. This statement suggests the necessity of collect a large amount of peaks sufficiently enough in order to guarantee a correct *GPD* fitting as it was reported during the *Case 0* analysis.

The EV for sensor S10 *Case 1 (R1-R5)* according to the selected return periods are summarized in table 6.11 whilst the percentage of difference in the EV estimation according to *Case 0* are summarized in table 6.12. The minimum percentage of difference at RP=100 hours is 42.03% (*Case 1-R2*). The maximum difference (at RP=100 hours) in this case corresponds to *Case 1-R1* and it is estimated in 264.45% which is a large difference with respect to *Case 0*. It can be concluded that special attention has to be paid into the correct selection of the fitting parameters, specially in the threshold selection, otherwise the EV can be inaccurately estimated.



| Case       | R1     |         | R2     |        | R3     |        | R4     |        | R5     |        |
|------------|--------|---------|--------|--------|--------|--------|--------|--------|--------|--------|
|            | W [Pa] | P [Pa]  | W [Pa] | P [Pa] | W [Pa] | P [Pa] | W [Pa] | P [Pa] | W [Pa] | P [Pa] |
| RP [hours] |        |         |        |        |        |        |        |        |        |        |
| 1          | 84729  | 87608   | 65203  | 65304  | 74065  | 70919  | 65820  | 67120  | 72973  | 66631  |
| 10         | 150673 | 214290  | 105975 | 118198 | 127954 | 145016 | 105580 | 120311 | 129351 | 123357 |
| 20         | 174199 | 279607  | 119799 | 139425 | 146884 | 178462 | 118957 | 141290 | 149518 | 146562 |
| 50         | 207868 | 396929  | 139112 | 172330 | 173776 | 233961 | 137577 | 173490 | 178416 | 182927 |
| 100        | 235267 | 517005  | 154483 | 201485 | 195509 | 286535 | 152348 | 201744 | 201957 | 215497 |
| 200        | 264314 | 673084  | 170491 | 234910 | 218423 | 350416 | 167691 | 233862 | 226936 | 253187 |
| 500        | 305224 | 953433  | 192607 | 286723 | 250501 | 456415 | 188825 | 283160 | 262150 | 312254 |
| 1000       | 338060 | 1240365 | 210040 | 332630 | 276104 | 556828 | 205441 | 326415 | 290439 | 365156 |

Table 6.11: Extreme Values (EV) *Case 1* (random cases R1-R5) for Sensor S10

| Case       | % Difference R1 |        | % Difference R2 |        | % Difference R3 |        | % Difference R4 |        | % Difference R5 |        |
|------------|-----------------|--------|-----------------|--------|-----------------|--------|-----------------|--------|-----------------|--------|
|            | W [Pa]          | P [Pa] | W [Pa]          | P [Pa] | W [Pa]          | P [Pa] | W [Pa]          | P [Pa] | W [Pa]          | P [Pa] |
| RP [hours] |                 |        |                 |        |                 |        |                 |        |                 |        |
| 1          | 27.54           | 26.03  | 1.85            | 6.05   | 11.49           | 2.03   | 0.92            | 3.44   | 9.84            | 4.14   |
| 10         | 39.22           | 100.42 | 2.08            | 10.55  | 18.23           | 35.63  | 2.44            | 12.52  | 19.52           | 15.37  |
| 20         | 42.33           | 137.58 | 2.12            | 18.47  | 20.01           | 51.64  | 2.81            | 20.05  | 22.16           | 24.53  |
| 50         | 46.19           | 201.64 | 2.16            | 30.96  | 22.22           | 77.79  | 3.24            | 31.84  | 25.48           | 39.01  |
| 100        | 48.96           | 264.45 | 2.19            | 42.03  | 23.79           | 101.99 | 3.54            | 42.22  | 27.87           | 51.91  |
| 200        | 51.60           | 343.07 | 2.21            | 54.63  | 25.28           | 130.67 | 3.82            | 53.94  | 30.17           | 66.66  |
| 500        | 54.93           | 478.21 | 2.23            | 73.88  | 27.15           | 176.79 | 4.15            | 71.72  | 33.07           | 89.37  |
| 1000       | 57.33           | 610.88 | 2.25            | 90.64  | 28.50           | 219.13 | 4.39            | 87.08  | 35.17           | 109.28 |

Table 6.12: Percentage of difference in the Extreme Values (EV) for *Case 1* vs *Case 0*, Sensor S10

Figures 6.28 and 6.29 are the fittings of *Weibull* and *GPD* respectively of the sensor S11 for the *Case 1 R1-R5*. At this point it is necessary to remind the reader that the *Case 1 R2* in sensor S10 followed almost the same *Weibull* distribution of the reference *Case 0* (see figure 6.26), nevertheless, although S10 and S11 are located alongside, curiously, by following the *Weibull* fitting for sensor S11 in the figure 6.28, it can be noticed that *Case 1 R2* shows the largest difference with respect to *Case 0*. This denotes a large variability of the registered pressure even at the vicinity of the selected sensors.

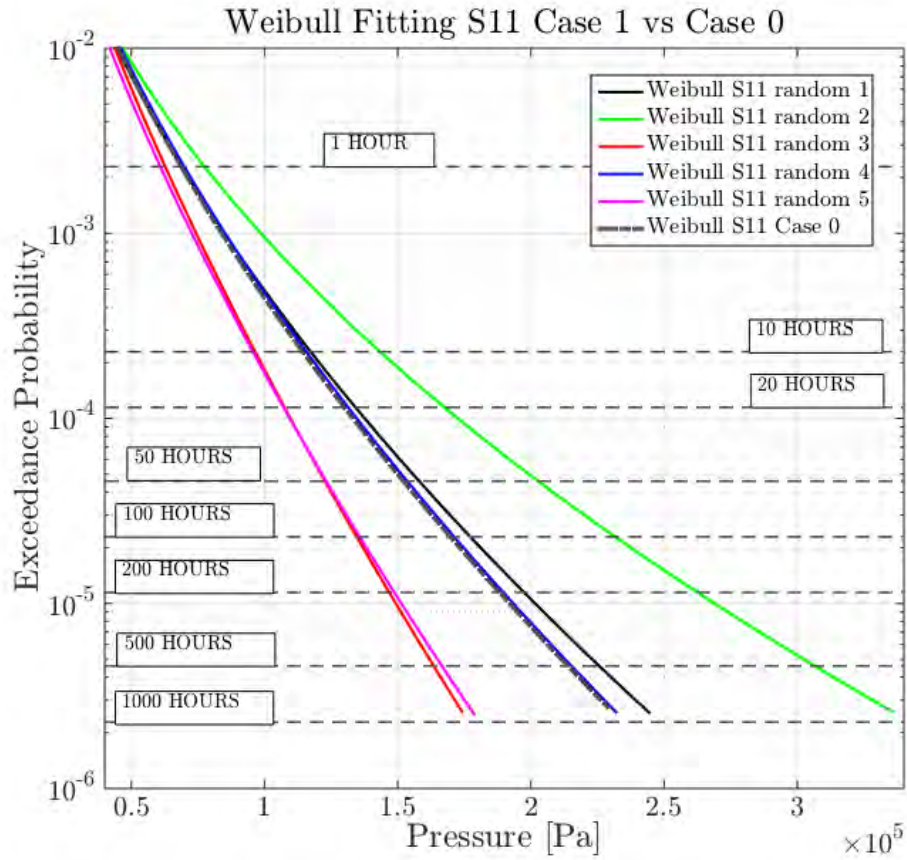


Figure 6.28: Weibull Fitting *Case 1* sensor S11

In both alongside sensors (S10 and S11), the *Case 1 R4* follows almost the same *Weibull* distribution of the reference *Case 0*. This means that the *Case 1 R4* induces not as much variability in the spatial pressure distribution, at least in the vicinity of the selected sensors, in comparison with the other cases. The *Case 1 R1* in sensor S11 follows almost the same *Weibull* distribution of the reference *Case 0* (see figure 6.28). It is remarkable that the same case (*Case 1 R1*) showed the largest difference with respect to *Case 0* in the alongside sensor S10. *Case 1 R3* and *Case 1 R5* shown a similar *Weibull* distributions among them as can be seen in figure 6.28. Similar behaviour it was noticed in the *Weibull* distribution for sensor S10 (see figure 6.28) but differences in terms of distribution shape and location of those cases ,for sensors S10 and S11, with respect to *Case 0* are clearly visible.

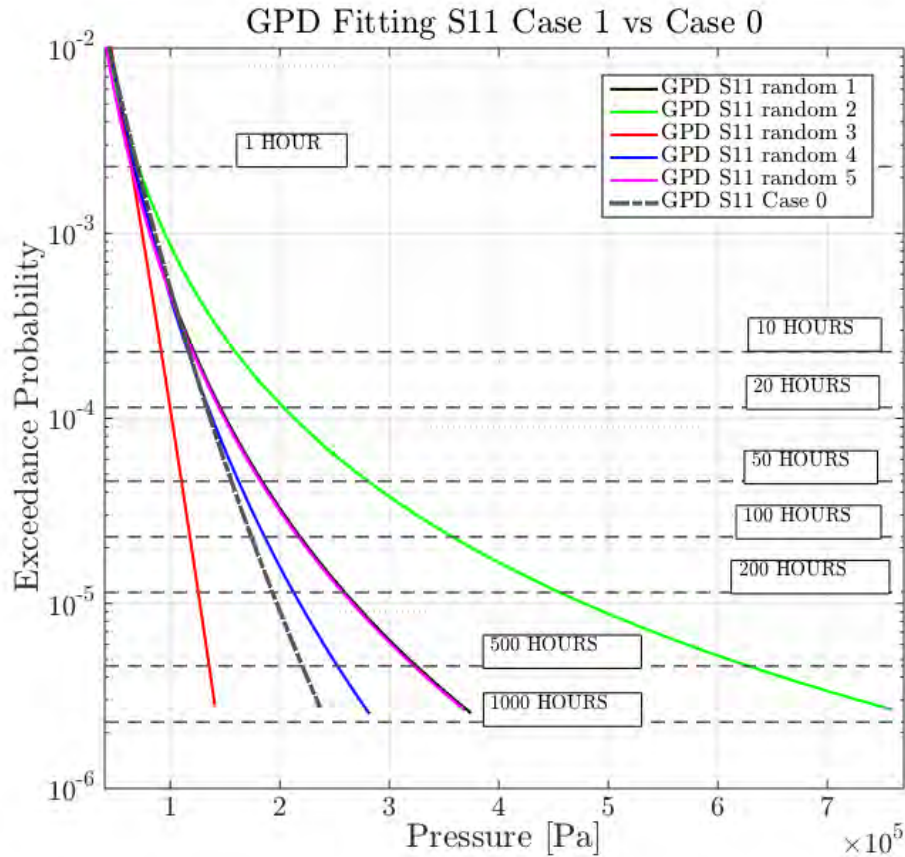


Figure 6.29: GPD Fitting *Case 1* sensor S11

The extreme values EV and percentage of difference in the EV estimation for sensor S11 *Case 1 (R1-R5)* according to the selected return periods (1,10,20,50,100,200,500 and 1000 hours) are summarized in tables 6.13 and 6.14 respectively. The minimum percentage of difference (*Weibull* fitting) with respect to *Case 0* at RP=100 hours for sensor S11 is estimated in 1.96% (*Case 1-R4*) as can be seen in table 6.14. In comparison with sensors S6 and S10, previously described, sensor S11 achieves the minimum percentage of difference in all the selected return periods, even though when increasing the RP to 1000 hours the percentage of difference with respect to *Case 0* decreases to 1.46% as can be seen in table 6.14.

From table 6.14 it also can be concluded that the *Case 1-R1* also presents small differences with respect to the *Case 0*: at RP=100 hours this percentage of difference is 5.69% and 7.00% at RP=1000 hours. The similarities between *Case 0*, *Case 1-R1* and *Case 1-R4* for sensor S11, indicate that at least 2 of the new random realizations follow almost the same *Weibull* distribution. The differences with respect to *Case 0* of *Case 1-R3* and *Case 1-R5* at RP=100 hours are 20.38% and 19.35% respectively. The maximum difference at RP=100 hours is 36.64% and corresponds to *Case 1-R2* (see table 6.14).

Figure 6.29 shows the *GPD* fitting of the sensor S11. It can be noticed immediately that there are not as much differences in the *GPD* fittings as those found in the previous analysis of sensor S10 where differences up to 264.45% (at RP=100 hours), when comparing with *Case 0*, were found. Nevertheless some differences with the *Weibull* fitting of the figure 6.28 can be noticed. *Case 1-R4* achieves the minimum percentage of difference at RP=100 hours (6.97%). The maximum difference in this case corresponds to *Case 1-R2* and it is estimated in 99.40% (at RP=100 hours). *Case 1-R1*, *Case 1-R3* and *Case 1-R5* report similar differences with respect to *Case 0* ,25.30%, 31.90% and 23.23% respectively. *Case 1-R2* fitting presents the largest extreme values, as can be appreciate in figure 6.29, and in table 6.13, similar to the S11 *Weibull* of the figure 6.28.

Noticeable differences can be appreciated in the *GPD* fitting for sensor S11 in comparing with the *GPD* fitting for sensor S10, in terms of percentage of difference with respect to *Case 0*. In general, at this point, it can be noticed that the *Weibull* fitting is the most suitable and accurate distribution when it is aimed to report the influence of the parameters used in the sensitive analysis of the sloshing pressure data collection, at least in short duration cases (10 hours) such the *Case 1* where the amount of collected peaks is reduced in compared with *Case 0*.

| Case       | R1     |        | R2     |        | R3     |        | R4     |        | R5     |        |
|------------|--------|--------|--------|--------|--------|--------|--------|--------|--------|--------|
|            | W [Pa] | P [Pa] | W [Pa] | P [Pa] | W [Pa] | P [Pa] | W [Pa] | P [Pa] | W [Pa] | P [Pa] |
| RP [hours] |        |        |        |        |        |        |        |        |        |        |
| 1          | 68259  | 63553  | 75278  | 67128  | 61182  | 62161  | 68955  | 65809  | 59882  | 61961  |
| 10         | 116326 | 118767 | 140279 | 151384 | 94685  | 89787  | 114559 | 113464 | 94407  | 116486 |
| 20         | 133110 | 142128 | 164201 | 193168 | 105670 | 97837  | 130216 | 131593 | 105891 | 139547 |
| 50         | 156885 | 179455 | 198945 | 266479 | 120774 | 108293 | 152218 | 158855 | 121790 | 176388 |
| 100        | 176050 | 213532 | 227598 | 339818 | 132622 | 116066 | 169824 | 182296 | 134339 | 210014 |
| 200        | 196214 | 253625 | 258302 | 433264 | 144818 | 123723 | 188239 | 208481 | 147322 | 249569 |
| 500        | 224382 | 317692 | 302051 | 597219 | 161455 | 133669 | 213799 | 247857 | 165128 | 312763 |
| 1000       | 246816 | 376178 | 337545 | 761235 | 174415 | 141063 | 234035 | 281714 | 179069 | 370441 |

Table 6.13: Extreme Values (EV) *Case 1* (random cases R1-R5) for Sensor S11

| Case       | % Difference R1 |        | % Difference R2 |        | % Difference R3 |        | % Difference R4 |        | % Difference R5 |        |
|------------|-----------------|--------|-----------------|--------|-----------------|--------|-----------------|--------|-----------------|--------|
|            | W [Pa]          | P [Pa] | W [Pa]          | P [Pa] | W [Pa]          | P [Pa] | W [Pa]          | P [Pa] | W [Pa]          | P [Pa] |
| RP [hours] |                 |        |                 |        |                 |        |                 |        |                 |        |
| 1          | 2.54            | 5.96   | 13.09           | 0.67   | 8.09            | 8.02   | 3.59            | 2.62   | 10.04           | 8.31   |
| 10         | 4.20            | 4.04   | 25.66           | 32.61  | 15.18           | 21.35  | 2.62            | 0.61   | 15.43           | 2.04   |
| 20         | 4.67            | 9.33   | 29.12           | 48.60  | 16.91           | 24.74  | 2.40            | 1.23   | 16.73           | 7.35   |
| 50         | 5.26            | 17.79  | 33.48           | 74.91  | 18.96           | 28.92  | 2.13            | 4.27   | 18.28           | 15.77  |
| 100        | 5.69            | 25.30  | 36.64           | 99.40  | 20.38           | 31.90  | 1.96            | 6.97   | 19.35           | 23.23  |
| 200        | 6.11            | 33.81  | 39.68           | 128.58 | 21.69           | 34.73  | 1.79            | 9.99   | 20.33           | 31.67  |
| 500        | 6.63            | 46.70  | 43.53           | 175.78 | 23.28           | 38.27  | 1.60            | 14.45  | 21.53           | 44.43  |
| 1000       | 7.00            | 57.81  | 46.34           | 219.34 | 24.39           | 40.82  | 1.46            | 18.18  | 22.37           | 55.40  |

Table 6.14: Percentage of difference in the Extreme Values (EV) for *Case 1* vs *Case 0*, Sensor S11

### 6.5.5 *Case 2*: Influence of the BIAS (1,2,5,10%) in the Spatial Pressure Distribution and Extreme Values Estimation

This section covers the results of the sensitivity analysis in the peak pressure data collection due to an induced malfunctioning of the sloshing rig in terms of reproducibility of the driving motion (C15), when a random BIAS (1,2,5,10%) is applied to the original driving motion signal. The new cases are called B1, B2, B5 and B10 according to the percentage of BIAS applied to the original signal. The random bias is applied to the original signal and every new sub case is repeated 10 times with the same bias level, giving a total of 40 hours of experiments. The estimated extreme values will be compared, for the selected sensors, with those obtained in the *Case 0* (100 runs).

Following the same procedure of the *Case 1*, this section will be structured as follows: a spatial pressure distribution will provide an indication of the P10 pressures accordingly to the array, sensors, and sub cases. This helps in understanding the spatial distribution variation of the pressure due to the BIAS influence. Then, empirical plots of the selected sensors (S6, S10, S11), according to every sub case, will provide an estimation of the dispersion in the impact pressure samples distributions. *KS2* tests will provide a statistical rejection criteria in order to check if the BIAS (1,2,5,10%) cases for the selected sensors, share similar underlying pressure distributions. Finally, the empirical distributions will be fitted by following the two extreme value models under consideration *Weibull* and *GPD*. The extreme pressure values will be estimated for every selected sensor and the influence in the extreme pressures calculation due to the BIAS will be reported.

#### Spatial Pressure Distribution

The spatial distribution of P10 for array 1 and array 2 of the *Case 2* can be appreciated in figures 6.30 and 6.31. Comparing with *Case 1*, where the spatial distribution changed their maximum and location according to the new driving motion realizations, the P10 plot of array 1 *Case 2* seems to be more consistent according to the BIAS increment as can be appreciate in 6.30 where the maximum is registered by sensor S6 for cases B1, B2 and B5. At this point it is necessary to remember that S6 registered the highest P10 during the *Case 0* realization. In the case B10, figure 6.30d, the maximum is registered by sensor S8. This indicates that B10 (10% BIAS) implies significant variations in comparison with the *Case 0*, at least, for the moment, in the spatial pressure distribution, which can be initially attained to the inherent random effects.

The spatial distribution of array 2 (figure 6.31) has important variations in comparison with array 1. During the *Case 0* realization the maximum reported P10 corresponds to S11. S10 was then included due to the reported behaviour in the *Case 1* discussion. In *Case 2* the spatial pressure distribution for array 2 has similar variations as those reported in *Case 1*. The P10 of case B1, as can be seen in 6.31a, reports similar high pressures for

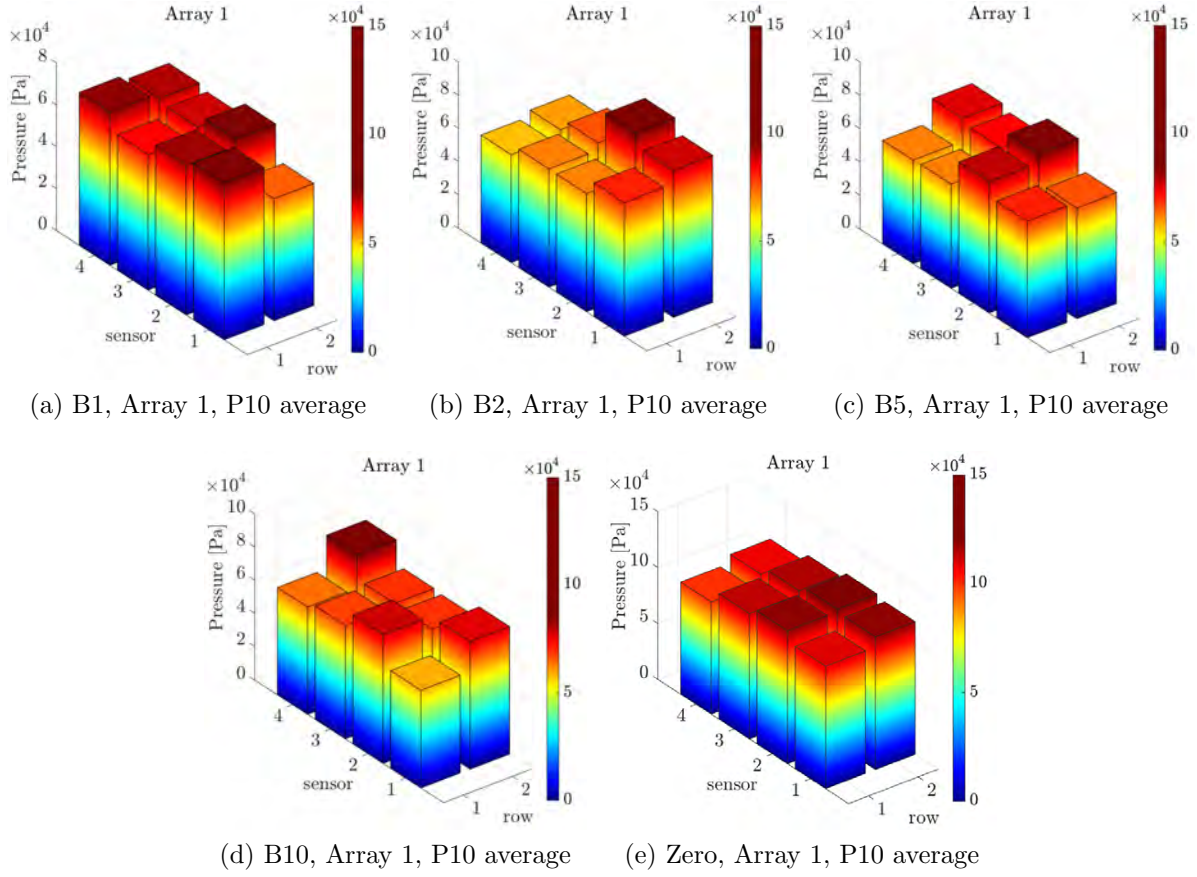


Figure 6.30: *Case 2* vs *Case 0*, Array 1, P10 [Pa] average sensors 1-8

sensors S10, S11 and S14. Sensor S12 reports the highest P10 in the case B2 (see figure 6.31b). Case B5, as can be seen in figure 6.31c, shows that the sensors S10 and S11 record the highest P10 in array 2. Looking at the figure 6.31d it can be noticed that the spatial pressure distributions seems to be more homogeneous but the maximum registered in this case corresponds to sensors S13 and S14. The influence of the BIAS in the spatial pressure distributions seems to be more significant in the array 2, where the highest global P10 were registered. Similar behaviour was noticed previously during the *Case 0* and *Case 1* discussion.



In both arrays the maximum registered pressure P10 of all sensors in all cases is less than the P10 reported in *Case 0*. Therefore, not extraordinary pressures of the same order of the reported in *Case 0* were recorded, as happened in *Case 1*.

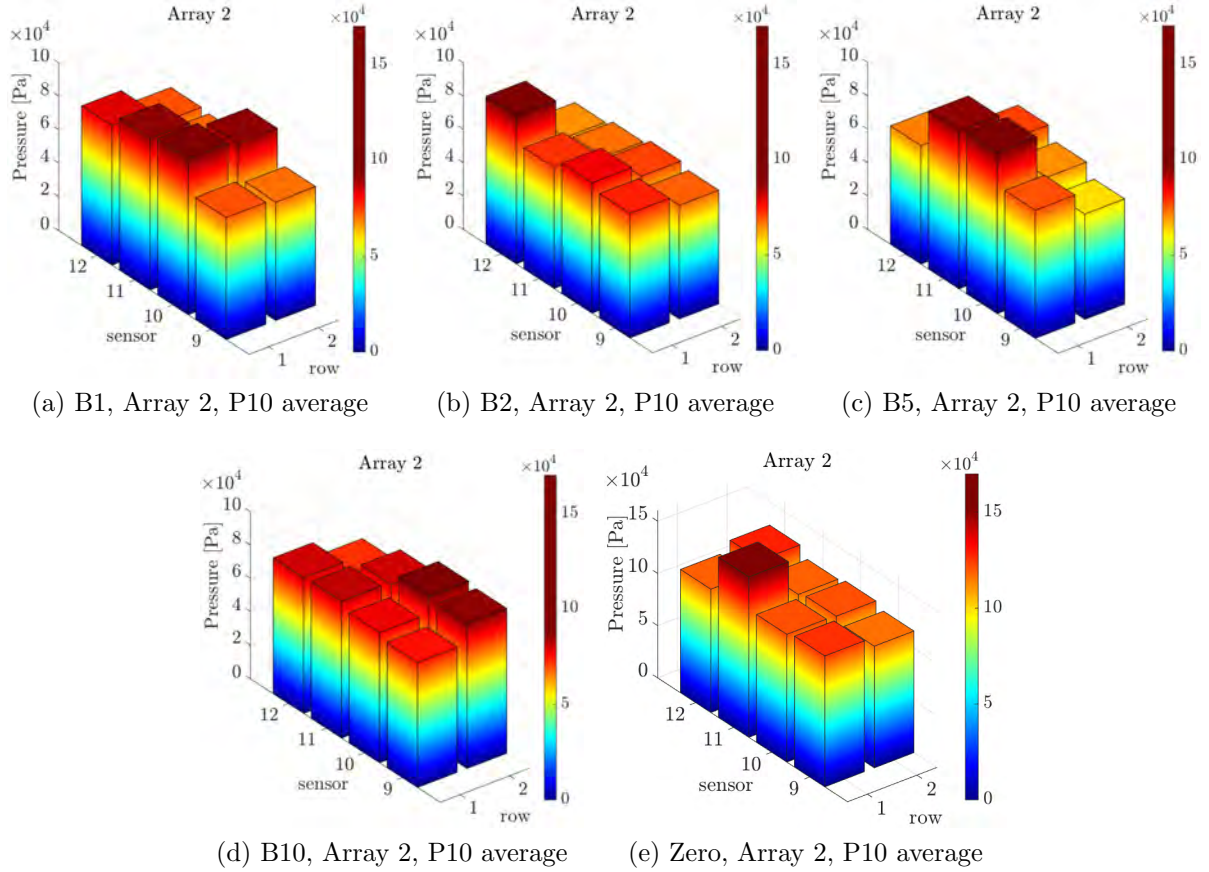


Figure 6.31: *Case 2* vs *Case 0*, Array 2, P10 [Pa] average sensors 8-16



### Exceedance Function (1-CDF) comparisons: *Case 0* vs *Case 2*

Figures 6.32, 6.33 and 6.34 represents the  $1 - CDF$  of sensors S6, S10 and S11 respectively. Similar dispersion as the reported in *Case 1* is immediately noticeable in the selected sensors. The  $KS2$  tests performed for *Case 2* (B1, B2, B5 and B10) against *Case 0* for

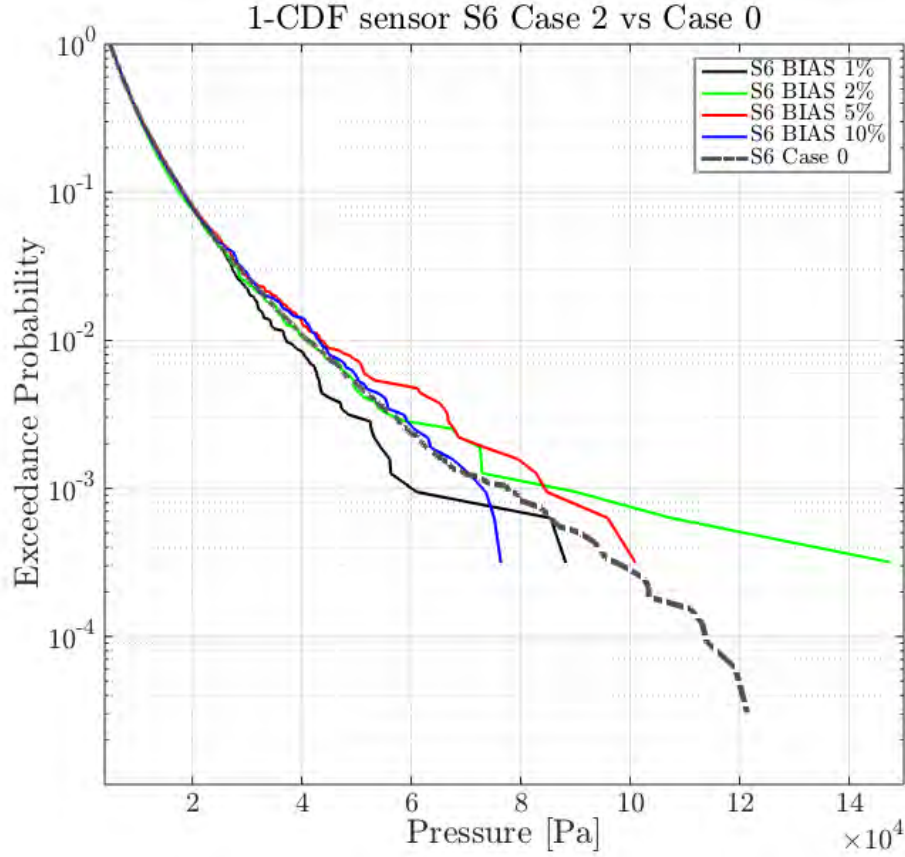


Figure 6.32:  $1 - CDF$  S6 *Case 2*

sensor S6, S10 and S11 are reported in the tables 6.15, 6.16 and 6.17 respectively. Only one rejection in all the cases was noticed (*B2* vs *Case 0*) ( $\alpha = 0.05$ ). In general the BIAS cases can be considered to be likely close to the underlying pressure probability distribution, in most of the cases with an acceptable  $p$  - value as a indication of a low probability to fail into accept the null hypothesis of equal underlying distributions.

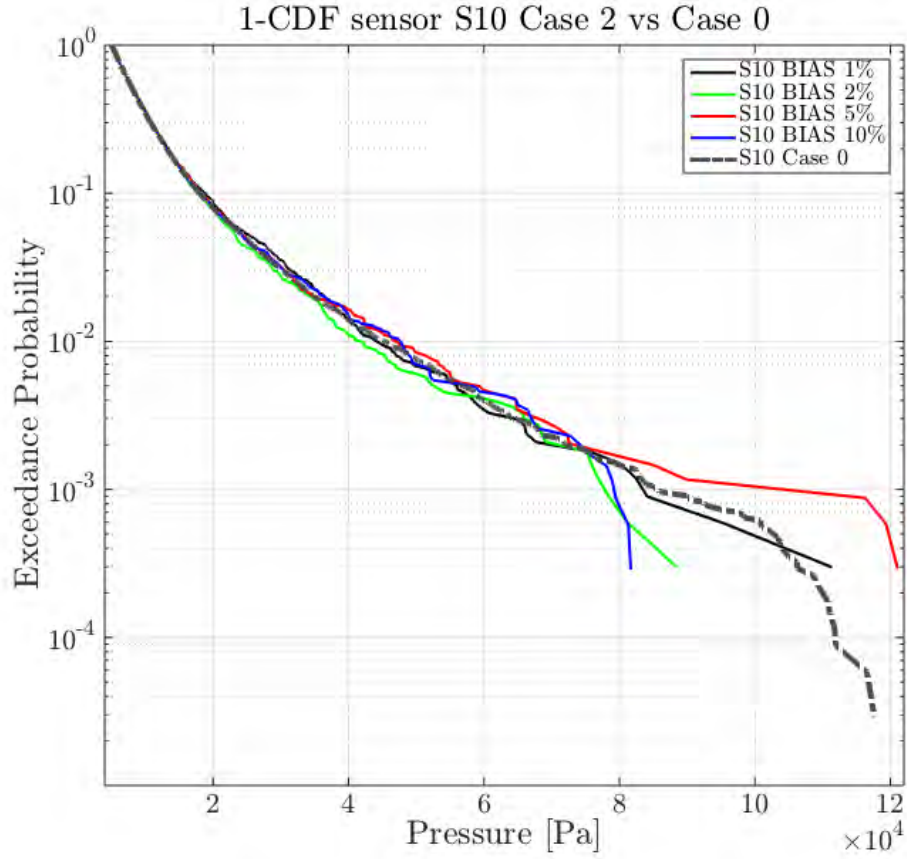


Figure 6.33: 1 –  $CDF$  S10 *Case 2*

Box plots of sensors S6, S10 and S11 (*Case 2*) are shown in figures 6.35, 6.36 and 6.37 respectively. The box plots report the following quantities estimated from the collected impact pressure samples of each sub case compared with *Case 0*:

- The lower and upper limit of each box indicate the 25% and 75% percentile levels, i.e. the lower and upper quartile respectively;
- The central mark indicates the 50% percentile level, i.e. the median;
- The whiskers indicate the observed minimum and the observed maximum;
- The lower and upper additional markers represent the estimated 5% and 95% percentile levels respectively.

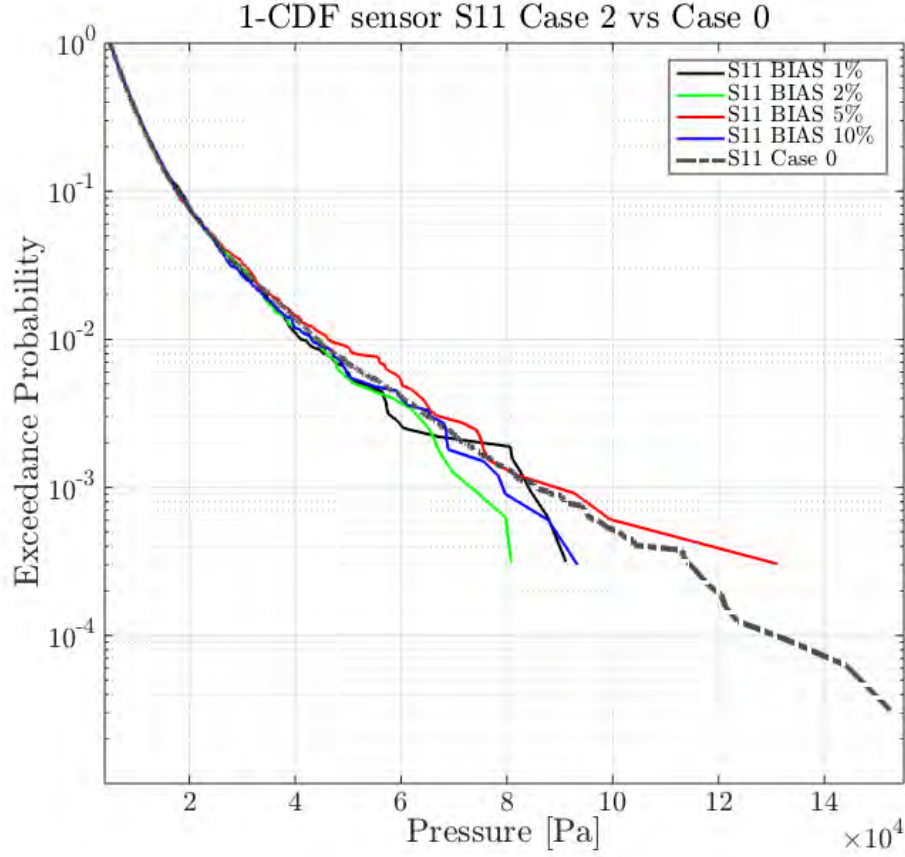


Figure 6.34: 1 – *CDF* S11 *Case 2*

Looking at the results of figures 6.35, 6.36 and 6.37 similar observations as those reported in the box plot analysis of *Case 1* can be done. The median pressure (%50 percentile level) of the collected impact pressure samples, does not exhibit a noticeable variation, similar behaviour can be appreciated in the 5% 25% and 75% and 95% percentile levels. For sensors S6, S10 and S11 the maximum variation in the median pressure value are  $\sim 400Pa$ ,  $\sim 300Pa$  and  $\sim 400Pa$  respectively.

In regards to the maximum values, large variability is noticed for all the selected sensors. Nevertheless, for sensor S6 case B2, it can be noticed the presence of an extraordinary peak of the same order of the maximum global recorded in all the experiments of (*Case 0*, S11). The presence of this extraordinary impact pressure peak is also correlated with the *KS2* test, where only one rejection *B2 vs. Case 0*, S11 was noticed. Previously it was commented that the larger pressure values are the responsible of the variations in the tail shape of the distributions and whose presence/elimination affects dramatically the probability distribution, tail fitting and the extreme values estimation (Kim et al., 2010).

| CASE                           | B2     | B5     | B10    | CASE 0 |
|--------------------------------|--------|--------|--------|--------|
| B1                             | 0      | 0      | 0      | 0      |
|                                | 0.1083 | 0.8428 | 0.5049 | 0.7912 |
|                                | 0.0303 | 0.0154 | 0.0206 | 0.0121 |
| B2                             | 0      | 0      | 0      | 1      |
|                                | 1      | 0.1703 | 0.0589 | 0.0288 |
|                                | 0      | 0.0278 | 0.0322 | 0.0271 |
| B5                             |        | 0      | 0      | 0      |
|                                |        | 1      | 0.6853 | 0.3444 |
|                                |        | 0      | 0.0179 | 0.0174 |
| B10                            |        |        | 0      | 0      |
|                                |        |        | 1      | 0.6494 |
|                                |        |        | 0      | 0.0136 |
| CASE 0                         |        |        |        | 0      |
|                                |        |        |        | 1      |
|                                |        |        |        | 0      |
| h (h=0 accepted, h=1 rejected) |        |        |        |        |
| p-value ( $\alpha = 0.05$ )    |        |        |        |        |
| test statistic                 |        |        |        |        |

Table 6.15: *KS2* Matrix Sensor S6 *Case 2* vs *Case 0*

### Extreme Values Estimation

The number of occurrences or pressure peaks  $n$ , the mean frequency between peaks  $\varsigma$  and the experimental time  $T$  of the *Case 2* sub cases (B1-B10) for sensors S6, S10 and S11 are summarized in table 6.18. This values will be used later in the estimation of the extreme values. Observing the results of the table 6.18, a similar conclusion as the one reported in *Case 1* can be done, the presence of a random BIAS (1,2,5,10%), applied to the original driving motion signal does not induces a strong variation in the collected pressure peaks  $n$  and in the mean frequency between peaks  $\varsigma$ .

| CASE                           | B2     | B5     | B10    | CASE 0 |
|--------------------------------|--------|--------|--------|--------|
| B1                             | 0      | 0      | 0      | 0      |
|                                | 0.6237 | 0.5444 | 0.2893 | 0.8529 |
|                                | 0.0183 | 0.0194 | 0.0237 | 0.0110 |
| B2                             | 0      | 0      | 0      | 0      |
|                                | 1      | 0.2177 | 0.3338 | 0.7055 |
|                                | 0      | 0.0255 | 0.0228 | 0.0127 |
| B5                             |        | 0      | 0      | 0      |
|                                |        | 1      | 0.6473 | 0.1971 |
|                                |        | 0      | 0.0177 | 0.0192 |
| B10                            |        |        | 0      | 0      |
|                                |        |        | 1      | 0.2408 |
|                                |        |        | 0      | 0.0183 |
| CASE 0                         |        |        |        | 0      |
|                                |        |        |        | 1      |
|                                |        |        |        | 0      |
| h (h=0 accepted, h=1 rejected) |        |        |        |        |
| p-value ( $\alpha = 0.05$ )    |        |        |        |        |
| test statistic                 |        |        |        |        |

Table 6.16: *KS2* Matrix Sensor S10 *Case 2* vs *Case 0*

Following the same procedure of the *Case 0* and *Case 1*, the empirical distributions ( $1 - CDF$ ) of the *Case 2* for sensor S6, S10 and S11 are fitted using the *Weibull* and *GPD* distributions. The extreme values of *Case 2*, according to the selected return periods (RP) are calculated for the selected sensors (S6, S10 and S11) and the results are then compared with the extreme values obtained in *Case 0*.

| CASE  | B2     | B5     | B10    | CASE 0 |
|---|--------|--------|--------|--------|
| B1  | 0      | 0      | 0      | 0      |
|   | 0.4077 | 0.8567 | 0.4801 | 0.7471 |
|   | 0.0222 | 0.0150 | 0.0208 | 0.0126 |
| B2  | 0      | 0      | 0      | 0      |
|   | 1      | 0.6455 | 0.2334 | 0.8044 |
|   | 0      | 0.0183 | 0.0256 | 0.0119 |
| B5  |        | 0      | 0      | 0      |
|   |        | 1      | 0.8586 | 0.6818 |
|   |        | 0      | 0.0148 | 0.0131 |
| B10   |        |        | 0      | 0      |
|   |        |        | 1      | 0.0928 |
|   |        |        | 0      | 0.0225 |
| CASE 0  |        |        |        | 0      |
|   |        |        |        | 1      |
|   |        |        |        | 0      |
| h (h=0 accepted, h=1 rejected)<br>p-value ( $\alpha = 0.05$ )<br>test statistic |        |        |        |        |

Table 6.17: *KS2 Matrix Sensor S11 Case 2 vs Case 0*

| Case                     | B1     | B2     | B5     | B10    | Case 0 |
|--------------------------|--------|--------|--------|--------|--------|
| <b>Sensor S6</b>         |        |        |        |        |        |
| n [peaks]                | 3174   | 3154   | 3168   | 3188   | 32503  |
| T [hours]                | 8.33   | 8.33   | 8.33   | 8.33   | 83.33  |
| $\varsigma$ [peaks/hour] | 380.88 | 378.48 | 380.16 | 382.56 | 390.03 |
| <b>Sensor S10</b>        |        |        |        |        |        |
| n [peaks]                | 3356   | 3343   | 3426   | 3478   | 34175  |
| T [hours]                | 8.33   | 8.33   | 8.33   | 8.33   | 83.33  |
| $\varsigma$ [peaks/hour] | 402.72 | 401.16 | 411.12 | 417.36 | 410.10 |
| <b>Sensor S11</b>        |        |        |        |        |        |
| n [peaks]                | 3187   | 3195   | 3287   | 3327   | 31918  |
| T [hours]                | 8.33   | 8.33   | 8.33   | 8.33   | 83.33  |
| $\varsigma$ [peaks/hour] | 382.44 | 383.40 | 394.44 | 399.24 | 383.01 |

Table 6.18: *Case 2* pressure peaks  $n$ , mean frequency between peaks  $\varsigma$  and experimental time  $T$

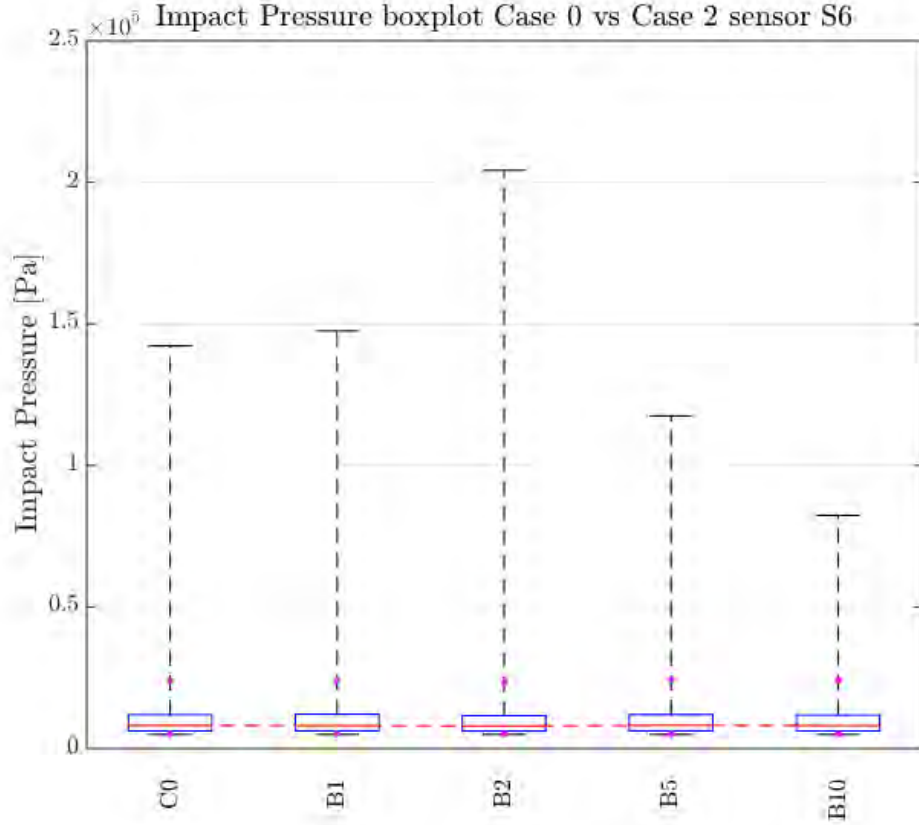


Figure 6.35: Box plot sensor S6 *Case 2* vs. *Case 0*, 5%, 25%, 75%, 95% percentile levels, minimum and maximum pressure

Figures 6.39 and 6.38 show respectively the *Weibull* and *GPD* fitting for sensor S6 *Case 2*. Both figures also include the *Case 0* in order to visualize the influence of the BIAS in the statistical fittings. In figure 6.39, at the comparing return period (100 hours), it can be observed that the maximum visible dispersion is achieved by the *Case 2-B2*.

*Case 2-B1* and *Case 2-B5* report also a visible difference at the tail of the distribution in comparison with the *Case 0* but not as much as *Case 2-B2*. Curiously *Case 2-B10*, in all the selected sensors report the lowest pressure values at the tail of the distribution. This reduction in the registered large peak pressures can be attributed in part to the substantial differences in the driving motion. It is necessary to remember that the *Case 2* induces both positive and negative random changes in the amplitude. Therefore, this noticeable difference in the amplitude seems to mitigate the impact pressure intensity of *Case 2-B10*.

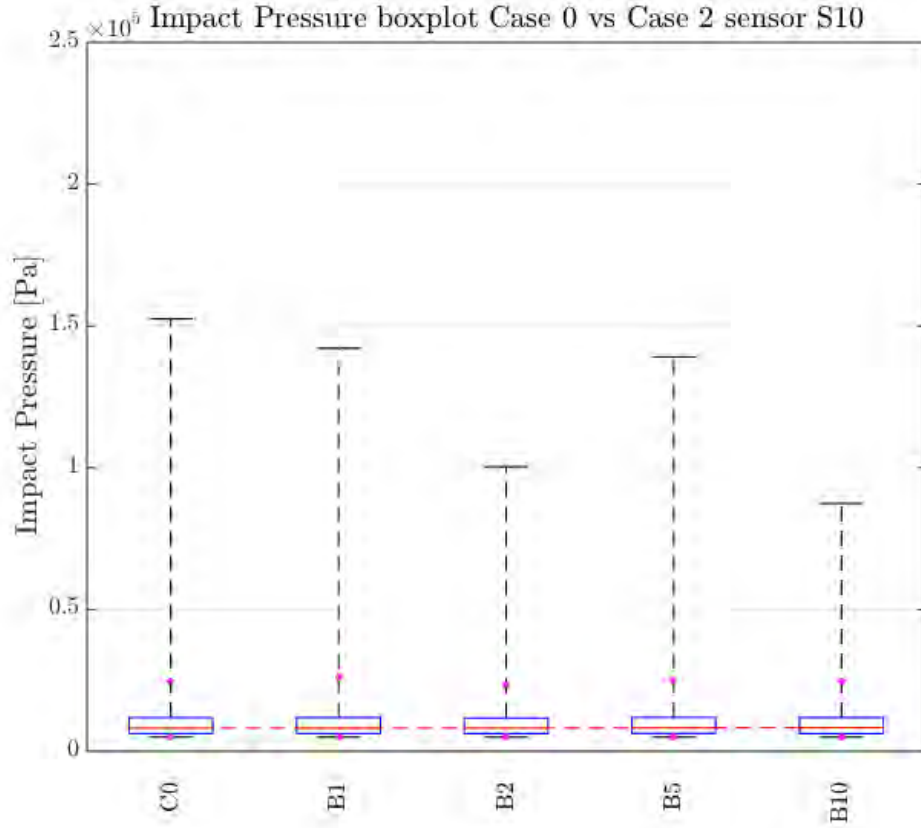


Figure 6.36: Box plot sensor S10 *Case 2* vs. *Case 0*, 5%, 25%, 75%, 95% percentile levels, minimum and maximum pressure

The *GPD* fitting, shown in figure 6.38, reports larger pressure values at the tail of the distributions in comparing with the *Weibull* fitting of the figure 6.39. The shape of the *GPD* fitting tends to overestimate the extreme values in greater return periods. The obtained extremes values for sensor S6 are summarized in the table 6.19. The percentages of difference with respect to *Case 0* for sensor S6 are collected in the table 6.20.



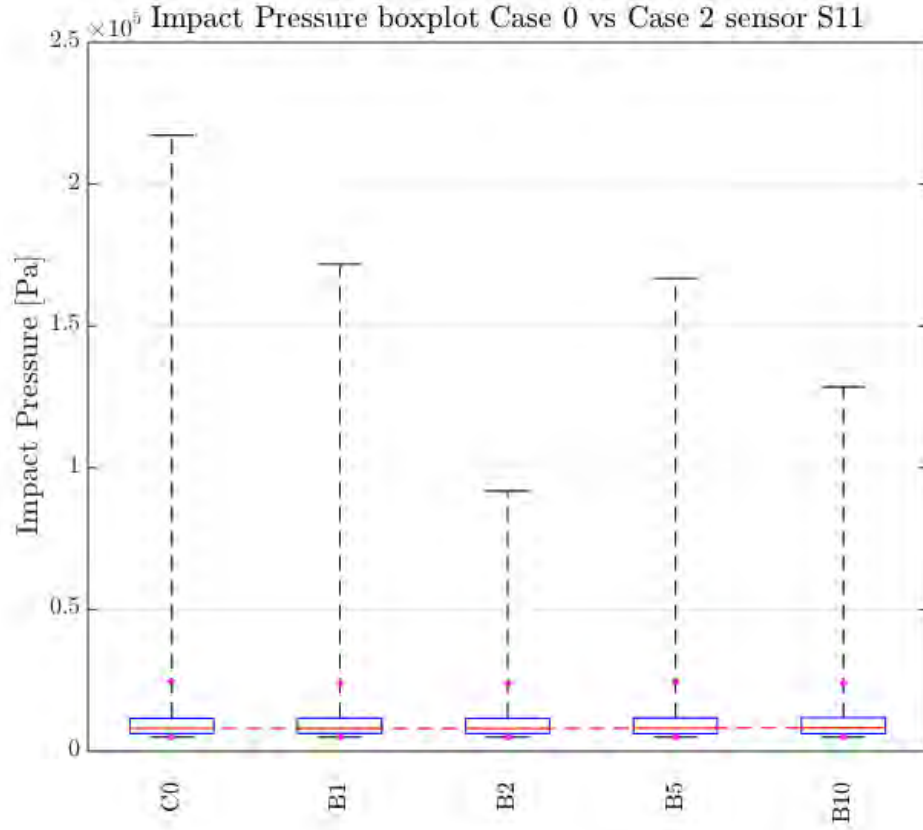


Figure 6.37: Box plot sensor S11 *Case 2* vs. *Case 0*, 5%, 25%, 75%, 95% percentile levels, minimum and maximum pressure

From tables 6.19 and 6.20, it can be extracted that the minimum percentage of difference (*Weibull* fitting) with respect to *Case 0* at RP=100 hours for sensor S6 is 8.19% and corresponds to *Case 2-B10* matching with the figure 6.39. The maximum difference with respect to *Case 0* is achieved by *Case 2-B2* and is estimated in 77.82%.

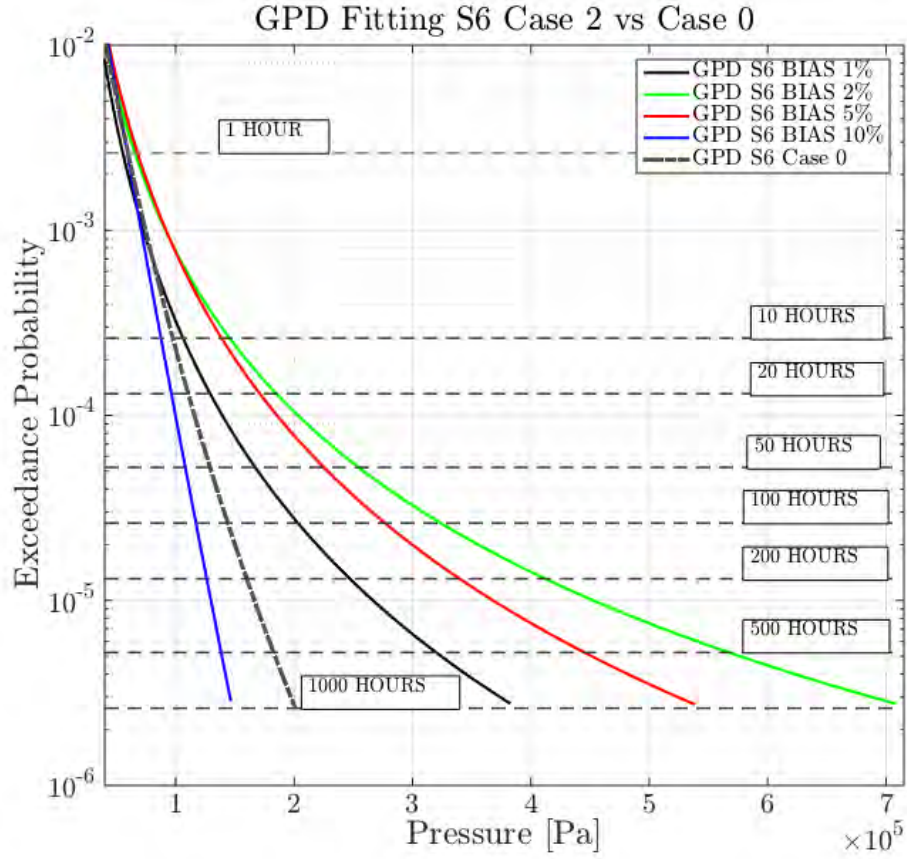


Figure 6.38: GPD Fitting *Case 2* sensor S6

It can be noticed that adding a 2% of BIAS in the original driving motion, the larger percentages of difference with respect to *Case 0* are obtained. *Case 2-B1* and *Case 2-B5* report a similar fitting shape and the percentage of difference at  $RP=100$  hours are 15.07% and 17.65% respectively.

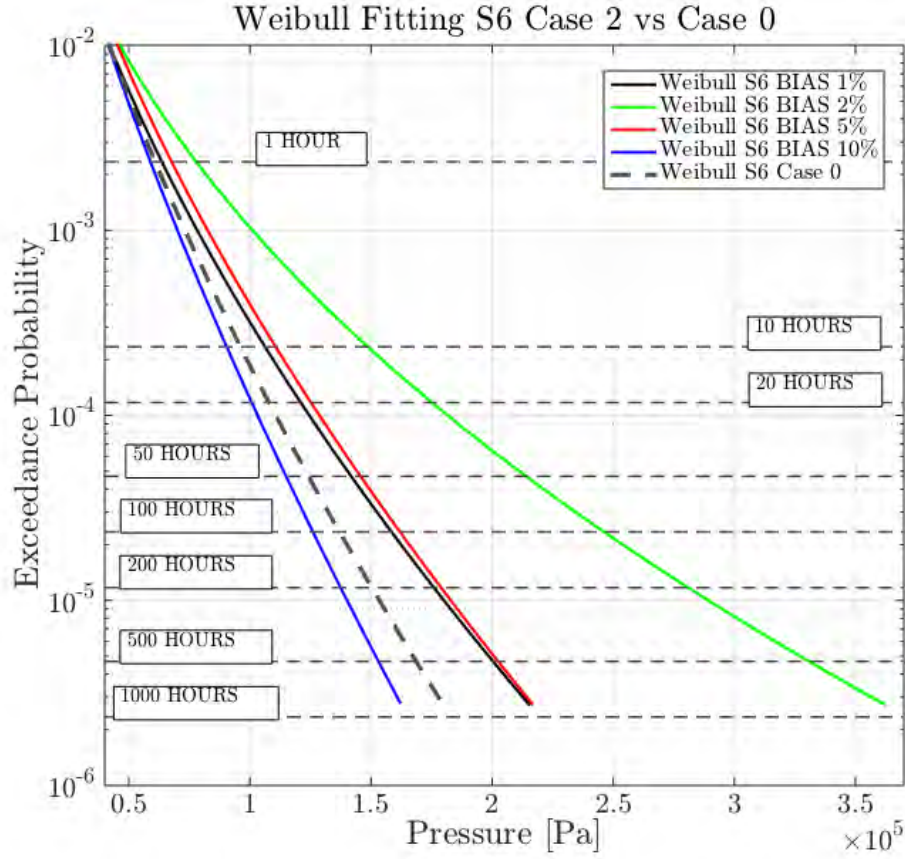


Figure 6.39: Weibull Fitting *Case 2* sensor S6

The percentages of difference with respect to *Case 0* in the *GPD* fitting for sensor S6 can be found in the second column of each BIAS case in 6.20. The minimum percentage of difference with respect to *Case 0* was also found in the *Case 2-B10 GPD* fitting (19.33%). Maximum difference is reported by *Case 2-B2* (120.36%). Meanwhile *Case 2-B1* and *Case 2-B5*, report a difference of 38.99% and 88.80% respectively.

| Case<br>RP [hours] | B1     |        | B2     |        | B5     |        | B10    |        |
|--------------------|--------|--------|--------|--------|--------|--------|--------|--------|
|                    | W [Pa] | P [Pa] | W [Pa] | P [Pa] | W [Pa] | P [Pa] | W [Pa] | P [Pa] |
| 1                  | 61923  | 54634  | 75062  | 64345  | 65879  | 66667  | 57648  | 58544  |
| 10                 | 104102 | 104846 | 144688 | 142972 | 108431 | 136595 | 88960  | 87015  |
| 20                 | 118716 | 127518 | 170808 | 181903 | 122927 | 168529 | 99222  | 95790  |
| 50                 | 139340 | 165145 | 209092 | 250148 | 143221 | 221880 | 113328 | 107539 |
| 100                | 155906 | 200795 | 240930 | 318358 | 159404 | 272758 | 124390 | 116540 |
| 200                | 173287 | 244119 | 275274 | 405200 | 176283 | 334939 | 135776 | 125641 |
| 500                | 197490 | 316020 | 324564 | 557428 | 199639 | 438823 | 151304 | 137825 |
| 1000               | 216711 | 384143 | 364821 | 709577 | 218077 | 537893 | 163398 | 147159 |

Table 6.19: Extreme Values (EV) *Case 2* (BIAS 1,2,5,10%) for Sensor S6

| Case<br>RP [hours] | % Difference B1 |        | % Difference B2 |        | % Difference B5 |        | % Difference B10 |        |
|--------------------|-----------------|--------|-----------------|--------|-----------------|--------|------------------|--------|
|                    | W [Pa]          | P [Pa] | W [Pa]          | P [Pa] | W [Pa]          | P [Pa] | W [Pa]           | P [Pa] |
| 1                  | 3,64            | 8,99   | 25,63           | 7,18   | 10,26           | 11,05  | 3,52             | 2,48   |
| 10                 | 9,84            | 7,08   | 52,67           | 46,02  | 14,41           | 39,51  | 6,13             | 11,13  |
| 20                 | 11,51           | 14,95  | 60,44           | 63,98  | 15,46           | 51,92  | 6,80             | 13,65  |
| 50                 | 13,59           | 27,59  | 70,45           | 93,27  | 16,75           | 71,43  | 7,62             | 16,91  |
| 100                | 15,07           | 38,99  | 77,82           | 120,36 | 17,65           | 88,80  | 8,19             | 19,33  |
| 200                | 16,49           | 52,12  | 85,05           | 152,50 | 18,50           | 108,72 | 8,73             | 21,71  |
| 500                | 18,27           | 72,49  | 94,36           | 204,25 | 19,55           | 139,52 | 9,39             | 24,77  |
| 1000               | 19,55           | 90,45  | 101,25          | 251,80 | 20,30           | 166,68 | 9,86             | 27,04  |

Table 6.20: Percentage of difference in the Extreme Values (EV) for *Case 2* vs *Case 0*, Sensor S6

Figure 6.40 and 6.41 represents the *Weibull* and *GPD* fitting for sensor S10 *Case 2*. Same as the previous fittings, *Case 0* is included in the figures in order to compare the results of the original C15 case against the BIAS influence. From figure 6.40, at the comparing return period (100 hours), it can inferred that the maximum visible dispersion in the *Weibull* fitting is reported by *Case 2-B5*. Second largest percentage of difference corresponds to *Case 2-B1* whose *Weibull* fitting shape is similar to *Case 2-B5* fitting. *Case 2-B2* and *Case 2-B10* fitting shapes are almost the same and their percentages of difference with respect to *Case 0* are similar.

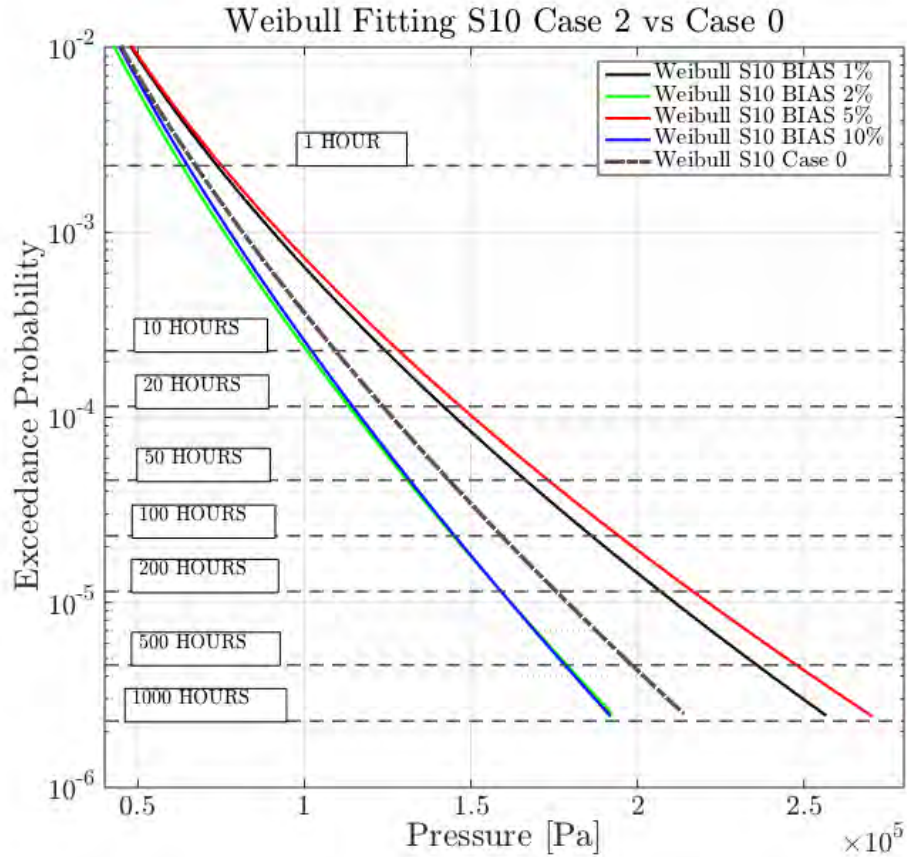


Figure 6.40: Weibull Fitting *Case 2* sensor S10

The *GPD* fitting of sensor S10, shown in figure 6.41, also presents a larger dispersion in comparison with the *Weibull* fitting similar to the previous results. In descending order, the maximum dispersion is achieved by the *Case 2-B5* followed by *Case 2-B1*, *Case 2-B2* and *Case 2-B10*.

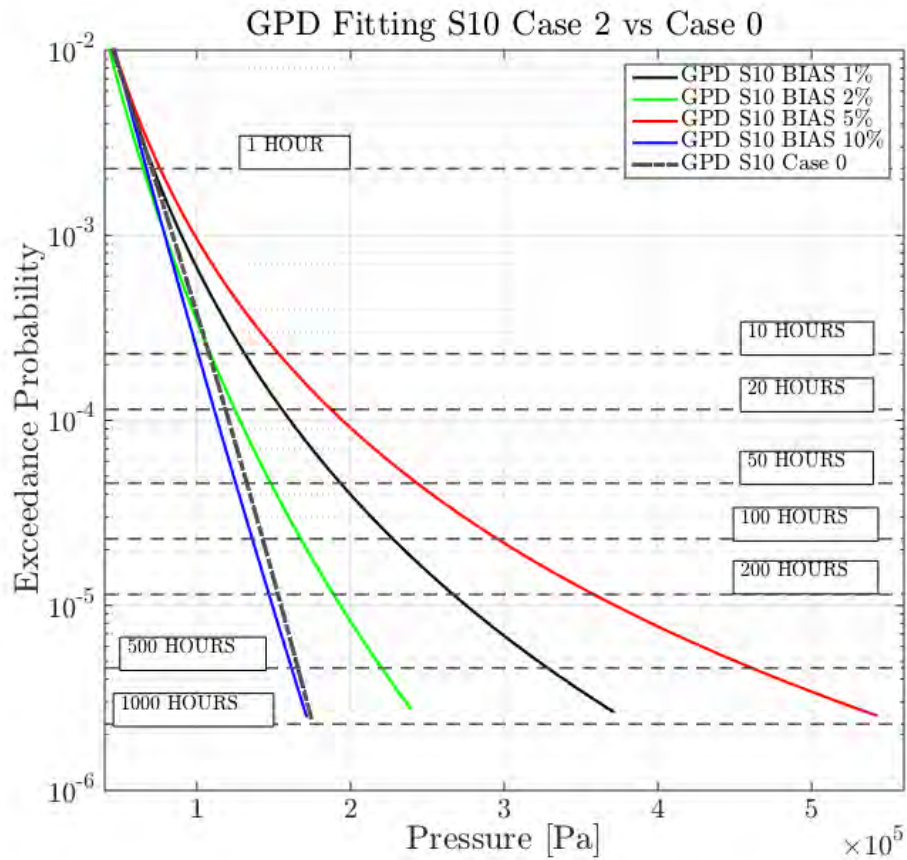


Figure 6.41: GPD Fitting *Case 2* sensor S10

Both *Weibull* and *GPD* extremes values and percentages of difference for sensor S10 are summarized in tables 6.21 and 6.22 respectively. From table 6.22, *Weibull* fitting, the minimum percentage of difference (8.57%) with respect to *Case 0* corresponds to *Case 2-B10*. In ascending order the percentages of difference are *Case 2-B2* (9.35%), *Case 2-B1* (16.57%) and *Case 2-B5* (22.05%). In comparison with sensor S6, the largest difference is obtained by *Case 2-B5* (22.05%) instead of *Case 2-B2* (77.82%). Nevertheless it is necessary to remember that sensors S6 and S10 are located in separated arrays. Adding a 5% of BIAS in the original driving motion induces the largest differences with respect to *Case 0* in the sensor S10.

The percentages of difference with respect to *Case 0* in the *GPD* fitting, can be found in the second column of each BIAS case of the 6.22, in ascending order, the percentages of difference are *Case 2-B10* (5.06%), *Case 2-B2* (15.50%), *Case 2-B1* (55.88%) and *Case 2-B5* (102.34%), which follows the same order of the *Weibull* fitting. Although, in most of the cases, the percentages of difference of the *GPD* fitting is higher than the *Weibull* fitting, it can be noticed that the percentage of the *GPD* fitting in *Case 2-B10* is lower even when the return period (up to 1000 hours) is increased. This suggests, that the *GPD* fitting of the *Case 2-B10* follows almost the same *GPD* fitting of the *Case 0*.

| Case<br>RP [hours] | B1     |        | B2     |        | B5     |        | B10    |        |
|--------------------|--------|--------|--------|--------|--------|--------|--------|--------|
|                    | W [Pa] | P [Pa] | W [Pa] | P [Pa] | W [Pa] | P [Pa] | W [Pa] | P [Pa] |
| 1                  | 72373  | 69250  | 62072  | 62983  | 74116  | 73532  | 64366  | 65946  |
| 10                 | 122503 | 127200 | 99406  | 106013 | 127001 | 148605 | 101505 | 99526  |
| 20                 | 139879 | 150873 | 111938 | 121660 | 145478 | 181781 | 113846 | 109939 |
| 50                 | 164405 | 187945 | 129363 | 144601 | 171657 | 236151 | 130925 | 123925 |
| 100                | 184112 | 221123 | 143171 | 163839 | 192765 | 287034 | 144400 | 134675 |
| 200                | 204793 | 259492 | 157501 | 184867 | 214978 | 348209 | 158336 | 145574 |
| 500                | 233599 | 319576 | 177223 | 215697 | 246012 | 448465 | 177444 | 160214 |
| 1000               | 256481 | 373349 | 192713 | 241551 | 270734 | 542290 | 192402 | 171467 |

Table 6.21: Extreme Values (EV) *Case 2* (BIAS 1,2,5,10%) for Sensor S10

| Case<br>RP [hours] | % Difference B1 |        | % Difference B2 |        | % Difference B5 |        | % Difference B10 |        |
|--------------------|-----------------|--------|-----------------|--------|-----------------|--------|------------------|--------|
|                    | W [Pa]          | P [Pa] | W [Pa]          | P [Pa] | W [Pa]          | P [Pa] | W [Pa]           | P [Pa] |
| 1                  | 8,94            | 0,38   | 6,57            | 9,39   | 11,56           | 5,78   | 3,11             | 5,13   |
| 10                 | 13,19           | 18,97  | 8,15            | 0,85   | 17,35           | 38,98  | 6,21             | 6,92   |
| 20                 | 14,29           | 28,19  | 8,54            | 3,37   | 18,86           | 54,46  | 6,98             | 6,59   |
| 50                 | 15,63           | 42,83  | 9,02            | 9,89   | 20,73           | 79,46  | 7,92             | 5,83   |
| 100                | 16,57           | 55,88  | 9,35            | 15,50  | 22,05           | 102,34 | 8,57             | 5,06   |
| 200                | 17,46           | 70,81  | 9,66            | 21,69  | 23,31           | 129,21 | 9,18             | 4,17   |
| 500                | 18,57           | 93,81  | 10,04           | 30,81  | 24,87           | 171,97 | 9,93             | 2,84   |
| 1000               | 19,36           | 113,98 | 10,31           | 38,44  | 26,00           | 210,80 | 10,46            | 1,73   |

Table 6.22: Percentage of difference in the Extreme Values (EV) for *Case 2* vs *Case 0*, Sensor S10



The *Weibull* and *GPD* fitting for sensor S11 *Case 2* are shown in figures 6.42 and 6.43. Table 6.23 summarizes the calculated extreme values for sensor S11 using the *Weibull* and *GPD* fittings. The percentages of difference of the table 6.24 were extracted from 6.23 and the reference extreme values of *Case 0*.

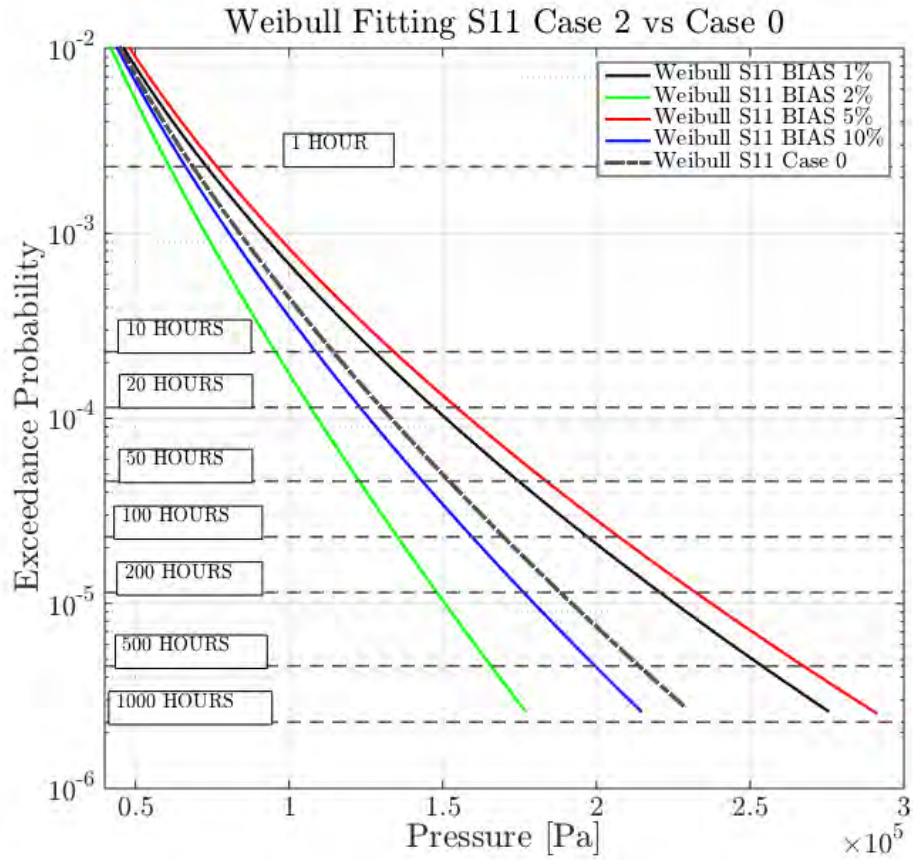


Figure 6.42: Weibull Fitting *Case 2* sensor S11

Following the same previous procedure, at the comparing return period (100 hours), the percentages of difference with respect to *Case 0* in ascending order, for the *Weibull* fitting, are *Case 2-B10* (5.40%), *Case 2-B1* (15.84%), *Case 2-B2* (20.13%) and *Case 2-B5* (22.50%). Those results can be observed in figure 6.42 and are summarized in the table 6.24. *Case 2-B10* remains as the case with the lowest percentage of difference as occurs in sensor S10 (neighboring S11 sensor). The same occurs in *Case 2-B5* which reports the higher difference in both S10 and S11 sensors.

The percentages of difference with respect to *Case 0* in ascending order, for the *GPD* fitting are *Case 2-B2* (24.90%), *Case 2-B10* (44.79%), *Case 2-B1* (45.71%) and *Case 2-B5* (51.31%). Some differences with respect to the *Weibull* fitting are immediately noticed. The *GPD* fittings of *Case 2-B1*, *B5* and *B10* follow almost the same distributions and their differences with respect to *Case 0* are of the same order (44.79%, 45.71% and 51.31%).

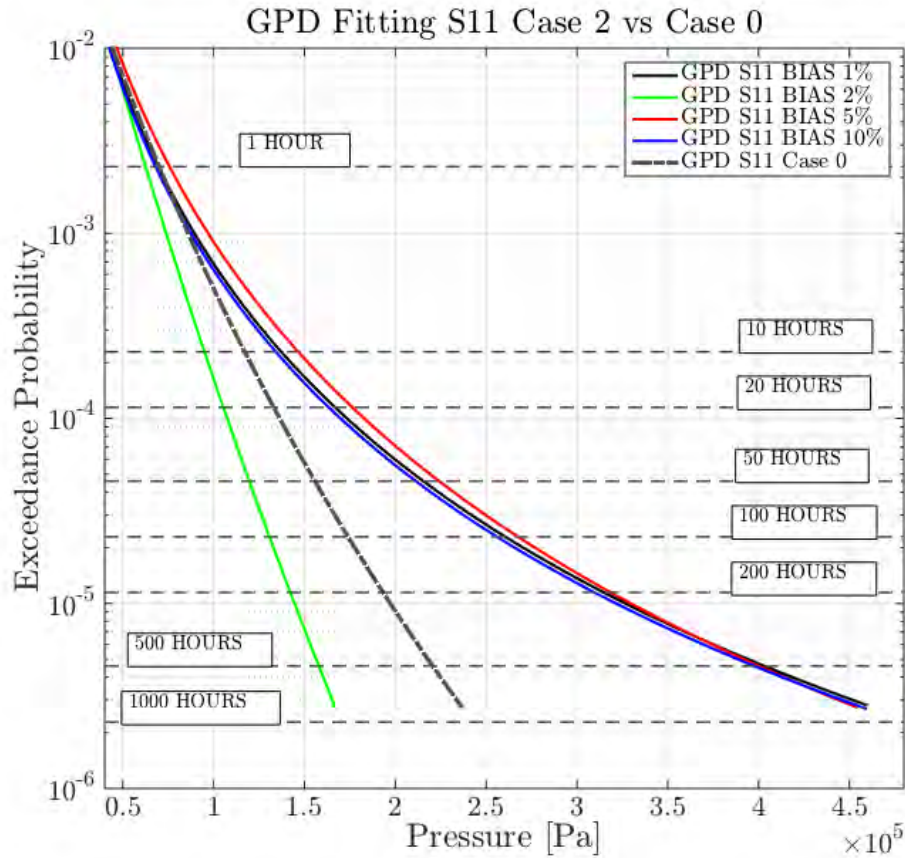


Figure 6.43: GPD Fitting *Case 2* sensor S11

| Case       | B1     |        | B2     |        | B5     |        | B10    |        |
|------------|--------|--------|--------|--------|--------|--------|--------|--------|
|            | W [Pa] | P [Pa] | W [Pa] | P [Pa] | W [Pa] | P [Pa] | W [Pa] | P [Pa] |
| RP [hours] |        |        |        |        |        |        |        |        |
| 1          | 70626  | 65863  | 59381  | 60266  | 74534  | 72368  | 64998  | 65285  |
| 10         | 124394 | 130433 | 93591  | 92466  | 131472 | 140817 | 107031 | 129165 |
| 20         | 143500 | 158797 | 104948 | 102796 | 151699 | 169713 | 121386 | 157367 |
| 50         | 170786 | 205120 | 120656 | 116929 | 180585 | 215828 | 141505 | 203557 |
| 100        | 192945 | 248322 | 133043 | 127995 | 204043 | 257873 | 157566 | 246759 |
| 200        | 216399 | 300108 | 145850 | 139393 | 228871 | 307289 | 174334 | 298674 |
| 500        | 249372 | 384682 | 163400 | 154988 | 263774 | 386151 | 197558 | 383703 |
| 1000       | 275790 | 463560 | 177132 | 167197 | 291739 | 458054 | 215910 | 463232 |

Table 6.23: Extreme Values (EV) *Case 2* (BIAS 1,2,5,10%) for Sensor S11

| Case       | % Difference B1 |        | % Difference B2 |        | % Difference B5 |        | % Difference B10 |        |
|------------|-----------------|--------|-----------------|--------|-----------------|--------|------------------|--------|
|            | W [Pa]          | P [Pa] | W [Pa]          | P [Pa] | W [Pa]          | P [Pa] | W [Pa]           | P [Pa] |
| RP [hours] |                 |        |                 |        |                 |        |                  |        |
| 1          | 6,10            | 2,54   | 10,80           | 10,82  | 11,97           | 7,09   | 2,36             | 3,40   |
| 10         | 11,43           | 14,25  | 16,16           | 19,00  | 17,77           | 23,35  | 4,12             | 13,14  |
| 20         | 12,84           | 22,16  | 17,47           | 20,92  | 19,29           | 30,55  | 4,55             | 21,06  |
| 50         | 14,59           | 34,63  | 19,04           | 23,25  | 21,17           | 41,66  | 5,06             | 33,61  |
| 100        | 15,84           | 45,71  | 20,13           | 24,90  | 22,50           | 51,31  | 5,40             | 44,79  |
| 200        | 17,02           | 58,33  | 21,13           | 26,46  | 23,76           | 62,12  | 5,73             | 57,57  |
| 500        | 18,50           | 77,64  | 22,35           | 28,43  | 25,34           | 78,31  | 6,12             | 77,18  |
| 1000       | 19,56           | 94,46  | 23,21           | 29,86  | 26,48           | 92,15  | 6,40             | 94,33  |

Table 6.24: Percentage of difference in the Extreme Values (EV) for *Case 2* vs *Case 0*, Sensor S11

## 6.6 Summary

Statistical post processing of long duration irregular sloshing tests using two fitting distributions (Weibull and GPD) have been carried out on high filling level tank, instrumented with two piezoelectric sensors arrays (8 sensors per array) in the upper corners and subjected to irregular roll motions under the influence of two parameters used in the sensitivity analysis. Special attention was paid to the sensitivity parameters previously documented in Loysel et al. (2012, 2013b), in order to reduce as much as possible the external factors and ensure a correct statistical influence in the extremes pressures due to the parameters used during the sensitivity analysis.

The first parameter investigated the sensitivity in the data collection and tail distribution of the impact pressure due to different realizations of the same motion spectrum. The second parameter investigated the sensitivity in the data collection and tail distribution of the impact pressure due of small variations in the amplitude of the driving motion.

The results were structured in three cases. *Case 0* which corresponds to the original irregular roll motion case C15 (Loysel et al., 2013b) with 100 repetitions, it summarizes the results of the impact pressure distributions of the 16 sensors together with a sensor selection and extreme values estimation. The impact pressure distributions of *Case 0* were considered as the reference impact pressures distributions for following comparisons. The *Case 1* (5 cases, 10 repetitions each), provides the influence in the pressure data collection, in terms of the impact pressure distribution and extreme values, due to the randomness introduced through different driving motion realizations (5 new random driving motion signals) for a given spectrum. The *Case 2* (4 cases, 40 repetitions each), reports the influence of the induced random BIAS (1,2,5,10%) in the impact pressure distribution and the extreme values. The summary below is divided according to the aforementioned cases.

### 6.6.1 Summary *Case 0*

Using the definition of impact pressure peak and pressure event, the impact pressure samples for each sensor was collected during the 100 runs of the experiment C15. The *Exceedance Distribution* ( $1 - CDF$ ) of the selected sensors were built using those impact pressure samples.

A P10 (average of the 10 largest impact pressure peaks) was derived from the impact pressure samples and the P10 plot provides information about the pressure spatial distribution in the corresponding sensor arrays. Using both,  $1 - CDF$  plots and P10 plots, the sensors S6, S10 and S11 were selected as the sensors which recorded the maximum pressure in each array.

Two statistical models (Weibull and GPD) were used in order to fit the set of impact pressure samples of the selected sensors. Using both distributions, the extreme values (EV) according to different return periods for the selected sensors were calculated. Both, impact pressure distributions and extreme values were used as the basis for the next cases comparisons.

The results obtained in the EV calculation show that the two selected models were able to fit the impact pressure samples of the sensors S6, S10 and S11. Only minor differences in the GPD EV with respect to the Weibull EV was noticed.

### 6.6.2 Summary *Case 1*

Using *Fourier* transformation, 5 new random driving motion realizations (R1-R5) were created and every new sub case was repeated 10 times. In total *Case 1* comprises 50 runs, 10 for each new sub case. The impact pressure samples of the selected sensors was collected and compared with those obtained in the *Case 0*.

The derived P10 plots of array 1, indicates, that the maximum pressure seems to change its location in every sub case. This displacement of the maximum pressure suggests that *Case 1* introduces variability in terms of the maximum pressure location, which can take place at any of the sensors of array 1. Pressure distribution seems to be more consistent in array 2, whose location in most of the cases coincides with sensor S10. Maximum P10 for *Case 1* was registered by sensor S10 in the sub case R1. This maximum was of the same order of the maximum P10 registered in *Case 0*. This indicates that *Case 1* affects the P10 location and induces high pressure values, similar to those recorded in *Case 0*.

Similar as happened in *Case 0*, the reported pressures in array 1 were smaller than in array 2. The impact pressure samples were then used to derive the  $1 - CDF$  plots of the selected sensors. *Case 1*, even under the assumption of equal motion spectrum, modifies considerably the shape of the  $1 - CDF$  of the selected sensors. Looking at the  $1 - CDF$  plots, at the comparing probability level of  $10^{-3}$  differences up to  $4.54 \cdot 10^4$  [Pa] with respect to *Case 0* were noticed. The *KS2* tests applied to the empirical impact pressure samples distributions of the selected sensors reports many rejections. Many rejections means significant dependence of the impact pressure distribution from the actual random signal. In conclusion, one single driving motion (5 in total for *Case 1*, each one repeated 10 times) is not sufficient and pressure data shall be collected for the same spectrum and different driving signals. Alternatively a long enough driving motion signal, in principle will provide a large enough impact pressures sample which it is statistically a good representation of the underlying impact pressure distribution. There is not clear how long or how many random driving motion realizations are needed in order to provide a good approximation of the underlying impact pressure distribution, this matter will be held for further investigations.

The Exceedance Distribution ( $1 - CDF$ ) of the selected sensors were fitted using the Weibull and GPD distributions and the EV were calculated. Table 6.25 show the absolute percentage of difference (Weibull fitting) of *Case 1* in comparing with *Case 0*, at RP=100 hours. The minimum absolute percentage of difference found in the Weibull fitting at RP=100 hours was 1.72% (S6 *Case 1-R3*) and the maximum 55.32% (S6 *Case 1-R4*). This denotes the large variability present in array 1, also noticed in the  $1 - CDF$  and P10 plots. As can be appreciated in table 6.25 big differences are obtained even in neighboring sensors (i.e S10 vs S11 *Case 1-R1*) in the same case.

| Case/Sensor | S6    | S10   | s11   |
|-------------|-------|-------|-------|
| R1          | 12.40 | 48.96 | 5.69  |
| R2          | 38.10 | 2.19  | 36.64 |
| R3          | 1.72  | 23.79 | 20.38 |
| R4          | 55.32 | 3.54  | 1.96  |
| R5          | 21.31 | 27.87 | 19.35 |

Table 6.25: Absolute percentage of difference (RP=100 hours) Weibull Fitting *Case 1* with respect to *Case 0*

The GPD fitting reports extremely big differences in comparison with *Case 0*. Table 6.26 summarizes the absolute percentage of difference (GPD fitting) of *Case 1* in comparing with *Case 0*, at RP=100 hours. Large differences, up to 264.45% (S10 *Case 1-R1*) were obtained. The differences in the EV calculation obtained in the Weibull and GPD fittings for *Case 1* in comparison with *Case 0*, suggests that the GPD fitting was not able to fit the empirical data at the tail of the distributions with the selected threshold and fitting parameters in experiments with only 10 repetitions where the collected impact pressure samples is reduced considerably in comparison with *Case 0*.

| Case/Sensor | S6    | S10    | s11   |
|-------------|-------|--------|-------|
| R1          | 31.51 | 264.45 | 25.30 |
| R2          | 80.47 | 42.03  | 99.40 |
| R3          | 3.85  | 101.99 | 31.90 |
| R4          | 69.76 | 42.22  | 6.97  |
| R5          | 56.19 | 51.91  | 23.23 |

Table 6.26: Absolute percentage of difference (RP=100 hours) GPD Fitting *Case 1* with respect to *Case 0*

### 6.6.3 Summary *Case 2*

A random BIAS (1, 2, 5 and 10%) was applied to the original C15 signal and 4 new biased driving motion signals were obtained. In total, *Case 2* comprises 40 runs, 10 runs for each sub case repeated with the same biased driving motion signal. The impact pressure samples was collected and compare with its *Case 0* reference.

The spatial pressure distribution in array 1 was more consistent in comparison with the random cases (*Case 1*). Same as *Case 0*, S6 reports the maximum P10 in most of the BIAS cases. Nevertheless, the spatial pressure distribution of array 2, seems to be more susceptible to the BIAS influence. In both arrays the maximum registered pressure P10 of all sensors in all cases is less than the P10 reported in *Case 0*. Therefore, not extraordinary pressures of the same order of the reported in *Case 0* were recorded, as happened in *Case 1*.

The Exceedance Distributions ( $1 - CDF$ ) of the sensors S6, S10 and S11 were built using the impact pressure samples and then compared with the Exceedance Distributions  $1 - CDF$  of *Case 0*. *Case 2*, as expected, modifies the shape of the  $1 - CDF$  of the selected sensors but not as much as happened in the *Case 1*. Therefore, the *KS2* tests applied to the empirical impact pressure samples distributions of the selected sensors reports a few rejections. Few rejections means, clear independence of the impact pressure distribution from the actual biased driving motion signal. Therefore, the impact pressure distributions of the samples collected in the BIAS cases, can be considered statistically a good representation of the impact pressure distribution of *Case 0*, in turn, assumed to be statistically a good representation of the underlying impact pressure distribution.

The Exceedance Distributions ( $1 - CDF$ ) of the selected sensors were fitted using the Weibull and GPD distributions and the EV were calculated. Table 6.27 show the absolute percentage of difference (Weibull fitting) of *Case 2*, at RP=100 hours.

| Case/Sensor | S6    | S10   | s11   |
|-------------|-------|-------|-------|
| B1          | 15.07 | 16.57 | 15.84 |
| B2          | 77.82 | 9.35  | 20.13 |
| B5          | 17.65 | 22.05 | 22.50 |
| B10         | 8.19  | 8.57  | 5.40  |

Table 6.27: Absolute percentage of difference (RP=100 hours) Weibull Fitting *Case 2* with respect to *Case 0*

The minimum absolute percentage of difference found in the Weibull fitting at RP=100 hours was 8.19% (S6 *Case 2-B10*) and the maximum 77.82% (S6 *Case 2-B2*). The 2% BIAS induces the largest absolute percentage of difference of all the cases, meanwhile, curiously the 10% BIAS case, where important amplitude variations were applied, reports a considerable reduction of the absolute percentage of difference in all sensors. This variations in the EV seems to be mainly due to the inherent random outcome of the process instead of the modifications in the impact pressure distribution shape due to the BIAS influence.

The GPD fitting reports big differences but not as extreme as those reported in *Case 1*. Table 6.28 summarizes the absolute percentage of difference (GPD fitting) of *Case 2*, at RP=100 hours. Same as Weibull fitting, the maximum absolute percentage of difference was reported for S6 *Case 2-B2*. In some of the cases, it was observed that the GPD fitting was not able to fit the empirical data at the tail of the distributions with the selected threshold and fitting parameters, i.e S10 *Case 2-B5*) whose differences in comparison with the Weibull fitting was considerable.

| <b>Case/Sensor</b> | <b>S6</b> | <b>S10</b> | <b>s11</b> |
|--------------------|-----------|------------|------------|
| B1                 | 38.99     | 55.88      | 45.71      |
| B2                 | 120.36    | 15.50      | 24.90      |
| B5                 | 88.80     | 102.34     | 51.31      |
| B10                | 19.33     | 5.06       | 44.79      |

Table 6.28: Absolute percentage of difference (RP=100 hours) GPD Fitting *Case 2* with respect to *Case 0*



# Chapter 7

## Coupled Sloshing and Angular Motion

### 7.1 General

The risk of occurrence of severe damage or structural failures in buildings during a catastrophic event like an earthquake or a hurricane can be reduced by adopting techniques to increase the damping characteristics of a structure. A tuned liquid damper (TLD) system represents an efficient and simple technique to increase the damping of a structure. It involves the attachment of one or multiple partially filled liquid- tanks to the structures. The TLD systems rely on the sloshing waves that appear at the free surface of the fluid to produce a counter force and torque thus dampening the initial motion. The growing interest in TLDs is due to their low capital and maintenance cost and their ease of installation into existing and new structures. Very important examples of these devices are the Shin Yokohama Prince Hotel, the Hobart Tower in Tasmania (Kareem et al., 1999) or the 1300t one installed in the Comcast Center in Philadelphia, PA, claimed to be the largest in the world.

TLDs are also used in the marine field, under the name of passive anti-roll tanks, to dampen the roll motion of, especially, fishing vessels (Bass, 1998), whilst for large cargo ships active anti-rolling tanks are usually preferred. However, in contrast to the civil engineering case, the dampening effect on roll given by the TLD is obtained through the moment generated by the tank as a consequence of an imposed angular motion. In the field of Naval Architecture, the roll motion equation was coupled with experimentally determined fluid moments for an oscillating free surface tank (Van Den Bosch and Vugts, 1966) whilst Francescutto and Contento (1994) exploited the mechanical equivalence developed by Graham and Rodriguez (1952) to provide a 2-DOF analytical model which is nonlinear in respect to roll, and linear in respect to the DOF associated to the fluid sloshing. SDOF models for roll are often used to simulate the roll behavior in beam seas (Bulian and Francescutto, 2009) and an example of analytical nonlinear SDOF descriptions of roll

motion coupled with direct CFD calculations for the free surface tank can be found in Armenio and Rocca (1996); Armenio et al. (1996a,b). Faltinsen et al. (2003) analyzed the coupled problem in the sway case of a box excited by waves, in comparison to experimental data.

In the existing literature two theories can be found to describe the response of a TLD to external excitations. The first one consists of imposing a periodic motion on the TLD by using a shaking table or a forced roll motion device and measuring the response in terms of lateral force or moment (Reed et al., 1998; Tait et al., 2005; Souto-Iglesias et al., 2006). This measurement is not usually straightforward because the response of the tank liquid cannot be completely detuned from the structure itself when registered. Therefore some superposition hypotheses on the Fourier analysis of the empty tank and partially filled tank responses aimed at extracting the liquid response are needed. The period of the forced motion is related with the natural period of the structure and the TLD is designed to have a maximum response at this excitation period. The design parameters are the shape of the tank, the liquid depth and the use of baffles inside the tank.

The other approach, more complex, and the one the present chapter deals with, is to consider the motion response of the coupled system tank-structure, subjected to external excitation in terms of force, moment or even induced motion to the tank. With this second approach, not only the natural period of the structure is considered; the damping characteristics, inertia and restoring terms are also relevant in the dynamic analysis. Real motions of the structure are the outcome of this process and such motions can be compared with design limit states, for instance (Banerji and Samanta, 2011; Frandsen, 2005; Delorme et al., 2006).

In this chapter <sup>1</sup>, a SDOF (single degree of freedom) structure with a partially filled tank is considered, with roll motion modelled by means of a 1-DOF approach. This means that the damper acts as an angular damper whilst most of the previously described works correspond to horizontal excitation. The motion is excited by the moment created by a transversally (in a tank fixed reference system) moving mass with imposed motion. Experiments have been performed using fluids of different viscosity in order to assess the influence of breaking. A similar approach was taken by Pirner and Urushadze (2007), be-

---

<sup>1</sup> The main materials of this chapter is linked with the following papers:

Bulian, G., Souto-Iglesias, A., Delorme, L., and Botia-Vera, E. (2010). SPH simulation of a tuned liquid damper with angular motion. *Journal of Hydraulic Research*, vol. 48.

Botia-Vera, E., Souto-Iglesias, A., Bulian, G., and Lobovsky, L. (2010). Three SPH Novel Benchmark Test Cases for free surface flows. In 5th ERCOFTAC SPHERIC workshop on SPH applications.

Pérez-Rojas, L., Bulian, G., Botia-Vera, E., Cercos-Pita, J. L., Souto-Iglesias, A., and Delorme, L. (2009). A combined experimental and SPH approach to sloshing and ship roll motions. 10th International Conference on Stability of Ships and Ocean Vehicles (STAB 2009).

cause water is not a suitable liquid to be used in footbridges which was the problem they were interested in.

## 7.2 Experimental Setup

### 7.2.1 Rig

The experiments were conducted with the sloshing rig described in chapter 4. The standard forced regular-irregular motion configuration of the device, used in the chapter 5 and chapter 6, was modified in order to allow the rig to rotate freely by disconnecting the linear actuator from the tank holding structure. The assembly freely to rotate, is excited by the moment created by a transversally moving mass with imposed motion by using a servo linear guide configuration as can be seen in figure 7.1. Thus allowing the coupling between the external excitation and fluid dynamics, both interacting with the structure dynamic characteristics, damping and inertia. The servo linear guide is 600mm long and

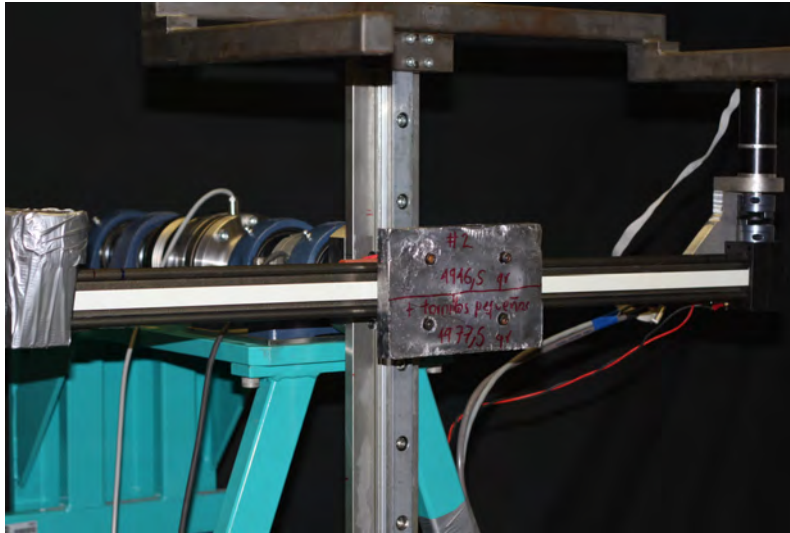


Figure 7.1: Servo linear Guide

it is placed just at the rotation center, aimed at simplifying the coupling problem. This linear guide consists of a servo motor that laterally moves a weight with an imposed motion with a maximum amplitude of 300 mm and a frequency of 1 Hz. This weight will mimic the external excitation to the system (e.g. the wave action on the roll motion).

### 7.2.2 Tank and Fluids

The tank used during the experimental campaign share the same dimensions as the one presented in chapter 4, the breadth of the tank is 62 mm. This is intended to have

Table 7.1: Test matrix (repeated for each liquid: water, sunflower oil and glycerin).

| $\omega/\omega_0$ -A | 50mm   | 100mm   | 150mm   | 200mm   |
|----------------------|--------|---------|---------|---------|
| 0.9                  | 0.9/5  | 0.9/100 | 0.9/150 | 0.9/200 |
| 1.0                  | 1.0/50 | 1.0/100 | 1.0/150 | 1.0/200 |
| 1.1                  | 1.1/50 | 1.1/100 | 1.1/150 | 1.1/200 |

predominantly a two dimensional flow. The center of rotation is located at 470mm from the bottom side of the tank in order to increase the stability of the rig. The natural

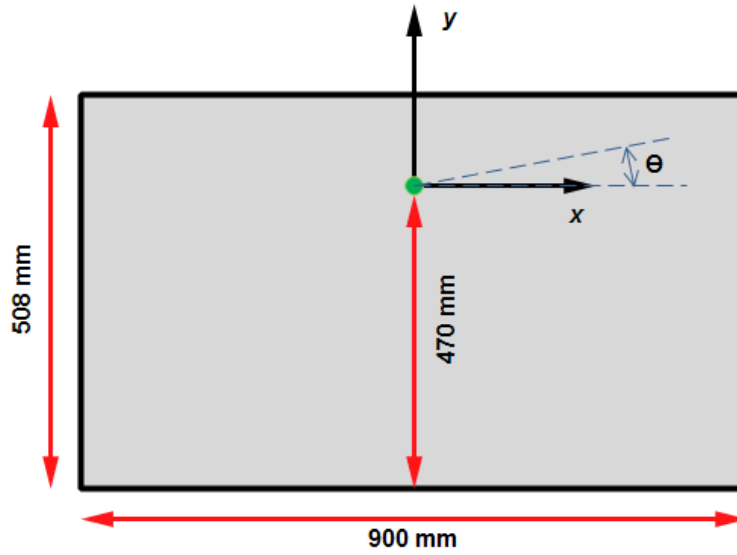


Figure 7.2: Tank

frequency of the rigid system with the empty tank , as will be later discussed, is  $\omega_0 = 3.26 rad/s$ . The water depth ( $H$ ) whose first sloshing frequency matches  $\omega_0$  has been chosen for the experiments (92mm). The test matrix is defined by choosing three moving weight frequencies  $0.9\omega_0$ ,  $\omega_0$  and  $1.1\omega_0$  and 4 moving weight motion amplitudes  $A$  (50mm, 100mm, 150mm and 200mm) for each of the three liquids under study (water, sunflower oil and glycerin). For all cases, the moving mass  $m$  is the same,  $m = 4.978 Kg$ . A summary of the test cases is reported in table 7.1. It is important to define which are the Reynolds numbers of our experimental flows. The characteristic velocity will be related to the bore front propagation velocity of the equal height dam-break ( $\sqrt{gh}$ ); the characteristic length will be taken as the water depth  $H$ . The physical constants of the three liquids and the corresponding Reynolds numbers are documented in table 7.2. According to the obtained Reynolds number, the water cases will be fully turbulent and the glycerin ones will be

Table 7.2: Physical properties (units SI) of the liquids:  $\rho$  for density,  $\mu$  for the dynamic viscosity,  $\nu$  for the kinematic viscosity and  $Re$  for the Reynolds number.

|          | $\rho$ | $\mu$   | $\nu$   | $Re$  |
|----------|--------|---------|---------|-------|
| Water    | 998    | 8.94e-4 | 8.96e-7 | 97546 |
| Oil      | 900    | 0.045   | 5e-5    | 1748  |
| Glycerin | 1261   | 0.934   | 7.4e-4  | 118   |

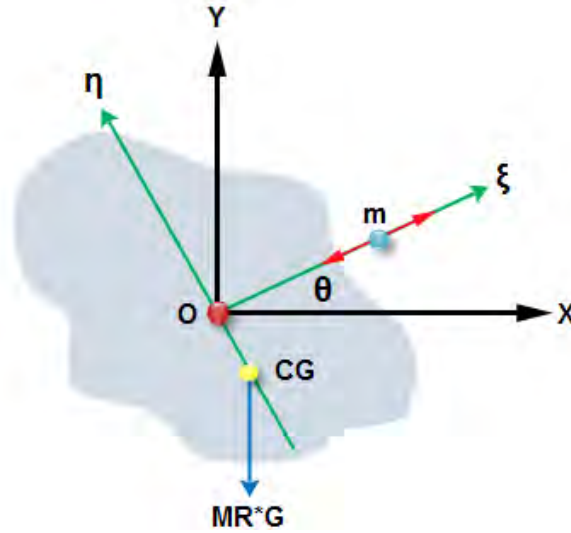


Figure 7.3: Analytical SDOF model

completely laminar. In the oil cases, as will be shown experimentally, there will be cases falling into either laminar, turbulent or transition regimes. In order to simulate the water cases, due to the small thickness of the boundary layers and the high resolution it would imply, a free slip condition will be used. We will focus on the water cases in the present chapter, using the other liquids' cases as reference regarding the onset of splashing and breaking waves and the influence of these phenomena on the damping effect of the TLD.

### 7.2.3 Analytical Model

An analytical model of the SDOF structural system (see figure 7.3) used in the experiments comparison was obtained by rigorously analyzing the dynamics of the system and by obtaining the coefficients after carefully analyzing a set of tests with the empty tank and thereafter finding a data-consistent damping term model. The analytical model used to describe the behavior of the system is, in general, is as follows:

$$[I_0 + m \cdot \xi_m^2(t)] \cdot \ddot{\theta} + 2 \cdot m \cdot \xi_m(t) \cdot \dot{\xi}_m(t) \dot{\theta} - g \cdot S_{CG} \cdot \sin(\theta) + m \cdot g \cdot \xi_m(t) \cdot \cos(\theta) = Q_{damp}(t) + Q_{fluid}(t) \quad (7.1)$$

$$Q_{damp}(t) = -K_{df} \cdot \text{sign}(\dot{\theta}) - B_\theta \cdot \dot{\theta} \quad (7.2)$$

Where :

- $\theta[\text{rad}]$  is the roll angle.
- $g[m/s^2]$  is the gravitational acceleration.
- $I_0[Kg \cdot m^2]$  is the polar moment of inertia of the rigid system with respect to the rotation axis.
- $m[Kg]$  is the mass of the moving weight.
- $\xi_m(t)[m]$  is the instantaneous (imposed) position of the excitation weight along the linear guide (tank-fixed reference system).
- $\dot{\xi}_m(t)[m/s]$  and  $\ddot{\xi}_m(t)[m/s^2]$  are the first and second time derivatives of  $\xi_m(t)[m]$ .
- $S_{CG} = M_R \cdot \eta_G[Kg \cdot m]$  is the static moment of the rigid system with respect to the rotation axis.
- $M_R[Kg]$  is the total mass of the rigid system.
- $\eta_G[m]$  is the (signed) distance of the centre of gravity of the rigid system with respect to the rotation axis (tank-fixed reference system).
- $Q_{damp}(t) = -K_{df} \cdot \text{sign}(\dot{\theta}) - B_\theta \cdot \dot{\theta}$  is the assumed form of roll damping moment comprising:
  - A dry friction term  $-K_{df} \cdot \text{sign}(\dot{\theta})$  with  $K_{df} [N \cdot m]$  being the dry friction coefficient.
  - A linear damping term  $-B_\theta \cdot \dot{\theta}$  with  $-B_\theta [N \cdot m/(rad/s)]$  being the linear damping coefficient.
- $Q_{fluid}(t)$  is the moment due to fluid action.

By using a set of inclining tests as well as decay tests, the unknown parameters can be determined, including the natural frequency  $\omega_0$  of the rigid system. The values of these parameters can be found in table 7.3.

Table 7.3: Mechanical parameters of the rigid system

| Quantity   | Units               | Value |
|------------|---------------------|-------|
| $S_{CG}$   | $Kg \cdot m$        | -29.2 |
| $I_0$      | $Kg \cdot m^2$      | 26.9  |
| $K_{df}$   | $N \cdot m$         | 0.540 |
| $B_\theta$ | $N \cdot m/(rad/s)$ | 0.326 |
| $\omega_0$ | $rad/s$             | 3.26  |

#### 7.2.4 Analytical model assessment (without fluid)

Before going to the simulation of the behavior of the rigid system coupled with a fluid in the tank, it is worth checking the simulation capabilities of model 7.1 when the fluid is absent. In absence of fluid, the model 7.1, with the damping term 7.2 reduces to the equation 7.3.

$$[I_0 + m \cdot \xi_m^2(t)] \cdot \ddot{\theta} + 2 \cdot m \cdot \xi_m(t) \cdot \dot{\xi}_m(t) \cdot \dot{\theta} - g \cdot S_{CG} \cdot \sin(\theta) + m \cdot g \cdot \xi_m(t) \cdot \cos(\theta) + K_{df} \cdot \text{sign}(\dot{\theta}) + B_\theta \cdot \dot{\theta} = 0 \quad (7.3)$$

where the parameters that will be used are those reported in table 7.3. In the case of decay tests,  $m = 0$ , whereas in the case of forced rolling tests, the motion of the shifting mass  $m$  is imposed during each experiment. Hence,  $\xi_m(t)$ ,  $\dot{\xi}_m(t)$  and  $\ddot{\xi}_m(t)$  are known functions of the time. To be more precise  $\xi_m(t)$  is directly measured, whilst  $\dot{\xi}_m(t)$  and  $\ddot{\xi}_m(t)$  are obtained from numerical derivation after fitting a least square cubic spline to the moving weight motion signal in order to mitigate the noise influence in the derivatives.

#### Free decays without fluid: comparison between simulations and experiments

Figures 7.4 and 7.5, shows a comparison between an experimental decay and a simulated decay using the parameters reported in 7.3. The agreement is excellent in the range of roll angles above about 2-3 deg. For smaller oscillations the assumed damping model overestimates the actual damping of the system, hence the simulated time histories are slightly over-damped in the tail region. A better modeling of the friction damping or a modification of the damping characteristics of the system would be therefore necessary in the case of interest in the region of small amplitude roll motions.

#### Forced roll without fluid: comparison between simulations and experiments

A series of tests with the empty tank and the moving mass have been performed in order to check the capability of the model in equation 7.1 to reproduce the experimentally

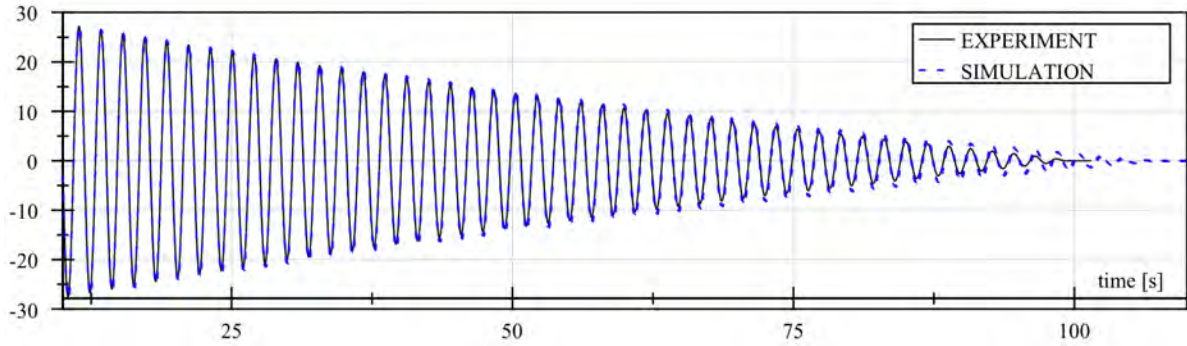


Figure 7.4: Comparison between experimental and simulated free decay angles (complete curve)

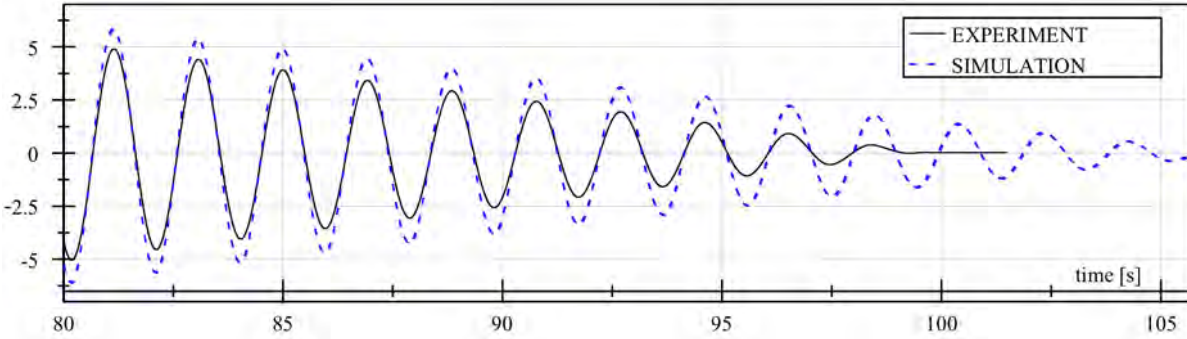


Figure 7.5: Comparison between experimental and simulated free decay angles (curve tail)

measured rolling motion of the system. The test matrix was described in table 7.1. It is extremely important to note that due to technical limitations in the control of the instantaneous position  $\xi_m(t)[m]$ , the motion  $\xi_m(t)[m]$  of the sliding mass is periodic with period  $T_{osc}$  but not purely sinusoidal. Instead, each period of  $\xi_m(t)[m]$  is obtained by joining, approximately, four parabolic branches. The actual position  $\xi_m(t)[m]$  of the sliding mass is measured during each experiment. See figure 7.6 for an example of the sliding mass motion curves.

## 7.3 Results

### 7.3.1 General

The natural period of the system is approximately 1.927s. The liquid height has been chosen so that the first sloshing period obtained from the linear theory will also be 1.927s. The most interesting cases correspond to the resonance ones, and in particular those for which the differences between the three fluids in the dampening effects are worth noting,



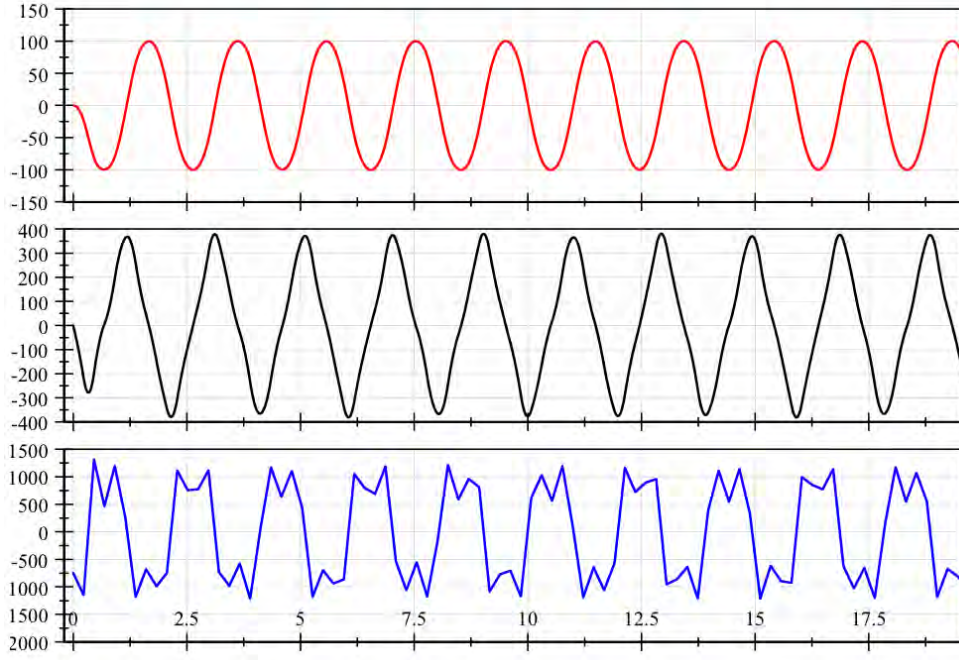


Figure 7.6: Empty tank:  $A = 100\text{mm}$ ,  $\omega = 0.9\omega_0$ ,  $\xi_m(t)$  (top),  $\dot{\xi}_m(t)$  (middle),  $\ddot{\xi}_m$  (bottom)

which correspond to the smallest moving mass amplitudes: 50mm and 100mm. Therefore the resonance cases are the scope of this chapter. For 50mm the roll angles are large enough to obtain results of reasonable accuracy. However, for these cases inaccuracies have been observed concerning the modelling of damping, and such inaccuracies could have influenced also the results from simulations. Therefore, the 100mm amplitude cases will be in principle the ones that merit further study. The resonance cases of higher amplitudes show in turn other important features, like for instance that some fluids are able to limit the structure motions whilst others, due to their viscosity, do not provide under the same conditions enough damping to put an upper limit the roll angle in resonance conditions. This will be later described.

### 7.3.2 Case Selection

In the resonance tank tests, for some of the combinations between the liquids and the sliding mass motion amplitudes, the structural damping was not enough to stop the growth of the roll angle before reaching the device limit (45 deg). One variable that will be discussed is the reduction ratio in amplitude between the partially filled tank and the empty tank roll angles (percentage) in a specific period of time. A ratio close to 100% will mean that the liquid has no dampening effect. A ratio close to 0%, will mean that the resulting amplitude

Table 7.4: Amplitude reduction ratio ( amplitude partially filled tank / amplitude empty tank)

| Amplitude | 50mm | 100mm | 150mm | 200mm |
|-----------|------|-------|-------|-------|
| Glycerin  | 28.4 | 43    | 58.7  | 66.2  |
| Oil       | 13.1 | 31.4  | 51.4  | 61.9  |
| Water     | 6.4  | 23.6  | 46.7  | 59.3  |

is very small. The ratio will be established taking the maximum values of the partially filled tank roll angle and the empty tank roll angle. The values of this reduction ratio are reported in table 7.4. The differences in this ratio for the three liquids are most substantial for the small amplitude cases, as expected. The 100mm amplitude case, which is the most significant will be described firstly, followed by the 50mm case. Cases are chosen to avoid the growth of the roll angle up to the established reaching device limit (45 deg) as happen in cases such the 150mm and 200mm amplitude, nevertheless their results are reported in table 7.4.

### 7.3.3 Amplitude=100 mm

In this case, the reduction ratio ranges from 23.6 for water to 43 for glycerin (table 7.4, analysis performed from 0 to 35s, end time in the empty tank experiment). The time evolution of the roll angle can be appreciated in figure 7.7 where it can be also appreciated that the tank roll angle is bounded for the three liquids (oil falls between water and glycerin case). There is a substantial difference between water and glycerin and the dynamics are

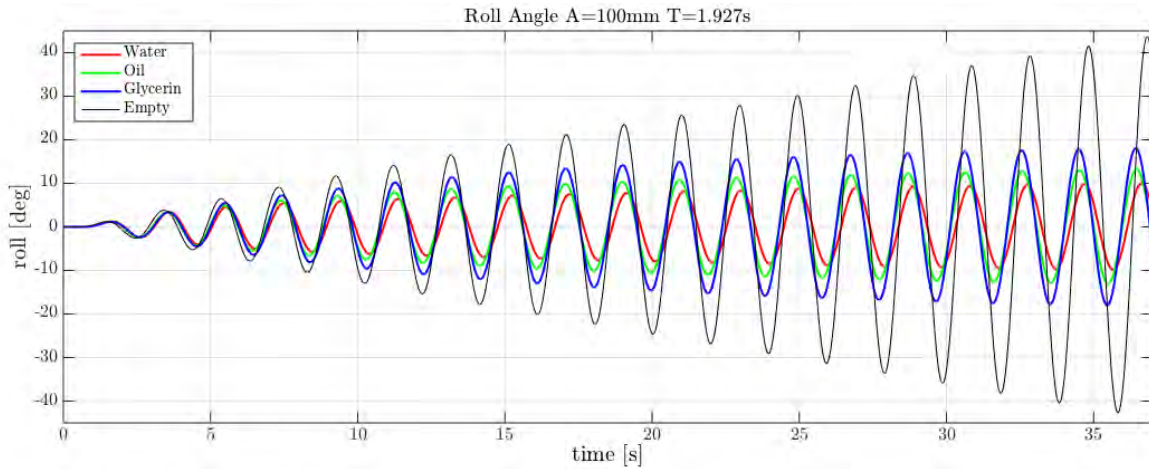


Figure 7.7: Roll angle,  $A = 100mm$ ,  $\omega = \omega_0$

quite different as well, as can be seen in figure 7.8(bottom and top) where the time is referred to the first sloshing period  $T_0$ . The glycerin gets stuck on the methacrylate wall after the wave passage which makes the visualization of its motion more difficult. On the other hand, there is not such a big difference between the global dynamics of the oil and water cases, but the differences in the dampening characteristics are very substantial. As can be appreciated in figure 7.8, in the water case there is the formation of a bore that will develop into a a plunging breaking wave, whilst in the oil case, a mild spilling wave is formed with presumably significantly less dissipation (see also figure 7.9). A specific dye was used for the sunflower oil instead of the fluorescein used for water and glycerin and that cannot be dissolved in oil. This is the reason for the different shade of the oil picture in figures 7.8 and 7.9.

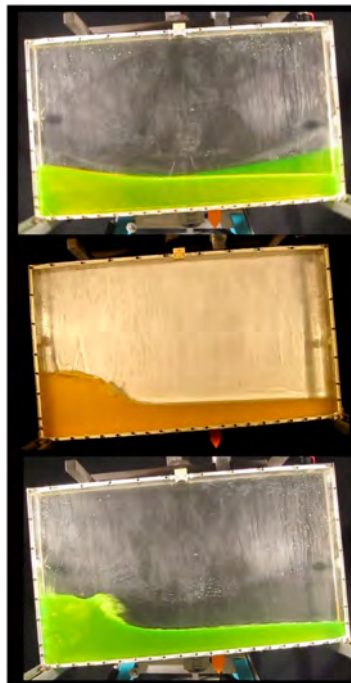


Figure 7.8: Nominal maximum shift 100mm, nominal oscillation period 1.927s.  $t/T_0=8.66$ . Glycerin (top), oil (middle), water

### **Amplitude=50 mm**

In figure 7.10 it can be also appreciated that the tank motion is limited by the three liquids. The difference in the damping characteristics of the three liquids is remarkable in this case. The values of the roll reduction ratio for this case are reported in table 7.4, the reduction ratio ranges from 6.4 for water to 28.4 for glycerin.

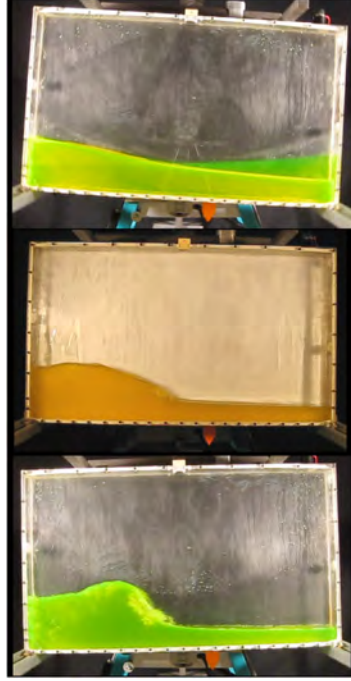


Figure 7.9: Nominal maximum shift 100mm, nominal oscillation period 1.927s.  $t/T_0=8.85$ . Glycerin (top), oil (middle), water

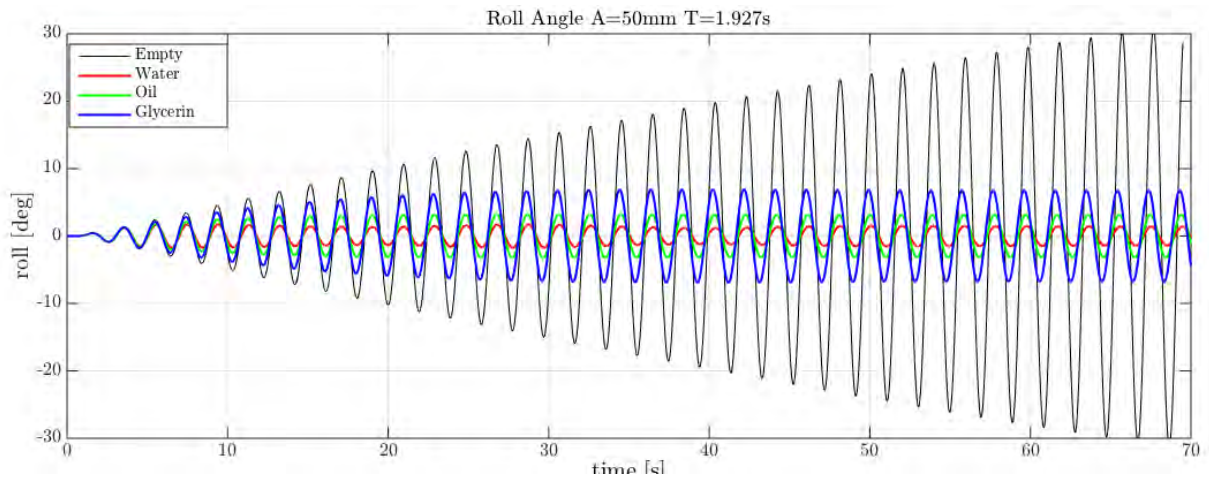


Figure 7.10: Roll angle,  $A = 50mm$ ,  $\omega = \omega_0$

## 7.4 Summary

The roll motion response of a single degree of freedom (SDOF) structural system to which a rigid rectangular partially filled liquid tank has been attached has been considered. The SDOF system has been described analytically and this description tested experimentally

by applying to the system periodic excitations, finding that the response is accurately reproduced by the model which enables this model to describe analytically the rigid system. Only some small deviations between the model and the experiments at small angles have been detected. A better modeling of the friction damping for the rigid system would be necessary in the case of interest in the region of small rolling amplitudes. Another option would be to modify the system in order to reduce the damping. The derivatives of the periodic excitations have been obtained after filtering the original signal. The effect of the type of filtering in the final results seems negligible but a detailed assessment of this matter remains for future research.

The tank performance as a tuned liquid damper (TLD) has been assessed experimentally and will serve as basis for future numeric validations of CFD and SPH software. In order to characterize the wave breaking effects on the response curves, tests have been performed with liquids of different viscosity, the increasing viscosity preventing the onset of breaking waves. It is not completely clear how to exactly quantify the influence of wave breaking on the damping characteristics of the three liquids in the cases studied in this chapter. Nevertheless, from the analysis of the experiments described it seems substantial.

The work presented in this chapter has dealt with a very controlled situation, with a simple dynamical system that can be analytically modeled with a level of accuracy such that the underlying analytical model for the dynamic system can be considered practically "exact" in engineering terms. According to this, the majority of the possible discrepancies between experiments and simulations with the partially filled tank have to be attributed to the simulations (apart from the case of small amplitude oscillations where the inaccurate modeling of damping could have been a not negligible source of differences).

# Chapter 8

## Fluid Structure Interaction (FSI)

### 8.0.1 General

FSI simulations have become more popular recently due to the availability of sufficient computer power, together with the maturity of the tools for CFD analysis, as a way to the simulation of flow problems of increasing complexity such the ones present during the sloshing phenomena covered mainly by experiments. Nevertheless FSI problems needs a experimental support in order to validate the results. Therefore FSI canonical cases, due to their reduced complexity and easy implementation, are emerging as the key of the connection between numerical and experimental solutions. In the literature, there are several comparisons between canonical experiments and numerical solutions for FSI problems involving engineering applications such FSI sloshing flows and FSI dam break problems.

FSI Sloshing flows can be found in the interaction of impact waves towards vertical walls located in coastal constructions or the walls and the pump-towers inside the LNG tanks, several works following this outline can be found in the literature. An interesting study was presented by Hattori et al. (1994). In this work a 35 mm thickness plastic plate is subject to different types of breaking waves generated in a flume water channel, for every case the resulting impact pressure is registered and compared. This provides a detailed information about the structural response of the plate under different kind of impact waves. Following the same outline more recent studies such the first full scale sloshing experiments involving a real LNGC membrane containment system subject to action breaking waves is presented by Kaminski and Bogaert (2009); Bogaert et al. (2010); Lafeber et al. (2012). In this extensive research, documented in several papers, different kinds of sloshing flows (aerated, air pocket, flip-trough and slosh) were generated in an unidirectional flume tank interacting with a LNGC flat (NO96) and corrugate plate (MarkIII), both designed by GTT. Several measurements such global forces on the membranes, pressure distributions and flow shape is provided by this study together with the hydroelastic response of the structure.

FSI dambreak problem is considered as another novel case used for numerical validations. In 1999, Zhou et al. (1999) validated their numerical scheme using an experimental work performed at the Maritime Research Institute of the Netherlands (MARIN) that provided a description of dam break wave kinematics as well as the data of a wave impact on a solid vertical wall downstream from the dam. Measurements of impact pressure at several locations were performed by force transducers with large diameter circular impact panels. The details on the experimental setup and applied force transducers were published in the work of Buchner (2002). The MARIN experimental setup was also used in the work of Wemmenhove et al. (2010) and Kleefsman et al. (2005). The former repeated and slightly altered the experiments of Lee et al. (2002) and the latter, Kleefsman et al. (2005), presented a fully three-dimensional FSI dam break problem.

An elementary research on FSI dam break problems was also conducted by Bukreev and colleagues (Bukreev, 2009; Bukreev and Zykov, 2008) who studied the overall forces exerted by the dam break wave on downstream vertical structures. A similar test case was studied by Gomez-Gesteira and Dalrymple (2004) and by Greco et al. (2012b) in order to validate their computational model. Besides describing and predicting the flood events, understanding the dynamics of dam break flows is also useful when assessing certain types of impact flows, such as those found in slamming and green water events (Greco et al., 2004, 2012a).

FSI sloshing flows and FSI dam break problems, well covered by several studies as previously mentioned, provide useful information for CFD validations by treating the interaction between different kind of flows and supposed rigid structures. Numerical comparisons following the canonical experiments presented in this chapter can be found in Yang et al. (2012); Liao and Hu (2013); Idelsohn et al. (2008); Degroote et al. (2010); Paik and Carica (2014). A benchmark case <sup>1</sup>, was proposed during 2010 in SPHERIC congress as a tool for numerical validations of SPH/CFD codes.

## 8.1 Experimental Setup

The experiments of the present chapter have been performed for a rectangular tank, following the same manufacturing process but slightly smaller than the one used for the test cases of the chapters 5 and 6, by using the testing rig facilities at UPM detailed in chapter 4. The rotation center match with the geometric center of the bottom of the tank, the coordinate system can be found in figure 8.1. The amplitude of the angular motion is 4 deg whilst the period can be regulated, aimed at matching the critical sloshing frequencies for different filling levels.8.2

---

<sup>1</sup> The main materials of this chapter is linked with the following paper: Botia-Vera, E., Souto-Iglesias, A., Bulian, G., and Lobovsky, L. (2010). Three SPH Novel Benchmark Test Cases for free surface flows. In 5th ERCOFTAC SPHERIC workshop on SPH applications.

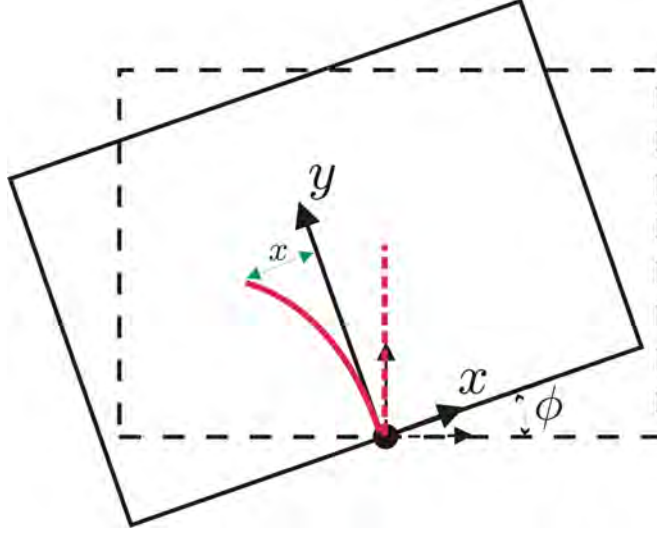


Figure 8.1: Coordinate system

Table 8.1: Physical properties (units SI) of the liquids:  $\rho$  for density,  $\mu$  for the dynamic viscosity,  $\nu$  for the kinematic viscosity,  $\sigma$  for surface tension

|       | $\rho$ | $\mu$   | $\nu$   | $\sigma$ |
|-------|--------|---------|---------|----------|
| Water | 998    | 8.94e-4 | 8.96e-7 | 0.0728   |
| Oil   | 900    | 0.045   | 5e-5    | 0.033    |

The liquids used in the experiments can be considered Newtonian at standard testing conditions and their physical properties are presented in table 8.1 Two liquid levels are considered 57.4 mm and 114.8 mm, for both water and oil. The first sloshing period referred to the corresponding filling level can be obtained from the shallow water dispersion relation in equation 8.1.

$$T_0 = 2\pi \sqrt{\frac{\pi g}{L} \tanh\left(\frac{\pi H}{L}\right)}^{-1} \quad (8.1)$$

The level of the clamped elastic beam immersed in a shallow depth oil and hanging elastic beam is  $H=57.4\text{mm}$  8.2, the breadth is  $L=609\text{ mm}$ , thus, the first sloshing period by using 8.1 is  $T1=1.646s$ . In the clamped elastic mid depth oil the filling level is  $H=114.8$ , the breadth is  $L=609\text{mm}$  and the sloshing period found using the equation 8.1 is  $T1=1.211s$ .

The container is closed in the upper wall, but two holes were made on the top in or-



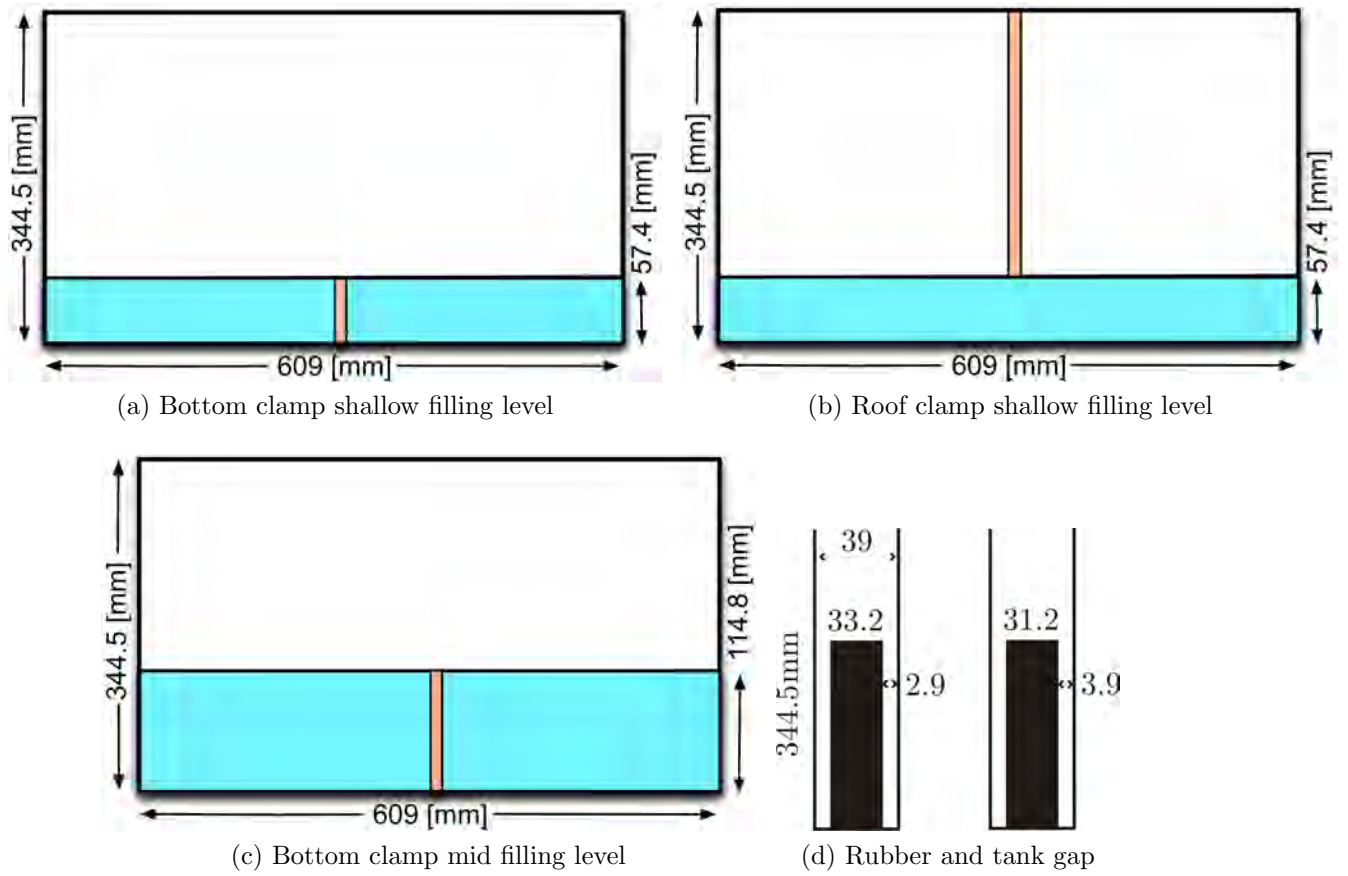


Figure 8.2: FSI tank and elastic body setup

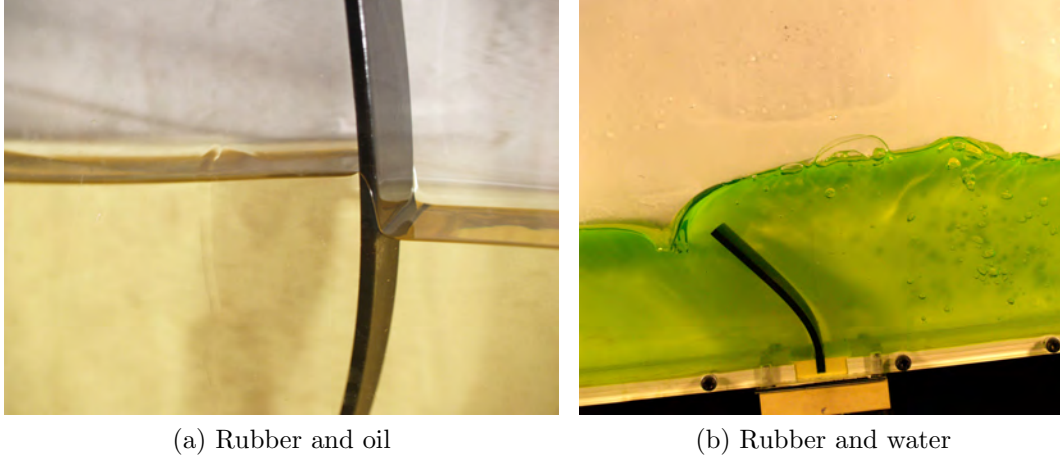


Figure 8.3: Rubber setup

der to let the air circulate freely without affecting the liquid and the solid body behavior. On the bottom wall or in the upper one, an elastic beam may be clamped to interact with the incompressible fluid. Clamped beam lengths are 57.4 mm and 114.8 mm and hanging beam length is 287.1 mm. The beams used have a thickness of 4 mm and a width of 33.2 mm which is enough to simulate a 2D flow without touching the lateral walls. The minimum admissible gap was found to be 2.9 mm for the longest configuration of the probes (287.1 mm). It would be desirable to have a smaller gap with the tank walls but due to the flexibility of the material, the rubber beam is prone to slightly bend on the front direction driven by capillarity and surface tension effects, thus touching the tank walls and invalidating the experiment. On top of this, it was discovered that smaller gaps made it extremely difficult the positioning of the clamp anchorage. Another rubber band with a wider gap was also tested in the same conditions and for every experiment the bands were placed in both symmetric configurations, to find no significant variations in the body displacements. An image of the fitting of the rubber inside the tank can be found in figure 8.2.

Figure 8.3 shows the clamped rubber to the bottom of the tank in both cases, oil and water. The properties of the rubber are summarized in table 8.2 (clamped rubber) and in table 8.3 (hanging rubber).

## 8.2 Results

A quantitative comparison between experimental results and simulations is based on the measurement of displacements of specific points at the elastic beam from their original positions. The displacement is measured in a local coordinate system of the tank. A com-

Table 8.2: Clamped rubber properties

| TYPE                          | POLYURETHANE RESIN, AXSON RE 11820-(9) |
|-------------------------------|--|
| X THICKNESS                   | 4 mm                                   |
| Y HEIGHT                      | 57.4 mm, 114.8 mm.                     |
| Z WIDTH                       | 33.2 mm (2.9 mm single gap).           |
| DENSITY                       | 1.10 gr/cm <sup>3</sup>                |
| YOUNG MODULUS (initial slope) | approx. 0.0033 GPa.                    |

Table 8.3: Hanging rubber properties

| TYPE                          | COMMERCIAL NEOPRENE          |
|-------------------------------|------------------------------|
| X THICKNESS                   | 4 mm                         |
| Y HEIGHT                      | 287.1 mm.                    |
| Z WIDTH                       | 33.2 mm (2.9 mm single gap). |
| DENSITY                       | 1.9 gr/cm <sup>3</sup>       |
| YOUNG MODULUS (initial slope) | approx. 0.004 GPa.           |

puter program using Labview vision assistant tool was implemented aimed at measuring the total displacement of the elastic beam at different heights. The program facilitates the analysis of the individual frames obtained from a conventional 25 FPS video register of the experiment. For the short beam cases 8.4 8.5, only the displacement of the end-point of the cantilever was measured. For the case with a long beam 8.6 where several bending modes appear, displacements have been measured at several points marked on the beam front. The elastic beam deformation is provided in conjunction with the roll motion and video registers for each case. Beam motion is accompanied with its corresponding derivative which is useful for any numeric simulation codes. The results discussions are :

- Clamped elastic beam immersed in a shallow and mid-depth oil: The first two experiments concern a clamped beam of different length immersed in sunflower oil. The bar length is exactly the same as the liquid depth which is 57.4 mm in the first case and 114.8 mm in the second one. Displacements of beam tip for both cases can be seen in figures 8.4 and 8.5. The beam deformation of the shallow case is small (between 6-10) as can be notice in figure 8.4, deformation shows a good behavior but seems not to be completely repeatable and symmetric even during the stationary regimen, in fact, this is due to some pre deformation of the beam in conjunction with some material hysteresis. Beam deformation period is at the same order of the angular motion of the experiment, this behavior is similar to the mid case as can be seen

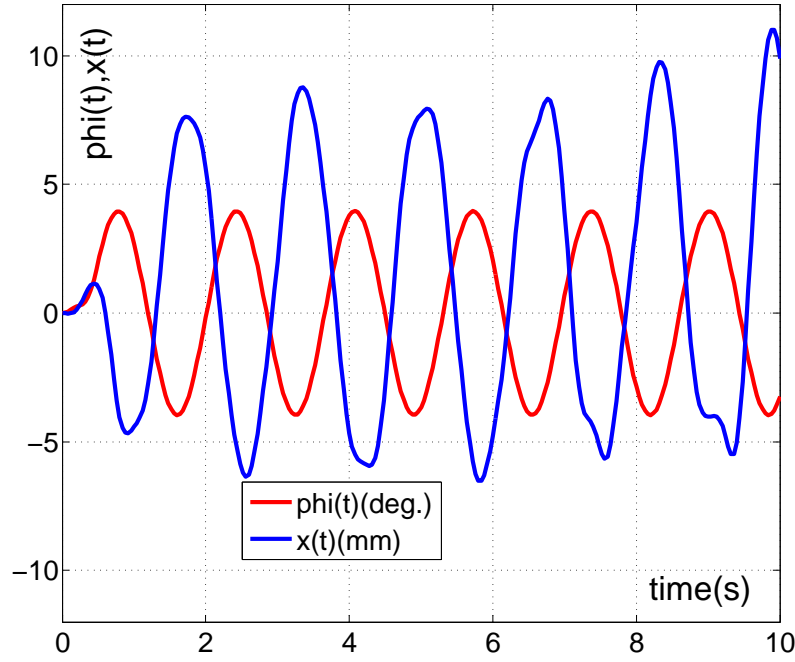


Figure 8.4: Clamped shallow oil

in figure 8.5 where also the repeatability and symmetry increase according to larger beam deformations.

- Hanging elastic beam with shallow water: This is the most difficult case. The beam is hanging from the upper wall in such a fashion that the interaction with the fluid can be attained only due to the waves generated during the motion. Otherwise there is no interaction between the beam and the fluid, since the length of the beam (287.1 mm) is supplemental with respect to the liquid depth (57.4 mm) and the tank height. Since several deformation modes develop, the motion of the beam is described using the displacements of points at 0.25, 0.5, 0.75 of the beam length and its tip (8.5).

There seem to be several uncertainties to be bound in this experiment. They have their origin on the gap effect in terms of the two-dimensionality of the case. Measurement of the displacement means around 2mm uncertainty. Dimensioning the solid body is also not trivial due to its flexibility. It is not completely stable in its long configuration due to own weight, etc. For the moment all these considerations have been discarded, waiting for an ampler experimental campaign focused on addressing these and other issues. There is work in progress regarding this test case, that will be included in future revisions of this experiment . It will comprise an experimental campaign with linear materials, mainly calibrated metals and PIV measurements.

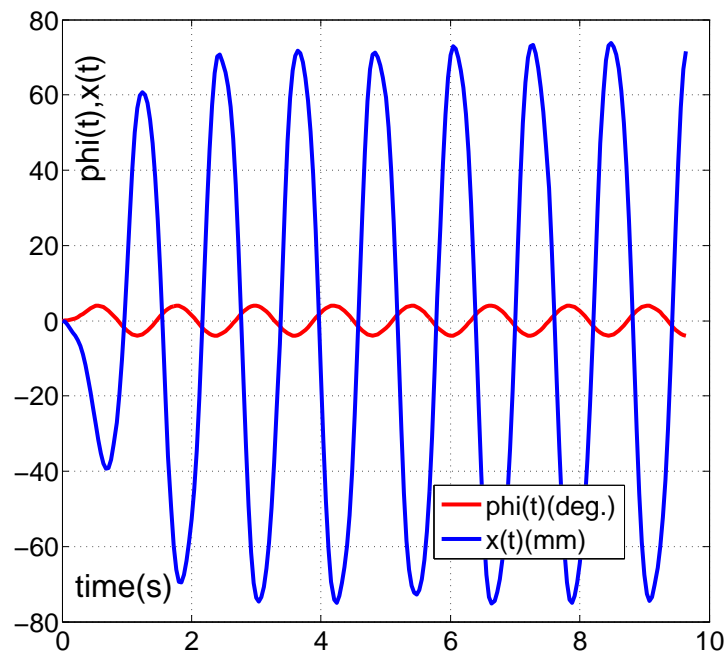


Figure 8.5: Clamped mid oil

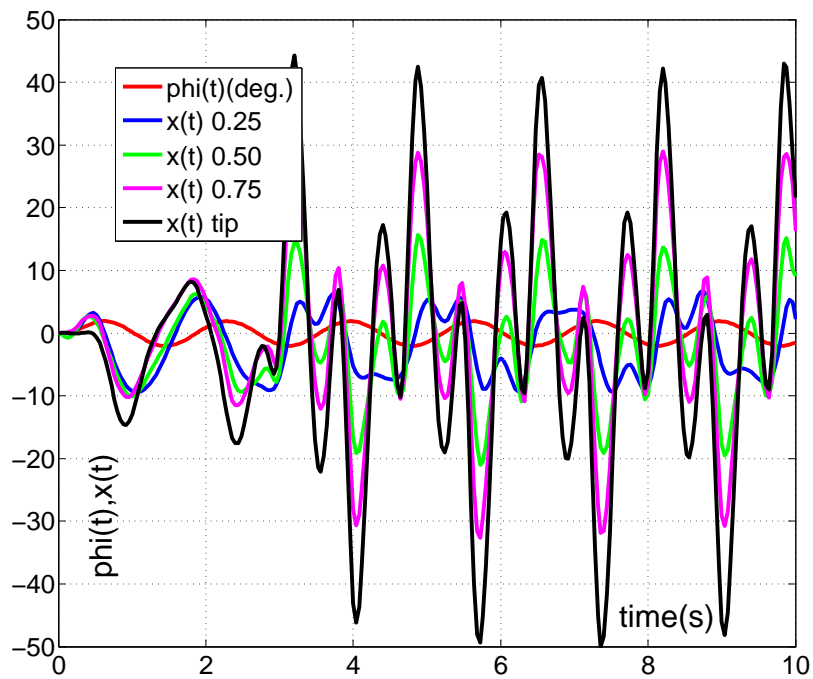


Figure 8.6: Hanging shallow water

### 8.3 Summary

A series of new experimental tests have been presented in this chapter aimed at providing data for the validation of FSI codes. The experiments have tried to document the interaction of confined sloshing flows with the deformations of elastic bars that interact with the free surface flows. The experiments show that the presence of the free surface is critical for some of the cases because on one hand the elastic body is a crucial factor in the wave amplitude response, and also the free surface waves can be crucial in the excitation of deformations in the bar for certain cases.

FSI problems are expected to evolve intensely in the near future. In wave impact problems, the interaction with the deforming container is crucial to assess the practical effects of peak pressure events. Since this case aims at serve as good validation tool for 2D codes, the 2D nature of the case will be assessed by studying deformations with thicker containers and a range of gaps. Like in the wave impact problems, it is important to perform PIV measurements of the velocity field together with wave elevation; it seems a lot of vorticity is shed from the bar tips onto the flow. A precise definition of the materials under analysis is also necessary for the future characterization of their viscoelastic behavior. Tests using materials with a linear elastic behavior (e.g. steel bars) are also under consideration.

# Chapter 9

## Conclusions

### 9.1 Conclusions

A summary of conclusions of the research work carried out during this Phd thesis follows:

1. Experimental work on selected sloshing canonical cases and subsequent statistical analysis have been the main topic of this thesis.
2. The experimental work covered by this thesis is mainly related to fluid dynamics phenomena screening in partially filled tanks in LNG carriers.
3. Due to the complexity of the sloshing phenomenon, and in order to try to understand the importance of the different factors that define this phenomenon, a simple configuration for the analysis has been chosen.
4. Such configuration has consisted on a rectangular tank subjected to a one degree of freedom angular motion.
5. The angular motion was imposed by a 1DOF sloshing rig specifically setup for this thesis.
6. A dedicated software for the data acquisition, post processing and statistical treatment has been developed.
7. With this configuration several problems have been investigated, progressively increasing their complexity.
8. The first problem investigated has been sloshing induced by a periodic harmonic forced motion, leading to lateral impacts. Pressure was measured with state-of-the-art miniature sensors.
9. A series of more than 100 experiments, each comprising more than 100 impact events has been conducted, seeking the highest feasible repeatability.

10. Even under regular repeatable excitations and exogenous disturbances control, the pressure impact at each impact event was characterized by a high cycle-to-cycle and run-to-run variability. Therefore, the analysis of regular impact pressure inevitably required making use of statistical tools treating the problem as a stochastic process.
11. It was demonstrated that the type of the sensor (piezo-electric or piezo-resistive) had a minor influence in the recorded pressure impact.
12. For the selected condition, a transient stage, having a length of about 5-10 impacts was identified by looking at the behaviour of the ensemble mean and standard deviation of the impact pressure through a systematic application of KS2 tests.
13. Removing the initial transient data was found necessary in order to provide a clean stationary sample for the analysis.
14. The achievement of a subsequent stationary stage after the 5-10 impacts, justifies the implicitly assumption of practical ergodicity.
15. Both single (long) experiment and single impact ensemble samples were considered equivalent from the statistical point of view. This justifies indeed the assumption of practical ergodicity.
16. The selected lateral impact pressure process was considered as "practically ergodic". This implies that the statistical characteristics of the process can be obtained from a single, "sufficiently long", experiment realization.
17. The thorough description of the whole experimental setup makes the presented data suitable for comparison purposes and for validation of theoretical/numerical approaches.
18. The second problem that has been investigated consisted in carrying more general motions, namely, those obtained from the realization of a roll motion spectrum, leading to irregular motion time histories which mimic more realistic scenarios than forced harmonic motion tests.
19. The irregular motion sloshing impact impacts analysis considered aspects that had not been treated in the literature such as the sensitivity of the extreme value distribution to different realizations of the same motion spectrum and variations in the underlying motion RAO's which lead to differences in the motion spectrum components.
20. Two statistical models (Weibull and Pareto) have been used in order to fit the recorded impact pressure samples of the selected sensors and the extreme values (EV) for different return periods were obtained. Both models have been able to accurately fit the recorded pressure of long duration tests.



21. The KS2 test, applied to the empirical distributions of the cases corresponding to different realizations of the same spectrum, rejects in all the cases the hypothesis of equal underlying distributions at  $\alpha = 5\%$ .
22. With the recorded impact pressures, induced by the variations in the driving motion due to modifications in the motion spectrum, the KS2 applied to the empirical distributions, rejects in all the cases the hypothesis of equal underlying distributions at  $\alpha = 5\%$ .
23. The third problem that has been dealt with, investigates the coupling motion of a SDOF system excited by an external moment which affects the fluid dynamics and the mechanical energy dissipation.
24. The sloshing rig was specifically modified in order to provide a free SDOF angular motion.
25. The SDOF system has been described analytically and contrasted experimentally, finding that the response is accurately described by the analytic model.
26. Experiments has been performed with fluids of different viscosity.
27. In all the cases, the selected fluid acts as a damper of the roll motion, with this capability influenced by the fluid viscosity. In this sense, the water damping characteristics were remarkable.
28. The work presented on this coupled system, has dealt with a very controlled situation, for which an analytical model and experimental results was provided, making this work ideal for CFD-SPH and general numerical validations.
29. The last problem that has been studied is the interaction between sloshing flows inside a rectangular tank and elastic clamped bodies.
30. A series of new experimental tests have been presented in this chapter aimed at providing data for the validation of FSI codes.
31. The experiments show that the presence of the free surface is critical for some of the cases because on one hand the elastic body is a crucial factor in the wave amplitude response, and also the free surface waves can be crucial in the excitation of deformations in the bar for certain cases.

## 9.2 Future work

Regarding the experimental setup although the experimental setup of the UPM sloshing rig has been improved in several ways, for a better understanding of the sloshing phenomena it would be necessary to perform some hardware improvements as follows:

1. Extend the DOF of the sloshing rig in order to achieve a more realistic scenario (6DOF). The most available in the market and widely used by other facilities is the 6DOF *Stewart-Gough* platform, which is able to reproduce the 6DOF translations and rotations (surge, sway, heave, roll, pitch and yaw).
2. The number of pressure sensors has to be increased in order to cover more tank areas and therefore obtain a more detailed information about the pressure distribution in the critical zones of the LNG tanks.
3. Together with the 6DOF platform, 3D scaled sloshing tanks have to be built in order to achieved a more realistic LNG fluid dynamics.
4. A pump system would be necessary in order to pressurize/depressurize the tanks and therefore modify the density ratio between the liquid/gas phase.

Further research along the line described in the chapter 5 (forced regular motion sloshing) should be aimed at applying the proposed methodology to a wider set of cases under regular excitation (different filling levels, excitation frequencies, amplitudes of forcing, etc.), to identify the presence of possibly different behaviours for the impact pressure, when considered as a stochastic process. Of particular interest, from the point of view of ensemble domain analysis, are likely to be those cases with free surface dynamics showing complex behaviour, beating, long transients, etc. (Faltinsen and Timokha, 2000; Faltinsen et al., 2006; Forbes, 2010). In such context, to have a better overall understanding of the phenomenon, it would also be useful to try correlating the results of the statistical analysis of impact pressure with free surface measurements. Further investigations should also focus on the possible role of the hydrodynamic damping in shaping the transient behaviour of the pressures ensemble statistics. Further research have to be carried out following the line described in chapter 6 (forced irregular motion sloshing) for which and extensive statistical study have to carried out in order to get a better understating of the influence in the peak pressure collection and fitting, due to the selected sensitivity parameters. It was noticed that the statistical fitting, specifically the *Pareto* fitting is highly sensible to the threshold selection when the POT method is applied. The quantile ( $q=0.87$ ) was selected by following the work of Graczyk et al. (2006), nevertheless a deep study regarding this quantile selection has to be carried out and its influence in the extreme values calculation must to be assessed. Further investigations should also focus on the study of new sensitivity parameters such variations in the filling level, tank misalignments, vibrations etc, type/brand of sensors, etc. Another interesting topic deserving attention is the idea of establish a statistical procedure to find the minimum number of irregular experiments

that are necessary in order to achieve similar statistical results as those obtained in large number of repetitions, in such context , the idea of the ergodicity applied in the chapter 6 has to be carefully extended from regular to irregular excitations.

Taking into account the good agreement of the results obtained in the chapter 7 (coupled sloshing and angular motion), which can be considered in general, good, there are still some improvements which could serve as a practical tool for the assessment of tanks' performances. The future work that could be followed along this path is:

1. Introduction and consequent experimentation / simulation of cases with the tank equipped with baffles as dissipation means.
2. Implementation of a mathematical model for ship motions. In such case, the numerical model could be used as a means to study, e.g., the effect of water on deck, in addition to the study of anti-rolling tank devices. Moreover, effects like parametric excitation induced by vertical ship motions on the fluid could also be studied. Another interesting topic deserving attention are the fluid impact effects due to the fluid sloshing in a tank coupled with the ship motions.

Further research have to be carried out following the line described in chapter 8 (fluid structure interaction) for which an extensive experimental approach of the FSI problem have to be performed by adding recent experimental measurement techniques and post-processing analysis. The future work can be summarized as:

1. It would be interesting to analyze more deeply the two-dimensionality of the case studies by checking the deformations with broader containers and by providing more accurate data regarding the dependance of the deformed bar shapes and the bar gaps with the container walls.
2. It would be interesting to have PIV measurements of the velocity field. It seems a lot of vorticity is shed from the bar tips onto the flow.
3. It would be necessary to have error bounds to the different data, by performing a rigorous uncertainty analysis.

# Thesis publications

## 9.2.1 Refereed papers

1. Souto-Iglesias, A., Bulian, G., Botia-Vera, E., 2015, A set of canonical problems in sloshing. Part 2: influence of tank width on impact pressure statistics in regular forced angular motion. *Ocean Engineering*, 115, 136-159. DOI: 10.1016/j.oceaneng.2015/06/016 Impact factor/ Factor de impacto 2014: 1.351. Quartile in Category/Cuartil en categoría ENGINEERING, MARINE Q1 (1/14) ENGINEERING, OCEAN Q2 (2/14).
2. Lobovsky, L., Botia-Vera, E., Castellana, F., Mas-Soler, J., and Souto-Iglesias, A. (2014). Experimental investigation of dynamic pressure loads during dam break. *Journal of Fluids and Structure*, 48. Impact factor/ Factor de impacto 2012: 2.051. Quartile in Category/Cuartil en categoría ENGINEERING, MECHANICAL: Q1 (13/125). Quartile in Category/Cuartil en categoría MECHANICS: Q1 (17/135).
3. Bulian, G., Botia-Vera, E., and Souto-Iglesias, A. (2014). Experimental sloshing pressure impacts in ensemble domain: transient and stationary statistical characteristics. *Physics of Fluids*, 26, 3. Impact factor/2012: 1.942. Quartile in Category/ MECHANICS: Q1 (21/135). Quartile in Category/PHYSICS, FLUIDS & PLASMAS: Q2 (12/31).
4. Souto-Iglesias, A., Botia-Vera, E., Martín, A., and Pérez-Arribas, F. 2011, A set of canonical problems in sloshing. Part 0: Experimental setup and data processing. *Ocean Engineering*, 38 (2011) 1823-1830. Impact factor/2010: 0.954. Quartile in Category/ENGINEERING, OCEAN: Q1 (3/15).
5. Bulian, G., Souto-Iglesias, A., Delorme, L., and Botia-Vera, E. (2010). SPH simulation of a tuned liquid damper with angular motion. *Journal of Hydraulic Research*, vol. 48, , Extra Issue, pp: 28-39. Impact factor/2012: 1.037. Quartile in Category/ENGINEERING, CIVIL: Q2 (47/122). Quartile in Category/WATER RESOURCES: Q3 (47/80).
6. Delorme, L., Colagrossi, A., Souto-Iglesias, A., Zamora-Rodriguez, R., Botia-Vera, E., 2009, A set of canonical problems in sloshing, Part I: Pressure field in forced roll–

comparison between experimental results and SPH, *Ocean Engineering*, 36, 2, 168-178. DOI: <http://dx.doi.org/10.1016/j.oceaneng.2008.09.014>. Impact factor/2006: 0.542. Quartile in Category/ENGINEERING, OCEAN: Q1 (3/15). (already claimed as a publication of L. Delorme Phd).

## 9.2.2 Conference papers

1. Bulian, G., Botia-Vera, E., Castellana, F., Souto-Iglesias, A., and Mas-Soler, J. (2012). Repeatability and practical ergodicity of 2D sloshing experiments. In 22nd International Offshore and Polar Engineering Conference (ISOPE). The International Society of Offshore and Polar Engineers (ISOPE).
2. Souto-Iglesias, A., Botia-Vera, E., and Bulian, G. (2012). Repeatability and Two-Dimensionality of model scale sloshing impacts. In International Offshore and Polar Engineering Conference (ISOPE). The International Society of Offshore and Polar Engineers (ISOPE).
3. Botia-Vera, E., Souto-Iglesias, A., Bulian, G., and Lobovsky, L. (2010). Three SPH Novel Benchmark Test Cases for free surface flows. In 5th ERCOFTAC SPHERIC workshop on SPH applications.
4. Pérez-Rojas, L., Bulian, G., Botia-Vera, E., Cercos-Pita, J. L., Souto-Iglesias, A., and Delorme, L. (2009). A combined experimental and SPH approach to sloshing and ship roll motions. In 10th International Conference on Stability of Ships and Ocean Vehicles (STAB 2009).
5. Cheng, L. Y., Souto-Iglesias, A., Simos, A., Cercos, J. L., Tsukamoto, M. M., Endo, C. Y., Marin, M. A., and Botia-Vera, E. (2009). Hydrodynamic impact pressure computations and experiments in an LNG tank section. In Kvamsdal, T., Pettersen, B., Bergan, P., Onate, E., and Garcia, J., editors, III International Conference on Computational Methods in Marine Engineering, pages 241-244. CIMNE.

## 9.2.3 Book chapters

1. A combined experimental and SPH approach to sloshing and ship roll motions, in "Contemporany Ideas on Ship Stability and Capsizing in Waves". Springer-Sciencie+Business Media, Fluid Mechanics and its Applications Series. (2011), pp. 735-749 by Pérez-Rojas, L., Bulian, G., Botia-Vera, E., Cercos-Pita, J. L., Souto-Iglesias, A., and Delorme, L.

# Bibliography

- Abrahamsen, B. C. and Faltinsen, O. M. The effect of air leakage and heat exchange on the decay of entrapped air pocket slamming oscillations. *Physics of Fluids*, 23(10):102107, 2011. doi: 10.1063/1.3638612. URL <http://link.aip.org/link/?PHF/23/102107/1>.
- Abramson, H. N., Bass, R. L., Faltinsen, O. M., and Olsen, H. A. Liquid slosh in LNG carriers. In *10th Symposium on Naval Hydrodynamics*, pages 371–388, June 1974.
- Abramson, H. The dynamic behavior of liquids in moving containers. Technical report, NASA National Aeronautics and Space Administration, Washington D.C., 1966.
- ABS. *Strength Assessment of Membrane-Type LNG containment Systems Under Sloshing Loads*. American Bureau of Shipping (ABS), 2006.
- Akyildiz, H. and Ünal, E. Experimental investigation of pressure distribution on a rectangular tank due to the liquid sloshing. *Ocean Engineering*, 32(11-12):1503–1516, 8 2005.
- Armenio, V. and Rocca, M. L. On the analysis of sloshing of water in rectangular containers: numerical study and experimental validation. *Journal of Ocean Engineering*, 23(8):705–39, 1996.
- Armenio, V., Francescutto, A., and La Rocca, M. On the roll motion of a ship partially filled unbaffled and baffled tanks - part i: Mathematical model and experimental setup. *Int. Journ. of Offshore and Polar Eng.*, 6(4):278–282, 1996a.
- Armenio, V., Francescutto, A., and La Rocca, M. On the roll motion of a ship partially filled unbaffled and baffled tanks - part ii: Numerical and experimental analysis. *Int. Journ. of Offshore and Polar Eng.*, 6(4):283–290, 1996b.
- Banerji, P. and Samanta, A. Earthquake vibration control of structures using hybrid mass liquid damper. *Engineering Structures*, 33(4):1291–1301, 2011.
- Bass, D. Roll stabilization for small fishing vessels using paravanes and anti-roll tanks. *Marine Technology*, 35(2):74–84, 1998.

- Bass, R. L., Jr, E. B. B., Trudell, R. W., Navickas, J., Peck, J. C., Yoshimura, N., Endo, S., and Pots, B. F. M. Modeling criteria for scaled LNG sloshing experiments. *Journal of Fluids Engineering, Transactions of the ASME*, 107(2):272–280, 1985.
- Baudin E., D. L. The second ISOPE Sloshing Benchmark: Bureau Veritas Sloshing Model Tests and CFD Calculations. In *23rd International Offshore and Polar Engineering Conference (ISOPE)*. The International Society of Offshore and Polar Engineers (ISOPE), June 2013.
- Belenky, V., Suzuki, S., and Yamakoshi, Y. Preliminary results of experimental validation of practical non-ergodicity of large amplitude rolling motion. In *Proceeding of the 5th International Workshop on Ship Stability and Operational Safety, Trieste*, volume 4, pages 1–4, 2001.
- Berg, A. Scaling laws and statistical distributions of impact pressures in liquid sloshing. Technical Report no. 87-2008, Det Norske Veritas (DNV), 1987.
- Bernstein, S. and Bernstein, R. *Schaum's Outline of Elements of Statistics II: Inferential Statistics*. Schaum's Outline Series. McGraw-Hill Education, 1999. ISBN 9780071346375. URL <http://books.google.es/books?id=3LhPwUhrVICC>.
- Bogaert, H., Lacuteonard, S., Brosset, L., and Kaminski, M. L. Sloshing and scaling: Results from the Sloshel project. In *International Offshore and Polar Engineering Conference (ISOPE)*. The International Society of Offshore and Polar Engineers (ISOPE), June 2010.
- Bouscasse, B., Antuono, M., Colagrossi, A., and Lugni, C. Numerical and Experimental Investigation of Nonlinear Shallow Water Sloshing. *International Journal of Nonlinear Sciences and Numerical Simulation*, 14(2):123–138, 2013.
- BP. Statistical review of world energy 2014. *BP Global (www.bp.com)*, 2014.
- Bredmose, H., Brocchini, M., Peregrine, D., and Thais, L. Experimental investigation and numerical modelling of steep forced water waves. *Journal of Fluid Mechanics*, 490: 217–249, 8 2003. ISSN 1469-7645. doi: 10.1017/S0022112003005238. URL [http://journals.cambridge.org/article\\_S0022112003005238](http://journals.cambridge.org/article_S0022112003005238).
- Brizzolara, S., Savio, L., Viviani, M., Chen, Y., Temarel, P., Couty, N., Diebold, L., Moirod, N., and Souto-Iglesias, A. Comparison of experimental and numerical sloshing loads in partially filled tank. *Ships and Offshore Structures*, 6(1,2):15–43, 2011.
- Buchner, B. *Green Water on Ship-type Offshore Structures*. PhD thesis, Delft University of Technology, 2002. URL <http://books.google.es/books?id=RzU5SwAACAAJ>.

- Bukreev, V. Force action of discontinuous waves on a vertical wall. *Journal of Applied Mechanics and Technical Physics*, 50:278–283, 2009. ISSN 0021-8944. URL <http://dx.doi.org/10.1007/s10808-009-0037-7>. 10.1007/s10808-009-0037-7.
- Bukreev, V. and Zykov, V. Bore impact on a vertical plate. *Journal of Applied Mechanics and Technical Physics*, 49:926–933, 2008. ISSN 0021-8944. URL <http://dx.doi.org/10.1007/s10808-008-0115-2>. 10.1007/s10808-008-0115-2.
- Bulian, G. and Francescutto, A. Experimental results and numerical simulations on strongly nonlinear rolling of multihulls in moderate beam seas. *Proceedings of the Institution of Mechanical Engineers - Part M - Journal of Engineering for the Maritime Environment*, 223(3-4):189–210, 2009. doi: 10.1243/14750902JEME126.
- Bulian, G., Francescutto, A., and Lugni, C. Theoretical, numerical and experimental study on the problem of ergodicity and ‘practical ergodicity’ with an application to parametric roll in longitudinal long crested irregular sea. *Ocean engineering*, 33(8):1007–1043, 2006.
- Chen, Z., Zong, Z., Li, H. T., and Li, J. An investigation into the pressure on solid walls in 2d sloshing using SPH method. *Ocean Engineering*, 59(0):129–141, 2013. doi: <http://dx.doi.org/10.1016/j.oceaneng.2012.12.013>. URL <http://www.sciencedirect.com/science/article/pii/S0029801812004222>.
- Cheng, L. Y., Souto-Iglesias, A., Simos, A., Cercos, J. L., Tsukamoto, M. M., Endo, C. Y., Marin, M. A., and Botia, E. Hydrodynamic impact pressure computations and experiments in an LNG tank section. In Kvamsdal, T., Pettersen, B., Bergan, P., Onate, E., and Garcia, J., editors, *III International Conference on Computational Methods in Marine Engineering*, pages 241–244. CIMNE, June 2009. URL [http://canal.etsin.upm.es/files/PAPERS\\_NUESTROS/CHENG\\_ETAL\\_MARINE09.pdf](http://canal.etsin.upm.es/files/PAPERS_NUESTROS/CHENG_ETAL_MARINE09.pdf).
- Choi, H. I., Park, J. H., Kwon, S. H., Lee, K. H., Lee, S. B., and Yang, Y. J. An Experimental Study on Hydro-Elasticity in Sloshing. In *ASME 31st International Conference on Ocean, Offshore and Arctic Engineering, OMAE2012*, June 2012.
- Choi, H., Choi, Y., Kim, H., Kwon, S., Park, J., and Lee, K. A study on the characteristics of piezoelectric sensor in sloshing experiments. In *International Offshore and Polar Engineering Conference (ISOPE)*. The International Society of Offshore and Polar Engineers (ISOPE), June 2010.
- Cousineau, D. Fitting the three-parameter weibull distribution: review and evaluation of existing and new methods. *Dielectrics and Electrical Insulation, IEEE Transactions on*, 16(1):281–288, 2009.



- Degroote, J., Souto-Iglesias, A., Paepegem, W. V., Annerel, S., Bruggeman, P., and Vierendeels, J. Partitioned simulation of the interaction between an elastic structure and free surface flow. *Computer Methods in Applied Mechanics and Engineering*, 199(33-36): 2085–2098, July 2010.
- Delorme, L. *Sloshing Flows. Experimental Investigation and Numerical Simulations with Smoothed Particle Hydrodynamics*. PhD thesis, Technical University of Madrid (UPM), 2009.
- Delorme, L., Bulian, G., Mc Cue, L., and Souto-Iglesias, A. Coupling between sloshing and ship roll motion: Comparison between nonlinear potential theory and sph. In *26th Symposium on Naval Hydrodynamics, Rome, Italy*, 2006.
- Delorme, L., Colagrossi, A., Souto-Iglesias, A., Zamora-Rodriguez, R., and Botia-Vera, E. A set of canonical problems in sloshing. Part I: Pressure field in forced roll. Comparison between experimental results and SPH. *Ocean Engineering*, 36(2):168–178, February 2009. doi: 10.1016/j.oceaneng.2008.09.014.
- Diebold, L. Methodology for LNG Terminals. In *International Offshore and Polar Engineering Conference (ISOPE)*. The International Society of Offshore and Polar Engineers (ISOPE), June 2010.
- DNV. Sloshing analysis of LNG membrane tanks, classification notes, no. 30.9. Det Norske Veritas. Technical report, Det Norske Veritas, 2006.
- Eric Gervaise, Thibaut Loysel. ISOPE 2013: Benchmark on sloshing model tests. Specification of the benchmark tests, ISOPE, 2013.
- Eswaran, M., Saha, U. K., and Maity, D. Effect of baffles on a partially filled cubic tank: Numerical simulation and experimental validation. *Comput. Struct.*, 87(3-4):198–205, 2009. ISSN 0045-7949. doi: <http://dx.doi.org/10.1016/j.compstruc.2008.10.008>.
- Faltinsen, O. M. and Timokha, A. N. Asymptotic modal approximation of nonlinear resonant sloshing in a rectangular tank with small fluid depth. *Journal of Fluid Mechanics*, 470:319–357, 2000.
- Faltinsen, O. M. and Timokha, A. N. *Sloshing*. Cambridge University Press, Cambridge, UK, 2009. ISBN 13: 9780521881111.
- Faltinsen, O. M., Rognebakke, O. F., and Timokha, A. N. Transient and steady-state amplitudes of resonant three-dimensional sloshing in a square base tank with a finite fluid depth. *Physics of Fluids*, 18(1):012103, 2006. doi: 10.1063/1.2160522. URL <http://link.aip.org/link/?PHF/18/012103/1>.
- Faltinsen, O., Rognebakke, O., and Timokha, A. N. Resonant three-dimensional nonlinear sloshing in a square-base basin. *Journal of Fluid Mechanics*, 487:1–42, 2003.

- Fillon, B., Diebold, L., Henry, J., Derbanne, Q., Baudin, E., and Parmentier, G. Statistical Post-Processing of Long-Duration Sloshing Test. In *21st International Offshore and Polar Engineering Conference (ISOPE)*. The International Society of Offshore and Polar Engineers (ISOPE), June 2011.
- Forbes, L. K. Sloshing of an ideal fluid in a horizontally forced rectangular tank. *Journal of Engineering Mathematics*, 66(4):395–412, 2010.
- Francescutto, A. and Contento, G. An experimental study of the coupling between roll motion and sloshing in a compartment. *ISOPE*, April 1994.
- Frandsen, J. Numerical predictions of tuned liquid tank structural systems. *Journal of Fluids and Structures*, 20(3):309 – 329, 2005. ISSN 0889-9746. doi: 10.1016/j.jfluidstructs.2004.10.003.
- Gervaise, E., de Sgraveeze, P. E., and Maillard, S. Reliability-based methodology for sloshing assessment of membrane LNG vessels. In *International Offshore and Polar Engineering Conference (ISOPE)*. The International Society of Offshore and Polar Engineers (ISOPE), June 2009.
- Gomez-Gesteira, M. and Dalrymple, R. A. Using a three-dimensional smoothed particle hydrodynamics method for wave impact on a tall structure. *Journal of Waterway, Port, Coastal and Ocean Engineering*, 130(2):63–69, 2004. doi: 10.1061/(ASCE)0733-950X(2004)130:2(63). URL [http://dx.doi.org/10.1061/\(ASCE\)0733-950X\(2004\)130:2\(63\)](http://dx.doi.org/10.1061/(ASCE)0733-950X(2004)130:2(63)).
- Graczyk, M. and Moan, T. A probabilistic assessment of design sloshing pressure time histories in LNG Tanks. *Ocean Engineering*, 35(8-9):834 – 855, 2008. ISSN 0029-8018. doi: DOI:10.1016/j.oceaneng.2008.01.020. URL <http://www.sciencedirect.com/science/article/B6V4F-4RSJF35-2/2/eb37150124347363ad426397dcb63935>.
- Graczyk, M., Moan, T., and Rognbakke, O. Probabilistic analysis of characteristic pressure for LNG Tanks. *Journal of Offshore Mechanics and Arctic Engineering*, 128(2): 133–144, 2006. doi: 10.1115/1.2185128. URL <http://link.aip.org/link/?JOM/128/133/1>.
- Graczyk, M., Moan, T., and Wu, M. Extreme sloshing and whipping-induced pressures and structural response in membrane LNG tanks. *Ships and Offshore Structures*, 2(3): 201–216, 2007. doi: 10.1080/17445300701423049. URL <http://dx.doi.org/10.1080/17445300701423049>.
- Graczyk, M., Berget, K., and Allers, J. Experimental investigation of invar edge effect in membrane lng tanks. *Journal of offshore mechanics and arctic engineering*, 134(3): 031801, 2012.

- Graham, E. and Rodriguez, A. The characteristics of fuel motion which affects airplane dynamics. *J. Applied Mechanics*, 19:381–388, 1952.
- Gran, S. Statistical distributions of local impact pressures in liquid sloshing. *Norwegian maritime research*, 9(2):2–12, 1981. URL <http://www.scopus.com/inward/record.url?eid=2-s2.0-0019667794&#38;partnerID=40&#38;md5=538f5aab2b5f85bca6ccd2a0c84b52d9>.
- Greco, M., Landrini, M., and Faltinsen, O. Impact flows and loads on ship-deck structures. *Journal of Fluids and Structures*, 19(3):251 – 275, 2004. ISSN 0889-9746. doi: 10.1016/j.jfluidstructs.2003.12.009. URL <http://www.sciencedirect.com/science/article/pii/S0889974604000088>.
- Greco, M., Bouscasse, B., and Lugni, C. 3-D seakeeping analysis with water on deck and slamming. Part 2: experiments and physical investigation. *Journal of Fluids and Structures*, 33(0):148 – 179, 2012a. ISSN 0889-9746. doi: 10.1016/j.jfluidstructs.2012.05.009. URL <http://www.sciencedirect.com/science/article/pii/S0889974612001132>.
- Greco, M., Bouscasse, B., and Lugni, C. 3-D seakeeping analysis with water on deck and slamming. Part 1: numerical solver. *Journal of Fluids and Structures*, 33(0):127 – 147, 2012b. ISSN 0889-9746. doi: 10.1016/j.jfluidstructs.2012.05.009. URL <http://www.sciencedirect.com/science/article/pii/S0889974612001132>.
- Hattori, M., Arami, A., and Yui, T. Wave impact pressure on vertical walls under breaking waves of various types. *Coastal Engineering*, 22(1-2):79 – 114, 1994. ISSN 0378-3839. doi: 10.1016/0378-3839(94)90049-3. URL <http://www.sciencedirect.com/science/article/pii/0378383994900493>. jce:title;Special Issue Vertical Breakwaters jce:title.
- Hemer, M. A description of extreme methods. *Project report*, page 14, 2006.
- Hosking, J. R. and Wallis, J. R. Parameter and quantile estimation for the generalized pareto distribution. *Technometrics*, 29(3):339–349, 1987.
- Hummel, R., Banga, S., and Hettmansperger, T. P. Better confidence intervals for the variance in a random sample. Technical report, Department of Statistics, The Pennsylvania State University, State College, PA 16802, 2005.
- Ibrahim, R. A. *Liquid sloshing dynamics : theory and applications*. Cambridge University Press, New York, 2005. ISBN 0-521-83885-1; 978-0-521-838856.
- Idelsohn, S., Marti, J., Souto-Iglesias, A., and Oñate, E. Interaction between an elastic structure and free-surface flows: experimental versus numerical comparisons using the PFEM. *Computational Mechanics*, 43(1):125–132, December 2008.

- Kaminski, M. L. and Bogaert, H. Full Scale Sloshing Impact Tests. In *19th International Offshore and Polar Engineering Conference (ISOPE)*, pages 125–134. The International Society of Offshore and Polar Engineers (ISOPE), June 2009.
- Kareem, A., Kijewski, T., and Tamura, Y. Mitigation of motions of tall buildings with special examples of recent applications. *Journal on Wind and Structures*, 2(3):201–251, 1999.
- Karimi, M. R., Kosinski, C., and Brosset, L. Comparison of sloshing model test results at scales 1:10 and 1:40. *Proceedings of the Twenty-third International Offshore and Polar Engineering Conference, Anchorage, AK, ISOPE*, 3:224–234, 2013.
- Khayyer, A. and Gotoh, H. Wave impact pressure calculations by improved SPH methods. *International Journal of Offshore and Polar Engineering*, 19(4):300–307, December 2009. ISSN 1053-5381.
- Kim, H. I., Kwon, S. H., Park, J. S., Lee, K. H., Jeon, S. S., Jung, J. H., Ryu, M. C., and Hwang, Y. S. An Experimental Investigation of Hydrodynamic Impact on 2-D LNG Models. In *International Offshore and Polar Engineering Conference (ISOPE)*. The International Society of Offshore and Polar Engineers (ISOPE), June 2009.
- Kim, S.-Y., Kim, K.-H., and Kim, Y. Comparative study on model-scale sloshing tests. *Journal of Marine Science and Technology*, 17:47–58, 2012. ISSN 0948-4280. URL <http://dx.doi.org/10.1007/s00773-011-0144-z>. 10.1007/s00773-011-0144-z.
- Kim, Y., Kim, S. Y., and Yoo, W. J. Statistical Evaluation of Local Pressures in Sloshing. In *International Offshore and Polar Engineering Conference (ISOPE)*. The International Society of Offshore and Polar Engineers (ISOPE), June 2010.
- Kim, Y., Kim, S. Y., Kim, J., and Lee, J. H. Comparison of sloshing pressures in 2D and 3D tanks. *International Journal of Ocean System Engineering*, 3(4):225–230, 2013.
- Kimmoun, Ratouis, A., and Brosset, L. Sloshing and Scaling: Experimental Study in a Wave Canal at Two Different Scales. In *International Offshore and Polar Engineering Conference (ISOPE)*. The International Society of Offshore and Polar Engineers (ISOPE), June 2010.
- Kleefsman, K. M. T., Fekken, G., Veldman, A. E. P., Iwanowski, B., and Buchner, B. A volume-of-fluid based simulation method for wave impact problems. *Journal of Computational Physics*, 206(1):363–393, 6/10 2005.
- Kuo, J. F., Campbell, R. B., Ding, Z., Hoie, S. M., Rinehart, A. J., Sandstrom, R. E., Yung, T. W., Greer, M. N., and Danaczko, M. A. LNG Tank Sloshing Assessment Methodology for The New Generation. In *International Offshore and Polar Engineering Conference (ISOPE)*. The International Society of Offshore and Polar Engineers (ISOPE), June 2009.

- Lafeber, W., Brosset, L., and Bogaert, H. Elementary loading processes (ELP) involved in breaking wave impacts: findings from the Sloshe project. In *22nd International Offshore and Polar Engineering Conference (ISOPE)*, pages 265–276. The International Society of Offshore and Polar Engineers (ISOPE), June 2012.
- Lee, T., Zhou, Z., and Cao, Y. Numerical simulations of hydraulic jumps in water sloshing and water impacting. *Journal of Fluids Engineering*, 124(1):215–226, 2002. doi: 10.1115/1.1436097. URL <http://link.aip.org/link/?JFG/124/215/1>.
- Liao, K. and Hu, C. A coupled FDM-FEM method for free surface flow interaction with thin elastic plate. *Journal of Marine Science and Technology*, 18(1):1–11, 2013. ISSN 0948-4280. doi: 10.1007/s00773-012-0191-0. URL <http://dx.doi.org/10.1007/s00773-012-0191-0>.
- Loysel, T., Chollet, S., Gervaise, E., Brosset, L., and DeSeze, P. E. Results of the First Sloshing Model Test Benchmark. In *22nd International Offshore and Polar Engineering Conference (ISOPE)*. The International Society of Offshore and Polar Engineers (ISOPE), June 2012.
- Loysel, T., Gervaise, E., Moreau, S., and Brosset, L. Results of the 2012-2013 Sloshing Model Test Benchmark. In *23rd International Offshore and Polar Engineering Conference (ISOPE)*. The International Society of Offshore and Polar Engineers (ISOPE), June 2013a.
- Loysel, T., Gervaise, E., Moreau, S., Brosset, L., et al. Results of the 2012-2013 sloshing model test benchmark. In *The Twenty-third International Offshore and Polar Engineering Conference*. International Society of Offshore and Polar Engineers, 2013b.
- LRS. Sloshing Assessment Guidance. Document for Membrane Tank LNG Operations. Lloyds Register of Shipping. Technical report, Lloyds Register of Shipping, May 2009.
- Lugni, C., Brocchini, M., and Faltinsen, O. M. Wave impact loads: The role of the flip-through. *Physics of Fluids*, 18(12):101–122, 2006.
- Lugni, C., Brocchini, M., and Faltinsen, O. M. Evolution of the air cavity during a depressurized wave impact. II. The dynamic field. *Physics of Fluids*, 22(5):056102, 2010. doi: 10.1063/1.3409491. URL <http://link.aip.org/link/?PHF/22/056102/1>.
- Mehl, B., Oppitz, J., and Schreier, S. Sensitivity Study on the Influence of the Exciting Motion in Liquid Sloshing in a Rectangular Tank. In *23rd International Offshore and Polar Engineering Conference (ISOPE)*. The International Society of Offshore and Polar Engineers (ISOPE), June 2013a.
- Mehl, B., Schreier, S., and Puettmann, A. Sensitivity Study on the Influence of the Filling Height on the Liquid Sloshing Behavior in a Rectangular Tank. In *24th International*

- Offshore and Polar Engineering Conference (ISOPE)*, volume 3, pages 278–285. The International Society of Offshore and Polar Engineers (ISOPE), June 2014.
- Mehl, B., Oppitz, J., Schreier, S., et al. Sensitivity study on the influence of the exciting motion in liquid sloshing in a rectangular tank. In *The Twenty-third International Offshore and Polar Engineering Conference*. International Society of Offshore and Polar Engineers, 2013b.
- Neugebauer, J., Moctar, O. E., and Potthoff, R. Experimental and numerical investigation of single impacts in a 2D tank. In *24th International Offshore and Polar Engineering Conference (ISOPE)*, volume 3, pages 286–295. The International Society of Offshore and Polar Engineers (ISOPE), June 2014.
- Novo, T., Varum, H., Teixeira-Dias, F., Rodrigues, H., Silva, M. F., Costa, A. C., and Guerreiro, L. Tuned liquid dampers simulation for earthquake response control of buildings. *Bulletin of Earthquake Engineering*, pages 1–18, 2013.
- Ochi, M. *Applied probability and stochastic processes in engineering and physical sciences*. Wiley series in probability and mathematical statistics: Applied probability and statistics. Wiley, 1990. ISBN 9780471857426. URL <http://books.google.es/books?id=ID3xAAAAAAAJ>.
- Olsen, H. Local impact pressures in basically prismatic tanks. In *Seminar on Liquid Sloshing*, pages 1–24. Det Norske Veritas (DNV), 1976.
- Paik, K.-J. and Carrica, P. M. Fluid-structure interaction for an elastic structure interacting with free surface in a rolling tank. *Ocean Engineering*, 84(0):201 – 212, 2014. ISSN 0029-8018. doi: <http://dx.doi.org/10.1016/j.oceaneng.2014.04.016>. URL <http://www.sciencedirect.com/science/article/pii/S0029801814001553>.
- Panigrahy, P., Saha, U., and Maity, D. Experimental studies on sloshing behavior due to horizontal movement of liquids in baffled tanks. *Ocean Engineering*, 36(3-4):213 – 222, 2009. ISSN 0029-8018. doi: DOI:10.1016/j.oceaneng.2008.11.002.
- Park, T. H., Lee, H. H., and Shin, H. C. Regular design wave based sloshing assessment procedure. In *21st International Offshore and Polar Engineering Conference (ISOPE)*. The International Society of Offshore and Polar Engineers (ISOPE), June 2011.
- Parkus, H. *Random processes in mechanical sciences: course held at the Departments for mechanics of deformable bodies and for automation and information, September-October 1969*. International centre for mechanical sciences. Springer, 1969. URL <http://books.google.es/books?id=mdJgAAAAAAAJ>.
- Pastoor, W., Lund, K., and Tveitnes, T. The LNG Producer - A generic design with great adaptability. In *Offshore Technology Conference*, 2009.

- Peregrine, D. Water-wave impact on walls. *Annu. Rev. Fluid Mech.*, 35:23–43, 2003.
- Pickands, J. Statistical inference using extreme order statistics. *Annals of Statistics*, 3: 119–131, 1975.
- Pirner, M. and Urushadze, S. Liquid damper for suppressing horizontal and vertical motions-parametric study. *Journal of Wind Engineering and Industrial Aerodynamics*, 95(9-11):1329 – 1349, 2007. ISSN 0167-6105. doi: 10.1016/j.jweia.2007.02.010.
- Pistani, F., Thiagarajan, K., Seah, R., and Roddier, D. Set-up of a Sloshing Laboratory at the University of Western Australia. In *International Offshore and Polar Engineering Conference (ISOPE)*. The International Society of Offshore and Polar Engineers (ISOPE), June 2010.
- Pistani, F. and Thiagarajan, K. Experimental measurements and data analysis of the impact pressures in a sloshing experiment. *Ocean Engineering*, 52(0):60 – 74, 2012. ISSN 0029-8018. doi: 10.1016/j.oceaneng.2012.06.002. URL <http://www.sciencedirect.com/science/article/pii/S0029801812001990>.
- Press, W. H., Teukolsky, S. A., Vetterling, W. T., and Flannery, B. P. *Numerical Recipes 3rd Edition: The Art of Scientific Computing*. Cambridge University Press, New York, NY, USA, 3 edition, 2007. ISBN 0521880688, 9780521880688.
- Reed, D., Yu, J., Yeh, H., and Gardarsson, S. Investigation of tuned liquid dampers under large amplitude excitation. *Journal of Engineering Mechanics*, 124(4):405–413, 1998.
- Repalle, N., Truong, T., Thiagarajan, K., Roddier, D., Seah, R. K. M., and Finnigan, T. The effect of sampling rate on the statistics of impact pressure. In *ASME 29th International Conference on Offshore Mechanics and Arctic Engineering, OMAE2010*, June 2010.
- Rossing T.D., F. N. *Principles of Vibration and Sound*. Springer, 2004. ISBN 0387405569.
- Schreier, S. and Mehl, B. Experimental investigation of 3D sloshing effects in thin rectangular tanks. In *22nd International Offshore and Polar Engineering Conference (ISOPE)*. The International Society of Offshore and Polar Engineers (ISOPE), June 2012.
- Song, Y., Chang, K.-A., Ryu, Y., and Kwon, S. Experimental study on flow kinematics and impact pressure in liquid sloshing. *Experiments in Fluids*, 54(9):1592, 2013. ISSN 0723-4864. doi: 10.1007/s00348-013-1592-5. URL <http://dx.doi.org/10.1007/s00348-013-1592-5>.
- Souto-Iglesias, A., Delorme, L., Pérez-Rojas, L., and Abril-Pérez, S. Liquid moment amplitude assessment in sloshing type problems with smooth particle hydrodynamics. *Ocean Engineering*, 33(11-12):1462–1484, 8 2006.

- Souto-Iglesias, A., Botia-Vera, E., and Bulian, G. Repeatability and Two-Dimensionality of Model Scale Sloshing Impacts. In *22nd International Offshore and Polar Engineering Conference (ISOPE)*. The International Society of Offshore and Polar Engineers (ISOPE), June 2012.
- Tait, M., Damatty, A. E., Isyumov, N., and Siddique, M. Numerical flow models to simulate tuned liquid dampers (tld) with slat screens. *Journal of Fluids and Structures*, 20(8):1007 – 1023, 2005. ISSN 0889-9746. doi: 10.1016/j.jfluidstructs.2005.04.004. URL <http://www.sciencedirect.com/science/article/pii/S0889974605000587>.
- Van Den Bosch, J. and Vugts, J. On roll damping by free-surface tanks. *Trans. RINA*, 1966.
- Wemmenhove, R., Gladso, R., Iwanowski, B., and Lefranc, M. Comparison of CFD calculations and experiment for the dambreak experiment with one flexible wall. In *International Offshore and Polar Engineering Conference (ISOPE)*. The International Society of Offshore and Polar Engineers (ISOPE), June 2010.
- Yang, Q., Jones, V., and McCue, L. Free-surface flow interactions with deformable structures using an SPH-FEM model. *Ocean Engineering*, 55(0):136–147, 2012. doi: 10.1016/j.oceaneng.2012.06.031. URL <http://www.sciencedirect.com/science/article/pii/S0029801812002557>.
- Yung, T.-W., Sandstrom, R., He, H., and Minta, M. On the physics of vapor/liquid interaction during impact on solids. *Journal of Ship Research*, 54:174–183(10), 2010. URL <http://www.ingentaconnect.com/content/sname/jsr/2010/00000054/00000003/art00003>.
- Zhou, Z. Q., Kat, J. O. D., and Buchner, B. A nonlinear 3D approach to simulate green water dynamics on deck. In *Seventh international conference on numerical ship hydrodynamics*, pages 1–4, 1999.